

# **For Reference**

---

**NOT TO BE TAKEN FROM THIS ROOM**

Ex LIBRIS  
UNIVERSITATIS  
ALBERTAEISIS





Digitized by the Internet Archive  
in 2023 with funding from  
University of Alberta Library

<https://archive.org/details/Hepburn1973>











F.B.

THE UNIVERSITY OF ALBERTA

RELEASE FORM

NAME OF AUTHOR John Duncan Hepburn .....

TITLE OF THESIS Generation and Acceleration of Charged  
Liquid Particle Beams .....

DEGREE FOR WHICH THESIS WAS PRESENTED Ph.D. ....

YEAR THIS DEGREE GRANTED Fall 1973 .....

Permission is hereby granted to THE UNIVERSITY OF  
ALBERTA LIBRARY to reproduce single copies of this  
thesis and to lend or sell such copies for private,  
scholarly or scientific research purposes only.

The author reserves other publication rights, and  
neither the thesis nor extensive extracts from it may  
be printed or otherwise reproduced without the author's  
written permission.



THE UNIVERSITY OF ALBERTA

GENERATION AND ACCELERATION OF  
CHARGED LIQUID PARTICLE BEAMS

by

(C) JOHN DUNCAN HEPBURN

A THESIS

SUBMITTED TO THE FACULTY OF GRADUATE STUDIES AND RESEARCH  
IN PARTIAL FULFILMENT OF THE REQUIREMENTS FOR THE DEGREE OF  
DOCTOR OF PHILOSOPHY

DEPARTMENT OF ELECTRICAL ENGINEERING

EDMONTON, ALBERTA

FALL, 1973



UNIVERSITY OF ALBERTA  
FACULTY OF GRADUATE STUDIES AND RESEARCH

The undersigned certify that they have read, and recommend to the Faculty of Graduate Studies and Research, a thesis entitled "Generation and Acceleration of Charged Liquid Particle Beams" submitted by John Duncan Hepburn in partial fulfilment of the requirements for the degree of Doctor of Philosophy.

.....



## ABSTRACT

In the initial phase of this study, factors influencing the stability of charged liquid particle (colloid) beams produced by electrohydrodynamically spraying sodium iodide doped glycerol fluid from a single capillary tube were studied. Included were investigations into capillary materials and size, source geometries, and an extensive investigation of the resistivity properties of the fluid. In addition to using a segmented surface electrical beam detector for beam detection, two new types of visually reacting beam detector (a phosphor screen and a liquid crystal screen) were developed to allow analysis of beam spatial distributions. Detailed parametric analyses of the charge to mass ratios of particles in the beams, and the spatial distributions of the beams, were made for a wide variety of source geometries and operating conditions. The second phase of this study involved design of a colloid source for installation in the 300 kV microparticle accelerator facility at the Electrical Engineering Department, University of Alberta. The accelerator was modified to accommodate the colloid beam experiments. After the source had been successfully operated in the accelerator, experiments on accelerated colloid beams were started. The main topics investigated were particle source-to-detector transit times, beam envelope shapes, and the optical properties of the microparticle accelerator.



#### ACKNOWLEDGEMENTS

The author wishes to thank the supervisors of this project, Dr. F.E. Vermeulen and Dr. F.S. Chute, for the direction, encouragement, and help received during the course of the study.

The able assistance of the Department of Electrical Engineering University of Alberta, technical staff is gratefully acknowledged. In particular, Mr. J.J. George, Mr. D. Pasechnik, and Mr. K. Doerbekker contributed much to the project.

The author is deeply indebted to Atomic Energy of Canada Limited for granting him educational leave of absence from the Chalk River Nuclear Laboratories, and for the educational grant received throughout the duration of the project.

Thanks are also extended to the University of Alberta for financial support, including a PhD Dissertation Fellowship, during the work.

Preparation of the thesis was aided by Miss A. Russon, who helped with the preliminary drafts; Mrs. F. Barnard, who typed the final manuscript; and Mr. J. Schmidt, who checked the manuscript.



## TABLE OF CONTENTS

CHAPTER	PAGE
1. INTRODUCTION .....	1
1.1 Microparticles: Definitions and Occurrences .....	1
1.2 Applications and Uses of Microparticles .....	2
1.2.1 Space Sciences .....	2
1.2.2 Non-Impact Printing .....	4
1.2.3 Microparticle Plasma .....	4
1.2.4 Energetic Microparticle-Surface Interactions ....	5
1.3 Laboratory Generation of Microparticles .....	6
1.3.1 Solid Microparticles .....	6
1.3.2 Colloids .....	7
1.4 The Present Study .....	7
2. COLLOID SOURCES .....	10
2.1 The Basic Technique .....	10
2.2 Droplet Stability .....	12
2.2.1 The Rayleigh Criterion .....	12
2.2.2 Ion Emission Limit .....	17
2.2.3 Summary .....	17
2.3 Charged Species in the Colloid Beam .....	20
2.4 Beam Formation Mechanisms .....	21
2.5 Beam Spatial Distributions .....	23
2.6 Space Charge in Colloid Beams .....	24
2.7 Beam Energy Losses .....	29
2.7.1 Introduction .....	29
2.7.2 Mass Evaporation from In-Flight Droplets .....	29



2.7.3	Beam Formation Losses .....	39
2.7.4	Implications of Energy Losses .....	40
2.8	Operating Parameters and Their Effects .....	40
2.9	Secondary Particles .....	41
3.	DETECTORS .....	43
3.1	Introduction .....	43
3.2	Time of Flight Method Using Current Detection .....	44
3.2.1	Introduction .....	44
3.2.2	Analysis of Time of Flight Data .....	47
3.3	Beam Spatial Distribution Measurement Methods .....	54
3.3.1	Introduction .....	54
3.3.2	Segmented Electrical Detectors .....	56
3.3.3	Visually Reacting Beam Detectors .....	56
3.3.3.1	Introduction .....	56
3.3.3.2	Phosphor Screen Detector .....	57
3.3.3.3	Liquid Crystal Screen .....	58
3.4	Alternative Beam Detection Methods .....	59
3.4.1	Introduction .....	59
3.4.2	Single Particle Detection .....	59
3.4.3	Time of Flight Measurements Using Charge Detection .....	60
3.4.4	Quadrupole Mass Spectrometer .....	60
4.	SOLUTIONS SUITABLE FOR COLLOID BEAM PRODUCTION .....	62
4.1	Desired Properties of Solutions .....	62
4.2	Suitable Materials .....	63
4.3	NaI-Glycerol Solution Resistivity and Fluid Treatment ..	65



4.4 Other Fluid Properties .....	73
 5. TEST BENCH APPARATUS .....	77
5.1 Introduction .....	77
5.2 Vacuum System .....	77
5.3 Experimental Chamber .....	79
5.4 Liquid Colloid Source, and Fluid Handling System .....	80
5.5 Time of Flight Apparatus .....	83
5.6 Photographic Procedure .....	88
5.7 Data Recording Methods .....	89
 6. TEST BENCH RESULTS .....	91
6.1 Introduction .....	91
6.2 Beam Stability .....	92
6.2.1 Introduction .....	92
6.2.2 Start-Up Procedures .....	93
6.2.3 Beam Modes in a Typical Experiment .....	94
6.2.4 Unstable Beams .....	95
6.2.5 Capillary Voltage Stability .....	96
6.2.6 Particle Charge to Mass Ratios in a Beam Containing Both dc and Pulse Modes .....	98
6.2.7 Corona and Sparking at the Capillary Tube Tip ...	100
6.3 Beam Detectors .....	101
6.3.1 Introduction .....	101
6.3.2 Electrical Detectors .....	102
6.3.3 Phosphor Detector .....	103
6.3.4 Liquid Crystal Detector .....	104
6.3.5 Operation of Detectors .....	108



6.4	Secondary Particles .....	114
6.4.1	Positively Charged Secondary Particles .....	114
6.4.2	Secondary Electrons .....	114
6.5	Source Extractor Experiments .....	116
6.6	Capillary Tube Experiments .....	118
6.7	Fluid Experiments .....	125
6.8	Beam Spatial Distributions .....	126
6.8.1	Introduction .....	126
6.8.2	Low Voltage Operating Region .....	126
6.8.3	High Voltage Operating Region .....	132
6.8.4	Summary .....	138
6.9	Parametric Analysis .....	139
6.9.1	Introduction .....	139
6.9.2	Results for the Low Voltage Operating Region ...	141
6.9.3	Results for the High Voltage Operating Region ..	145
6.10	Experimental Sources of Inconsistency, Uncertainty, and Error .....	162
6.10.1	Introduction .....	162
6.10.2	Experimental Problems .....	163
6.10.3	Factors Influencing the Accuracy of Time of Flight Measurement Results .....	165
6.10.4	Discussion of Errors in Experimental Results ..	170
6.11	Comments on Beam Formation .....	170
6.12	Summary .....	171
7.	A COLLOID SOURCE FOR THE 300 KV MICROPARTICLE ACCELERATOR ..	173
7.1	Design Criteria .....	173
7.2	Mechanical Details of the Colloid Source .....	175



7.2.1	Description of the Pressure Converter .....	175
7.2.2	Mechanical Details of the Colloid Source .....	179
7.3	Tests of the Pressure Converter .....	187
7.3.1	Vacuum Leaks and Gas Diffusion .....	187
7.3.2	Pressure Calibration .....	188
7.3.3	Fluid Chamber Filling Procedure .....	193
7.4	Test Bench Results .....	195
8.	THE 300 kV MICROPARTICLE ACCELERATOR .....	196
8.1	Introduction .....	196
8.2	Operational Concepts .....	196
8.3	Vacuum System .....	202
8.4	Electronic Design of the Dome Circuitry .....	203
8.4.1	Introduction .....	203
8.4.2	General Description of the Circuit Blocks .....	204
8.4.3	Discussion of Individual Circuits .....	207
8.4.3.1	26 V Generator and Regulator .....	207
8.4.3.2	Bias Voltage Supply .....	209
8.4.3.3	Pulse Circuit .....	210
8.4.3.4	Grid Driver Circuit .....	212
8.4.3.5	Variable dc Regulator .....	215
8.4.3.6	High Voltage Supply .....	217
8.4.3.7	Tetrode Circuit .....	217
8.4.3.8	Optical Link Circuit .....	220
8.5	Pneumatic Control Scheme .....	222
8.6	Detectors .....	224
9.	ACCELERATED COLLOID BEAMS .....	226



9.1	Introduction .....	226
9.2	Operating Procedures for the Experiments .....	227
9.2.1	Operating Procedures for the Accelerator .....	227
9.2.2	Operation of Control Systems .....	228
9.3	The Colloid Source .....	231
9.3.1	Introduction .....	231
9.3.2	Experimental Development of the Colloid Source .	231
9.3.3	Experiments with the Electron Retarding Ring in the Collimator .....	235
9.3.4	Use of the Source, and Source Cleaning Procedures .....	236
9.4	Experiments Concerning the Accelerator Vacuum System ..	237
9.5	The Properties of the 300 kV Accelerator .....	244
9.5.1	Introduction .....	244
9.5.2	Isolation of the Accelerator Dome .....	245
9.5.3	Breakdown Across the Accelerator Gap .....	245
9.5.4	Measurement of X-Ray Radiation .....	249
9.6	Beam Detectors .....	250
9.6.1	Introduction .....	250
9.6.2	Electrical Detector .....	250
9.6.3	Visually Reacting Beam Detectors .....	252
9.7	Acceleration of Colloid Beams .....	255
9.7.1	Introduction .....	255
9.7.2	Presentation of Experimental Data .....	256
9.7.3	Currents Available from the Colloid Source .....	256
9.7.4	Secondary Electrons .....	259
9.7.5	Transit Time Experiments .....	262
9.7.5.1	Introduction .....	262



9.7.5.2	Theory of Particle Transit Times .....	264
9.7.5.3	Experimental Investigation of Particle Transit Times .....	269
9.8	Spatial Distributions of Accelerated Colloid Beams ....	273
9.8.1	Introduction .....	273
9.8.2	Theoretical Discussion of Accelerator Focussing Properties .....	274
9.8.3	Results of the Optics Experiments .....	276
9.8.3.1	Presentation of Data .....	276
9.8.3.2	Beam Shapes and Alignment .....	280
9.8.3.3	Beam Radii with No Acceleration, and Space Charge Effects .....	282
9.8.3.4	Focussing Properties of the Accel- erator .....	285
9.9	Summary .....	289
10.	CONCLUSIONS .....	291
REFERENCES	.....	296
APPENDIX A:	The Distribution of Charge, Mass, and Charge to Mass Ratio among Particles in the Colloid Beam .....	304
APPENDIX B:	Assembly Procedure for the Colloid Source .....	309
VITA	.....	312



LIST OF TABLES

Table		Page
1	Interactive Phenomena Associated with Energetic Microparticles and the Acceleration Potentials Required to Produce Them.	5
2	Maximum Values of Charge, Mass and Radius for Stable Glycerol Droplets as Calculated from the Rayleigh Criterion.	16
3	Beam Envelope Radius and Slope Angle Due to Space Charge in an Initially Cylindrical Beam of Radius $2.032 \times 10^{-4}$ m, at a Distance 0.3 m from the Source.	28
4	Summary of Results Available from a Time of Flight Measurement.	53
5	A Summary of Some of the Fluids and Doping Agents Used in Colloid Beam Production.	64
6	Values of Resistivity for NaI-Glycerol Solutions, as Quoted in the Literature.	66
7	Physical Constants of Pure Glycerol.	74
8	Vapour Pressure Versus Temperature of Glycerol.	76
9	Beam Current Waveforms, as a Function of Capillary Potential.	95
10	Types of Unstable Beam, with Possible Causes of Instability.	97
11	Capillary Tube Dimensions, Materials, and AWG Numbers, which Are Used in This Thesis as Identification for Capillary Sizes.	120
12	Technical Details for the Results Shown in Figures 19 and 20.	129
13	Technical Parameters and Measured Results for Colloid Beams Illustrated in Figures 23 and 24.	137
14	Source Parameters for the High Voltage Region Parametric Analyses Shown in Figures 27 to 34.	146
15	Experimental Parameters for Time of Flight Measurement Results Shown in Figures 35 to 37.	158
16	Time of Flight Measurement Results for the Measurements Shown in Figures 36 and 37.	162



17	Sources of Error in Time of Flight Measurements.	168
18	Dimensions of Bellofram Diaphragms Used in the Pressure Converter.	177
19	Part Descriptions of the Colloid Source.	180
20	Dimensions for the Two Accelerator Geometries Used in the Experiments.	235
21	Sparking Threshold Potentials across Various Accelerator Gap Widths, as Given by the Kilpatrick Criterion.	247
22	Parameters for Three Experiments on Transit Time Measurements, Corresponding to the Results Shown in Figure 63.	272
23	Experimental Details for the Results Displayed in Figures 68 to 70.	281
24	Comparison of Measured and Calculated Beam Radii (No Acceleration) at the Detector Position.	285



## LIST OF FIGURES

Figure		Page
1	Schematic of a Single Capillary Tube Colloid Source.	10
2	Forces on the Surface of a Charged Liquid Drop.	13
3	Stability Criteria for Charged Liquid Droplets.	19
4	Schematic of a Time of Flight Measurement Using Beam Current Detection, Showing the Apparatus and the Ideal and Actual Detected Current Waveforms.	45
5	Resistivity Cell Impedance Magnitude for Six Out-gassed NaI-Glycerol Solutions, as a Function of Measurement Frequency.	68
6	Temperature Dependence of NaI-Glycerol Solution Resistivity for Outgassed 5 g and 30 g NaI/100 mL Glycerol Solutions.	70
7	NaI-Glycerol Solution Resistivity, as a Function of Solution Doping Level.	72
8	Schematic of the Test Bench Apparatus and Colloid Source.	78
9	Cross-sectional View of the Colloid Source.	82
10	Schematic of the Capillary Potential Switching Circuit.	85
11	Capillary Potential Switching Circuit Waveforms.	87
12	Time of Flight Measurement Results on a Mixed Mode Colloid Beam.	99
13	Colour Photograph Depicting Results Obtained Using Phosphor, Liquid Crystal, and Segmented Electrical Detectors on One Particular Colloid Beam.	110
14	Comparison of Results Obtained Using Phosphor, Liquid Crystal, and Segmented Electrical Detectors on One Particular Colloid Beam.	111
15	Photographs of a Phosphor Detector, Comparing the Pattern of Light Emitted with the Corresponding Pattern of Deposited Glycerol.	113
16	Three Different Capillary Tube Tip Shapes Used in Colloid Beam Research.	119



17	Beam Current Spatial Distribution as a Function of Capillary Voltage, in the Low Voltage Operating Region.	127
18	Beam Current Spatial Distribution as a Function of Fluid Feed Pressure, in the Low Voltage Operating Region.	127
19	Beam Spatial Distribution as a Function of Capillary Voltage in the Low Voltage Operating Region, as Shown on the Phosphor Detector.	130
20	Comparison of Detector Results for the Phosphor, Liquid Crystal, and Segmented Electrical Detectors, Showing the Spatial Distribution of a Beam in the Low Voltage Operating Region.	131
21	Beam Current Spatial Distribution as a Function of Capillary Voltage, in the High Voltage Operating Region.	133
22	Beam Current Spatial Distribution as a Function of Fluid Feed Pressure, in the High Voltage Operating Region.	133
23	Three Beam Spatial Distributions for Beams in the High Voltage Operating Region, as Shown on the Phosphor Detector.	135
24	Spatial Distribution of a Beam Produced in the High Voltage Operating Region, as Observed on the Phosphor, Liquid Crystal, and Segmented Electrical Detectors.	136
25	A Parametric Analysis of the Low Voltage Operating Region, Showing the Measured Values of Charge to Mass Ratio in the Beam, in coul/kg.	142
26	Results of a Time of Flight Measurement on a Beam in the Low Voltage Operating Region.	144
27	Results of a Parametric Analysis of Colloid Source Behaviour in the High Voltage Operating Region.	147
28	Results of a Parametric Analysis of Colloid Source Behaviour in the High Voltage Operating Region.	148
29	Results of a Parametric Analysis of Colloid Source Behaviour in the High Voltage Operating Region.	149
30	Results of a Parametric Analysis of Colloid Source Behaviour in the High Voltage Operating Region.	150



31	Results of a Parametric Analysis of Colloid Source Behaviour in the High Voltage Operating Region.	151
32	Results of a Parametric Analysis of Colloid Source Behaviour in the High Voltage Operating Region.	152
33	Results of a Parametric Analysis of Colloid Source Behaviour in the High Voltage Operating Region.	153
34	Results of a Parametric Analysis of Colloid Source Behaviour in the High Voltage Operating Region.	154
35	Results of a Time of Flight Measurement on a Beam in the High Voltage Operating Region.	159
36	Results of a Time of Flight Measurement on a Beam in the High Voltage Operating Region.	160
37	Results of a Time of Flight Measurement on a Beam in the High Voltage Operating Region.	161
38	Schematic of the Pressure Converter.	178
39	Schematic Diagram of a Bellofram Rolling Rubber Diaphragm.	178
40	Cross-sectional Drawing of the Pressure Converter and Colloid Source.	182
41	Photographic Views of the Partly Assembled Colloid Source.	183
42	Photographic Views of the Assembled Colloid Source.	184
43	Schematic Diagram of the Pressure Calibration Scheme for the Pressure Converter.	189
44	Pressure Converter Calibration Curves for Four Piston Positions.	191
45	Apparatus Required for Filling the Source Chamber.	194
46	Side View of the 300 kV Microparticle Accelerator.	197
47	Plan View of the 300 kV Microparticle Accelerator.	198
48	Photographs of the 300 kV Microparticle Accelerator.	199
49	Schematic Diagram of the High Voltage Dome Circuitry.	206
50	Circuit Diagram of the Field Regulator.	208
51	Circuit Diagram of the Bias Power Supply.	211



52	Circuit Diagram of the Pulse Circuit.	213
53	Circuit Diagram of the Tetrode Grid Driver.	214
54	Circuit Diagram of the Variable dc Regulator.	216
55	Circuit Diagram of the High Voltage Supply.	218
56	Circuit Diagram of the Tetrode Circuit.	219
57	Circuit Diagram of the Optical Link.	221
58	Schematic Diagram of the Pneumatic Control Scheme.	223
59	Schematic Diagram of the Colloid Source Installed in the Source Chamber, and the Accelerating Electrodes.	233
60	Residual Gas Analysis Results for the Accelerator Vacuum System Prior to Colloid Source Operation.	241
61	Residual Gas Analysis Results for the Accelerator Vacuum System During Colloid Source Operation.	243
62	Dimensions of the Thirteen Segment Electrical Detector.	251
63	A Sequence of Transit Time Measurements on Accel- erated Colloid Beams, as a Function of Normalized Accelerating Potential.	257
64	Sketch of the Electrodes Used for Secondary Particle Experiments at the Detectors.	260
65	Sketch of the Approximation to the Potential Distribution across the Electrode Gap.	267
66	Schematic of the Accelerator, Showing the Potential of Components Relative to Laboratory Ground.	267
67	Experimental Transit Times Compared to the Theoretical Curve.	270
68	Comparison of Painted Surface and Segmented Elec- trical Detector Results for Beams Undergoing Zero Acceleration, and Normalized Acceleration of 2.28.	277
69	Comparison of Black Surface and Segmented Elec- trical Detector Results for Beams Undergoing Zero Acceleration, and Normalized Acceleration of 1.58.	278
70	Comparison of Black Surface and Segmented Elec- trical Detector Results for Beams Undergoing Zero Acceleration, and Normalized Acceleration of 4.57.	279



71	Beam Envelopes in the Accelerator, With and Without Space Charge Forces.	284
72	Results Showing the Reduction of Beam Radius Ratio as a Function of Normalized Acceleration Voltage.	287
73	Hypothetical Portrayal of the Fundamental Distribution of Particles over Charge and Mass.	305



## CHAPTER 1

### INTRODUCTION

#### 1.1 Microparticles: Definitions and Occurrences

The term 'microparticle' as applied to the work described in this thesis refers to a particle of matter, either in the solid or liquid state, whose size is of the order of microns ( $10^{-6}$  m) or less. A typical aluminum microparticle, for example, might have a radius of one micron, a mass of  $1.2 \times 10^{-19}$  kg, and contain  $2.4 \times 10^{11}$  atoms. In general the term 'colloid' refers to a suspension of material in a fluid, or discrete microparticles suspended in a medium. Examples of colloids might be a solution of starch in water, or by the second definition, liquid droplets in fog, solid particles in smoke, or bubbles in foam. Since the present work concerns the production and investigation of liquid microparticles in a vacuum, the terms 'colloid' and 'colloidal particle' will be taken to refer exclusively to individual liquid droplets. Thus, a source of small liquid droplets is referred to as a colloid source.

In a laboratory, the production, manipulation, acceleration, and investigation of microparticles is most easily carried out by charging them and then subjecting them to controlled electric fields. Use of magnetic forces is impractical because of the high magnetic field intensities required to exert significant forces on these charged particles. For example, a microparticle having a typical charge to mass ratio of 100 coul/kg and a typical velocity of  $10^3$  m/sec requires a field of  $100 \text{ wb/m}^2$  to bend it on a path of 0.1 m radius. However,



commercially available electromagnets with a pole face of 0.1 m diameter can generate magnetic fields of only 2 or 3 wb/m<sup>2</sup>.

The creation processes of naturally occurring microparticles involve the fracturing, erosion, or dispersion of matter. Due to the attendant rubbing and friction, particles thus created can often carry an electric charge. Additional charge can be deposited on these microparticles as they experience fluid friction in the air. The total charge, as well as the minute size of the microparticles, aids them in diffusing through the air and hinders particle agglomeration and settling.

Some occurrences of solid microparticles include coal dust in mines, dust created in grain handling, dust in smoke, and dust from volcanic eruptions. Clouds of micron sized particles, or micrometeoroids, are known to exist in space. Alexander<sup>1</sup> reports micrometeoroid flux rates of about 300 particles/m<sup>2</sup> sec for particles with masses between  $10^{-16}$  and  $10^{-14}$  kg. Liquid microparticles can be found in ocean spray, in the air spaces of oil tankers, in clouds and fog, and in the spraying of liquids to form aerosols.

## 1.2 Applications and Uses of Microparticles

### 1.2.1 Space Sciences

Information on the sizes, fluxes and composition of micrometeoroids provides insights into cosmic processes. In addition, designers of spacecraft must know the effects of the continual bombardment of spacecraft by micrometeoroids in order to prevent equipment damage and failure. Spacecraft components affected by micrometeoroid bombardment include optical surfaces, solar cell arrays and heat



exchangers. Unfortunately, experiments to investigate extra-terrestrial microparticles are expensive, time-consuming, and difficult to perform.

Interest in the laboratory simulation of micrometeoroids has instigated much of the work on solid microparticles. Several schemes for charging, accelerating, and detecting the microparticles have been used<sup>2,3,4,5</sup>. Experiments performed have included investigations of microparticle-surface impact phenomena<sup>6</sup>, studies of electrical breakdown across a gap initiated by the impact of microparticles on one of the gap electrodes<sup>7</sup>, and space probe detector design and calibration (Vermeulen<sup>2</sup> reviews some of this work).

Colloidal particles do not physically resemble micrometeoroids. However, they show much promise as laboratory aids to the study of solid microparticles. For instance, the properties of a microparticle accelerator, such as the limits on the energy and momentum of the incoming particles, the energy and momentum of the output particles, focussing, and acceleration can be readily measured using a continuous stable beam of colloids with a narrow distribution of charge to mass ratio. Such a beam is relatively more easily generated than a beam of solid microparticles, and its parameters are more easily varied. Once the properties of the accelerator are known, the simulation of micrometeoroids using solid microparticles can be undertaken, using a low intensity beam.

A second application of microparticles is in rocket engines, or thrusters. Mission analyses for space flights have shown that electric rocket engines are potentially the most suitable type for certain missions<sup>8,9</sup>. An important class of electric propulsion rocket utilizes



microparticles which are charged, accelerated, and expelled at high velocity. Efforts to construct efficient practical solid microparticle thrusters have not been successful. On the other hand, liquid colloid thrusters have been developed to the point where they are ready for in-flight testing<sup>10</sup>. Potential applications of colloid thrusters include attitude control and stationkeeping, where easily controllable thrusters with a long lifetime are required. Colloid thrusters are also suitable for interplanetary missions, if rockets with sufficient thrust can be developed.

### 1.2.2 Non-Impact Printing

The need for fast, quiet printers compatible with computers has led to much research into the electrohydrodynamic spraying of ink jets onto paper (Kamphoefner<sup>11</sup> presents a comprehensive review paper). Either arrays of capillary tubes are controlled, or a single ink jet is deflected electrostatically to form the printed characters. In all cases, problems such as beam spatial characteristics, beam stability, fluid characteristics and operating parameters are the same as those associated with colloid sources in other applications. Little interest has been shown to date in solid microparticles in this application.

### 1.2.3 Microparticle Plasma

One interesting but as yet purely fundamental application of colloids is the generation of a microparticle plasma. James and Vermeulen<sup>12</sup> have shown that a 'mixture' of positively and negatively charged colloids exhibits many of the phenomena characteristic of the standard electron-ion plasmas. No practical application of microparticle plasmas has as yet been found.



#### 1.2.4 Energetic Microparticle-Surface Interactions

The possibilities of energetic microparticle-matter interactions for various ranges of particle velocities have been discussed by Harrison<sup>13</sup>. Table 1 summarizes some of Harrison's results. The acceleration potentials required to achieve various particle velocities using particles with charge to mass ratios of 5 and  $5 \times 10^4$  coul/kg are also given.

Table 1: Interactive Phenomena Associated with Energetic Microparticles and the Acceleration Potentials Required to Produce Them.

Particle Velocity v*	Energy per Nucleon, e* (typical of a 1 micron diameter particle)	Temperature of Impact Area*	Impact Phenomenon*	Acceleration Potential Req'd for Charge to Mass Ratio	
(m/sec)	(eV)	(°K)		5 coul/kg (V)	$5 \times 10^4$ coul/kg (V)
$10^3 < v < 10^4$	$10^{-2} < e < 1$	$10^4$	cratering	$> 10^5$	$> 10$
$10^4 < v < 10^5$	$1 < e < 10^2$	$10^5$	dense, cool plasma	$> 10^7$	$> 10^3$
$10^5 < v < 10^6$	$10^2 < e < 10^4$	$10^7$	dense, hot plasma	$> 10^9$	$> 10^5$
$10^6 < v < 10^7$	$10^4 < e < 10^6$	$10^9$	fusion conditions	$> 10^{11}$	$> 10^7$
$10^7 < v$	$10^6 < e$	-	thermo-nuclear phenomena	$> 10^{13}$	$> 10^9$

\* from Harrison<sup>13</sup>



Table 1 shows that solid microparticles, charged by currently available methods<sup>2</sup> to between  $10^{-3}$  and 10 coul/kg, would require excessively large accelerators to produce hot plasma or fusion phenomena since acceleration potentials of greater than  $10^9$  volts are required. On the other hand, colloids have been produced with charge to mass ratios<sup>14</sup> in excess of  $10^4$  coul/kg, and hence show some promise of being accelerated to the hypervelocities shown in the table without requiring unduly large accelerators.

A ramification of the figures quoted in Table 1 is discussed by Pozwolski<sup>15</sup>. He describes, in a patent application, a nuclear reactor consisting of a beam of energetic microparticles (containing uranium, deuterium and tritium) impinging on a heavy metal such as uranium. Sufficiently energetic particles could cause fusion and fission in the target area, thus initiating the release of large amounts of energy.

### 1.3 Laboratory Generation of Microparticles

#### 1.3.1 Solid Microparticles

Previous work in this laboratory has exclusively been carried out with solid microparticles<sup>2,16</sup>. Carbonyl iron, carbon, and aluminum particles in the size range 0.5 to 20 microns diameter have been charged and accelerated. Recently a 300 kV dc accelerator has been built for microparticle studies. Several methods of charging solid microparticles can be used in laboratory experiments. In contact charging, the particles touch an electrode held at high potential, receive a charge during the contact, then are expelled at high velocity in the strong electric field at the electrode surface<sup>2,16,17</sup>.



Particles can also be charged by ion bombardment<sup>18</sup>, or in the gap of a parallel plate capacitor<sup>19</sup>. Typical charge to mass ratios for solid particles range between  $10^{-3}$  and 10 coul/kg. Thus, the net charge on a microparticle with mass  $10^{-14}$  kg and charge to mass ratio 1 coul/kg is  $10^{-14}$  coul, or about  $6 \times 10^4$  electronic charges.

### 1.3.2 Colloids

Liquid colloidal particles are produced by forcing a conducting non-volatile fluid, such as a solution of glycerol doped with sodium iodide, through a capillary tube held at high potential opposite an aperture in a grounded plane. The intense electric field at the capillary tip produces a filament of charged fluid, which subsequently breaks up into tiny charged droplets. Particles with charge to mass ratios of  $10^{-1}$  to  $10^4$  coul/kg can be produced. Estimates on the basis of certain electrohydrodynamic stability criteria (Section 2.2) show that a droplet with a charge to mass ratio of  $10^3$  coul/kg contains at most  $6 \times 10^{-17}$  coul (~400 electronic charges) and at most  $6 \times 10^{-20}$  kg of fluid. As the charge to mass ratio is increased, the particles contain less charge and less mass. Many researchers have investigated liquid colloids, and the works of Wineland and Burson<sup>20</sup>, Kidd<sup>21</sup>, and Cohen, Burson, and Herren<sup>14</sup> give representative results.

### 1.4 The Present Study

The existing research program of the microparticle study group has concentrated on the charging, acceleration, focussing and transport of solid microparticles<sup>2,16,22</sup>. The main laboratory facility is a 300 kV dc single gap accelerator.



The present study is concerned with colloid sources. The goals of the study are to develop a source producing a well focussed beam of charged colloids with a narrow range of charge to mass ratios with average values from 1 to 500 coul/kg. The emphasis is on developing a very versatile source that can be easily manipulated while in the 300 kV dome, and which can generate reproducible beams with particles of predetermined charge to mass ratios. Once suitable colloid beams have been established, these beams will be accelerated in the 300 kV accelerator.

In the initial phases of the study, a colloid source was built and set up in a test bench vacuum chamber. Colloidal particle beam detectors for measuring the beam current were developed, along with visually reacting detectors for observing beam spatial distributions. Source parameters such as source geometry, working fluid resistivity, operating voltage, and fluid pressure were varied and their effects on the colloid beam were noted. When a stable, continuous beam current had been established, the charge to mass ratio distribution and average value of the beam were measured, and the beam spatial distribution was observed.

Once a set of source operating conditions that produced a suitable beam had been found, a parametric analysis of the colloid source was performed. The average charge to mass ratio of particles in the beam and charge to mass ratio distribution were measured as the capillary tube size, fluid resistivity, capillary voltage, and fluid pressure were varied through an operating range.

The results of these investigations showed that a colloid source would be suitable for use in the 300 kV accelerator. Accordingly, a



new source was designed and built for this purpose. The accelerator was extensively modified to allow more convenient usage during the experiments, and to permit control and operation of the colloid source.

In the final experiments, the colloid source was operated in the accelerator, and the beam accelerated through potentials of up to 90 kV. The observed behavior of the beam was compared to the results of a theoretical discussion of the focussing and accelerator properties. The operation of the source in the accelerator and the acceleration of the colloid beam showed that colloid beams can be used in energetic microparticle research.



## CHAPTER 2

### COLLOID SOURCES

#### 2.1 The Basic Technique

Most of the current understanding of colloid sources has come from research specifically oriented towards microthruster applications. As a result, emphasis has been on high charge to mass ratio, high thrust beams. Much work in the field<sup>21,23,24</sup> has used a simple device consisting of a single capillary tube, as shown in Figure 1. Dimensions and operating parameter values shown are typical of both the present study and single capillary colloid sources reported in the literature. The working fluid, typically sodium iodide doped glycerol, is forced from the tip of the capillary by the feed pressure, charged at the capillary tip, and expelled at high velocity out through the hole in the extractor plate.

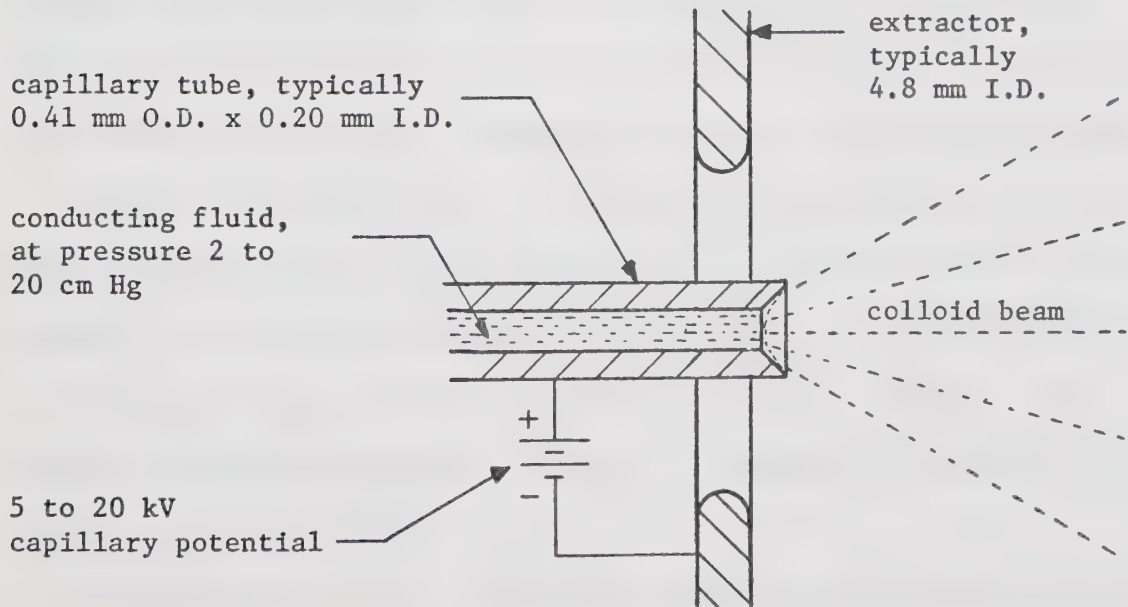


Figure 1: Schematic of a Single Capillary Tube Colloid Source



Variations on this apparatus have included various capillary sizes and shapes<sup>25,26</sup>, arrays of capillary tubes<sup>10,27</sup>, linear slits<sup>25</sup>, and annular slits<sup>28,29,30</sup>. In each case the beam is formed in the same fashion as in the single capillary tube version. Since this thesis is concerned with producing a stable, focussed beam with a relatively low charge to mass ratio, the single capillary tube apparatus in its simplest form appears to be adequate for the current experiments.

Spacecraft are electrically isolated in space, so there must be no net charge flow in the electric microthruster exhaust beam. Development of colloid thrusters with no net charge flow has led to investigation of positively and negatively charged colloid beams. One microthruster design uses two interposed arrays of capillary tubes, one of them operating at positive capillary potential and the other at negative potential<sup>31</sup>. Another method of producing no net charge flow beams is to operate a single capillary needle with an alternating current high voltage waveform on it<sup>32</sup>. Again, the specific application of the colloid source developed in the present work for use in the microparticle accelerator requires only positively charged beams, which are produced by applying a positive dc voltage to the capillary tube.

Several different types of beam detector can be used. For the purpose of discussion in this chapter, only a current detector is considered. The beam is intercepted by a metal plate, and the current carried by the beam is then fed through a resistor to ground. The voltage generated across the resistor is monitored to show the magnitude of the beam current.

The remainder of this chapter deals with colloid beams as reported in the literature, and problems associated with using them. Only the



section on spray mechanisms (Section 2.4) refers specifically to single capillary sources; the remaining discussion applies to colloid beams in general.

## 2.2 Droplet Stability

### 2.2.1 The Rayleigh Criterion

A charged liquid drop is stable provided the repulsive forces of the surface charge do not exceed the cohesive forces of surface tension. In 1882 Lord Rayleigh discussed the stability of a charged liquid drop by examining the Legendre Polynomial expansion of the equation describing the surface shape of a perturbed spherical drop<sup>33</sup>. It was found that the drop was stable provided that

$$q^2 \leq 16\pi a^3 \gamma , \quad (2.1)$$

where  $q$  is the drop charge,  $a$  the drop radius, and  $\gamma$  the surface tension in e.s. units. This work was discussed and rederived by Hendricks and Schneider<sup>34</sup>, in 1963. In MKSA units the Rayleigh Criterion becomes

$$q^2 \leq 64\pi^2 \epsilon_0 a^3 \gamma . \quad (2.2)$$

This result can also be derived by considering a force balance for an increment of surface area on a charged droplet. As shown in Figure 2, the three force components acting on the droplet surface increment are the outward electrostatic force per unit area  $f_e$  due to the net droplet charge, the inward pressure  $f_s$  due to surface tension, and the outward pressure  $f_h$  due to the internal hydrostatic pressure in the fluid.



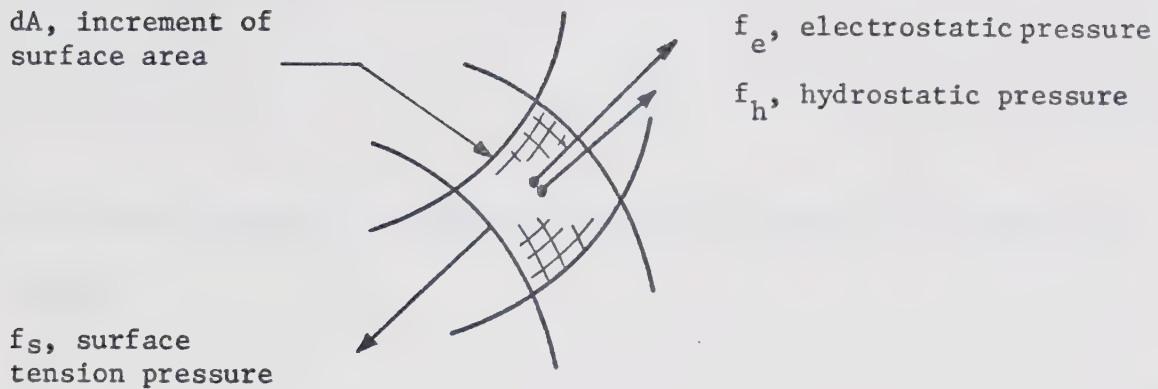


Figure 2: Forces on the Surface of a Charged Liquid Drop

The surface tension pressure and hydrostatic pressure are taken relative to the pressure of the medium surrounding the drop. The fluid is assumed to be incompressible, so the droplet has a constant radius  $a$ , constant surface tension pressure  $f_s$ , and the hydrostatic pressure  $f_h$  varies as charge is added to or removed from the drop.

The force balance equation for the three forces on the unit area  $dA$  is

$$f_s dA = f_h dA + f_e dA , \quad (2.3)$$

where the force directions are defined in Figure 2. From electrostatics<sup>35</sup> the electric field  $E$  at the surface of a spherical drop of radius  $a$ , carrying a charge  $q$  is

$$E = \frac{q}{4\pi\epsilon a^2} , \quad (2.4)$$

where  $\epsilon$  is the permittivity of the medium surrounding the drop. Also,



the outward electrostatic force per unit area is

$$f_e = \frac{\epsilon E^2}{2} . \quad (2.5)$$

The outward hydrostatic pressure due to an internal fluid pressure  $p$  is just

$$f_h = p . \quad (2.6)$$

The general equation for the inward pressure differential created between media with static pressures  $p_1$  and  $p_2$  across a curved surface with radii of curvature  $r_1$  and  $r_2$  is

$$p_1 - p_2 = \gamma \left( \frac{1}{r_1} + \frac{1}{r_2} \right) , \quad (2.7)$$

where  $\gamma$  is the surface tension<sup>36</sup>. For a spherical drop of radius  $a$ ,  $r_1 = r_2 = a$ . Thus the surface tension pressure, from equation 2.7, is

$$f_s = \frac{2\gamma}{a} . \quad (2.8)$$

Substitution of equations 2.4, 2.5, 2.6, and 2.8 in the force balance equation 2.3 gives

$$\frac{2\gamma}{a} = \frac{q^2}{32\pi^2 \epsilon a^4} + p . \quad (2.9)$$

If the droplet is initially uncharged, the surface tension force is balanced by the internal pressure. As charge is progressively increased on the droplet, the internal pressure decreases to maintain



surface stability by equalizing the forces on the unit surface area.

At some value of charge,  $q_1$ , the internal pressure is exactly zero, and from equation 2.9,

$$q_1^2 = 64\gamma\pi^2\varepsilon a^3 .$$

If the total charge  $q$  is increased above  $q_1$ , the outward electrical force on the surface increment exceeds the inward surface tension force and the drop fractures. The drop cannot expand because the fluid is incompressible, and for the same reason internal pressure cannot be negative. Therefore the drop is stable for charges  $q$  such that

$$q \leq q_1$$

or

$$q^2 \leq 64\pi^2\gamma\varepsilon a^3$$

which is the Rayleigh Criterion.

Using the relationship between the mass  $m$ , density  $\rho$  and radius  $a$  of a spherical droplet

$$m = \frac{4}{3} \pi \rho a^3 ,$$

the criterion can be rewritten in several forms, where  $K$  is a constant given by

$$K = 48\pi\gamma/\rho . \quad (2.10)$$

These equivalent forms are

$$q^2 \leq Km , \quad (2.11)$$

$$q \leq K(m/q) , \quad (2.12)$$



and

$$m \leq K(m/q)^2 , \quad (2.13)$$

$$a \leq \left( \frac{12\epsilon\gamma}{\rho^2} \left( \frac{m}{q} \right)^2 \right)^{1/3} . \quad (2.14)$$

In equations 2.11, 2.12, and 2.13, the parameters mass, charge, and charge to mass ratio appear. If one of these parameters is given, the limiting values of the remaining two can be calculated from the Rayleigh Criterion equations 2.11, 2.12, and 2.13. For example, these equations have been written with the charge to mass ratio,  $q/m$ , as the independent variable, and charge, mass, and therefore particle radius, can be calculated from it.

Table 2 shows some values of the upper limits on charge, mass and drop radius calculated as functions of charge to mass ratio using equations 2.10 through 2.14. The physical constants for pure glycerol given in Section 4.4 have been used.

Table 2: Maximum Values of Charge, Mass and Radius for Stable Glycerol Droplets of Given Charge to Mass Ratio, as Calculated from the Rayleigh Criterion.

Charge to Mass Ratio	Charge (coul)	Mass (kg)	Radius (m)
$10^{-2}$	$6.8 \times 10^{-12}$	$6.8 \times 10^{-10}$	$5.1 \times 10^{-5}$
$10^{-1}$	$6.8 \times 10^{-13}$	$6.8 \times 10^{-12}$	$1.1 \times 10^{-5}$
1	$6.8 \times 10^{-14}$	$6.8 \times 10^{-14}$	$2.3 \times 10^{-6}$
10	$6.8 \times 10^{-15}$	$6.8 \times 10^{-16}$	$5.1 \times 10^{-7}$
$10^2$	$6.8 \times 10^{-16}$	$6.8 \times 10^{-18}$	$1.1 \times 10^{-7}$
$10^3$	$6.8 \times 10^{-17}$	$6.8 \times 10^{-20}$	$2.3 \times 10^{-8}$
$10^4$	$6.8 \times 10^{-18}$	$6.8 \times 10^{-22}$	$5.1 \times 10^{-9}$



### 2.2.2 Ion Emission Limit

A second type of droplet stability limit arises from consideration of the field emission of ions from the surface of the droplet. Electron field emission does not occur because the droplets are positively charged. A conducting droplet of radius  $a$  and charge  $q$  has a surface electric field of

$$E = \frac{q}{4\pi\epsilon_0 a^2} . \quad (2.15)$$

Experimentally it has been shown that there exists a value of surface field,  $E_\ell$ , at which ions are emitted from that surface. The value of  $E_\ell$  for tungsten<sup>37</sup> is about  $10^{10}$  V/m. No corresponding data for charged liquid surfaces were found. Thus, for a given charge and limit field, the droplets are stable for

$$q \leq 4\pi\epsilon_0 a^2 E_\ell . \quad (2.16)$$

In terms of droplet mass this becomes

$$q \leq \left( \frac{36\pi m}{\rho} \right)^{1/3} \epsilon_0 E_\ell . \quad (2.17)$$

### 2.2.3 Summary

Figure 3 shows plots of both the Rayleigh Criterion and the ion emission limit, using equations 2.10, 2.11, and 2.17. Numerical values for constants used are those of glycerol, as given in Section 4.4. Curves for ion emission field limits of  $10^9$ ,  $10^{10}$ , and  $10^{11}$  V/m are shown, since the field limit for a glycerol surface is unknown. Values for charge to mass ratio calculated from equation 2.13 are



indicated along the Rayleigh Criterion curve. It can be seen that, for the conservative field limit of  $10^9$  V/m, the ion emission limit may be more restrictive than the Rayleigh Criterion at the charge to mass ratio values of interest in this study, which range from 1 coul/kg to 500 coul/kg. At a field limit of  $10^{10}$  V/m, the Rayleigh Criterion is the sole limiting factor for charge to mass ratios in this range.

Some experiments were performed by Hendricks<sup>38</sup> to investigate the Rayleigh Criterion. A plot of measured charge to mass ratio versus droplet radius for octoil droplets having charge to mass ratios in the range  $10^{-2}$  to 5 coul/kg showed that less than 0.3% of the droplets measured were in the predicted unstable region. It appeared that, at a given charge to mass ratio, the most probable droplet radius was of the order of 2/3 the maximum allowable value predicted by the Rayleigh Criterion. It is difficult if not impossible to test the criterion for higher values of charge to mass ratio because the very small charge values involved are below the single particle detector sensitivity limit, as shown in Section 3.4.2. Great care must be taken in applying the Rayleigh Criterion. For instance, charge flow limited or mass flow limited beam formation processes may produce stable droplets very close to or very far from the theoretical charge to mass ratio limit. At best, then, the criterion provides bounds on any two of the parameters charge, mass, and charge to mass ratio given a value for the third parameter. An additional problem is that the surface tension of the liquid may decrease as the bulk of liquid decreases, as shown in a theoretical discussion by Tolman<sup>39</sup>. Macroscopic values of the surface tension have been used throughout this work.



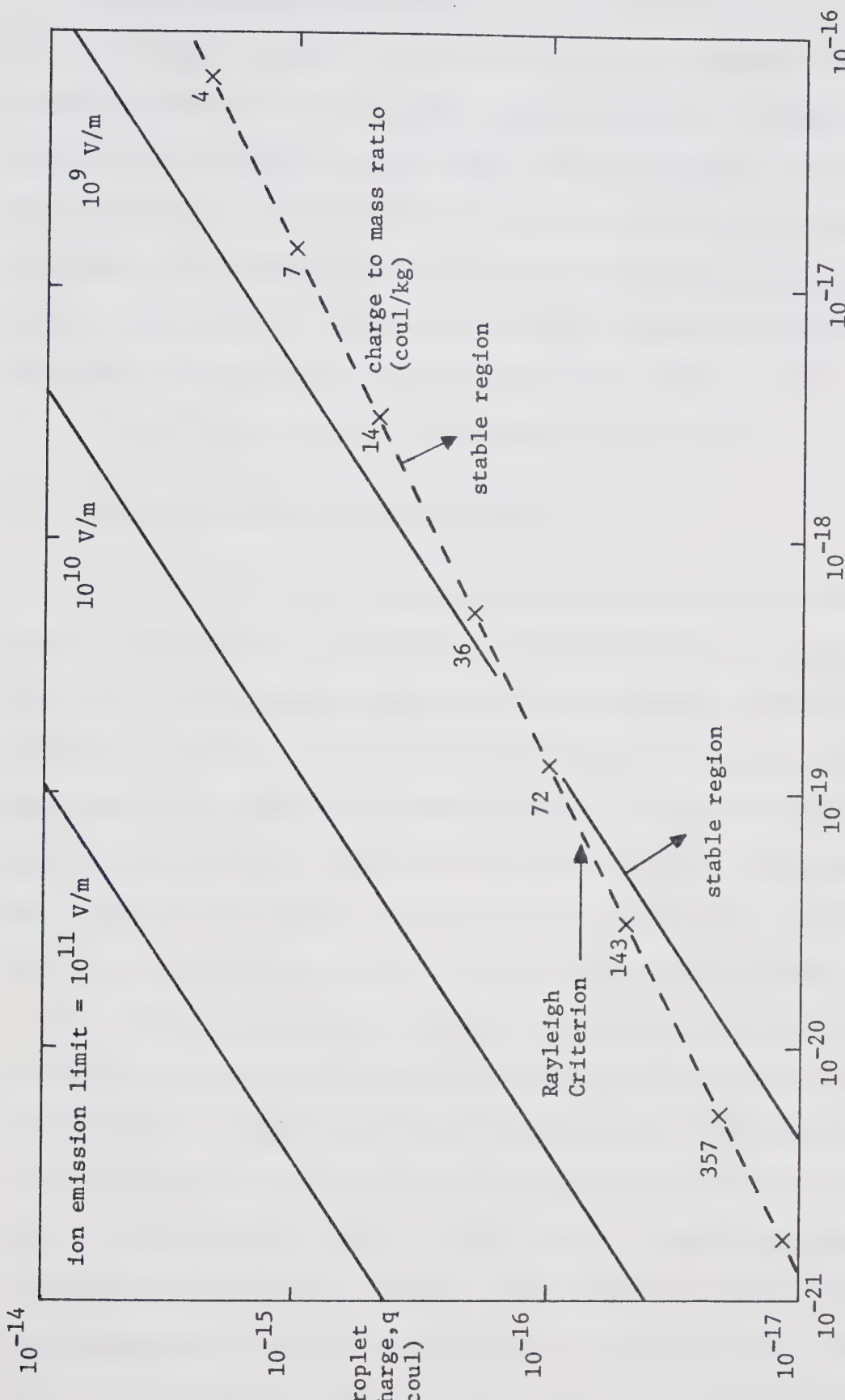


Figure 3: Stability Criteria for Charged Liquid Droplets



From the foregoing discussion it can be concluded that if a droplet is too highly charged, there are two mechanisms whereby it can be transformed into one or more stable droplets--particle breakup or ion emission. If a droplet splits in half, the two daughter droplets have the same charge to mass ratio as the parent, but each has a charge 0.707 times the theoretical maximum charge a droplet of its mass could stably carry (equation 2.11). In the second mechanism, ejection of ions from a charged droplet rapidly reduces the charge to mass ratio of the original large droplet, thus making it more stable.

### 2.3 Charged Species in the Colloid Beam

In any colloid beam there can exist a great variety of charged species. For instance, it is observed experimentally that ions are often produced when high charge to mass ratio colloidal particles are produced<sup>40</sup>. This occurs when highly conducting fluids, high capillary potentials, or low mass flow rates are used. Ions are also produced when poor vacuum at the capillary tip (caused by fluid out-gassing, poor vacuum in the system, or gaseous electrolysis products in the fluid) allows electrical corona to appear at the capillary tip.

The incidence of neutral particles in the beam is not usually detectable, because detection schemes generally utilize beam current. The fluid feed pressure, capillary dimensions, and fluid viscosity are such that with no applied capillary voltage, fluid drips very slowly from the capillary tip. Thus no neutral particles can be mechanically sprayed down the beam axis. There is some evidence, however, that fluid evaporates from droplets in flight (see Section 2.7.2). The free neutral fluid molecules so created may have a velocity partially



directed down the beam axis.

Under normal operating conditions, the majority of charge and mass transport occurs in droplets having charge to mass ratios close to the average value of charge to mass ratio for the entire beam. The width of the beam current versus charge to mass ratio distribution typically covers a range of one decade in charge to mass ratio, and the distribution width increases with increasing mass flow rate, charge to mass ratio, fluid conductivity, or capillary voltage.

#### 2.4 Beam Formation Mechanisms

In order to discuss colloid source operating modes, some terms defining the distinctive beam current waveforms are required. In the "pulse mode", the beam consists of groups of particles travelling together which produce regularly shaped, regularly spaced current pulses at the detector. The "dc mode" is characterized by a continuous, constant current level at the detector. A "current burst" is associated with the appearance of corona in the beam at the capillary tip and the production of many ions in the beam. The corresponding detected current waveform starts as an unstable pulse mode, changes to a wildly unstable dc mode, then falls to zero current for a short while.

Researchers using single capillary tube colloid sources have reported two stable types of beam--the pulse mode and the dc mode. (See, for example, Wineland and Burson<sup>20</sup>.) In general the pulses are formed when the source is operated at the low end of the operating capillary voltage range. As the voltage increases, the pulse period decreases, At some threshold voltage an abrupt shift to a stable dc mode is observed. The magnitude of the dc current increases as voltage is



increased, until further instabilities appear.

Some of the first attempts to photograph a capillary operating in the pulse mode were made by Carson and Hendricks<sup>41</sup>, and Hendricks et al<sup>42</sup>. Their results indicated that a pulse started when a large drop of fluid collected at the capillary tube tip, then was ejected by the electric field. Accompanying the large drop was a filament of fluid joining the drop to the fluid adhering to the needle tip. When this filament ruptured, it broke into highly charged droplets which travelled to the detector along with the initial, lowly charged drop. After a few milliseconds the fluid spray stops and fluid starts collecting at the capillary tip again. Since fluid accumulates in a drop on the end of the capillary tube in this mode, it may be said that this pulse mode is accompanied by a convex fluid meniscus at the capillary tip. Wuerker<sup>43</sup>, in a detailed study of pulsing beams using laser holography and flash shadowgraph photography, confirmed these results. He showed that the fluid filament connecting the initial large drop to the capillary tube tip, which could be up to several centimetres long, broke up subject to two or three types of instability, which could be theoretically related to electrohydrodynamic forces. The filament, or in some cases multiple filaments, originated at the tip of a conical meniscus. Taylor<sup>44</sup>, in studying fluid-fluid interactions in the presence of surface tension and electrostatic forces, illustrated the cone-and-filament phenomenon for other fluids, which tends to corroborate the work on colloid sources.

It appears that the capillary tip phenomena are quite different when the beam is operating in the stable dc beam mode instead of in the previously described pulse mode. Huberman and Cohen<sup>25</sup> have



published photographs of an operating capillary tip at 44.5 X magnification for a sequence of four voltages between 4.6 kV and 5.6 kV. These photographs show that the droplets are produced from many tiny jets of fluid distributed around the rim of the capillary tube. The jets are much smaller than the tube diameter. The overall fluid meniscus is concave, with the number of jets appearing on the capillary rim increasing as voltage is increased.

The pulse and dc modes of beam formation can be observed in one experiment by merely varying the operating voltage. Thus the two mechanisms do not represent any contradiction in results.

## 2.5 Beam Spatial Distributions

In addition to exhibiting a predictable sequence of beam types as operating parameters are varied (Section 2.4), colloid sources produce a series of different beam spatial distributions. Few detailed results are available on this topic because researchers generally have used detectors which measure total beam currents over large angles off the central beam axis. Geis<sup>24</sup>, and Geis and Turner<sup>45</sup>, showed that, for a stable dc beam created by a colloid source operating at typical values of source parameters, the beam is a hollow cone of discrete jets. The beam is anisotropic in mass flow rate, thrust, and charge to mass ratio. The hollow cone can have an included half-angle of up to 35°. Beam divergence increases with increasing mass flow rate, and decreases with increasing capillary voltage. The effects of beam divergence and anisotropy are of some importance in colloid microthruster applications and can be allowed for in thrust calculations. Beam divergence and anisotropy are of extreme importance to the present study,



which seeks a focussed, axial beam.

Section 6.8 shows that, in addition to the previously reported divergent beam shape, operating conditions can be found such that the beam consists of a cluster of discrete jets close to the central axis.

## 2.6 Space Charge in Colloid Beams

A question arising from the preceding discussion of large beam divergences (up to  $35^{\circ}$  off axis) is whether or not space charge effects in the beam contribute significantly to this beam divergence. Space charge forces are the electromagnetic forces on particles in the beam arising from the mutual electrostatic repulsion of the charged particles, and the constrictive force on the beam due to the magnetic field created by the beam current.

Space charge forces can be estimated using the following assumptions:

- (a) The beam is sufficiently diffuse that the beam current is not space charge limited, which means that all particles in the beam travel at a constant axial velocity  $v$  which is determined only by the source potential and is not influenced by the interaction of charged particles in the beam.
- (b) The beam diverges slowly, so that calculation of the electric and magnetic fields surrounding the beam can be based on a cylindrical beam shape.
- (c) The beam current is distributed uniformly over the cross-sectional area of the beam.

The following derivation of space charge effects follows Livingood<sup>46</sup> and Spangenberg<sup>47</sup>. The beam consists of a cylinder of



charged particles having charge to mass ratio  $q/m$  and axial velocity  $v$ . The cylinder is of radius  $r$ , carries a current  $i$ , and charge per unit length  $Q$ . The effects of space charge are evaluated by introducing a test particle also having charge to mass ratio  $q/m$ , charge  $q$ , mass  $m$ , and velocity  $v$ , travelling at radius  $r$  parallel to and at the surface of the cylindrical beam. The test particle represents a beam particle at the edge of the beam, therefore the radial motion of the test particle indicates the motion of the beam envelope in general. The electrostatic force on the test particle is

$$F_e = qE .$$

Here

$$E = \frac{Q}{2\pi\epsilon_0 r}$$

is the electric field at the surface of the beam, and  $\epsilon_0$  is the permittivity of free space. Since

$$Q = i/v ,$$

$$F_e = \frac{qi}{2\pi\epsilon_0 vr} . \quad (2.18)$$

This force tends to push the test charge outward. The inward magnetic force on the test particle due to the circumferential magnetic field  $B$  surrounding the current  $i$  is

$$F_m = qvB ,$$

where

$$B = \frac{\mu_0 i}{2\pi r} ,$$

and  $\mu_0$  is the permeability of free space. Thus the total outward force on the particle is



$$F = F_e - F_m$$

or

$$F = \frac{qi}{2\pi\epsilon_0 vr} (1 - \epsilon_0 \mu_0 v^2) . \quad (2.19)$$

The velocity  $v$  can be related to the source potential  $V$  by

$$v = \left( \frac{2qV}{m} \right)^{\frac{1}{2}} , \quad (2.20)$$

thus

$$F = \frac{qi}{2\pi\epsilon_0 r} \left( \frac{m}{2qV} \right)^{\frac{1}{2}} \left[ 1 - 2\epsilon_0 \mu_0 V \frac{q}{m} \right] . \quad (2.21)$$

Evaluation of the second term in equation 2.21 for typical values of source potential (20 kV), and charge to mass ratio (100 coul/kg) shows that the magnetic force  $F_m$  is  $4.5 \times 10^{-11}$  times smaller than the electrostatic force  $F_e$ , so  $F_m$  can be completely neglected. Therefore the equation of radial motion for the test particle is

$$m \frac{d^2r}{dt^2} = F_e , \quad (2.22)$$

or, by equation 2.18,

$$\frac{d^2r}{dt^2} = \frac{qi}{2\pi\epsilon_0 vm} \times \frac{1}{r} . \quad (2.23)$$

This equation can be transformed into a trajectory equation with variables beam radius  $r$  and axial position  $z$ , then normalized with respect to the initial beam radius  $r_0$ . Thus



$$\frac{d^2 r}{dt^2} = \frac{d^2 r}{dz^2} \left( \frac{dz}{dt} \right)^2 , \quad (2.24)$$

where  $dz/dt = v$  is a constant. Therefore equation 2.23 becomes

$$\frac{d^2 r}{dz^2} = \frac{q_i}{2\pi\epsilon_0 mv^3} \times \frac{1}{r} . \quad (2.25)$$

If  $R = r/r_o$  and  $Z = z/r_o$ , equation 2.25 becomes

$$\frac{d^2 R}{dZ^2} = \frac{q_i}{2\pi\epsilon_0 v^3 m} \times \frac{1}{R} . \quad (2.26)$$

This equation is integrated by multiplying through by  $dR/dZ$ , and yields

$$\left( \frac{dR}{dZ} \right)^2 = \frac{q_i}{2\pi\epsilon_0 v^3 m} \ln R + R_o'^2 . \quad (2.27)$$

Here  $dR/dZ = R'_o$  at  $R = 1$  and  $Z = 0$ . Equation 2.27 is reduced by transposing variables. An integration then gives

$$Z = \left( \frac{q_i}{2\pi\epsilon_0 v^3 m} \right)^{\frac{1}{2}} \int_1^R \frac{dR}{(\ln RA)^{\frac{1}{2}}} , \quad (2.28)$$

where

$$A = \exp \left( \frac{R_o' q_i}{2\pi\epsilon_0 v^3 m} \right) . \quad (2.29)$$

A transformation of variable  $t = (\ln RA)^{\frac{1}{2}}$  in this equation gives

$$Z = \left( \frac{2q_i}{\pi\epsilon_0 v^3 m} \right)^{\frac{1}{2}} \int_{(\ln A)^{\frac{1}{2}}}^{(\ln RA)^{\frac{1}{2}}} e^{-t^2} dt .$$



Using equation 2.20 to eliminate particle velocity yields the final expression

$$Z = \left( \frac{i}{\pi \epsilon_0 V^{3/2}} \left( \frac{2m}{q} \right)^{1/2} \right)^{1/2} \int_{(\ln A)^{1/2}}^{(\ln RA)^{1/2}} e^{-t^2} dt . \quad (2.30)$$

Equation 2.30 has been evaluated for various typical values of beam current, source potential, and particle charge to mass ratio at a fixed value of initial beam radius  $r_o = 2.032 \times 10^{-4}$  m, which is the outer diameter of the capillary tube used in much of the present work. Initial beam divergence has been set to zero ( $A = 1$  in equations 2.29 and 2.30). Table 3 shows results for beam envelope radius and beam envelope divergence angle at a distance 0.3 m downstream from the source.

Table 3: Beam Envelope Radius and Slope Angle Due to Space Charge in an Initially Cylindrical Beam of Radius  $2.032 \times 10^{-4}$  m, at a Distance 0.3 m from the Source.

Source Potential (kV)	Beam Current (amp)	Charge to Mass Ratio (coul/kg)	Beam Envelope Radius (m)	Beam Envelope Divergence (degrees)
20	$1 \times 10^{-9}$	100	$2.5 \times 10^{-4}$	$0.2^\circ$
20	$1 \times 10^{-7}$	10	$5.9 \times 10^{-3}$	$1.5^\circ$
5	$1 \times 10^{-6}$	100	$4.4 \times 10^{-2}$	$10.0^\circ$
5	$1 \times 10^{-6}$	10	$8.7 \times 10^{-2}$	$18.0^\circ$



Detailed comment on these results is difficult without comparison of an observed beam spatial distribution with the space charge effect calculated from the observed experimental beam parameters. However, it appears that the divergence angles calculated due to space charge may be as high as half the observed beam divergence. The values in Table 3 show that in applications of colloid sources requiring an axially focussed beam, space charge must be considered.

## 2.7 Beam Energy Losses

### 2.7.1 Introduction

The energy loss of the beam during the droplet formation processes and the energy loss during transit are important for two reasons. Firstly, droplet formation losses result in errors in the beam parameters calculated from the nominal value of capillary potential. Secondly, mass evaporation of fluid from a droplet means that the droplet charge to mass ratio increases and kinetic energy of the droplet decreases as it drifts along its trajectory. In colloid microthruster applications, only the formation loss is significant, while in microparticle accelerators both effects are important.

### 2.7.2 Mass Evaporation from In-Flight Droplets

In the present work, a system vacuum pressure of  $2 \times 10^{-6}$  torr was typical during colloid source operation. Gas analysis results for the gas in the vacuum chamber (Section 9.4) show that about half of the pressure, or  $1 \times 10^{-6}$  torr, could be attributed to glycerol vapour, and the remaining  $1 \times 10^{-6}$  torr was made up of residual gas and fractionated glycerol. Vapour pressure data for glycerol are presented in



Section 4.4, and show that at a vapour pressure of  $1 \times 10^{-6}$  torr the glycerol temperature is  $-19^{\circ}\text{C}$ . For lack of specific data it is assumed that the initial temperature of droplets formed at the colloid source is  $25^{\circ}\text{C}$ . At this temperature, the glycerol vapour pressure is  $1 \times 10^{-4}$  torr. As the  $25^{\circ}\text{C}$  glycerol is sprayed into the vacuum, glycerol is evaporated from the droplets because the vapour pressure at the glycerol surface is higher than the surrounding partial pressure of glycerol vapour. The energy needed to evaporate this mass from the drop must come from the thermal energy of the drop and its temperature falls until the drop becomes stable, at a temperature of  $-19^{\circ}$  and a vapour pressure of  $1 \times 10^{-6}$  torr.

Once this first phase of evaporation is complete, glycerol evaporation continues at a rate dependent on other considerations. Fluid must continue to be evaporated in order to replenish the vapour removed by the pumping system. However, most of this may in fact come from fluid deposited on the collimators or beam targets rather than from the beam in flight. Evaporation from the glycerol droplets in flight is nearly adiabatic. Thus the droplets will remain constant in size, once they have cooled to a temperature which equalizes droplet vapour pressure to the system partial pressure of glycerol, since heat cannot be transferred to the droplets in flight. Clearly this second stage of evaporation depends on several intangible considerations such as pumping speeds, conductances, and the amount of glycerol previously deposited on system surfaces.

An estimate of the speed of the gaseous glycerol molecules can be made from the average energy of one molecule,  $e_{\text{ave}}$ , which is found from gas dynamics<sup>48</sup> to be



$$e_{ave} = \left( \frac{1}{2} mv^2 \right)_{ave} = \frac{3}{2} kT , \quad (2.31)$$

where  $m$  is the molecule mass,  $v$  the molecule velocity,  $T$  the molecule temperature, and  $k$  is Boltzmann's Constant. If  $T$  is assumed to be  $300^{\circ}\text{K}$ , the root mean square molecule speed is found to be  $280 \text{ m/sec}$ . Now, a glycerol droplet with a charge to mass ratio of  $50 \text{ coul/kg}$  formed at a source potential of  $15 \text{ kV}$  (conditions typical of this study) travels at  $1.2 \times 10^3 \text{ m/sec}$ . When a molecule evaporates from the droplet, its thermal velocity (which is in a random direction) adds vectorially to its translational velocity directed towards the target. Because the translational velocity is of the same order of, or larger than, the thermal velocity, many of the evaporated molecules can be directed towards the beam detector as a neutral particle flux.

In 1965 Hunter and Wineland<sup>40</sup> calculated the mass loss and the time required to cool glycerol droplets from various initial temperatures down to the freezing point at  $18^{\circ}\text{C}$ , using a theory described by Gayle et al<sup>49</sup>. They calculated the mass loss of a particle cooling from an initial temperature of  $25^{\circ}\text{C}$  to be about 3% of the initial mass. The time required for the cooling process was  $4 \times 10^{-4} \text{ sec}$  for a particle of  $10^{-7} \text{ m}$  diameter, and  $4 \times 10^{-5} \text{ sec}$  for a particle of  $10^{-8} \text{ m}$  diameter.

Huberman and Cohen<sup>25</sup> reported beam energy losses of 23% for colloid beams with specific charge between  $10^3$  and  $1.5 \times 10^4 \text{ coul/kg}$ , capillary tube voltages between 6 and 13 kV, and a source to detector drift distance of 0.11 m. Beam energy at the detector was measured by observing the beam current transmitted through a variable potential retarding the incoming beam. The value of potential at which half the



beam was transmitted gave the equivalent beam energy at the detector.

Subsequently Huberman<sup>50</sup> performed further experiments which allowed separation of beam formation and evaporation effects. In these experiments the beam was directed through slits at the ends of an arc by electrostatic deflection, and beam energy was deduced from the potential applied to the deflecting electrodes. Examination of the particle energy data allowed measurement of the beam formation energy, which was found to be the equivalent of  $400 \pm 200$  volts on the capillary potential. The remaining loss, up to 23% of the capillary potential, was without further discussion, attributed to evaporative loss.

Because of the appreciable mass loss indicated by Huberman and Cohen<sup>25</sup>, an attempt to calculate mass loss due to evaporation is made here. Since the NaI-glycerol solutions used here are relatively dilute ( $\leq 1/10$  saturation), the physical constants for pure glycerol (as given in Section 4.4) are used. Newman<sup>51</sup> states that glycerol readily supercools to  $-83^{\circ}\text{C}$ , therefore calculations of mass loss during droplet cooling from  $25^{\circ}\text{C}$  to  $-19^{\circ}\text{C}$  are done for both the case where the fluid supercools to  $-19^{\circ}\text{C}$  and the case where it freezes at  $18^{\circ}\text{C}$  then cools to  $-19^{\circ}\text{C}$  as a solid. As pointed out above,  $-19^{\circ}\text{C}$  is the estimated temperature of glycerol in the experimental chamber. For both the supercooling and freezing cases, the calculated mass loss is found to be essentially independent of the thermal conductivity of glycerol, by considering the two limiting cases of very high and very low thermal conductivity. The calculations for these four cases are:

Case 1: Supercooled fluid, with very high thermal conductivity.

In this case, the droplet cools uniformly. The amount of heat  $dQ$  which must be removed to cool the mass  $m$  through a



temperature range  $dT$ , at specific heat  $c_{\ell}$  is<sup>52</sup>

$$dQ = c_{\ell} m dT , \quad (2.32)$$

while the heat required to evaporate a mass  $dm$  with latent heat  $\ell_e$  is

$$dQ = \ell_e dm . \quad (2.33)$$

Since these two amounts of heat must be equal,

$$\ell_e dm = c_{\ell} m dT . \quad (2.34)$$

Integration of this equation gives

$$\ln \left( \frac{m_f}{m_i} \right) = \frac{c_{\ell}}{\ell_e} (T_f - T_i) , \quad (2.35)$$

where the subscripts f and i denote final and initial values respectively. For the parameter values from Section 4.4 ( $c_{\ell} = 0.54 \text{ cal/gm}^{\circ}\text{C}$ ,  $\ell_e = 21 \text{ kcal/mole}$ ) and a temperature range of  $25^{\circ}\text{C}$  to  $-19^{\circ}\text{C}$ , the ratio of final to initial mass is

$$\frac{m_f}{m_i} = 0.92 . \quad (2.36)$$

Case 2: Supercooled fluid, with very low thermal conductivity.

For this case the surface of the drop cools immediately, hence the surface temperature is always  $-19^{\circ}\text{C}$  while the droplet interior cools gradually. Thus the entire initial mass  $m_i$  must be cooled through the complete temperature range. In this case the amount of heat lost is equivalent to

$$Q = c_{\ell} m_i \Delta T . \quad (2.37)$$



The mass of fluid lost to remove heat  $Q$  is just

$$\Delta M = \frac{Q}{\frac{\lambda}{e}} . \quad (2.38)$$

Thus,

$$\frac{m_f}{m_i} = 1 + \frac{c_\ell}{\frac{\lambda}{e}} (T_f - T_i) . \quad (2.39)$$

The numerical value for the mass ratio is

$$\frac{m_f}{m_i} = 0.90 .$$

Comparison of results for Case 1 and Case 2 show that the difference between the two values for mass loss is less than 3%, therefore an averaged value of  $m_f/m_i = 0.91$  can be used for these cases, in which the glycerol droplets supercool from  $25^\circ\text{C}$  to  $-19^\circ\text{C}$ . Thus about 9% of the initial droplet mass evaporates.

Case 3: Frozen fluid, with very high thermal conductivity.

In this case three distinct steps must be considered: cooling from the initial temperature of  $25^\circ\text{C}$  to the freezing point at  $18^\circ\text{C}$ , freezing at  $18^\circ\text{C}$ , then cooling from  $18^\circ\text{C}$  to  $-19^\circ\text{C}$ . The cooling of the liquid phase is described by equations 2.32 to 2.35. When equation 2.35 is evaluated for the temperature range  $25^\circ\text{C}$  to  $18^\circ\text{C}$ ,

$$\frac{m_\ell}{m_i} = 0.98 , \quad (2.40)$$

where  $m_\ell$  is the mass of liquid at  $18^\circ\text{C}$ . The drop is assumed to freeze from the outer surface inward, so the entire mass  $m_\ell$  must be frozen, and mass evaporation takes place from the frozen



surface. The amount of heat  $Q$  released by freezing a mass  $m_l$  with latent heat of fusion  $\lambda_f$  is

$$Q = \lambda_f m_l . \quad (2.41)$$

The amount of mass  $\Delta m$  evaporated by this amount of heat  $Q$  is

$$Q = \lambda_s \Delta m \quad (2.42)$$

where  $\lambda_s$  is the latent heat of sublimation.  $\lambda_s$  is assumed to be given by<sup>51</sup>

$$\lambda_s = \lambda_e + \lambda_f .$$

Now

$$\Delta m = m_l - m_s , \quad (2.43)$$

where  $m_s$  is the mass of frozen glycerol at  $18^\circ\text{C}$  left after the freezing process is completed. Therefore, from equations 2.41, 2.42, and 2.43,

$$\frac{m_s}{m_l} = 1 - \frac{\lambda_f}{\lambda_s} , \quad (2.44)$$

which has numerical value

$$\frac{m_s}{m_l} = 0.83 . \quad (2.45)$$

In the third stage of cooling, the solid mass  $m_s$  at  $18^\circ\text{C}$  is cooled to  $-19^\circ\text{C}$ . Since the solid has very high thermal conductivity, the mass cools uniformly and

$$dQ = c_s m dT \quad (2.46)$$



is the heat required to cool the mass through a temperature range  $dT$ , where  $c_s$  is the specific heat of solid glycerol. A solid mass  $dm$  is evaporated by heat  $dQ$ , as

$$dQ = \lambda_s dm . \quad (2.47)$$

Equations 2.46 and 2.47 give

$$\frac{\lambda_s}{c_s} dm = m dT , \quad (2.48)$$

which integrates to yield

$$\ln \left( \frac{m_f}{m_s} \right) = \frac{c_s}{\lambda_s} (T_f - T_s) . \quad (2.49)$$

Here  $m_f$  is the final mass at temperature  $T_f$ , and  $m_s$  is the mass of solid at temperature  $T_s = 18^\circ C$ . Numerical evaluation of equation 2.48 gives

$$\frac{m_f}{m_s} = 0.96 . \quad (2.50)$$

The total mass loss is given by

$$\frac{m_f}{m_i} = \frac{m_f}{m_s} \times \frac{m_s}{m_i} \times \frac{m_i}{m_f} \quad (2.51)$$

or, by equations 2.40, 2.45 and 2.51,

$$\frac{m_f}{m_i} = 0.77 .$$

Case 4: Frozen fluid with very low thermal conductivity.

In this case, the droplet cools and freezes from the



outside in. At any instant, the surface of the droplet is frozen at  $-19^{\circ}\text{C}$ , while the interior of the droplet is warmer. Therefore, the amount of heat released during the cooling process is the same as if the entire initial mass was cooled to the freezing point of  $18^{\circ}\text{C}$ , then the entire initial mass was frozen at  $18^{\circ}\text{C}$ , then the entire initial mass was cooled to  $-19^{\circ}\text{C}$  from  $18^{\circ}\text{C}$ . This heat is removed by the sublimation of glycerol from the frozen surface, at  $-19^{\circ}\text{C}$ . For the amount of heat  $Q_1$  released by the initial cooling of the liquid, equation 2.37 between the limits of  $25^{\circ}\text{C}$  and  $18^{\circ}\text{C}$  applies. Thus

$$Q_1 = c_l m_i \Delta T = -3.78 m_i \text{ cal/gm} . \quad (2.52)$$

The amount of heat  $Q_2$  released in freezing a mass  $m_i$  follows from equation 2.41, hence

$$Q_2 = \lambda_f m_i = -47.5 m_i \text{ cal/gm} . \quad (2.53)$$

The amount of heat  $Q_3$  released in cooling the solid mass  $m_i$  through a range  $18^{\circ}\text{C}$  to  $-19^{\circ}\text{C}$  is (from equation 2.45)

$$Q_3 = c_s m_i \Delta T = -1.11 m_i \text{ cal/gm} . \quad (2.54)$$

Therefore the total heat  $Q$  released by cooling the droplet is

$$Q = Q_1 + Q_2 + Q_3$$

or, from equations 2.52, 2.53, and 2.54,

$$Q = -52.4 m_i \text{ cal/gm} . \quad (2.55)$$



The mass of fluid sublimated by heat  $Q$  (from equation 2.42) is

$$\Delta m = \frac{Q}{\frac{l}{s}}$$

or, using equation 2.54,

$$m_f - m_i = -0.2 m_i .$$

This reduces to

$$\frac{m_f}{m_i} = 0.80 , \quad (2.56)$$

as the ratio of final to initial masses.

Comparison of Cases 3 and 4 shows that the value of thermal conductivity has only a small effect on the calculation of evaporative mass loss assuming the droplet freezes while cooling from 25°C to -19°C. Therefore an average value of 0.79 for the ratio of final to initial droplet mass can be used.

In summary, these calculations indicate a significant amount of the mass of a droplet evaporates, as the droplet cools to a temperature where the vapour pressure of the glycerol is in equilibrium with the partial pressure of glycerol in the vacuum chamber. For a partial pressure of glycerol of  $1 \times 10^{-6}$  torr, the amount of mass loss of a droplet is 9% if the glycerol supercools, and 21% if the glycerol freezes.

The mass loss of 3% for the cooling of a liquid drop from 25°C to 18°C derived by Hunter and Wineland<sup>40</sup> is consistent with the present calculation (equation 2.40 gives 2% for the same result). The mass loss of up to 23% measured by Huberman and Cohen<sup>25</sup> is in agreement with



the present calculation, in which a mass loss of 21% was found for the case where the droplets freeze.

The experimental parameters used by Huberman and Cohen<sup>25</sup> have been described earlier in this section. Their results show that for a particle formed at 6 kV and having a charge to mass ratio of  $10^4$  coul/kg, the particle traverses the source to detector distance in  $1 \times 10^{-5}$  sec and loses 23% of its mass in this time. On the other hand, Hunter and Wineland<sup>39</sup> calculated that a particle of  $10^{-8}$  m diameter loses 3% of its mass in  $4 \times 10^{-5}$  sec. The Rayleigh Criterion (equation 2.14) shows that a particle of  $10^{-8}$  m diameter has a charge to mass ratio of  $10^4$  coul/kg or less. Thus for similar particles taken over about the same evaporation time interval, results of 3% and 23% mass loss are indicated by the two different authors. Presumably this discrepancy can be attributed to specific assumptions leading to the calculated value of 3%, or specific experimental conditions in the measured value of 23%. However, it appears that the overall mass loss of a droplet injected into the vacuum is less than 25%.

### 2.7.3 Beam Formation Losses

While no complete theory of colloid beam formation exists, it is reasonable that the maximum energy of the droplet, given by the nominal capillary potential, may be reduced due to mechanisms such as ohmic losses during the charging of the fluid, fluid viscosity, and surface tension. As discussed in the previous section, Huberman<sup>50</sup> measured the droplet formation loss to be the equivalent of a  $400 \pm 200$  volt reduction in capillary potential.



#### 2.7.4 Implications of Energy Losses

The effect of energy losses on experimental measurements depends on the measurement method used. For methods using current detection, such as the time of flight method, only the particle formation loss affects the accuracy. Beam current is measured at the detector, and nominal source potential is used to calculate all other beam parameters. Therefore, if the beam charge is conserved, the time of flight method gives the beam parameters as they existed immediately beyond the particle creation point. Thus, the beam formation potential loss of about 400 volts should be subtracted from the capillary potential prior to these calculations. On the other hand, if charge is not conserved as the beam moves from the source to the detector, the time of flight method gives beam parameters derived from particle charge at the detector, particle mass at the source, and the nominal source potential.

Methods using retarding potential or electrostatic deflection analyzers measure particle energy at the point of measurement. Thus, all energy losses prior to the instant of measurement are included.

In this study only beam current detection has been used to perform measurements. Thus the results quoted here refer to beam properties very close to the source, not necessarily those at the point of measurement. Beam formation losses as reported by Huberman<sup>50</sup> were no larger than 6% in the present experiments and have been neglected.

#### 2.8 Operating Parameters and Their Effects

Much work has been done on parametric analyses of colloid beam sources. Kidd<sup>21</sup> gives extensive, representative results. The average charge to mass ratio of the beam is influenced by two classes of



effect--those which increase the fluid mass flow rate, and those which increase the electric field at the capillary tip. The increase in mass flow rate lowers the charge to mass ratio, and can be achieved by increasing capillary inner diameter, lowering fluid viscosity (by heating the fluid or choosing a different fluid), or increasing fluid feed pressure. The increase in electric field increases the charge to mass ratio, and is accomplished by decreasing capillary outer diameter, decreasing the capillary to extractor distance, or increasing the operating voltage. Increasing fluid conductivity also increases the charge to mass ratio.

There is an additional problem in choosing operating parameters because the beam is not stable for all combinations of parameters. For this reason much of the work discussed in Chapter 6 concerns trial-and-error experiments to find suitable operating conditions.

## 2.9 Secondary Particles

Several researchers report investigations into the production of secondary particles when a colloid beam strikes a surface<sup>25,27,28</sup>. The secondary particles may be either neutral or charged glycerol particles, or electrons. The glycerol secondary particles may be from shattered beam droplets, or from the mass of glycerol previously deposited on the target surface.

The secondary electrons present several problems. Firstly, the measured beam current is the sum of the positive charge arriving at the detector and the negative charge leaving it. Huberman and Cohen<sup>25</sup> show data where the secondary electron current is 4 or 5 times the incident positive beam current. Secondly, if the secondary electrons



are allowed to backstream towards the colloid source, the electrons cause instabilities in the colloid beam. These instabilities appear as short (less than 100  $\mu$ sec), positive- or negative-going spikes on the otherwise stable dc current level. Thirdly, prolonged bombardment of the capillary tube tip by secondary electrons leads to the build-up of a black, tar-like deposit on the capillary tip. This deposit may be a polymerized form of glycerol<sup>25</sup>. Finally, since the beam is positively charged, the electric field surrounding the positively charged beam can trap low energy electrons present in the experimental chamber. The trapped electrons may then combine with, and neutralize, the charged colloidal particles. The trapping of these electrons means that the measured beam current is less than the true current due to all the positive particles in the beam.

Successful operation of a colloid source often depends on the correct application of bias voltages on components in the experimental chamber to suppress the secondary electrons. Generally speaking, most researchers report using a suppression grid biased at -30 to -100 V directly in front of the detector surface. Also, the extractor in the colloid source is often biased at -300 to -500 V with respect to the experimental chamber walls in order to present an electron barrier to secondary electrons drifting towards the colloid source.



## CHAPTER 3

### DETECTORS

#### 3.1 Introduction

This chapter reviews some of the methods available for detecting and analyzing charged colloidal particle beams. The theoretical bases behind the detection methods used later in the experimental work are outlined. However, all material pertaining to development and realization of the detectors is presented in Section 6.3.

Choice of beam detection methods clearly depends on the information required. For the present study, the information must include:

- (a) the beam current,
- (b) the average charge to mass ratio of particles in the beam, and some estimate of the charge to mass ratios present on the particles in the beam,
- (c) the mass flow rate in the beam,
- (d) the spatial distribution of the beam.

The first three requirements are related to understanding the colloid source behavior and to assessing the suitability of the source for use in the microparticle accelerator. The fourth condition is essential to use of the colloid source in the microparticle accelerator, since the accelerator application requires a focussed axial colloid beam.

Detection methods described in the literature include: single particle detection<sup>2,38</sup>, time of flight methods utilizing current detection<sup>21,24,25</sup>, and the use of a quadrupole mass spectrometer<sup>40</sup>. Also, three completely new detection methods, namely time of flight methods



using charge detection, and two types of visually reacting beam detector, were investigated in the present work. Of all these methods, it was decided to use the time of flight method using current detection and the two visually reacting detectors in the experimental work. Reasons for these choices are given in the remaining sections of this chapter.

### 3.2 Time of Flight Method Using Current Detection

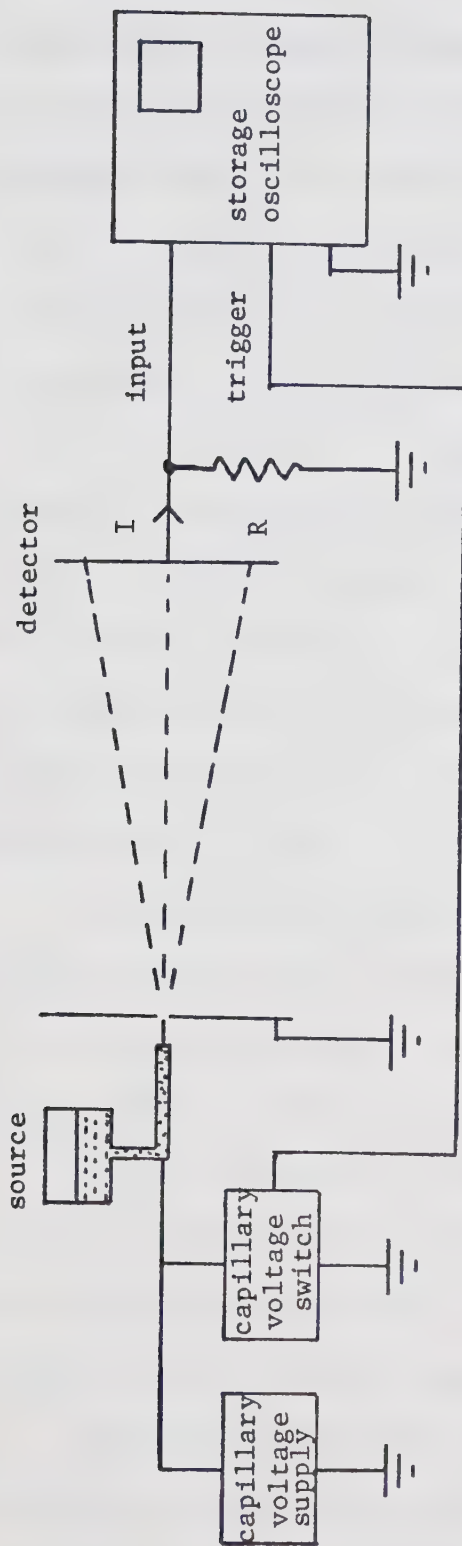
#### 3.2.1 Introduction

The time of flight measurement method was first used by Shelton and Cohen, and later described by Cohen<sup>53</sup> in 1964. It has been used for nearly all colloidal beam research performed since then. In this method, beam current is collected by a metal plate intercepting the beam. The current is fed through a resistor to ground and the voltage across the resistor is monitored on an oscilloscope to give the beam current waveform. Because only beam current is detected, the method gives average or total values of the parameters describing the beam.

Figure 4a illustrates the apparatus used in a time of flight experiment. The colloid source and current detector are indicated schematically. At some time  $t=0$ , the capillary voltage switch is activated to remove the source operating voltage, and the source ceases to produce particles. For some time after  $t=0$ , particles continue to arrive at the detector because they were traversing the source to detector drift distance at time  $t=0$ . Eventually all the particles have reached the detector and no further current is detected.

Physically speaking, the beam consists of a finite number of sub-beams, each of which contains particles of a given charge to mass ratio.





(a) Apparatus



(b) Ideal Detected Current Waveform

(c) Actual Detected Current Waveform

**Figure 4:** Schematic of a Time of Flight Measurement using Beam Current Detection, Showing the Apparatus and the Ideal and Actual Detected Current Waveforms. (Time  $t$  Indicates Elapsed Time after the Capillary Voltage Switch has been Activated to Shut Off the Source.)



Thus, the particles in the beam are distributed over discrete values of charge to mass ratio. This distribution will be referred to as the distribution of charge to mass ratios in the colloid beam. Since all particles are created by the same source voltage, the particles in each sub-beam travel at the same velocity. However, the various sub-beams travel at different velocities. Figure 4b, which shows the ideal current decay curve in a time of flight measurement, illustrates this phenomenon. At time  $t=0$ , the beam is turned off at the source. The dc current is observed to be constant until time  $t=t_1$ . At  $t=t_1$ , the particles comprising the fastest sub-beam have all arrived at the detector, hence the detected current decreases by an amount equal to the current contributed by the fastest sub-beam. The process of current decay continues until time  $t=t_f$ , when the last particles of the slowest sub-beam have all arrived at the detector, and the detected current falls to zero.

In practice, the measured current decay curve is a smooth curve because there are many sub-beams of particles in the total beam, and the method cannot resolve the individual sub-beams of particles. The actual curve is illustrated in Figure 4c.

Because the measured current decay curve appears as a smooth function of the measurement time  $t$ , the discussion and analysis of the time of flight method will assume a continuous, rather than a discrete, distribution of the charge to mass ratios of the particles in the beam.

Analysis of the time of flight data, which is described in the following section, yields much information on the properties of the colloid beam. Of this information, parameters of direct interest to the present investigation of colloid sources for use in the



microparticle accelerator are: total beam current, average charge to mass ratio, total mass flow rate, and an estimate of the charge to mass ratio distribution in the beam. The remaining information is applicable to colloid microthrust rocket research, and includes such parameters as: thrust, specific impulse, and beam efficiency<sup>24,25,32</sup>.

### 3.2.2 Analysis of Time of Flight Data

In this section, a detailed derivation of some of the parameters available from a time of flight measurement is given. The derived results give values for total current, total mass flow rate, and average charge to mass ratio in terms of the observed current decay curve. The remaining parameters are discussed in less detail.

The previous section has shown that a time of flight measurement yields a current decay curve  $I(t)$ , where  $t$  is the time elapsed since the measurement was initiated. Also, it is clear that at any instant  $t$ , the current  $I(t)$  is maintained by the current of all particle species in the beam with velocities

$$v \leq D/t , \quad (3.1)$$

where  $D$  is the source to detector drift distance. A function  $i(t)$  defined by

$$i(t) = \frac{-dI(t)}{dt} \quad (3.2)$$

gives the amount of current  $i(t)dt$  due to particles having a velocity between  $u(t)$  and  $u(t + dt)$ , where

$$u(t) = D/t . \quad (3.3)$$



(It must again be noted that this entire discussion assumes continuous distributions for all parameters describing the particles in the beam.)

Clearly

$$I(t) = \int_t^\infty i(t)dt . \quad (3.4)$$

The upper limit of integration in equation 3.4 could also be  $t_f$  since

$I(t) = i(t) = 0$  for all times  $t \geq t_f$ .

The kinetic energy of the particles is related to the source potential  $V$ , by

$$\frac{1}{2}mu^2 = qV , \quad (3.5)$$

where  $m$  = particle mass,  $q$  = particle charge, and  $u$  = particle velocity.

The charge to mass ratio of the particle  $c(t)$  is given by

$$c(t) = \frac{q}{m} = \frac{u^2}{2V} ,$$

or, by equation 3.3,

$$c(t) = \frac{D^2}{2Vt^2} . \quad (3.6)$$

The first result available from the time of flight measurement is a value for the total steady state beam current,  $I_0$ . This is given by

$$I_0 = I(0) = \int_0^\infty i(t)dt . \quad (3.7)$$

The mass flow rate of the beam is now considered.  $M(t)$  is defined as the mass flow rate incident on the detector at measurement time  $t$ .



A function  $\dot{m}(t)$ , defined as the distribution of mass flow rate over the measurement time  $t$ , is given by

$$\dot{m}(t) = - \frac{d}{dt} \dot{M}(t) . \quad (3.8)$$

In summary, then,  $i(t)dt$  represents the current, and  $\dot{m}(t)dt$  represents the mass flow rate, due to particles having velocity between  $u(t)$  and  $u(t + dt)$  and charge to mass ratio between  $c(t)$  and  $c(t + dt)$ . The function  $i(t)$  is defined as the distribution of current over measurement time  $t$ , and  $\dot{m}(t)$  is the corresponding mass flow rate distribution. The use of  $t$  as a parameter for the current distribution  $i(t)$  and mass flow rate distribution  $\dot{m}(t)$  allows immediate calculation of the current or mass flow rate contributed by particles having a given charge to mass ratio  $c(t)$  (from equation 3.6) or velocity  $u(t)$  (from equation 3.3). (It must be emphasized that the dot operator, '.', is not equivalent to the operator 'd/dt' since the former refers to the flow rate of charge or mass in the steady state beam, while the latter refers to times in the time of flight measurement period.)

The steady state mass flow rate for the complete beam is given by

$$\dot{M}_o = \dot{M}(0) = \int_0^\infty \dot{m}(t)dt . \quad (3.9)$$

The function  $\dot{m}(t)$  is now related to the function  $i(t)$  so that the integral in equation 3.9 can be evaluated in terms of the experimentally observed current decay curve. At some time  $t$ , consider only those particles having charge to mass ratio  $c(t)$  and velocity  $u(t)$ . These particles contribute a current  $i(t)dt$  and a mass flow rate  $\dot{m}(t)dt$  to



the entire colloid beam. Now,

$$i(t)dt = \frac{\text{charge}}{\text{unit beam length}} \times u(t) ,$$

and

$$\dot{m}(t)dt = \frac{\text{mass}}{\text{unit beam length}} \times u(t) .$$

The ratio of the two quantities gives

$$\frac{i(t)}{\dot{m}(t)} = \frac{\text{charge/unit beam length}}{\text{mass/unit beam length}} . \quad (3.10)$$

Since all the individual particles considered have charge to mass ratio  $c(t)$ , the right-hand side of equation 3.10 is also  $c(t)$ , and

$$i(t) = \dot{m}(t)c(t) . \quad (3.11)$$

Using equation 3.11, equation 3.9 becomes

$$\dot{M}_o = \int_0^\infty \frac{i(t)}{c(t)} dt$$

and, by use of equation 3.6,

$$\dot{M}_o = \frac{2V}{D^2} \int_0^\infty t^2 i(t)dt . \quad (3.12)$$

The integral

$$Y = \frac{1}{2} \int_0^\infty t^2 i(t)dt$$

can be integrated by parts to give

$$Y = \int_0^\infty t I(t)dt . \quad (3.13)$$



Hence, the total mass flow rate is given by

$$\dot{M}_o = \frac{4V}{D^2} Y . \quad (3.14)$$

In accelerator applications, the most useful value of charge to mass ratio that could be assigned to the entire beam would be the charge to mass ratio corresponding to the greatest particle flux. Calculation of such a charge to mass ratio would involve knowledge of the charge and mass on individual particles, which is not available through the time of flight method. An alternative value of charge to mass ratio for the entire beam will be called the nominal charge to mass ratio, and is defined as the value of charge to mass ratio contributing the maximum current to the beam. The nominal charge to mass ratio is given by

$$c_n = \frac{D^2}{2Vt_m^2} , \quad (3.15)$$

where  $t_m$  is the measurement time at which  $i(t)$  has a maximum and  $I(t)$  has a maximum slope. The value  $t_m$  has been indicated on the current decay curves in Figure 4.

It has been shown that  $i(t)dt$  gives the current contributed to the beam by particles having charge to mass ratio between  $c(t)$  and  $c(t + dt)$ . This gives no information about the number of particles in this charge to mass ratio range. However, the range of charge to mass ratio over which  $i(t)$  is non-zero indicates the range of charge to mass ratios present in the beam. This charge to mass ratio range has been used in describing the experimental results given in Chapters 6 and 9.



Because a colloid source suitable for use in the microparticle accelerator was being developed, the values of total beam current, total mass flow rate, nominal charge to mass ratio, and the range of charge to mass ratios present in the beam were of most interest.

Table 4, Part B, summarizes these results. The values given in Table 4, Part C, are used in colloid microthrust rocket research, and are discussed by Geis<sup>24</sup>, Huberman and Cohen<sup>25</sup>, and Burson and Herren<sup>32</sup>.

In the early stages of the present experimental work, it was desirable to correlate the present results to the results quoted in the literature. A short computer program (not discussed here) was used to numerically integrate the time of flight measurement current decay curve to obtain values for all the results listed in Table 4. Results of the time of flight measurements are given in Chapters 6 and 9.

It was stated above that the time of flight method yields only "average" values for various beam parameters and yields no information about the numbers of particles in the beam having a certain charge, mass, or charge to mass ratio. In Appendix A, a discussion of this problem is made by defining a function  $f(q,m)$ , which is equal to the number of particles per unit beam length per unit charge per unit mass having charge  $q$  and mass  $m$ . This function is then manipulated to show that the time of flight method experimental results cannot be reduced to give any information about particle numbers, and that the results listed in Table 4 are indeed a complete analysis of the time of flight results.

The analysis of time of flight measurement data depends on two assumptions. These are:



Table 4: Summary of Results Available From a Time of Flight Measurement. Part A Defines Symbols, Part B Gives Results Used in the Present Work, and Part C Gives Results Relevant to Micro-thrust Rocket Research, as Defined by References 24, 25, and 32.

Parameter	Symbol	Derivation
<u>Part A</u>		
- measurement elapsed time	t	measured
- source to detector distance	D	measured
- measured current decay curve	I(t)	measured
- source operating potential	V	measured
- integral	X	$X = \int_0^{\infty} I(t)dt$
- integral	Y	$Y = \int_0^{\infty} tI(t)dt$
- acceleration due to gravity	g	constant
- charge to mass ratio (see text)	c(t)	$c(t) = D^2/2Vt^2$
<u>Part B</u>		
- total beam current	$\dot{I}_o$	$\dot{I}_o = I(t)$
- total mass flow rate	$\dot{M}_o$	$\dot{M}_o = 4VY/D^2$
- nominal charge to mass ratio	$c_n$	$c(t)$ corresponding to point of maximum slope of $I(t)$ .
- range of charge to mass ratio	--	$c(t)$ for $t_1 < t < t_f$
<u>Part C</u>		
- mass flow rate averaged charge to mass ratio	$c_a$	$c_a = \dot{I}_o / \dot{M}_o = \dot{I}_o D^2 / 4VY$
- square mean root mass flow rate averaged charge to mass ratio	$c_r$	$c_r = D^2 X^2 / 8VY^2$
- distribution efficiency	e	$e = c_a / c_r$
- total beam thrust	T	$T = 2VX/D$
- specific impulse	S	$S = T/M_o g = DX/2gY$



- (a) the particles are created and accelerated through the source voltage  $V$  in a distance short compared to the source to detector drift distance;
- (b) the source to detector drift region is field free.

There is also an inherent assumption that the charge and mass of the particle remain constant during the source to detector drift time. Since mass influences the particle velocity only during the short acceleration period, mass loss during the drift time does not alter the time of flight measurement result. Particle charge influences particle velocity only during the particle acceleration, also. However charge loss appears as a decrease in detected current. If the charge loss affects all the particles in the beam equally, the shape of the detected current decay curve is unchanged, and the time of flight measurement gives particle charge to mass ratios as they existed at the particle source, prior to any drift period.

### 3.3 Beam Spatial Distribution Measurement Methods

#### 3.3.1 Introduction

While it is not difficult to produce a stable dc beam in a colloid source, the spatial distribution of the beam is usually complex and often asymmetric. As the source operating voltage is increased through the operating range, the beam typically changes through the following patterns: a few discrete jets located on the arc of a hollow cone, a complete hollow cone of jets, a diffuse hollow cone, and a focussed axial beam. Since the beam is produced by intense electric fields at the capillary tip, factors such as tip shape, extractor hole shape and capillary alignment strongly affect the beam distribution.



Knowledge of the spatial distribution of the colloid beam is essential in both accelerator and microthruster applications. In an accelerator, the beam must be on the axis. Beam shape is useful in determining collimator design, source efficiency, and the amount of wasted beam. In microthrust rockets, the beam shape fundamentally affects thrust efficiency and direction. Measurement of beam thrust using standard time of flight methods assumes that the beam is entirely along the thrust axis. Any deviation from this assumption, such as a hollow cone beam, results in less thrust than that calculated from time of flight measurement data. Clearly, any asymmetry in the beam results in undesirable side thrust components. These problems indicate the necessity for a rapid reliable method of checking the beam shape whenever any physical or operating parameters are changed.

Several approaches have been used to determine beam distribution. Analysis of time of flight data using point by point sampling of the beam is the most complete method<sup>45</sup>. However, it is laborious, time consuming, and relies on maintaining perfect beam stability for the duration of the sampling process. A beam current detector with several concentric rings is easier to use but determines only the average current striking a given section and tells little about beam symmetry or alignment. Observation of beam deposition on a surface is a reliable method but it represents an average over time. None of these methods can illustrate the beam shape during instabilities or transients.

In the present study, it was decided that use of segmented electrical detectors would be useful but would not provide sufficient detail on beam distributions. For this reason, considerable effort was devoted to developing visually reacting beam detectors which would give



a rapid qualitative description of beam intensity and spatial distribution. The theories behind the different types of spatial distribution detectors are now described, while all information concerning construction, testing and use of the detectors is given in Chapters 6 and 9.

### 3.3.2 Segmented Electrical Detectors

Section 3.2 has described the time of flight measurement method using beam current detection. The only detector required for the method is a metallic plate to intercept the beam, which collects the beam current. By dividing the metallic surface into a series of electrically isolated segments connected to a switch box, three different measurements can be performed by examining the beam currents on the various detector segments. The three measurements are: time of flight measurements on the entire beam, time of flight measurements on portions of the beam, and beam current measurements on portions of the beam. The latter can be interpreted as a rough estimate of the beam spatial distribution.

The number of segments in an electrical detector is limited by two features: the number cannot be so large that the measured portions of the beam current are below some detection threshold, and the number cannot be so large that the measurement process becomes unwieldy. Detectors with four, five, and thirteen segments have been used in the present work, as described in Chapters 6 and 9.

### 3.3.3 Visually Reacting Beam Detectors

#### 3.3.3.1 Introduction

It was felt that if suitable visual detectors could be



discovered and developed, much valuable information on beam spatial distributions could be obtained. The advantages of having a visible representation of beam shape are many. The fine structure of the beam, such as discrete jets, is displayed. Short term instabilities can be seen, as well as pulse or steady current modes. Photographic data are readily taken, which can later be correlated with electrical data measurements. Moreover, a rapid visual display greatly simplifies the adjustment of operating parameters to obtain a desired beam shape.

Two ideas which gave useful visual detector results (a phosphor screen detector and a liquid crystal detector) are described in the following two sections. Only the theory is given here; experimental results are given in Chapters 6 and 9.

### 3.3.3.2 The Phosphor Screen Detector

While luminescent screens have long been used as atomic particle, electron and photon detectors, their reaction to microparticle beams is of interest here. The phosphor used is zinc orthosilicate with 0.5% manganese activation (Sylvania Type P161). Green light of wavelength 526 nm is emitted when electrons, excited by external means, are returned to the ground state by a 3d spin flip transition in the divalent manganese ions substituted for zinc ions in the phosphor lattice<sup>54</sup>. The crystal electrons can be excited by heat, electromagnetic fields, or mechanical impact.

There are two possible phosphor excitation mechanisms. The droplets in a typical beam (operating voltage = 10 kV, charge to mass ratio = 50 coul/kg) are about 1/20<sup>th</sup> of the phosphor grain size of 3 to 5 microns, and have a terminal velocity of 1 km/sec. Thus the



droplets can shatter upon impact, with molecules or fragments of molecules entering the phosphor lattice, causing electron excitation. Alternatively the surface electric field of the droplets, which may approach  $10^8$  to  $10^9$  V/m, is sufficient to cause local breakdown (i.e. electron excitation) in the crystal lattice.

### 3.3.3.3 Liquid Crystal Screen

Liquid crystals have been used to detect small temperature gradients in a variety of applications<sup>55,56</sup>. When cholesteric type liquid crystals of suitable range are heated and illuminated, they are optically active, and the wavelength of reflected light is temperature dependent<sup>57</sup>. The liquid crystal screen is usually prepared as a layer of black paint, a layer of clear plastic, and a layer of liquid crystal material. The screen is heated, and the liquid crystal material is illuminated. The black paint absorbs the component of the incident light that is transmitted through the liquid crystal layer, thus making the reflected light more visible.

In the present application, local heating caused by the dissipation of the kinetic energy of the incident droplets results in a colour pattern on the sheet that is characteristic of the spatial distribution of the beam. The low thermal conductivity of the liquid crystal sheet prevents the coloured areas from spreading beyond the incident beam area, thermal stability being achieved by radiation and the cooling effect of evaporating glycerol. When the energy of the incident beam is itself insufficient to produce marked colour changes, the liquid crystal sheet is thermally biased towards the blue end of the spectrum with a heat lamp. Then, weak heating shows more clearly,



or alternatively the cooling effect of the evaporating glycerol defines the beam as a cool spot on the background of the sheet.

An additional method of beam detection arises from the use of liquid crystal screens. When the colloidal beam is incident on the black surface of the screen, the glycerol deposited by the beam is readily visible. Thus the black surface also acts as a visual detector.

### 3.4 Alternative Beam Detection Methods

#### 3.4.1 Introduction

Section 3.1 outlined the various colloidal beam detection methods considered for use in the present work. Sections 3.2 and 3.3 have described the detection methods actually selected for use, while this section now discusses the reasons for rejection of the alternative methods.

#### 3.4.2 Single Particle Detection

Detection of single charged microparticles can be accomplished by measuring the charge deposited in a Faraday cup by the particle, or by measuring the charge induced on a metal electrode placed near the particle trajectory<sup>2,38</sup>. The charge sensitive amplifier available for the present work<sup>58</sup> has a detection limit of about  $4 \times 10^{-14}$  coul because of the presence of noise in the amplifier. The Rayleigh Criterion (equation 2.11) shows that particles carrying  $4 \times 10^{-14}$  coul of charge have a charge to mass ratio less than 1.7 coul/kg. Thus this amplifier cannot detect particles in the range of interest of this study, since these particles have charge to mass ratios between 10 coul/kg and 500 coul/kg, which correspond to charges of  $6.8 \times 10^{-15}$  coul and  $1.3 \times 10^{-16}$  coul, respectively.



It was deemed impractical to construct a more sensitive charge sensitive amplifier, so single particle detection experiments were not performed.

#### 3.4.3 Time of Flight Measurements Using Charge Detection

A modification of the current detection time of flight measurement was evaluated, since the idea has not previously appeared in the literature. In the method, the current detector is replaced by a long, hollow metal tube surrounding the beam. The total charge induced on the tube is the sum of all charge contained within the tube at any given instant. Thus the time of flight measurement data are presented as an integrated form of the current decay curve  $I(t)$  found by the corresponding current detector method described in Section 3.2.

In practice, the method suffers from three disadvantages:

- (a) it is difficult to design a charge measuring amplifier with a suitably long input time constant;
- (b) it is difficult to mechanically design the charge measuring tube so that no beam intercepts it;
- (c) the current detector method provides the same information using a more easily designed apparatus.

For these reasons, no experiments were undertaken on charge detection with the time of flight method.

#### 3.4.4 Quadrupole Mass Spectrometer

Use of a quadrupole mass spectrometer to analyze colloid beams has been reported<sup>40</sup>. In this device, dc and rf voltages are applied to the rails of an electrostatic quadrupole. For certain voltages and rf frequencies, the device transmits particles of a given charge to mass



ratio. Thus measurements of beam current as a function of charge to mass ratio can be performed, and these yield exactly the same information as current detection time of flight measurements.

The use of a quadrupole mass spectrometer was not considered here because:

- (a) the device is expensive, and difficult to design and build,
- (b) the device has a very small entrance aperture, so it can analyze only small portions of the beam,
- (c) the method does not provide any more information than the current detection time of flight method.



## CHAPTER 4

### SOLUTIONS SUITABLE FOR COLLOID BEAM PRODUCTION

#### 4.1 Desired Properties of Solutions

Careful choice of the working fluid can make operation of any colloid source much easier and more reliable. The following is a discussion of some desirable fluid properties, together with some of the reasons behind their importance.

A fluid with the lowest possible vapour pressure should be selected for several reasons. Primarily, the problem of maintaining a suitable vacuum pressure in the experimental chamber is reduced. The droplets in flight will be more stable, and lose less mass because of evaporation. Any reduction of fluid evaporation at the capillary tip reduces gas discharges and corona in the beam, which are the result of poor vacuum in the region surrounding the capillary tip. The possibility of sparking between the capillary tube and the extractor is also reduced. High surface tension aids droplet stability in general, and allows a higher charge to mass ratio on the droplets as shown by the Rayleigh Criterion for droplet stability (equation 2.11). High fluid viscosity results in a conveniently low mass flow rate ( $\sim 10^{-9}$  kg/sec) through reasonably sized capillary tubes ( $\sim 0.2$  mm inner diameter). The fluid should be non-corrosive, in order to allow long storage periods and ease of handling, and to increase the lifetime of capillary tubes, detectors and system components.

The fluid properties profoundly affect the stability of colloid source operation and the charge to mass ratio of the particles produced.



It has been found that certain solutions work well for only one of the possible types of capillary potential (positive dc, negative dc, or high voltage ac). While the electrochemical processes in the charging mechanism are not fully understood, it is reasonable that for positive capillary potential, the charging process is an electrolytic one with the capillary as anode, and the charged fluid as ionic medium. Therefore the fluid must not undergo gaseous dissociation at the capillary tip, since the gas so produced would cause unstable beams and raise the vacuum pressure in the capillary tip area.

It has been found that solutions with bulk resistivity of 1 kohm-cm produce beams with charge to mass ratios of the order of  $10^4$  coul/kg, and 20 kohm-cm solutions produce  $10^2$  coul/kg beams. Most pure fluids have resistivities in the megohm-cm range, so they must be doped with ionic salts to reduce these bulk resistivities to suitable values in the kilohm-cm range.

No fluid has all the desired properties. The general approach is to select a fluid with a low vapour pressure and use solutes to change the fluid resistivity. It is fortunate that other desired properties such as high viscosity and surface tension are associated with low vapour pressure.

#### 4.2 Suitable Materials

Within the general guidelines for fluid selection, there are many choices of fluid and doping agent available. Table 5 is a summary of the more common fluid choices listed in the literature, and the type of source operation they give. Some other combinations are discussed in the literature but are not presented here because they produce unstable



Table 5: A Summary of Some of the Fluids and Doping Agents Used In Colloid Beam Production.

Solvent	Solute	Capillary Voltage Polarity	Ref.	Comments <sup>a</sup>
glycerol	-	+	40	very low charge to mass ratio
octoil	-	+	40	
triethylene glycol	-	+	40	
tetraethylene glycol	-	+	40	
glycerol	NaI <sup>b</sup>	+ ac	21, 25, 31, 59	wide range of charge to mass ratio available
glycerol	C <sub>2</sub> H <sub>3</sub> ONa <sup>c</sup>	+	25	
glycerol	NiCl <sub>2</sub> <sup>d</sup>	+	60	
glycerol	ZnCl <sub>2</sub> <sup>e</sup>	+	60	
glycerol	TEAC <sup>f</sup>	- ac	31 32	low charge to mass ratio
glycerol	H <sub>2</sub> SO <sub>4</sub> <sup>g</sup>	-	31	difficult to outgas; corrosive
glycerol	NaOH <sup>h</sup>	+	25, 28	leaves precipitate on capillary tip
oleic acid	TEAC <sup>f</sup>	- , +	31, 32	low charge to mass ratio

a stable operation is implied for all entries

b sodium iodide

c sodium ethylate

d nickel chloride

e zinc chloride

f tetra-ethyl ammonium chloride

g sulphuric acid

h sodium hydroxide



beams, or beams with too low a charge to mass ratio value (see Hogan<sup>23</sup>, for example). Because of the general success of researchers using sodium iodide dissolved in glycerol, it has been the only fluid--solute combination used in the present work. It should be noted that solutions of tetra-ethyl ammonium chloride dissolved in glycerol or oleic acid are also possible for use, since they produce suitably low charge to mass ratio beams. However, adequate results were obtained by varying the NaI-glycerol solution concentrations.

#### 4.3 NaI-Glycerol Solution Resistivity and Fluid Treatment

In the course of this study, fluid bulk resistivity was found to be a very significant parameter. The charge to mass ratio of a beam produced in a colloid source increases as fluid resistivity decreases. The resistivity of a solution of known strength is a reliable indicator of the presence of contaminants in the fluid, since contaminants markedly decrease fluid resistivity. Some theories of the droplet charging process use resistivity as a parameter<sup>42</sup>. A literature review of NaI-glycerol resistivity values and solution strengths revealed a scarcity of experimental details on fluid preparation, and some inconsistencies. These values are listed in Table 6.

The importance of the resistivity values, the variation in quoted values, and the scarcity of experimental information prompted a study into the resistivity of NaI-glycerol solutions. The effects of measurement frequency, temperature, outgas procedure, glycerol purity, and doping levels were determined. The solutions were made by accurately weighing the glycerol and NaI, dissolving the mixture, then outgassing the solution. Both reagent and USP grade glycerol contained 5% water



by weight as they were used in solution preparation. The NaI was not dehydrated prior to weighing.

The resistivity was obtained from the measured resistance of a cell of fluid. The resistance cell was a glass tube, 3.93 cm long and 1.88 cm in diameter, with aluminum end plates. One end plate was fastened to the glass tube with epoxy, while the other was fastened to the cell by means of two sections of threaded rod joining the two end flanges. The cell was filled with the glycerol to be measured, and all air bubbles were removed through a small notch cut in one rim of the glass tube.

Initial experiments to measure cell resistance were inconclusive because the cell resistance changed continuously as a function of the time after the dc voltage was applied between the cell end plates. Cell resistance was also a function of the applied dc voltage.

Table 6: Values of Resistivity for NaI-Glycerol Solutions, as Quoted in the literature.

Solution Concentration (g NaI/100 ml glycerol)	Resistivity (kohm-cm)	Measurement Temperature (°C)
0	2000. <sup>59</sup>	25
5	68.0 <sup>60</sup>	-
10	30.0 <sup>60</sup>	-
15	7.28 <sup>25</sup>	25
20	20.1 <sup>60</sup>	-
20	2.5 <sup>31</sup>	-
30	4.65 <sup>59</sup>	25

The next series of experiments used an ac voltage applied to the resistance cell. The cell impedance was measured for frequencies



between 5 Hz and 500 kHz using a Hewlett Packard Model 4800A Vector Impedance Meter. Figure 5 shows the cell impedance magnitude versus frequency curves for six outgassed NaI-glycerol solutions.

At high frequencies, the cell impedance magnitude decreased, while the corresponding impedance phase changed from near zero degrees towards minus ninety degrees. Using the impedance data and a cell equivalent circuit consisting of a resistor and capacitor in parallel, the values of the equivalent circuit resistor and capacitor were found. For all impedance curves measured, the data were consistent with a resistance independent of frequency in parallel with a capacitance of 10 pf. The shunt capacitance was attributed to cell and test lead capacitance. An impedance measurement on the empty resistivity cell yielded a measured capacitance value in agreement with the calculated 10 pf.

At frequencies below 300 Hz, the cell impedance magnitude increased while the impedance phase was negative. Attempts to model the low frequency dependence of the cell impedance by both parallel and series resistor-capacitor combinations were inconclusive because the equivalent circuit resistance always had a frequency dependence, which showed that simple equivalent circuit models of the cell were inadequate. The low frequency cell impedance increase could be attributed to polarization of the ionic solution within the cell<sup>61,62</sup>. This interpretation is also consistent with the observed cell behaviour with dc applied voltages.

When cell impedance is purely resistive, the fluid resistivity can be unambiguously found from the relationship

$$\rho = RA/L , \quad (4.1)$$

where  $\rho$  is the resistivity, R is the cell resistance, A is the cell



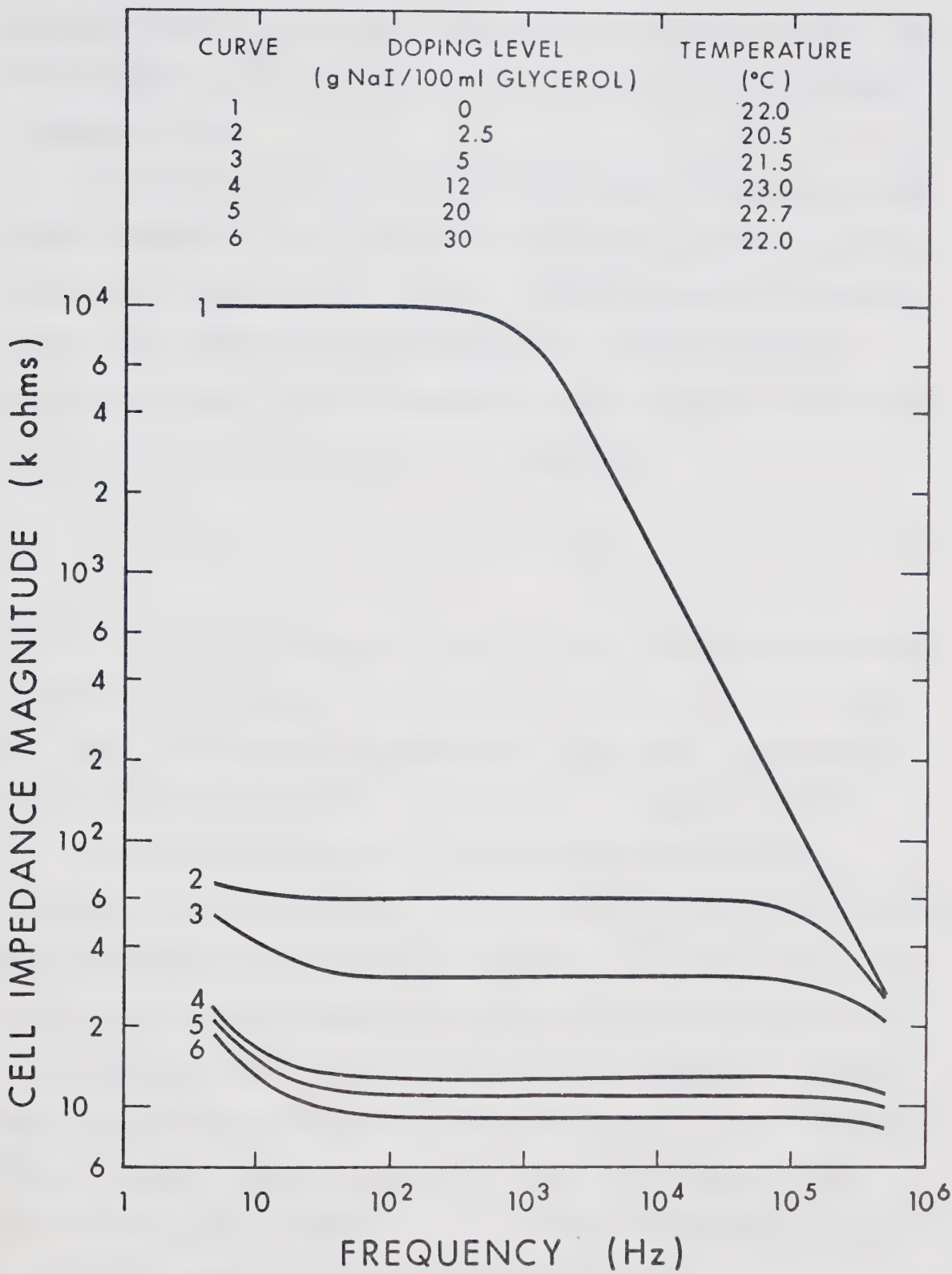


Figure 5: Resistivity Cell Impedance Magnitude for Six Outgassed NaI-Glycerol Solutions, as a Function of Measurement Frequency.



area, and L is the cell length. All values of resistivity used in the present work were found using equation 4.1 at a reference measurement frequency of 1 kHz.

NaI-glycerol solution resistivity was known to be extremely temperature dependent<sup>21</sup>. As a result, the effect was experimentally investigated in the present work. Figure 6 shows the results of resistivity versus fluid temperature measurements on 5 g and 30 g NaI/100 ml glycerol solutions. Over the temperature range 10°C to 35°C, both sets of data are empirically described by an equation

$$\rho = \rho_0 10^{-0.0364(T-T_0)} , \quad (4.2)$$

where  $\rho$  is the fluid resistivity and T is fluid temperature in degrees Centigrade. Thus the resistivity decreases approximately one decade for each 27.5°C increase in temperature. This result is consistent with a 30°C/decade dependence estimated from data given by Kidd<sup>21</sup>.

Throughout the present work, fluid resistivities have been measured at room temperatures of between 20°C and 23°C, then the results have been normalized to 25°C using equation 4.2. During each measurement, a series of measurements were made at half-hour intervals until the resistivity value found was constant, which ensured that thermal equilibrium had been established. The fact that the 5 g and 30 g NaI/100 ml glycerol solutions showed the same temperature dependence justified the use of equation 4.2 to temperature normalize all the resistivity results for all solution concentrations.

Solutions were outgassed by liquid nitrogen trapped pumping on about 50 ml of solution in a 250 ml Erlenmeyer flask immersed in a



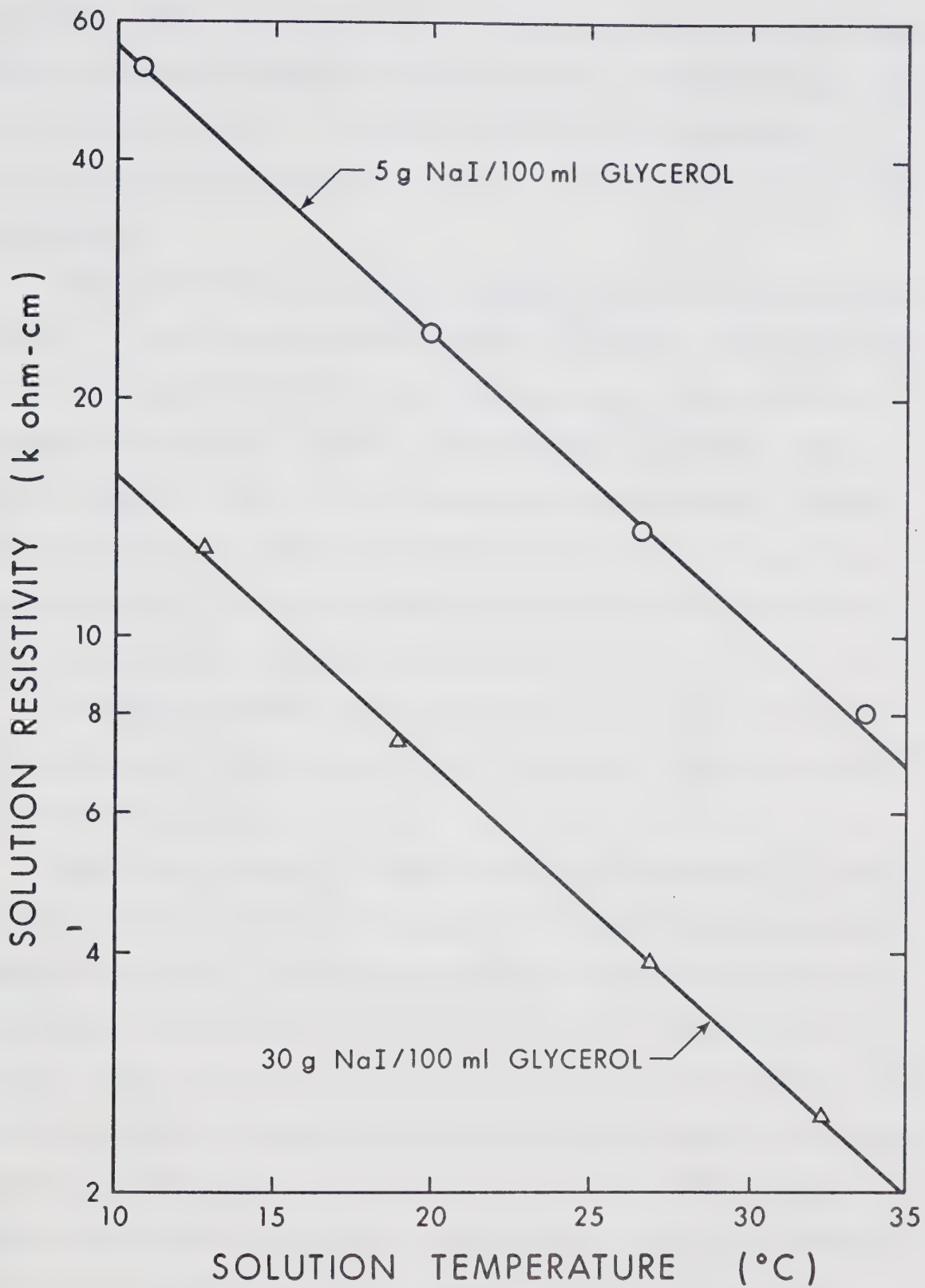


Figure 6: Temperature Dependence of NaI-Glycerol Solution Resistivity for Outgassed 5 g and 30 g NaI/100 ml Glycerol Solutions.



65°<sup>o</sup>C bath. The resistivity of a 30 g NaI/100 ml glycerol solution rose from 2.6 kohm-cm initially to 4.5 kohm-cm after two hours of outgassing, and rose only 15% more in a further sixteen hours of outgassing. A standard time of five hours of outgassing at 65°<sup>o</sup>C was used for solution preparation.

The resistivities of various NaI-glycerol solutions are shown in Figure 7. Two different glycerol grades were tested. The resistivity of USP grade glycerol solutions was initially lower than that of the reagent grade glycerol solutions, but outgassing essentially removed the difference. A total of six doping levels was measured, ranging from pure glycerol to 30 g NaI/100 ml glycerol, in both original and outgassed form. It was found that solutions with a particular resistivity value could be reproduced within ±5%.

The measured resistivity values show general agreement with the values from the literature (Table 6). The values of Makin and Bright<sup>60</sup> are inexplicably high.

Some recommendations on solution resistivity measurement procedure can be made from the observed dependence of resistivity on the experimental conditions. The frequency dependence of cell impedance must be examined to find a range in which the impedance is independent of frequency, thus allowing an unambiguous determination of resistivity. The strong temperature dependence of resistivity makes temperature control essential. This can be done by using a controlled environment or applying an empirical temperature normalization, but the cell must be allowed to completely stabilize before measurement in either case. Solutions should be outgassed before measurement. Once outgassed, solution resistivity depends only on doping level, and is stable under



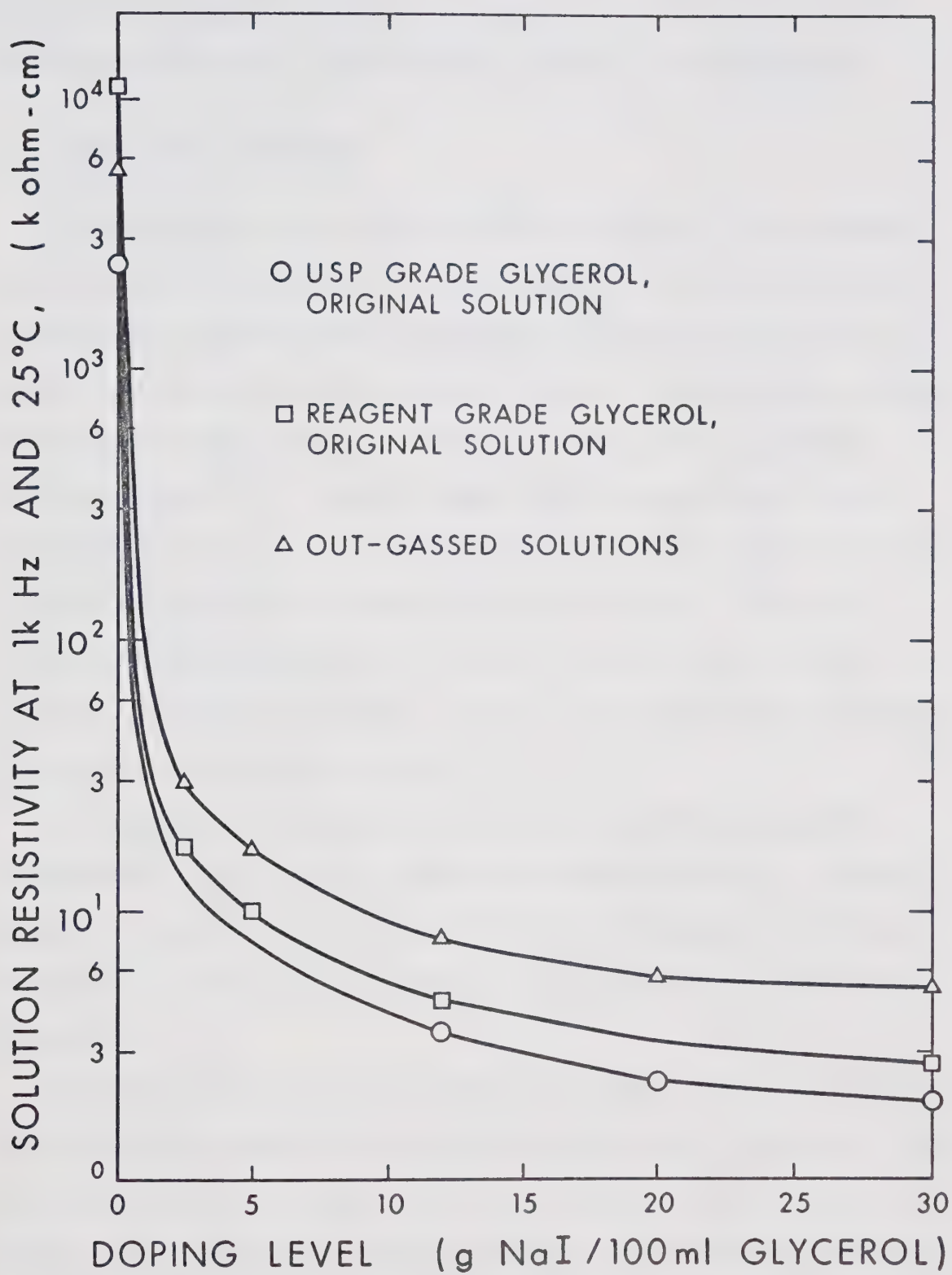


Figure 7: NaI-Glycerol Solution Resistivity, as a Function of Solution Doping Level.



vacuum. If these precautions are observed the resistivities of NaI-glycerol solutions are clearly defined, stable, and reproducible.

#### 4.4 Other Fluid Properties

In microthruster applications of colloid sources, the researcher must maximize the thrust per consumed power ratio of the source while maintaining a specified fuel consumption efficiency (specific impulse). Control and manipulation of parameters such as fluid viscosity, density and surface tension can play an important role in this microthrust rocket operation<sup>21,25</sup>. In the present work, the major goal is the production of a beam with specified nominal charge to mass ratio with a narrow distribution of charge to mass ratio values. This less stringent condition has been satisfied by varying system voltage, feed pressure, and fluid resistivity. Control of the additional parameters mentioned above was not necessary.

One parameter which was required in the solution preparation measurements is the specific gravity of the glycerol in its original form, which was measured to be 1.25 for both the reagent and USP grade glycerol. A value of 1.26 is given in the literature for anhydrous glycerol<sup>51</sup>.

Throughout the duration of the present study, various calculations concerning the behavior of NaI-glycerol solutions have been made. (An example of these is the mass evaporation calculations in Section 2.7.2.) Because these calculations required values of the physical constants of glycerol, these constants have been included in this thesis as Table 7. For reasons of completeness, the physical constants have been presented here as a group rather than scattered throughout the thesis. Most of



Table 7: Physical Constants of Pure Glycerol.

Parameter	Value	Measurement Condition	Ref.
<b>Physical Data:</b>			
- chemical formula	$C_3H_8O_3$	-	65
- specific gravity	1.263	20°C	51
- surface tension	63.4 dyne/cm	20°C	51
- viscosity	3900 cp	10°C	51
	1410 cp	20°C	51
	612 cp	30°C	51
- vapour pressure	-- see Table 8 --		
<b>Electrical Data:</b>			
- conductivity	$5 \times 10^{-8}$ mhos/cm	20°C	51
- dielectric constant	41.14	20°C	51
<b>Thermodynamic Data:</b>			
- latent heat evaporation	21.1 kcal/mole	55°C	51
fusion	47.49 cal/g	18.07°C	63
sublimation	use sum of evaporation and fusion		63
- specific heat of liquid	.510 cal/g/°C	-20°C	63
and vitreous states	.540 cal/g/°C	0°C	64
	.600 cal/g/°C	50°C	64
	.669 cal/g/°C	100°C	64
- specific heat of solid	.330 cal/g/°C	0°C	64
	.217 cal/g/°C	-100°C	64
	.115 cal/g/°C	-200°C	64
- boiling point	290.0°C	760 torr	51
- freezing point	18.17°C	-	51
	17°C to 18°C	-	51
	17.1°C	-	63
	17.1°C	-	64
- thermal conductivity	$6.8 \times 10^{-4}$ cal/ g/°C/sec	20°C	51
- thermal expansion of volume	$4.7 \times 10^{-4}$ /°C	20°C	51



the data are from Newman's book entitled "Glycerol"<sup>51</sup>, while some values from the Perry<sup>63</sup>, Lange<sup>64</sup>, and Chemical Rubber Company<sup>65</sup> handbooks of chemical data are included. Only where the references disagree on a certain value are multiple references given. One additional piece of information stressed by Newman<sup>51</sup> is that glycerol shows "remarked proneness" to supercool down to -83°C (well below the freezing point of 18°C). In the supercooled state, the substance is in a vitreous form whose physical constants are close to those of the liquid.

Vapour pressure data for pressures below 1 torr of glycerol could not be found in the literature. However, data were given at 1 torr and 10 torr, for fluid temperatures of 125.5°C and 167.3°C respectively<sup>51</sup>. Perry<sup>63</sup> states that vapour pressure data can be empirically fitted by a function of the form

$$\ln P = \frac{A}{T} + B \quad (4.3)$$

where P is the vapour pressure in torr, T is the temperature in °K, and A and B are constants. When this equation is fitted to the vapour pressure-temperature data given above for glycerol at 1 torr and 10 torr pressures, the resulting equation is

$$\ln P = -\frac{9.7 \times 10^{-3}}{T} + 24.3 \quad (4.4)$$

In spite of the fact that the points at 1 torr and 10 torr used to evaluate the constants A and B in equation 4.3 lie very close together, it is felt that the fit is reasonably accurate over a large range of vapour pressure. The reasons for this confidence in the fit are that the same values for A and B were found using alternate known data



points at 5 torr and 20 torr, and that the functional form of equation 4.3 forces the curve to go through the point P=0, T=0.

Equation 4.4 has been evaluated for a variety of glycerol vapour pressures, and the results are presented in Table 8. It must be noted that the values in Table 8 are an extrapolation from vapour pressure data given in the literature into a region where the vapour pressure data were not given in the literature, using equation 4.4. These extrapolated vapour pressure data have been used in Section 2.7.2.

Table 8: Vapour Pressure versus Temperature of Glycerol.

Vapour Pressure <sup>a</sup> (torr)	Temperature (°K)	Temperature (°C)
1	399	126
$10^{-1}$	364	91
$10^{-2}$	336	63
$10^{-3}$	311	38
$10^{-4}$	289	16
$10^{-5}$	272	-1
$10^{-6}$	254	-19
$10^{-7}$	240	-33
$10^{-8}$	227	-46



## CHAPTER 5

### TEST BENCH APPARATUS

#### 5.1 Introduction

As mentioned in Section 2.1, a colloid source consisting of a single capillary needle, similar to that shown in Figure 1, was used for experiments described in this thesis. In the preliminary studies of source behavior, the source, vacuum system, fluid feed system and detectors were designed so that any one of the individual components could be readily altered without requiring major modifications to the remaining system components. This chapter outlines the physical layout of the test bench apparatus, while the results obtained using the test bench systems are described in the next chapter.

Figure 8 is a schematic diagram of the test bench apparatus. The various components are discussed in the remainder of this chapter.

#### 5.2 Vacuum System

The experimental chamber is in the shape of a cross, made of six-inch diameter Corning Pyrex glass pipe. Adjacent to this cross is a manifold containing a six-inch diameter flat valve, liquid nitrogen trap, chevron baffle (not cooled in this application), and ports for air inlet valves, roughing line and vacuum gauges. The pump assembly consists of a 260  $\ell/\text{sec}$  Welch Model 3102D turbomolecular pump, 8.3  $\ell/\text{sec}$  roughing pump, and the associated cooling and lubrication systems necessary for the turbomolecular pump. Use of the turbomolecular pump requires a special effort to isolate the pump vibrations from the test



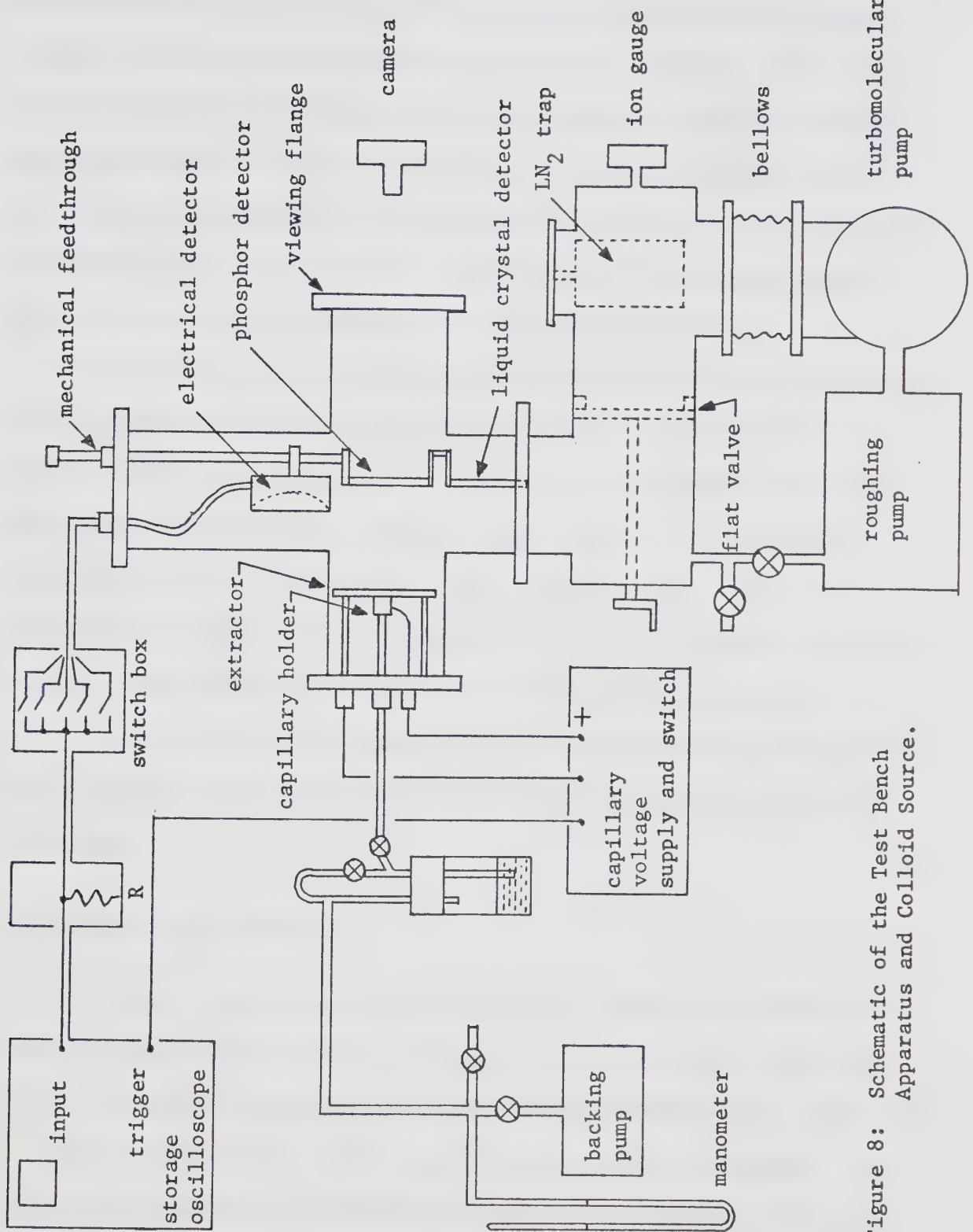


Figure 8: Schematic of the Test Bench Apparatus and Colloid Source.



chamber, particularly during start-up or shut-down. A six-inch diameter stainless steel bellows without bellows extenders is inserted between the turbomolecular pump and the vacuum manifold. Because no bellows extenders can be used, the table supporting the test chamber and manifold has to withstand the full vacuum load downward, which is the 1800 newtons generated by atmospheric pressure acting on the cross-sectional area of the six-inch diameter bellows. The pump itself is bolted to the floor to withstand an equal force upward.

A Consolidated Vacuum Corporation Model GIC-004 thermocouple gauge, Model GIC-028-2 ion gauge, and a Model GIC-110C gauge controller measure system vacuum pressures. With the ion gauge port adjacent to the liquid nitrogen pump, measured vacuum pressures are inevitably lower than the actual pressures at the colloid source. After ten hours of trapping pumping, measured pressures in the entire system were about  $5 \times 10^{-7}$  torr, while typical pressures during source operation were about  $1 \times 10^{-6}$  torr. Beam instabilities, corona at the capillary tube tip, or fluid outgassing caused pressure bursts measured in the  $10^{-5}$  torr range.

### 5.3 Experimental Chamber

The glass cross used as the experimental chamber has three ports free for installation of the apparatus. The colloid source (Section 5.4) is installed on a flange fitted to one horizontal arm of the cross.

The vertical arm of the cross houses the detector assembly. As explained in Chapter 3, much work was done to develop beam detection methods. The detector assembly shown in Figure 8 allows simultaneous installation of up to three detectors, which are usually chosen to be



one electrical detector and two visually reacting detectors. The three detectors are mounted on a mechanical feedthrough, so that any detector can be positioned to intercept the beam.

The design of the visual detectors allows the beam spatial distributions to be observed on the active surface on the side away from the incident beam. In order that photographs of the detected beam distributions can be taken, the arm of the experimental chamber opposite to the arm containing the colloid source is sealed with a clear lucite flange. Also, this arm of the cross is fitted with a black sleeve to prevent light from reflecting into the camera lens. The camera position, which is shown in Figure 8, can be as close as 0.25 m to the detector surfaces.

#### 5.4 Liquid Colloid Source, and Fluid Handling System

As shown in Figure 8, the colloid source in the test bench is made up of an extractor mounted on the experimental chamber flange, a capillary tube holder to align the capillary in the extractor, and a feed tube connecting the capillary to the fluid reservoir.

Several versions of the source geometry were tried before the design shown here was evolved. Problems which were encountered in these sources were:

- (a) poor capillary tube alignment,
- (b) high voltage breakdown between the capillary tube holder and the extractor,
- (c) poor vacuum seals in the glass feed tube sections,
- (d) glassware breakages due to stressing and vibration.

The present design eliminates most of these problems.



Details of the source are shown in Figure 9. Different extractor designs and positions can be tested (see Section 6.5). The capillary tube is soldered to a stainless steel cap with eutectic solder. This cap is screwed onto the tube holder with teflon tape as a joint sealant. An O-ring seal joins the tube holder and glass feed tube.

The fluid used has high electrical conductivity, hence the entire body of fluid from the capillary back to the reservoir is at high potential during source operation. High voltage insulation is achieved by making the entire feed system of glass, from the capillary holder to the backing pump manifold. The vacuum feedthrough on the source flange is an O-ring squeezed against the glass feed tube. Manipulation of the four valves on the fluid reservoir, backing pump and air inlet allows the fluid line to be completely evacuated, or the fluid to be forced up the feed tube with a given pressure, as measured on the mercury manometer. Actual fluid pressure at the capillary tip is the manometer reading less the glycerol head in the feed tube; the extremely low feed rate ( $\sim 10^{-9}$  kg/sec) implies that there is no pressure loss in the feed tube and capillary tube. The operating pressures of 5 to 20 cm Hg make the glycerol-air interface susceptible to corona and glow discharge, which cause fluctuations in capillary voltage and electrolyze the solution, producing contaminants. A coiled 2 m length of glass tubing was inserted between the reservoir and backing pump with no significant reduction of the glow discharge. An acceptable solution to the problem is to float a 5 mm layer of Dow Corning 704 diffusion pump oil on top of the glycerol layer to act as voltage insulation. The oil and glycerol are immiscible.



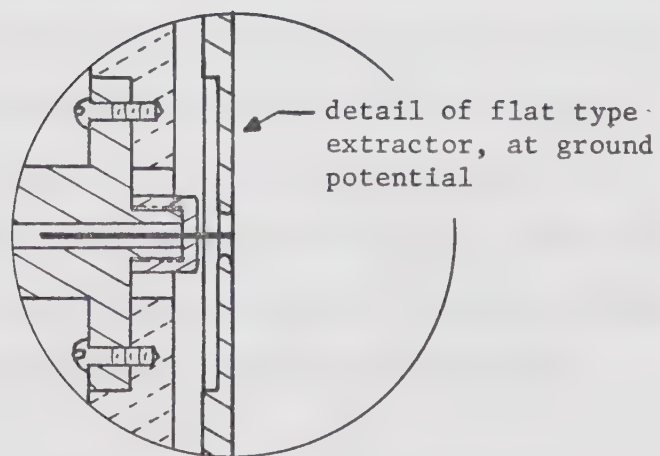
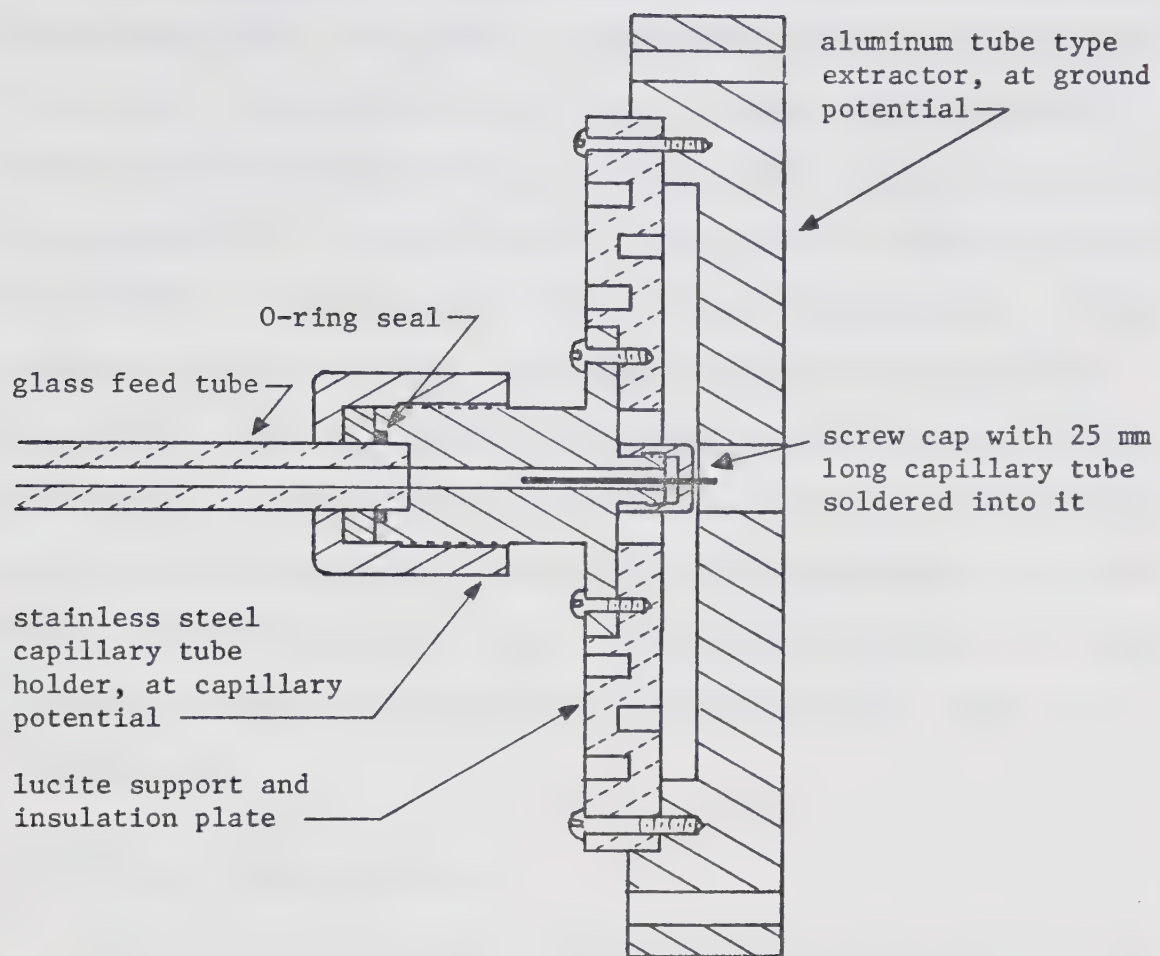


Figure 9: Cross-sectional view of the colloid source.



The most serious limitation to this system is that the source can not be turned off, then turned on again later, without being dismantled and cleaned. The reason for this is as follows. When the source is turned off, the feed pressure is removed in order to prevent fluid from being squeezed out the capillary tip. This means the fluid in the feed line separates into sections of fluid with voids between them. If the pressure is returned with no high voltage applied to the capillary, droplets are slowly squeezed out the capillary tip. However, if the high voltage is applied first, the voids transmit current, causing electrolysis of the fluid with accompanying fluid contamination. Starting with a clean feed tube means that a solid column of fluid can be pushed up to the capillary holder, then the high voltage can be turned on successfully.

### 5.5 Time of Flight Apparatus

Of the various schemes for measuring beam parameters discussed in Chapter 3, the current detection time of flight method (Section 3.2) was selected for use in the experiments. Briefly, the beam is interrupted suddenly by grounding the capillary tube by means of an electric switch. This switch will be referred to as the 'capillary voltage switch'. Then the decay of beam current intercepted by a plate in front of the source is observed on a storage oscilloscope. The oscilloscope is operated in the single sweep, externally triggered, storage mode, and is triggered at the instant the capillary potential is switched to ground.

A hydrogen filled thyratron (English Electric Valve Co., type 5C22) is used as the capillary voltage switch. The tube is rated to



withstand 16 kV, and can transmit 0.25 A average current when conducting. However, voltages up to 20 kV were switched without difficulty. The anode voltage of the tube in the conducting state is about 300 volts, well below the beam production threshold voltage of 2.5 kV.

Figure 10 is a diagram of the capillary potential switching circuit. The 5C22 thyratron is non-conducting for zero volts on the grid, and conducts when a positive going grid pulse is applied. The grid pulse is generated by transistor Q7 from the 150 V supply. Diode D1 protects the transistor from the transient appearing on the tube grid when the tube conducts. The .01  $\mu$ f capacitor and 56 kohm resistor (C3 and R9) pick off a signal which triggers the storage oscilloscope, as shown in Figure 8. The transistor Q7 receives its base drive signal from one of three sources:

- (a) Switch SW2 can be closed to position 'a', which turns Q7 off and hence the thyratron is held in the conducting state regardless of the position of Switch SW1.
- (b) With Switch SW2 in position 'b' and Switch SW1 in position 'b', the train of pulses from the astable multivibrator switches the thyratron repetitively. This mode of circuit operation is useful for circuit testing.
- (c) With Switch SW2 in position 'b' and Switch SW1 in position 'a', the output of the one-shot is used as the driving pulse. Normally the thyratron is held in the non-conducting state. When a time of flight measurement is desired, the remote push button Switch SW3 is closed, and the single pulse from the monostable multivibrator turns the thyratron on for 15 msec, thus interrupting the beam for



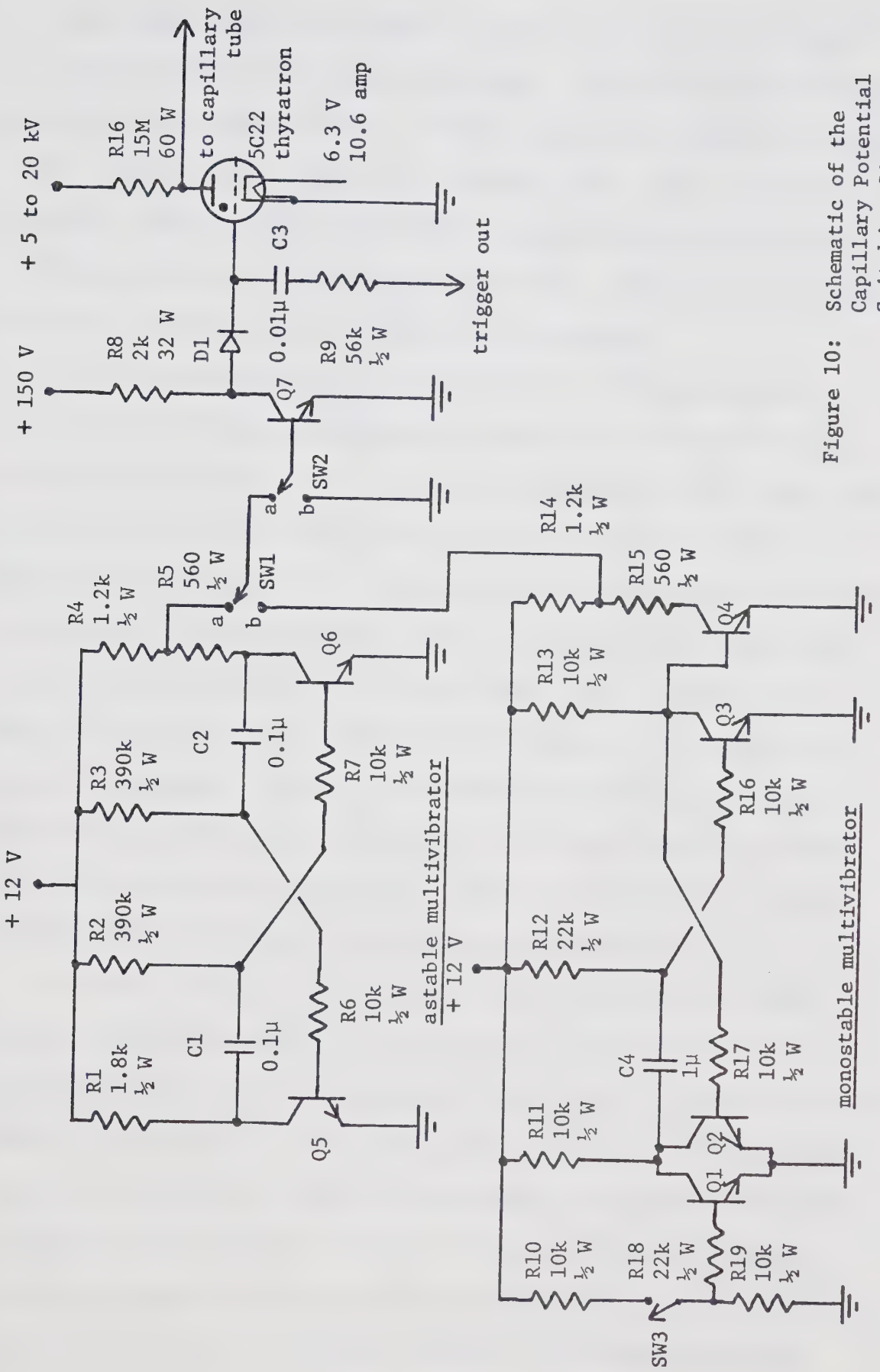


Figure 10: Schematic of the Capillary Potential Switching Circuit.



that time. The multivibrator circuits are of standard design<sup>66</sup>.

Figure 11 shows the circuit waveforms. The oscilloscope is triggered off the firing transient, in order to give the correct starting point for the time of flight trace, within 1  $\mu$ sec. The relatively slow fall time (10 msec) of the high voltage pulse is caused by the thyratron and output circuit capacitance being charged through the 15 Mohm anode resistor when the thyratron is turned off.

The transient generated by the thyratron suddenly conducting appears on all the ground potential points in the test bench for up to five microseconds. For this reason, measurement of the first 5  $\mu$ sec of the time of flight current decay curve is perturbed. Thus, for a beam of given velocity, the source to detector drift distance has to be sufficiently long that the time scale of the beam current decay curve is much longer than the 5  $\mu$ sec perturbation. For the fastest beams used in this phase of the study ( $\sim 7 \times 10^3$  m/sec), a 0.3 m drift distance was adequate. Efforts to eliminate the thyratron switching transient by altering the geometries of the ground leads on the test bench components were unsuccessful. However, the problem is a minor one which does not affect the measurements appreciably.

As shown in Figure 8, the signals from a segmented electrical detector (which is discussed in Section 6.3.2) are fed to a switch box. Each of the signal lines coming into the switch box is connected to the wiper of a SPDT toggle switch. Thus each component of detected beam current can either be connected to the signal output, or be switched to ground to bleed off the collected current. The current signal selected by the switch box is directed through the detector resistor R to ground, while the oscilloscope monitors the voltage generated



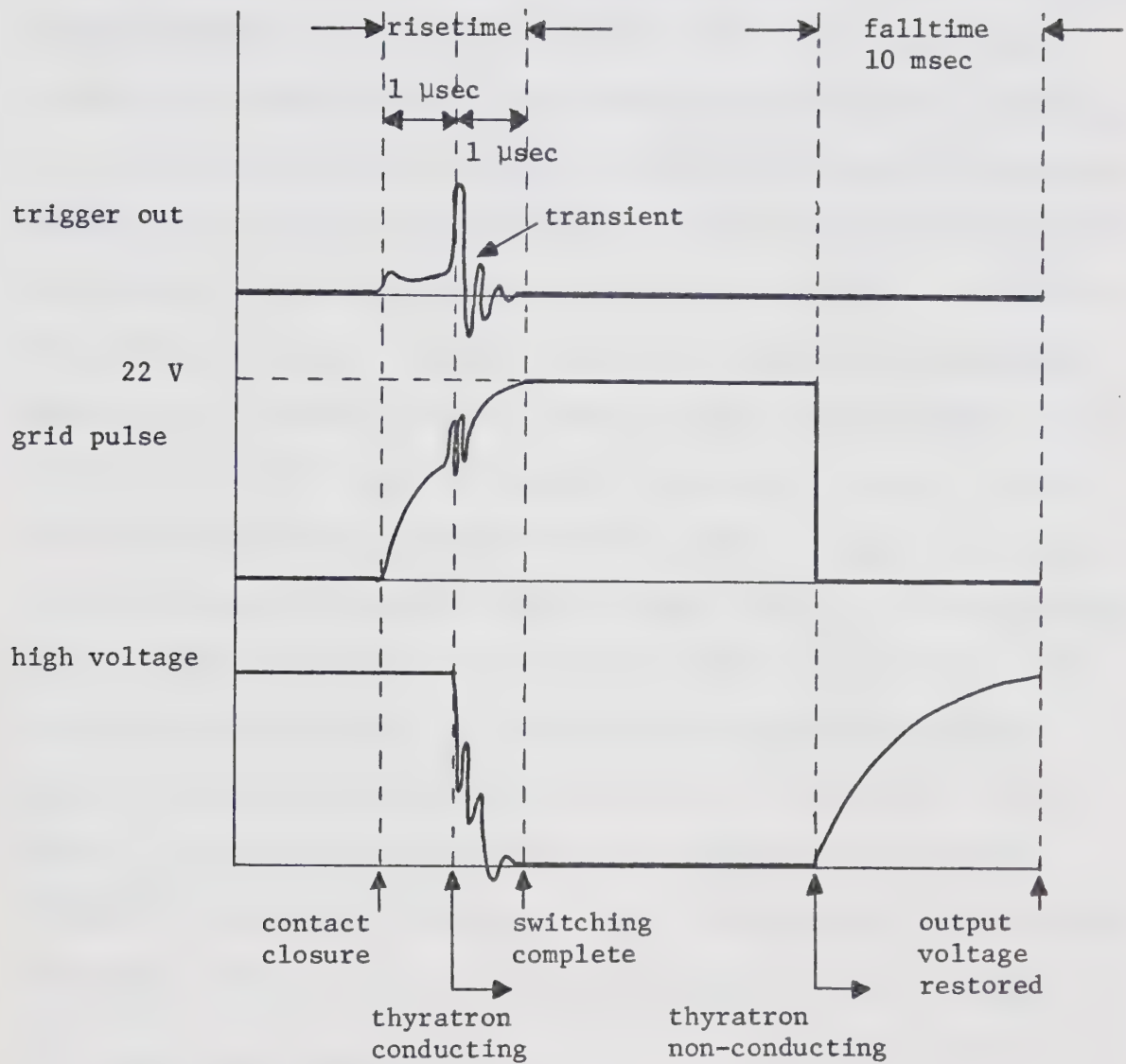


Figure 11: Capillary Potential Switching Circuit Waveforms.



across this resistor.

The oscilloscope used is a Tektronix Model 549 Storage Oscilloscope with a Model 1A7A preamplifier, which is capable of measuring signals in the microvolt range. One useful feature of the preamplifier is the adjustable high frequency signal cutoff, which can be used to reduce high frequency noise in the preamplifier or detector circuitry.

Choice of the value of detector resistor R is based on three considerations. Firstly, R must be much less than the oscilloscope input resistance of 1 Mohm. Secondly, R must be large enough that the smallest beam current to be detected can be seen above the preamplifier noise level of about 5  $\mu$ V peak. Thus for 100 nA beam currents, R must be greater than 500 ohms for a signal to noise ratio of 10. Thirdly, the time constant of the entire detector circuit, which is determined by the resistor R in parallel with the capacitance of the oscilloscope input, cables, and detector, must be much less than the fastest time constant of the time of flight current decay curve to be observed. Since a total capacitance of 1 nf and a current decay curve time constant of 10  $\mu$ sec are typical, R has to be much less than 10 kohms. Therefore R can have values between about 500 ohms and 1 kohm for this particular configuration. A value of 1 kohm was usually selected.

### 5.6 Photographic Procedure

A major advantage of the phosphor and liquid crystal types of visually reacting beam detector is that the beam distributions displayed on the detectors can be photographed directly from the detectors during an experiment. The phosphor screen reacts by emitting green light where the beam strikes it, while the liquid crystal screen



changes colour (from red through blue) as it is locally heated by the kinetic energy of the incident beam. Therefore it was thought desirable to photograph the detectors on 35 mm format colour slides.

It was found that the lighting conditions during the experiments required the fastest possible film speeds. Two types of slide film were tried. It was found that, in this particular application, Kodak High Speed Daylight Ektachrome (nominal ASA 160) taken and developed at ASA 600 gave a more realistic colour rendition than did GAF Ansco-chrome 500 film taken and developed at an ASA 1000 rating. The 35 mm format pictures were taken with various lens and extension tube combinations mounted on a Pentax Spotmatic II camera, depending on the information to be recorded.

In addition to the colour slide photography, some results were taken using Type 47 Polaroid film (ASA 3000) in a Graflex camera using a 135 mm, f/4.7 lens to give black and white photographs.

Specific details of equipment and exposure times are given with each result presented in Chapter 6.

### 5.7 Data Recording Methods

During the course of the test bench experimental program, a great many (probably thousands) time of flight measurements were made. Early in the program, it was decided that most of the time of flight measurement data would be copied by hand from the oscilloscope screen onto graph paper in laboratory notebooks rather than use oscilloscope cameras to record each measurement. Factors influencing the decision were:



- (a) it was realized that most of the measurements would only be used to give a qualitative impression of source behavior and that only a few of the measurements would be quantitatively analyzed,
- (b) it would be expensive to photograph a great many measurement results,
- (c) the data would be more easily sorted, identified, and classified if they were drawn in notebooks than if they were recorded as individual photographs,
- (d) it was felt that measurement accuracy would not be unduly sacrificed, since the largest uncertainty in data extraction was associated with oscilloscope trace width and reading the oscilloscope graticule. This uncertainty affected both methods of data recording equally,
- (e) experiments were done to show that, for randomly chosen cases, the two methods gave results within 10% of each other.

Of course, some time of flight measurement results were recorded on film for demonstration purposes.

The visually reacting detectors were most often used to give a subjective interpretation to the beam distributions recorded by the segmented electrical detector. For specific experiments investigating beam shapes, a complete data set consisted of a time of flight measurement using all detector rings, measurement of the beam current on each detector ring, and 35 mm colour slides of the two visually reacting detectors.



## CHAPTER 6

### TEST BENCH RESULTS

#### 6.1 Introduction

This chapter discusses the results and observations taken using the test bench colloid source. The overall goal of the experiments was to develop the colloid source to a point where focussed, dc beams with nominal charge to mass ratio between 10 coul/kg and 500 coul/kg could be reliably produced. Such a source could then be adapted for use in the microparticle accelerator.

Before the desired level of colloid source operation was achieved, much of the work produced results of general interest to colloid source understanding but of little specific interest to the research goal. Some of these results are presented here with the view to providing insight into colloid source operation. In addition, many of these results are subjective in nature. The general order of the section headings follows the sequence of experiments performed in the laboratory--once suitable colloid beams could be produced, beam detectors were developed, then a parametric analysis was performed on beams produced by the colloid source.

Because of the difficulty experienced in achieving absolute reproducibility of beam shapes and beam parameters, time of flight and beam distribution measurements were taken whenever experimental changes were made. This procedure ensured that source behavior was recorded throughout each experiment.

Generally speaking, the colloid beam phenomena observed in the present work agreed with those presented in the literature. One



pertinent discovery made here is the presence of a region of operating parameters within which the dc beam current is focussed much closer to the central axis than in any results previously presented.

## 6.2 Beam Stability

### 6.2.1 Introduction

At this point it is useful to reiterate the descriptions of beam modes as evidenced by the waveform of the detected beam current. In a "pulse" mode, the beam appears as a periodic series of uniformly shaped pulses, with no current being detected between pulses. In the "dc" mode, the beam is detected as a constant, uniform current. The pulse and dc beam modes are called stable if the current waveform re-establishes itself after the source has been interrupted by a time of flight measurement. All other possible beam current conditions will be referred to as unstable beams. One particular example of an extremely unstable beam will be called a "current burst". Experimentally it is identified as a period of a few seconds in which the beam current increases erratically then suddenly falls to zero for a period of a few tens of seconds. The current burst is associated with corona and glow discharge in the beam close to the capillary tip of the source. Such conditions produce many ions in the beam.

During any given source trial it was found that, if capillary tip shape, fluid condition, and vacuum system pressure were suitable, a range of fluid feed pressure and capillary potential could usually be found where the observed current was at a stable dc level. On the other hand, types of unstable beams were easily recognized and often could be correlated to one or more faulty operating conditions. Beam



stability as observed from the waveform of detected current had little relation to the beam spatial distribution simultaneously observed. In other words, pulse or unstable beams often had the same spatial distributions as dc beams.

Because beam stability was always the most troublesome experimental problem, the colloid source operating conditions were always chosen or varied to try to achieve a stable beam. Once the beam was produced, measurements were performed.

#### 6.2.2 Start-up Procedures

When fluid was forced out of the capillary tip with the capillary tube at extractor potential, the surface tension forces in the fluid allowed a large drop (~1 to 2 mm dia.) to collect on the tube tip before it fell off under the force of gravity. Any smaller drop would remain on the capillary tip as the capillary potential was increased to about 2.5 kV to 3 kV, then the drop was gently pulled free. Above this potential, the pulse mode of beam current usually appeared, and the potential could be varied continuously above 3 kV. Because this initial large drop often fell on the extractor and severely distorted the electric field pattern at the capillary tip, it was found advisable to use an alternative start-up sequence. In this sequence, the capillary voltage switch (thyatron) was turned into the 'on' state, and the capillary potential then selected on the high voltage power supply. The capillary voltage switch was turned 'off' and the operating potential applied quickly to the source. Then the feed pressure was increased from zero, to force fluid into the feed tube from the reservoir. Thus the beam started operation at a desired operating



point rather than being moved to a desired operating point after the beam was established.

It was found that the sharp transitions between types of beam current waveform exhibited hysteresis as a function of capillary voltage. In addition, once a certain type of beam was established, it was often difficult to initiate the transition to the next beam type as capillary potential was raised. The capillary voltage switch proved useful here. For example, initial operation at 17.5 kV capillary potential and 10 cm Hg feed pressure might produce a pulse mode. Stable dc current could often be achieved merely by turning the capillary voltage switch 'on' for about 1 second, then turning it 'off'. By the same token, this procedure sometimes initiated an unstable beam type which was even more difficult to change!

#### 6.2.3 Beam Modes in a Typical Experiment

This section contains a qualitative description of the types of beam current observed under typical experimental conditions, as capillary potential or fluid pressure was varied. Usually the greatest range of beam types was available by varying capillary voltage at constant fluid pressure. In Table 9, various beam current modes are listed as a function of typical capillary potential between 3 kV and 20 kV, at an unspecified, suitable, fixed fluid feed pressure.

The sequence of beam types shown in Table 9 was found experimentally over a wide range of capillary tube sizes, extractor geometries, and fluid solution strengths. In Table 9, there are two capillary potential regions--the low capillary potential region between 5 and 8 kV, and the high capillary potential region between 14 and 20 kV--



which could produce stable dc beams. At no time was a continuous dc region between 5 to 20 kV found. The high capillary potential region is of great interest for two reasons. Firstly, the existence of this region has not been previously reported. Secondly, in this region the beams are produced with a spatial distribution much closer to the central axis than beams produced in the low capillary potential region. Both these potential regions are discussed in detail later in this chapter.

Table 9: Beam Current Waveforms, as a Function of Capillary Potential.

Capillary Potential (kV)	Observed Beam Current Waveform	Comments
3 to 5	pulse train	Pulse width and frequency increase with increasing potential.
5 to 8	stable dc	Charge to mass ratio increases through the potential range.
8 to 10	dc + pulses	Pulses increase in number and randomness. At 10 kV, there is high beam current and high charge to mass ratio. Some ions produced.
10 to 14	very unstable beam	Appears as many large, overlapping pulses. No regular patterns observable.
14 to 16	pulse train	May or may not appear.
14 to 20	stable dc	Sudden shift to lower current, lower charge to mass ratio. Charge to mass ratio and beam current increase slowly through the potential range.
>20	dc + pulses, then unstable	Tends to repeat instabilities seen in 8 to 14 kV region.

While it was found that variations in capillary potential produced predictable variations in beam type, variations in feed pressure had a



much less definite effect. Between the limits 2 to 20 cm Hg, the feed pressure was usually varied to produce small changes in beam type. Only one range of fluid pressure gave a stable dc beam. This range of perhaps 5 or 10 cm Hg could be located anywhere in the range 2 to 20 cm Hg. The location of the suitable range varied from one experimental trial to the next.

#### 6.2.4 Unstable Beams

It was not always possible to produce the types of beam shown in Table 9, and the source exhibited various types of instabilities. While certain types of unstable beam were caused by more than one faulty experimental condition, possible causes could be assigned as shown in Table 10.

It must be emphasized that the two potentially stable operating areas, 5 - 8 kV and 14 - 20 kV, exhibited much the same behavior as capillary potential was increased through them. Thus in Table 10, "voltage too low" might refer to either the 5 kV or 14 kV operating point, and "voltage too high" might refer to either 8 kV or 20 kV.

#### 6.2.5 Capillary Voltage Stability

For the present experimental arrangement, the only cause of beam instability suitable for quantitative investigation was capillary voltage instability. In one experiment, a resistive load was placed across the capillary voltage power supply to increase power supply ripple. A ripple of 50 V pp on 6 kV dc was reflected by ripple on the observed dc beam. Similarly, a 50 V square wave pulse applied to the extractor plate (which was normally held at ground potential) could easily be seen in the detected beam current. Thus power supply regulation better



Table 10: Types of Unstable Beam, with Possible Causes of Instability.

Observed Beam Current	Possible Cause of Instability
Single periodic pulse train.	Voltage too low. If pulse height increases instead of pulse width and frequency as voltage is increased, source may prefer to operate in pulse rather than dc mode. Possibly feed pressure too low.
Two or more periodic pulse trains, asynchronous.	Good dc not likely to be found. May be rough capillary tube rim or gassy fluid.
Many overlapping pulses with no apparent pattern. Presence of ions possible.	Gassy fluid.
Stable dc can be established but changes to pulses after some time.	Feed pressure or voltage too low.
Stable dc with one or more asynchronous pulse trains on it.	Rough capillary tube rim or slightly gassy fluid.
dc with many pulses on it. Ions probably present.	Gassy fluid, or voltage or feed pressure too high. Poor vacuum at capillary tip.
dc with high ion content. Corona in beam at capillary tip.	Voltage or feed pressure too high. Poor vacuum at capillary tip.
Current "bursts" at regular periods. Many ions. <u>Very</u> unstable beam.	Very gassy fluid. Most probably very bad vacuum at capillary tip. This mode tends to spray fluid on walls of tube extractor. Usually cannot be rectified.
dc with sharp spikes in it (either higher or lower current value)	Electrons hitting source area.
Stable dc with regular waveform superimposed on it, or occasional gaps in beam.	High voltage supply ripple or instability.



than about 0.5% was essential.

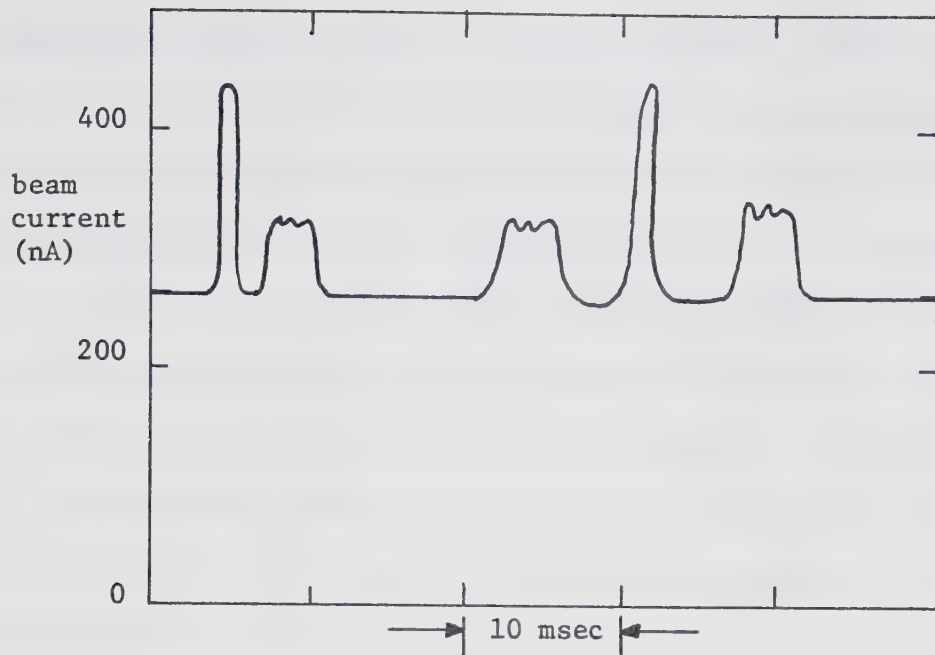
An indirect voltage instability inevitably arose when a surge of current from the capillary tip (for example an ion burst caused by gassy fluid) dropped the capillary voltage due to the large anode resistor on the capillary voltage switch. This instability tended to protect the colloid source, since lower capillary voltage produced a lower beam current.

With an external 1  $\mu$ f, 50 kV capacitor across the high voltage supply and a 17 Mohm anode resistor on the thyratron, normal power supply regulation in these experiments was measured to be 0.03%.

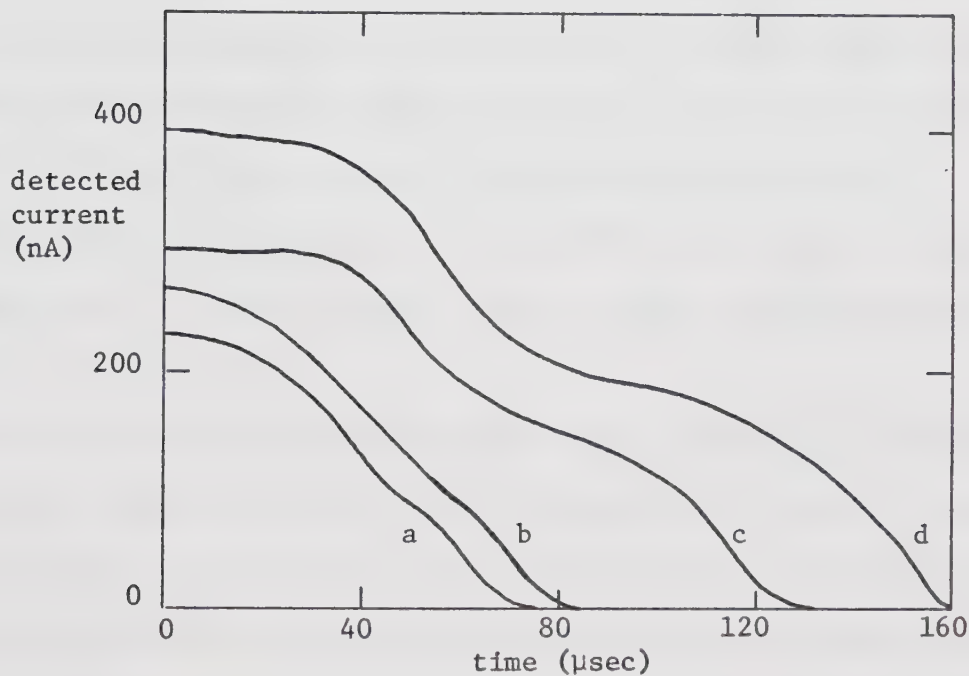
#### 6.2.6 Particle Charge to Mass Ratios in a Beam Containing Both dc and Pulse Modes

Figure 12a is a sketch of the detected beam current waveform for a mixed-mode beam upon which several time of flight measurements were made. The beam was only slightly unstable, and consisted of two pulse trains asynchronously superimposed on a dc beam. Four time of flight current decay curves sketched from the time of flight measurements are shown in Figure 12b. The duration of the time of flight current decay curves was at most 160  $\mu$ sec, while the widths of the pulses on the current waveform were between 1 msec and 5 msec, hence the time of flight measurements were of short duration compared to the beam pulses. This observation, together with the fact that the current decay curves are of the correct shape, shows that the variations in the shape of the measured current decay curves were not a result of the beam current instabilities, during or immediately prior to the time of flight measurements.





(a) Observed Current Waveform



(b) Time of Flight Measurement Current Decay Curves

Figure 12: Time of Flight Measurement Results on a Mixed Mode Colloid Beam. Curves a through d in Part (b) of the Figure are the Results of Four Measurements on the Beam Current Waveform Shown in Part (a).



Comparison of the four time of flight measurement curves in Figure 12b with the current waveform depicted in Figure 12a shows that curves c and d were initiated during pulses of beam current, while curves a and b were initiated during the dc part of the beam. The two distinct changes in slope of the curves c and d reveal that these curves depict the superposition of a beam similar in velocity to the beam measured by curves a and b, and a beam with much slower velocity. This in turn implies that the beam in Figure 12a consisted of a dc beam of higher charge to mass ratio particles with two pulsed beams made up of lower charge to mass ratio particles superimposed on it.

For this beam, source conditions were: capillary voltage 13 kV, feed pressure 4 cm Hg, fluid doping level 5 g NaI/100 ml glycerol, capillary tube #31 (see Section 6.6). The beam spatial distribution was constant as a cluster of jets in a cone. Measured nominal charge to mass ratios for the four cases in Figure 12b were: curve a, 318 coul/kg; curve b, 293 coul/kg; curve c, 155 coul/kg; and curve d, 71 coul/kg. The presence of the two pulse trains superimposed on the dc current was probably due to a poor capillary tube rim shape or possibly due to slightly gassy fluid.

This experiment demonstrated that beams consisting of superimposed dc and pulse beam modes contain more than one nominal value of charge to mass ratio on the particles. Thus, for a narrow, well-defined charge to mass ratio distribution in a colloid beam, mixed beam modes cannot be tolerated.

#### 6.2.7 Corona and Sparking at the Capillary Tube Tip

Corona in the sprayed beam was easily seen in the observed beam current as a large unstable increase in beam current, with ions present.



The beam usually disappeared for several seconds, then exhibited more current bursts. The basic cause for the corona was poor vacuum in the capillary tube tip region. The poor vacuum could in turn be caused by gassy fluid, high mass flow rate, high voltage, or poor pumping geometry. During corona the beam tended to become a general spray over a cone whose axial half-angle was often greater than  $45^{\circ}$ . Thus the beam could intercept the extractor and cause further problems, such as direct sparking and a worsening of the local vacuum pressure. Usually once current bursts were observed, no alteration of feed pressure or capillary voltage would restore stable beam operation.

Also, if the beam were allowed to strike a metal surface closer than about 2 cm from the capillary tube tip, corona formed in the beam. This problem imposed a restraint on the design and positioning of apparatus such as biasing electrodes, beam collimators, or detectors.

### 6.3 Beam Detectors

#### 6.3.1 Introduction

As discussed in Section 3.3, any complete investigation of a colloid source must include an assessment of the spatial distributions of the colloid beams produced. Because the segmented electrical detectors and point-by-point electrical beam sampling are either inconvenient or give incomplete results, some effort in the present work was devoted to improving the beam detection system. Sections 6.3.2 to 6.3.4 describe development of a segmented electrical detector, and development of the two types of visually reacting detector discussed in Section 3.3. Section 6.3.5 compares some results illustrating concurrent use of the three beam detectors.



### 6.3.2 Electrical Detectors

The electrical detectors are constructed as a series of concentric aluminum rings mounted with narrow gaps between them. The lucite backing plate holding the rings has grooves in it behind each of the gaps between the metal rings, in order to prevent accumulated glycerol from the beam from shorting out the adjacent rings. An electrical connection from each ring is passed through a vacuum feedthrough and fed to the external switch box. By selecting the detector output using the switch box, measurements of beam current incident on any ring or combination of rings can be made, as are time of flight measurements.

For measurements on well focussed or high velocity beams, a four ring detector with a flat surface of 0.114 m outer diameter was placed 0.3 m from the source. The distance from the source to the detector rings was 0.3 m for the center ring and 0.305 m for the outermost ring. The detector accepted beams up to  $11^\circ$  off axis.

For meaningful measurements on divergent colloid beams, the detector had to measure beams up to  $45^\circ$  off axis. Accordingly, the size of the experimental chamber forced the detector to be mounted close to the colloid source. To accomplish this, a five-ring detector was machined as part of an 0.07 m radius spherical surface, and the source capillary tube tip was positioned at the center of curvature to ensure equal drift distances for all beam components. The outer edges of the five detector rings form half-angles of  $5^\circ$ ,  $15^\circ$ ,  $25^\circ$ ,  $35^\circ$ , and  $45^\circ$ , with respect to the central axis.

For either detector, the entire detector surface is placed in a grounded enclosure and the output signal leads are shielded in order to reduce noise pickup. Two planar wire grids are placed directly in



front of the detector surface to allow application of a bias voltage to control the secondary electrons produced by the beam striking the detector surface. The outer screen is grounded to prevent the bias voltages from perturbing the electric fields in the experimental chamber. The inner screen is insulated from the rest of the detector, and was biased negatively by means of an external electrical lead. The wire grids are made of 0.076 mm diameter stainless steel wire wound on a square grid. The wires are 3.18 mm apart, and the area of the wires in each screen was calculated to be 5% of the total screen area.

In general, the operation of these electrical detectors was satisfactory. Two problems were caused by the beam hitting the bias grids prior to hitting the detector surface. The first of these occurred when an intense jet of the beam intercepted one or more wires of the bias grid. Over a period of perhaps 10 minutes a large drop of glycerol would collect on the wire. This drop could intercept a significant fraction of the total current incident on that particular area, and thus cause an error in detected current. The second problem was the scattering of the beam by the grids. The scattering caused a broadening of the true spatial distribution of the beam, and at times appeared to contribute a long-duration "tail" on the current decay curve of a time of flight measurement. The scattered particles were either original beam particles slowed down and deflected, or secondary glycerol particles knocked off the grids at low velocity.

#### 6.3.3 Phosphor Detector

In order to test the basic concept of the phosphor detector, phosphor powder (Sylvania type P161<sup>67</sup>) was deposited on a piece of clean sheet aluminum. The aluminum backing served as a means to bleed



off accumulated charge, since the phosphor powder itself is non-conducting. The powder was ground using a mortar and pestle, and then mixed as a suspension in a large container of water. The aluminum detector plate was then placed at the bottom of the water tank, and the phosphor allowed to settle to the bottom of the tank (the settling process took about 5 to 10 hours, typically). Finally the clear water was carefully siphoned out of the tank, and the detector plate left to dry. It must be emphasized that the phosphor powder was very lightly bonded to the backing plate, so great care had to be taken not to mark the phosphor layer both in the drying process and in routine detector use. The depth of the phosphor layer was roughly regulated to correspond to a weight of  $5 \text{ mg/cm}^2$ , by weighing the total amount of phosphor powder used and calculating the areas of the backing plate and the bottom surface of the water container. In their phosphor products catalogue, Sylvania<sup>67</sup> states that a layer thicker than  $5 \text{ mg/cm}^2$  absorbs too much of the phosphorescent light produced.

Direct bombardment of the phosphor coating on the detector clearly showed the beam spatial distribution. Because of the geometry of the experimental chamber, photographs of the surface of this particular detector could not be taken. The phosphor layer depth seemed quite adequate.

The next (and final) detector design incorporated a transparent backing for the phosphor powder layer. A 6.35 mm thick glass plate was covered with a transparent layer of sputtered chromium on one side. The chromium layer, which bled off accumulated beam charge, had a resistance of about 5 kohm between the center of the glass plate and an outer grounded mounting ring. Phosphor was deposited in the manner



described above, to about the same thickness. With the optically transparent backing, the pattern of light generated by the incident beam could be viewed from either side of the detector, and photographed through the detector backing.

Two detectors of 0.14 m diameter active surface were made, and were used interchangeably. The detector mounts allow beams up to 45° off axis to be viewed.

While the detector can be viewed in dim light, successful photography of the beam spatial distribution requires a darkened room. Since the detector shows only the beam spots, a spatial reference for the detector was provided during photography of the beam shape by briefly flashing two small incandescent lamps placed on the source extractor plate, facing the detector and camera. These gave a spot of light on each side of the detector plate and also faintly illuminated the detector surface. Details of photographic procedures are given whenever individual detector results are presented.

It was found that the phosphor ceased to function once a visible deposit of glycerol had collected. Either the built-up layer absorbed the momentum of the incoming droplets, or it shielded the crystals from the electric fields surrounding the charged droplets, since the glycerol solution is conducting. However, if the glycerol on the detector was allowed to evaporate, the screen was re-usable. Eventually the NaI from the solution accumulated, the phosphor crystals themselves deteriorated, and the phosphor response weakened.

#### 6.3.4 Liquid Crystal Detector

All of the liquid crystal materials used in this work were obtained from the Edmund Scientific Company<sup>68</sup>. As explained in Section 3.3.3.3,



the conceptual design of each of the liquid crystal detectors used is a layer of black plastic (either painted clear plastic or black mylar) coated with liquid crystal material. In order to bleed off the accumulated beam charge, the detectors were mounted against a wire grid, and were bombarded from that side. The liquid crystal material was illuminated and viewed from the side facing away from the beam.

The first detector tried was made up from a "kit" containing three solutions and some black mylar sheets. Solution mixtures yielded a liquid crystal solution which, when painted on the black plastic, dried to give a waxy material. Some experimentation yielded a recipe for the material which responded visibly to temperature changes near room temperature. Tests of this liquid crystal screen showed that the beam did contain enough energy to cause visible colour changes in liquid crystal material. Problems encountered included: difficulty in reproducing the liquid crystal characteristics, unevenness of the liquid crystal layer thickness which gave different thermal capacity to different parts of the screen, vulnerability of the exposed liquid crystal material to contaminants which changed its colour, contamination from the glycerol which penetrated the 0.05 mm thick mylar sheet, and the inability to clean the detector. Several attempts to solve these problems were unsuccessful.

The next liquid crystal detector tried was of the same configuration, but the liquid crystal material was obtained in a prefabricated sheet. The sheet consists of a layer of clear mylar, a layer of liquid crystal material in the form of encapsulated inert spheres of 20 to 40 microns diameter, and a layer of black paint. The encapsulation of the liquid crystal material makes the screen resistant to solvents and



abrasion. In the final configuration, the wire grid used to bleed accumulated beam charge off the detector was the same as those used on the electrical detector. The liquid crystal detector is 0.108 m in diameter, and displays beams up to 37° off axis. The detector has a nominal sensitive range of 25° to 31°C.

Use of the liquid crystal sheets means that the material is viewed through the clear plastic layer. In order to prevent reflections from the shiny plastic surface, the detector was illuminated at an acute angle by fluorescent lamps placed on each side of the glass cross forming the experimental chamber. When viewed along the surface normal, an even hue was seen on the detector. Care was necessary to illuminate the screen uniformly and thus prevent variations in colour due to the temperature changes caused by uneven lighting.

Beam pile-up was a minor problem with this detector, since accumulated glycerol merely increased the thermal inertia of the detector but did not interfere with the basic detection mechanism. The screen was cleaned by washing it in distilled water, and was found to withstand many cleaning cycles. Detector deterioration, when it happened, was obvious because the even background colour of the liquid crystal screen became blotched and mottled, probably as the result of chemical changes in the liquid crystal material<sup>57</sup>.

The response of the liquid crystal screen was found to closely indicate the intensity distribution of the incident beam. The spreading of colour outside an intense beam jet was small. Also, the colour pattern observed agreed closely with the pattern of glycerol deposited on the black side of the detector, and with the display on the phosphor screen. These correlations are demonstrated in the next section.



### 6.3.5 Operation of Detectors

This section contains some discussions of the results obtained from the three beam detectors for measurements on the same beam. Emphasis is placed on the detector, rather than beam, properties. In the electrical detector results, ring solid angles have not been factored out, hence the currents measured on the outer rings appear over-emphasized. Collection of results for the three detectors on one beam generally took 10 to 20 minutes, but the beam distribution and current did not seem to change significantly during this period. The time was required to take photographs and record data; the detectors themselves could be used and viewed in a matter of seconds.

The two cases are presented for comparison of the detectors in Figures 13 and 14. Figure 13 is a colour reproduction of the original 35 mm format colour slides, while Figure 14 shows black and white reproductions of the colour slides. The beam was at a stable dc level in both cases. The photographs of the entire liquid crystal screen were taken with a 50 mm lens with one short extension tube. Exposures were typically 1/30 second at f/1.4. Close-up photographs of the liquid crystal detector used a 105 mm lens and three extension tubes, with typical exposures of 1/2 second at f/2.8. All photographs of liquid crystal detectors shown here have been masked to show the entire detector surface but only a portion of the mounting ring. Photographs of the phosphor screen were taken with the 50 mm lens at exposures of 20 seconds at f/1.4. In all cases the capillary tube tip to detector drift distance was 0.07 m along the central axis, and the spherical, five ring, electrical detector was used to measure beam currents.

Figure 13 depicts colour photographs of detector results for a



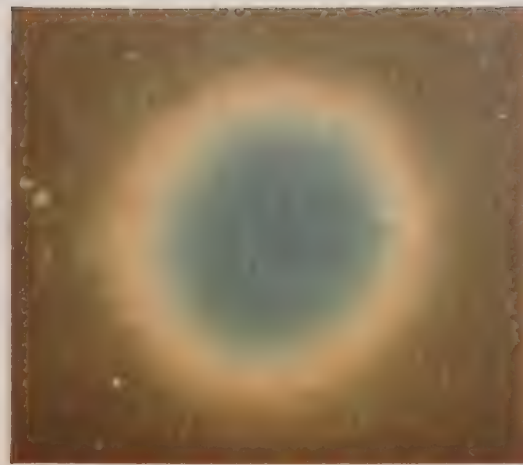
well focussed axial beam formed at a capillary potential of 20 kV using 5 g NaI/100 ml glycerol fluid and a 25 mm long, #27 platinum-iridium capillary tube. Fluid feed pressure was 7.8 cm Hg. Figure 13b is a close-up photograph of the beam spot on the liquid crystal detector shown in Figure 13a. The blue central area, which represents an intense beam spot, is surrounded by less intense beam areas which give rings of colour from blue to red at the fringe of the beam spot. The background of the beam spot is a normal reddish-brown because no thermal biasing was used. The bright area on the edge of the screen in Figure 13a is glare from the external illumination. The phosphor screen of Figure 13c gives more detail in the beam than the liquid crystal screen. Figure 13d shows the distribution of detected beam current, which totalled 430 nA. The electrical detector shows a well focussed beam, in agreement with the visual detectors. The nominal charge to mass ratio of 58 coul/kg and the mass flow rate of 7.4  $\mu\text{g}/\text{sec}$  were found from time of flight data on the total beam current.

Figure 14 shows black-and-white photographs of the detector results for a beam which is fairly well focussed but off axis, produced at 9.4 kV and 7 cm Hg fluid feed pressure. A broad horizontal section of the liquid crystal screen has been thermally biased from reddish-brown to orange, accounting for the large light coloured area in Figure 14a. The detector shows two yellow-green spots, indicating two jets of sufficient kinetic energy to heat the screen. The diffuse area between the jets, which is reddish-brown in colour, indicates a portion of the beam in which the kinetic heating is insufficient to overcome the cooling effect of the evaporating glycerol. In this case the phosphor screen in Figure 14b shows less beam detail than the liquid

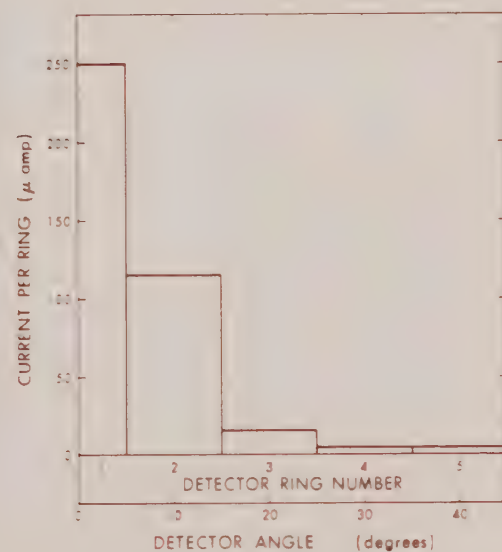




(a) LIQUID CRYSTAL DETECTOR

(b) LIQUID CRYSTAL DETECTOR,  
CLOSE-UP

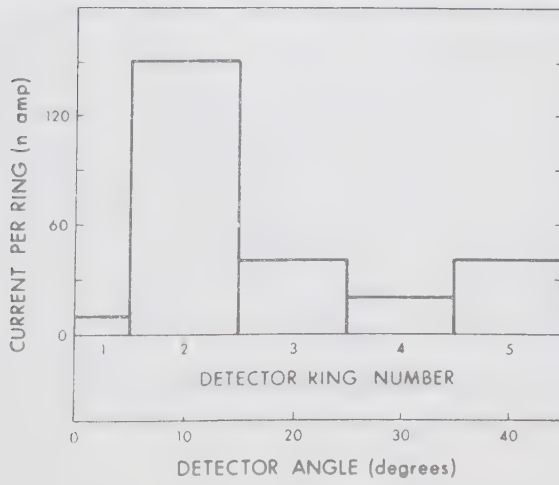
(c) PHOSPHOR DETECTOR



(d) CONCENTRIC RING CURRENT DETECTOR

Figure 13: Colour Photograph Depicting Results Obtained Using Phosphor, Liquid Crystal, and Segmented Electrical Detectors on One Particular Colloid Beam.





(c) CONCENTRIC RING CURRENT DETECTOR

**Figure 14:** Comparison of Results Obtained Using Phosphor, Liquid Crystal, and Segmented Electrical Detectors on One Particular Colloid Beam.



crystal screen. A beam angle of  $\sim 15^\circ$  off axis was estimated from the visual detectors, which coincides with the maximum detected current shown in Figure 14c. The 260 nA beam had a nominal charge to mass ratio of 37 coul/kg and a mass flow rate of 7.3  $\mu\text{g/sec}$ .

Generally, the liquid crystal detector reached a stable colour pattern perhaps 15 seconds after the beam was directed on the screen. Because the screen returned to a uniform colour when the beam was removed, and because the screen could be easily cleaned, the colour change of the liquid crystals was due to a temperature effect and was not a chemical reaction with the NaI-glycerol.

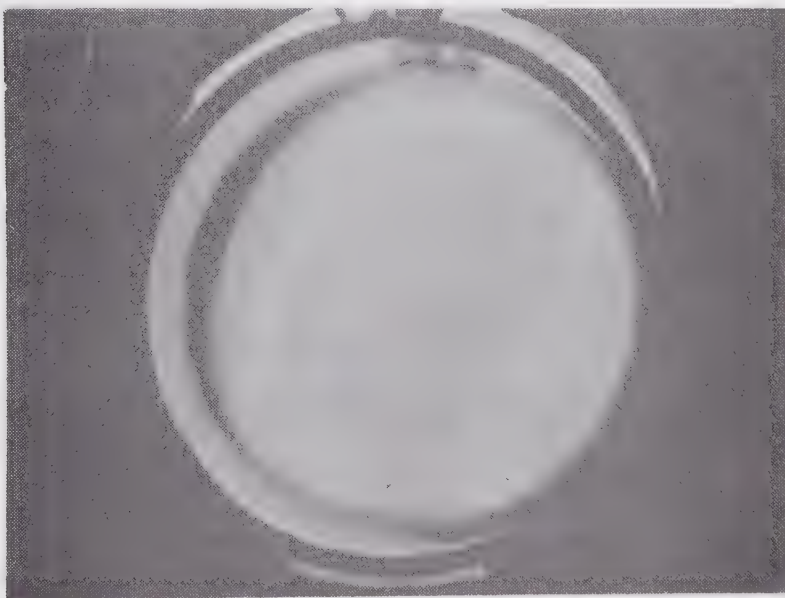
For the beams shown here, beam pile-up on the phosphor screen caused a deadening of detector response after perhaps 20 seconds. In order to get good photographs of the detector, the detector was cleaned and re-installed immediately after only one type of beam was investigated. In normal use the detector could be used much longer by moving it in front of the beam, and by ignoring the few dead spots on the detector surface.

Figure 15 shows a convincing demonstration of the fidelity of the phosphor screen detector. Figure 15a is a photograph of the phosphorescent beam spot in the center of the back-lit screen. The photograph required a 40 second exposure on 3000 ASA Polaroid film, using an f/4.7 Graflex camera. Operational beam parameters were: 13 kV, 12.5 cm Hg, 2.5 g NaI/100 ml glycerol, #29 stainless steel capillary tube, tube type extractor. Measured beam parameters were: 95 nA, 12 coul/kg, 8.1  $\mu\text{g/sec}$ . Figure 15b is a picture of the same screen after the beam had run for 10 minutes, taken in full room light. The clear spot on this photograph is glycerol deposited by the beam, and its shape and position





(a) Image of Colloid Beam, Showing Phosphorescent Light in the Center of the Phosphor Detector.



(b) The Phosphor Detector of (a) Has Been Photographed in Room Light. The Glycerol Deposited on the Detector Shows as a White Spot in the Center of the Detector.

Figure 15: Photographs of a Phosphor Detector, Comparing the Pattern of Light Emitted with the Corresponding Pattern of Deposited Glycerol.



correspond closely to that of the phosphorescent beam spot in Figure 15a.

While not shown here, it should be noted that the liquid crystal screen showed beam intensities just as well as the phosphor screen did in the case illustrated in Figure 15. The area warmed by the beam agreed closely with the deposited glycerol seen on the black surface of the detector.

#### 6.4 Secondary Particles

##### 6.4.1 Positively Charged Secondary Particles

In the very early attempts to operate the test bench colloid source, it was inadvertently found that the charged glycerol beam could be scattered off the glass walls of the experimental chamber, and be detected in the electrical detector. As the experiment progressed, wet spots appeared on the glass wall where the beam struck the glass cross prior to scattering. The scattering phenomenon occurred throughout the experiment, indicating that the scattering took place initially from the clean glass surface and later from the spot on the glass wet by the incident glycerol.

It is clear that colloid beam experiments must be designed to minimize the possibility of scattered glycerol particles entering the beam detector.

##### 6.4.2 Secondary Electrons

The discussion of secondary electrons in Section 2.9 showed that a careful investigation of the effects of secondary electrons on colloid source operation must be made. Accordingly, tests of secondary electron effects were made periodically throughout the present study, whenever



major changes to the source or detector geometry were made. The following is a summary of these results:

- (a) At no time was the secondary electron current a significant part of the positive beam current. In other words, beam current and time of flight measurements appeared to be independent of bias voltages applied to various retarding electrodes.
- (b) Biasing the source extractor or the grid in front of the detector did not change stable beams very much, noticeably stabilized partly unstable beams, and did not improve unstable beams very much. Thus the source could be operated in a stable mode without any biasing, and unstable source operation is caused by effects other than backstreaming electrons.
- (c) Application of detector grid bias greatly reduced the fluorescence of the glass walls of the experimental chamber. This fluorescence appeared occasionally during high voltage, high charge to mass ratio trials of the colloid source.
- (d) Application of source extractor bias improved beam stability to about the same degree as did the detector screen bias, but extractor bias did not prevent the secondary electrons from leaving the detector surface.
- (e) Tar-like deposits were never seen on the capillary tube tip in contrast to observations reported by Huberman and Cohen<sup>25</sup>.
- (f) The tar-like deposits were seen on the detector surface, particularly after an experiment using high capillary voltage or high charge to mass ratio beams.
- (g) The production of secondary electrons was much greater if ions were present in the colloid beam.



During the experiments, the presence of secondary electrons was deduced from observations of small, short-term instabilities in the detected dc beam current. A reliable indicator of secondary electrons was the occurrence of fluorescence on the walls of the glass experimental chamber.

It was found to be better and easier to apply a bias of between -30 V and -100 V to the detector grid than to bias the source extractor to suppress secondary electrons. The threshold of -30 V was chosen by observations that evidence of secondary electrons in the experimental chamber disappeared for bias voltages more negative than about -25 V. Stark and Sherman<sup>28</sup> report that a bias of -22 V was sufficient for secondary electron suppression.

It seemed that fewer secondary electron effects were observed in the present work than have been reported in the literature. This result was attributed to the fact that beams of much lower charge to mass ratio ( $\leq 100$  coul/kg as opposed to  $\geq 1000$  coul/kg) have been produced in the present study. Also, for beams in these experiments, no ions were produced in the colloid source.

## 6.5 Source Extractor Experiments

Two basic types of source extractor plate, which have been shown in Figure 9, Chapter 5, were tested. The flat type has a thickness of 0.8 mm, an inner diameter of 4.75 mm, and the edge of the central hole is rounded to a radius of 0.4 mm. The capillary tube tip is positioned flush with the outside of the extractor plate. The tube type of extractor has the capillary tube positioned along the axis of a tube, 9.5 mm in diameter and 20.5 mm long.



In general, the extractor hole diameter does not have a fundamental influence on the source behavior. If the hole is relatively large, the capillary can be operated at a higher potential to get the same electric field intensity as for a smaller diameter extractor run at a lower potential.

Experimentally the two extractors behaved in a very similar fashion for the same source conditions. Where divergent beams were to be studied, the flat extractor had to be used so that the beam did not strike the extractor. Where axial beams were used, either type of extractor was suitable. In fact the choice of the tube extractor diameter and tube length is somewhat arbitrary. The approach taken for the design used in these experiments was to select the tube length as 20.5 mm in order that the electric fields surrounding the capillary tube be contained almost completely inside the tube extractor. Then the diameter was chosen to provide an adequate aperture for the emerging beam. The diameter of 9.5 mm used here allows production of beams up to  $15^{\circ}$  off axis.

Sparking from the capillary tube tip to the extractor was never a problem for the dimensions used in these experiments. It seemed that, when the vacuum pressure in the capillary-extractor region rose enough to increase the danger of sparking, beam instabilities appeared first. These beam instabilities required suspension of source operation prior to any capillary to extractor sparking.

The advantages of the flat type extractor design are:

- (a) the beam can never collide with the extractor, so all shapes of beam can be studied,
- (b) it is easier to maintain good vacuum in the capillary tip region.



The advantages of the tube type extractor design are:

- (a) the electric field shape at the capillary tip is dependent on capillary alignment in the extractor, but not on its axial position,
- (b) the electric field at the capillary tip is well shielded from any other potentials or electrodes present in the experimental system,
- (c) the tube type extractor helps shield the capillary tube from secondary electrons in the system.

Wherever possible, the tube type extractor was used for the experiments described in Chapter 6. The only exceptions were the cases in which the results showed widely divergent colloid beams.

## 6.6 Capillary Tube Experiments

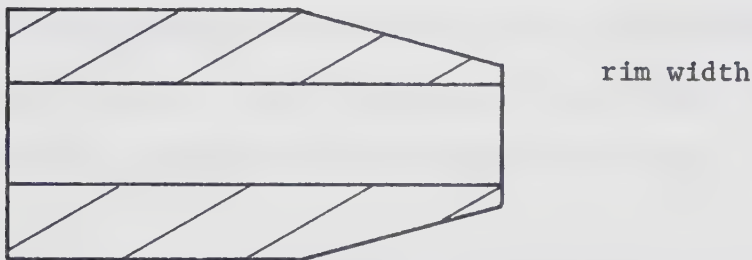
A literature search showed that the best microthrust rocket results were obtained with platinum or platinum-iridium alloy capillary tubes. Stainless steel capillary tubes were reported to show some erosion after use in colloid sources. The most commonly used capillary tubes had dimensions of about 0.1 mm inner diameter, 0.25 mm outer diameter, and had lengths of about 25 mm. It was also repeatedly shown that the shape of the capillary tube tip had a strong effect on colloid source behaviour.

Figure 16 shows the most commonly described capillary tip shapes, together with some definitions of terms required for the present discussion of the tip shapes. The following list of tip shapes mentioned in the literature is arranged in an order representing increasing colloid beam stability: flat end with sharp corners<sup>40</sup>, flat end with rounded corners<sup>28,40</sup>, thin rounded rim formed by an outside taper<sup>28,40</sup>,

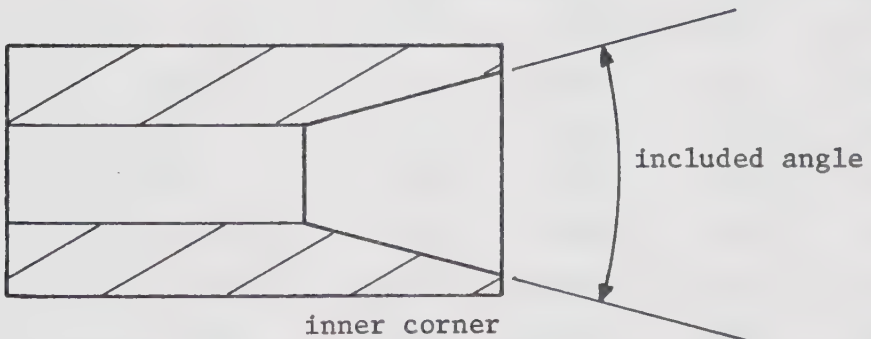




(a) flat end style



(b) outer taper style



(c) inner taper style

Figure 16: Three Different Capillary Tube Tip Shapes Used in Colloid Beam Research.



thin rim formed by a shallow inside taper ( $90^\circ$  included angle)<sup>69</sup>, thin rim formed by a deep inside taper ( $<60^\circ$  included angle)<sup>14, 21, 28, 69</sup>.

Cohen and Huberman<sup>69</sup> attribute erosion of the  $90^\circ$  included angle inner tapered tip to the relatively large included angle; they prefer to use a  $40^\circ$  included angle.

In the present work, a variety of capillary tube sizes and tip shapes was used. Both #304 stainless steel (hereafter denoted SS) and 90% platinum-10% iridium alloy (hereafter denoted Pt-Ir) materials were used. Table 11 shows the capillary dimensions and materials used, together with the AWG number (based on capillary outer diameter) which is used to identify capillary tubes throughout this thesis. The capillary tubing was obtained from the Hamilton Company, Whittier, California<sup>70</sup>.

Table 11: Capillary Tube Dimensions, Materials, and AWG Numbers, which are Used in this Thesis as Identification for Capillary Sizes.

AWG Number (based on O.D.)	Material	Nominal Outer Diameter (mm)	Nominal Outer Diameter (in)	Nominal Inner Diameter (mm)	Nominal Inner Diameter (in)
#26	SS <sup>a</sup>	0.46	0.018	0.25	0.010
#29	SS	0.33	0.013	0.18	0.007
#31	SS	0.25	0.010	0.13	0.005
#33	SS	0.20	0.008	0.10	0.004
#26	Pt-Ir <sup>b</sup>	0.46	0.018	0.25	0.010
#27	Pt-Ir	0.41	0.016	0.20	0.008

a #304 stainless steel

b 90% platinum-10% iridium

Experiments performed to investigate the effects of varying capillary tube size show (as expected) that the larger inner diameter tubes produced a higher fluid mass flow rate and a correspondingly lower



nominal charge to mass ratio in the colloid beam. However, the #26 and #27 size capillaries had such a large mass flow rate that it was difficult to maintain adequate vacuum in the experimental chamber when the source was producing dc beams. Thus the #26 capillaries were not used after some initial testing, while #27 capillaries were sometimes used. Pt-Ir capillaries of size smaller than #27 could not be purchased from the usual supplier<sup>70</sup>. As an alternative to purchasing smaller capillaries from another supplier, fluid flow in the #27 Pt-Ir capillaries was restricted by inserting a piece of stainless steel wire into the bore of each capillary. The wire inserts were either 0.08 mm diameter by 20 mm long, or 0.13 mm diameter by 10 mm long. In the present experiments, the best results were obtained with #29, #31, and #27 (with wire insert) capillaries.

As described in Section 5.5, the capillary tubes were soldered into stainless steel caps which can be screwed onto the capillary holder on the end of the fluid feed line. The 25 mm long capillary tubes were soldered to the caps with 4 mm protruding towards the extractor, and 21 mm inserted into the feed line. The caps, which were kept permanently soldered to the tubes, were convenient for holding the capillaries during shaping, cleaning, or storage.

The problem of shaping the capillary tube tip is a formidable one. If the tip is to be formed by accurately machining the capillary tube, the machining must be done under a microscope. In addition to the problem of close tolerances on the small dimensions involved, the capillary tube materials are difficult to machine. Cohen<sup>71</sup> described a process whereby the capillary tube is forced over a preformed mandrel to flare the tip to the desired shape. The excess material is machined



off, and the rim then polished.

In the present work, the various capillary tube tip shapes were formed by spinning the capillary tube and support cap in a lathe or drill chuck, and using #800 cutting grit and miniature spade drills to cut the tube tip. While this method did not produce a closely reproducible tip shape, it was sufficient to form tip shapes for testing. Of the various possible shapes mentioned in the literature (which were referred to earlier), only those having an inner taper would produce stable dc beams when tried in the present experiments. The other tip shapes appeared to be unsuitable.

The tip shape used in all subsequent colloid source experiments described in this thesis corresponds to Figure 16c. The included angle of the inner taper was  $120^{\circ}$ . The rim widths were  $(0.03 \pm 0.02)$  mm. The outer corner of the rim had a radius of about 0.01 mm. This tip shape was produced as follows:

- (a) The capillary tube and support cap were spun in a lathe or drill chuck.
- (b) Using #800 corundum grit and light machine oil on an aluminum backing, the tube tip was ground square and flat. Frequent cleaning of the tube with 0.08 mm or 0.12 mm diameter stainless steel wire was essential here to prevent the tube from clogging.
- (c) A spade drill of diameter just larger than the capillary outer diameter was used to cut the taper to a closely reproducible included angle of  $120^{\circ}$ . The spade drill was hand-held against the spinning capillary tube when cutting the taper. The drill was held loosely enough that it could be self-centered in the capillary tube in spite of the small vibrations of the spinning capillary



tube. The taper was cut until the rim width was of the order of 0.03 mm.

- (d) The burrs on the rim were removed either by cutting with the #800 grit, or by burnishing the rim on a smooth steel surface.
- (e) The burrs on the inner corner of the taper were removed by running a wire down the inner bore of the tube.
- (f) When the tip was of the correct shape, the tube was cleaned by forcing reagent-grade methanol through it from a hypodermic syringe.
- (g) The wire insert, when one was to be used, was formed in a "U" shape. One arm of the "U" was inserted inside the end of the capillary away from the formed tip, while the other arm of the "U" was tack-soldered to the outer surface of the capillary. This method ensured the wire insert would stay in position.
- (h) The assembly was cleaned again in methanol.

Some problems were encountered using this method of tip shaping. The #800 grit was not fine enough to produce a polished finish on the tip surfaces. (The spade drill, if sharp, left a smooth shiny surface on the tapered section.) Burrs left from the drilling were difficult to remove. The greatest problem was that in step (b) the end could seldom be cut perfectly square to the tube axis, so that after the taper was cut, an uneven rim width resulted.

While the angle of the tapered section is probably not steep enough for optimum performance, these capillary tubes worked adequately. After some practice and familiarity with the production method, capillary tips could be made in less than one-half hour each. Repairs or improvements to existing tips generally took only a few minutes.



Two microscopes were available for inspecting capillary tubes. The most useful was a binocular microscope with between 12.5x and 100x magnification. The depth of field of this instrument allowed examination of the entire tip shape at once. More detailed examination could be done with a standard microscope at magnifications of up to 1000x.

It appeared that when the source was operated in the 3 to 10 kV region, the shape and quality of the rim at the tip was quite important. On the other hand, at 14 to 20 kV, the shape of the inner corner of the taper was more important than the rim shape. This phenomenon is corroborated later by the discussions of capillary tip erosion.

It is realized that the method of producing capillary tube tip shapes gave non-ideal tip shapes. Reproducibility was also a problem. However, a better method would have required much more elaborate tooling and much more development time. The inconsistencies between successive experiments found after quantitative measurements of beam parameters (Section 6.9) were quite possibly partly due to variations in the capillary tube tip shapes used.

As discussed in Section 4.1, it is possible that electrolysis of the working fluid of a colloid source takes place at the capillary tube tip. Thus erosion of the tube tip may be expected. When operated below 10 kV, SS capillaries showed some erosion of the tapered surface and rim, but could be reliably operated for one-half hour or more. In this voltage range, Pt-Ir capillaries showed very little erosion. When operated between 14 and 20 kV, the SS capillaries eroded severely in a matter of 15 minutes or less, while Pt-Ir capillaries lasted several hours. For any voltage or either capillary material, the presence of corona in the beam was always associated with heavy erosion on all



the surfaces of the tube tips. In the 14 to 20 kV region, erosion of the Pt-Ir capillaries took two forms. If the beam produced was at a stable dc level, erosion occurred only on the one-third of the tapered surface closest to the inner end of the taper. The corner between the inner bore of the capillary and the taper was uniformly rounded off. On the other hand, any form of beam instability resulted in an erosion pattern uniform over the entire tapered surface.

### 6.7 Fluid Experiments

Early in this work it was discovered that fluid doping levels of 2.5 to 7.5 g NaI/100 ml glycerol produced beams with sufficiently low charge to mass ratio. Colloid microthruster applications normally use 20 to 30 g NaI/100 ml glycerol. This discovery of a suitable NaI-glycerol solution strength is the main reason beams with nominal charge to mass ratios between 10 and 100 coul/kg were successfully produced.

No special attempts were made to filter the solutions before use, but capillaries of the dimensions used here never clogged because of solids in the fluid. Since glycerol is hygroscopic, the fluids, once outgassed, had to be kept under vacuum as much as possible. If the fluid was exposed to air too often or too long due to source cleaning or other experimental changes, it had to be heated and outgassed again. The deterioration of fluid condition resulted in a more unstable beam. Fluid outgassing at room temperature was a very slow process because of the extreme viscosity of the glycerol. The surface layer of fluid would outgas well but the main body of fluid would remain contaminated. A teflon-coated magnet was often agitated in the fluid reservoir while the fluid was under vacuum, in order to aid outgassing by presenting a



different part of the fluid to the fluid-vacuum interface.

Once the solutions were properly outgassed, all the solution strengths between 2.5 and 7.5 g NaI/100 ml glycerol produced stable beams. The relationship between fluid doping level and beam nominal charge to mass ratio is investigated in Section 6.9, the discussion of the parametric analysis.

## 6.8 Beam Spatial Distributions

### 6.8.1 Introduction

This section describes the results of spatial distribution measurements on stable dc colloid beams. Information was obtained by observing and photographing the beam on the two visually reacting detectors, and recording the current per detector ring on the electrical detector.

As in the beam stability and parametric study discussions, two distinct modes of operation were found. The 5 to 10 kV 'low voltage' region produced beams of wider divergence than did the 14 to 20 kV or 'high voltage' region.

### 6.8.2 Low Voltage Region

Generally speaking, the results in the 5 to 10 kV region agreed with published results<sup>21,45</sup>. As voltage was increased through this region, the beam changed from a few discrete jets scattered on the arc of a hollow cone, to many discrete jets on the cone, to a diffuse hollow cone. The cone half-angle decreased from about 45° off axis to 20° off axis over the same voltage range.

Figure 17 shows the electrical detector (five ring, spherical surface) results for the beam angular distribution as a function of



detected beam current per detector segment (nA)

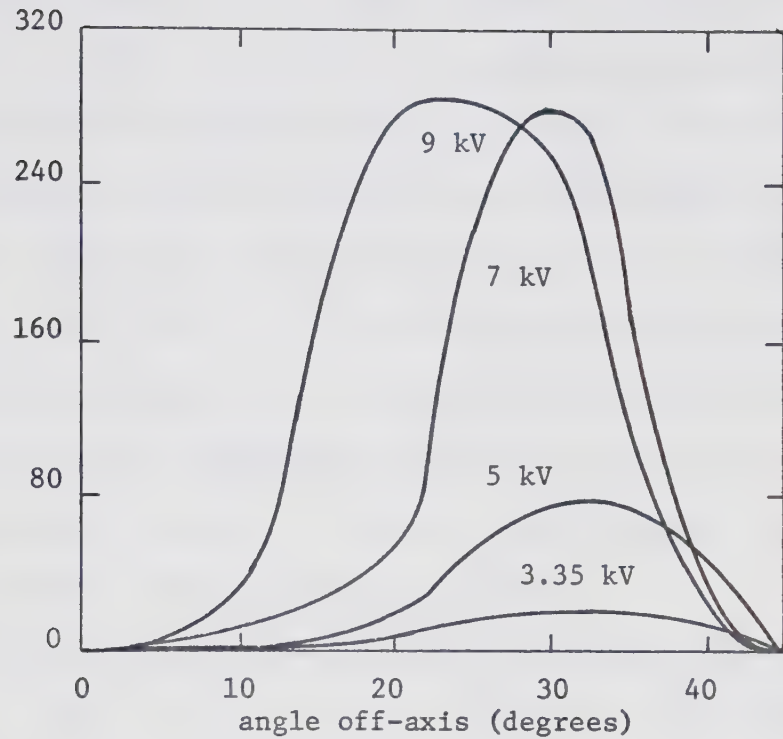


Figure 17: Beam Current Spatial Distribution as a Function of Capillary Voltage. Voltage is Shown as a Parameter Beside the Various Curves in the Figure. The Results are Taken in the Low Voltage Operating Region.

detected beam current per detector segment (nA)

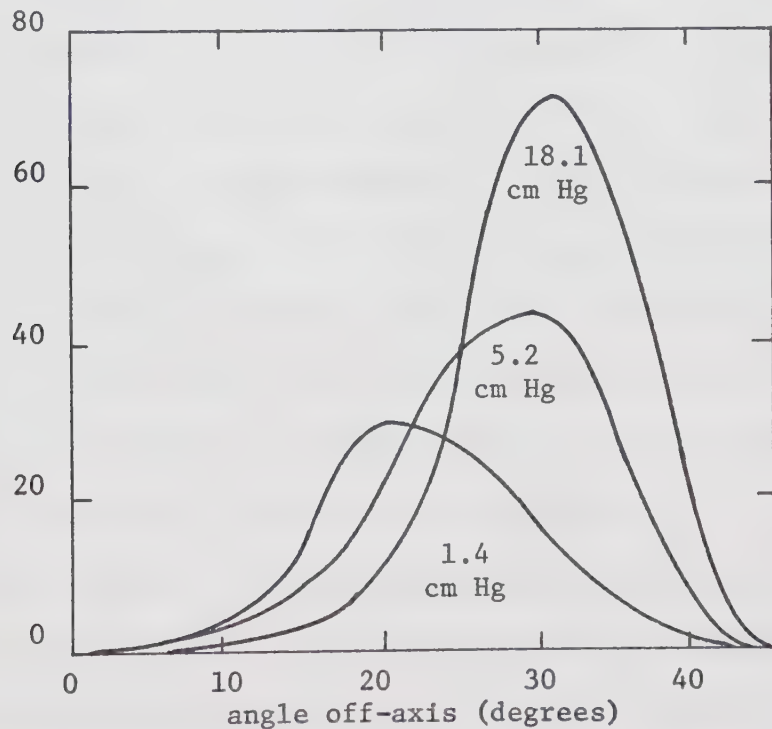


Figure 18: Beam Current Spatial Distribution as a Function of Fluid Feed Pressure. Pressure is Shown as a Parameter Beside the Various Curves in the Figure. The Results are Taken in the Low Voltage Operating Region.



voltage, at a fixed pressure of 5.2 cm Hg. The beam was always divergent but the results indicate a trend to increasing current and decreasing divergence as the voltage increases from 3.35 to 9 kV. Note that nothing can be said about the shape of the beam hitting a certain detector ring--the beam on any ring could have been either a single jet, or a complete ring of jets. Here the beam was produced using a #29 stainless steel capillary, and 2.5 g NaI/100 ml glycerol fluid.

Figure 18 displays the complementary case where voltage is fixed at 7 kV, while pressure is varied. A trend to more divergent, higher current beams was observed with increasing pressure.

During the many trials performed in these experiments, axial beams were observed only twice. However, these beams were not reproducible.

Figure 19 illustrates clearly the changes in the colloid beam spatial distribution as operating voltage is changed. The figure shows three beam shapes, for 5, 7, and 9 kV, as they appeared on the phosphor detector. Technical details of the beams and photographs are given in Table 12, together with the same information for the next case to be discussed, Figure 20. Beam currents and nominal charge to mass ratios are not available for the cases in Figure 19. In Figure 19b, some of the individual jets in the beam appear to be hollow rings on the phosphor screen. This is due to beam pile-up on the detector, which has in turn made the phosphor inactive. Figure 19c shows some dark spots in the beam pattern, which are also caused by beam pile-up.

Figure 20 shows a different type of hollow cone beam distribution--one formed of many discrete jets. The photographs of the visually reacting detectors were originally taken as 35 mm colour slides, and the technical details are shown in Table 12. The liquid crystal screen



Table 12: Technical Details For the Results Shown in Figures 19 and 20.

Figure Number	Feed Pressure (cm Hg)	Capillary Voltage (kV)	Detector Type	Photographic Exposure (sec)	Estimated Beam Divergence (degrees off-axis)
19a	7.0	5.0	phosphor	40	36°
19b	7.0	7.0	phosphor	15	33°
19c	7.0	9.0	phosphor	10	25°, 45°
20a	2.8	10.0	liquid crystal	1/60	20°
20b	2.8	10.0	phosphor	20	20°
fixed parameters: #27 Pt-Ir capillary 5 g NaI/100 ml glycerol fluid phosphor photographs--50 mm lens, f/1.4 liquid crystal photographs--50 mm lens with one short extension tube, f/1.4					

shows the beam as a yellow colour on the reddish-brown background.

Thermal biasing was not used. The liquid crystal and phosphor detectors corroborate each other very well. It is noted that a higher magnification factor has been used for the liquid crystal photograph. The current distribution on the five-ring spherically shaped electrical detector shows a more divergent beam than that indicated in the photographs. The beam was estimated to be 20° off axis from the visual detectors, while the electrical detector shows it to be about 40° off axis.

Part of this disagreement in divergence angle is due to the fact that the electrical detector ring solid angles have not been taken into account, hence the outer rings appear over-emphasized. On the other hand, the current on the outer electrical detector rings may be due to beam components too diffuse to record on the photographs or beam components may be scattered from the electrical detector grids. The





**Figure 19:** Beam Spatial Distribution as a Function of Capillary Potential in the Low Voltage Operating Region, as Shown on the Phosphor Detector.



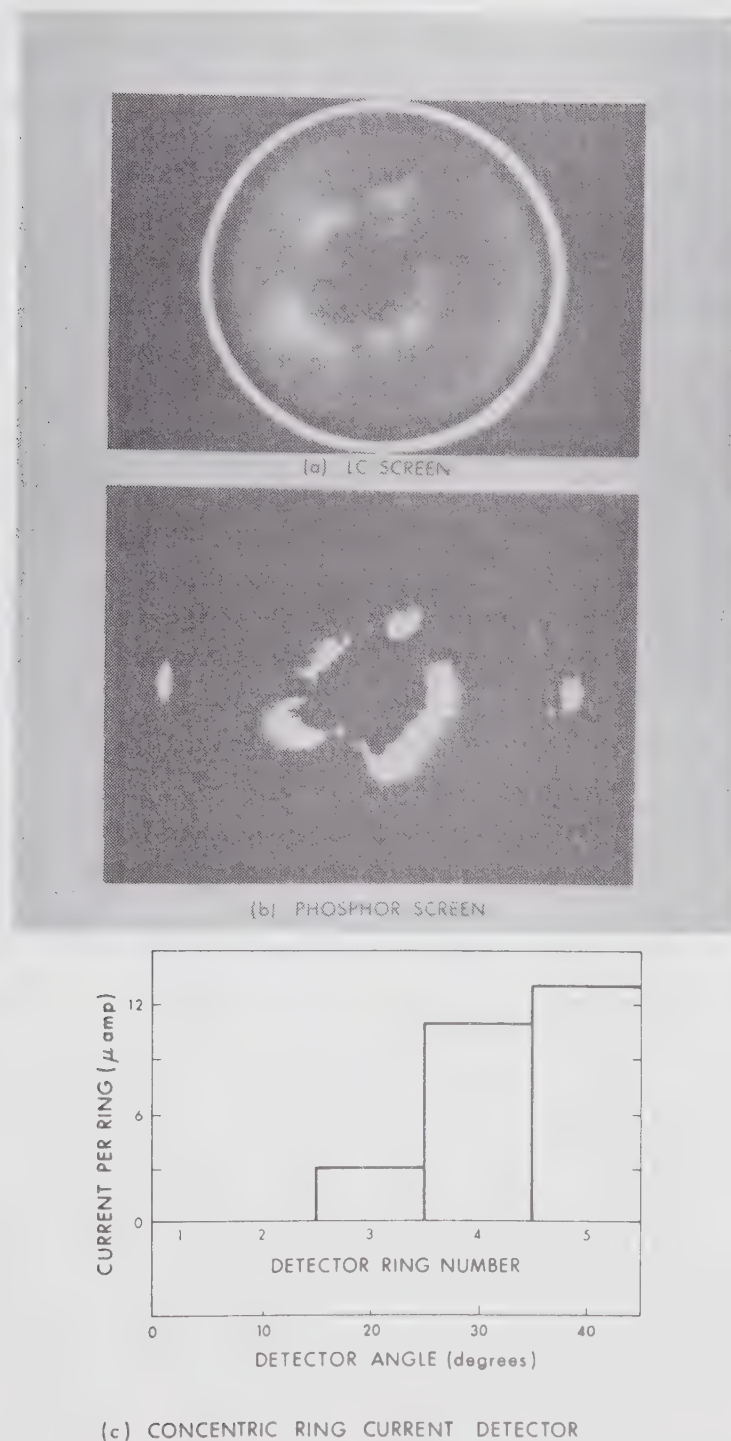


**Figure 20:** Comparison of Detector Results for the Phosphor, Liquid Crystal, and Segmented Electrical Detectors, Showing the Spatial Distribution of a Beam in the Low Voltage Operating Region.



disagreement between the electrical and visual detector results was not always observed, so it was probably due to some aspect of this particular case. Measured parameters were: beam current 28  $\mu$ amp, nominal charge to mass ratio  $\gtrsim 10^3$  coul/kg, and mass flow rate 18.1  $\mu$ g/sec.

No significant differences in the beam shapes observed throughout the low voltage region experiments were found for variations in capillary tube size or material, or fluid doping levels (in the range 2.5 to 7.5 g NaI/100 ml glycerol).

#### 6.8.3 High Voltage Region

This section discusses the beam spatial distributions observed when the colloid source was operated between 14 and 20 kV. Occasionally, lower voltages are included to help accentuate trends in beam shape as a function of voltage. For all beams discussed here, the detected current was at a stable dc level as measured on the five-ring spherical surface detector.

The beams produced in the high voltage region were focussed as a cluster of jets close to the central axis of the colloid source. While the beams did not have the same shape as those in the low voltage region, the trends of beam intensity, angular divergence, and number of beam jets as a function of capillary voltage were similar.

Figure 21 shows the beam angular distribution as a function of capillary voltage. Fixed source parameters were: 7.4 cm Hg feed pressure, #29 SS capillary, and 2.5 g NaI/100 ml glycerol fluid. For the cases at 10 kV and 12.5 kV, the visual detectors did not show complete hollow cone beams, but showed one or two off-axis jets.

The effects of varying pressure at fixed voltage are shown in



detected beam current per detector segment (nA)

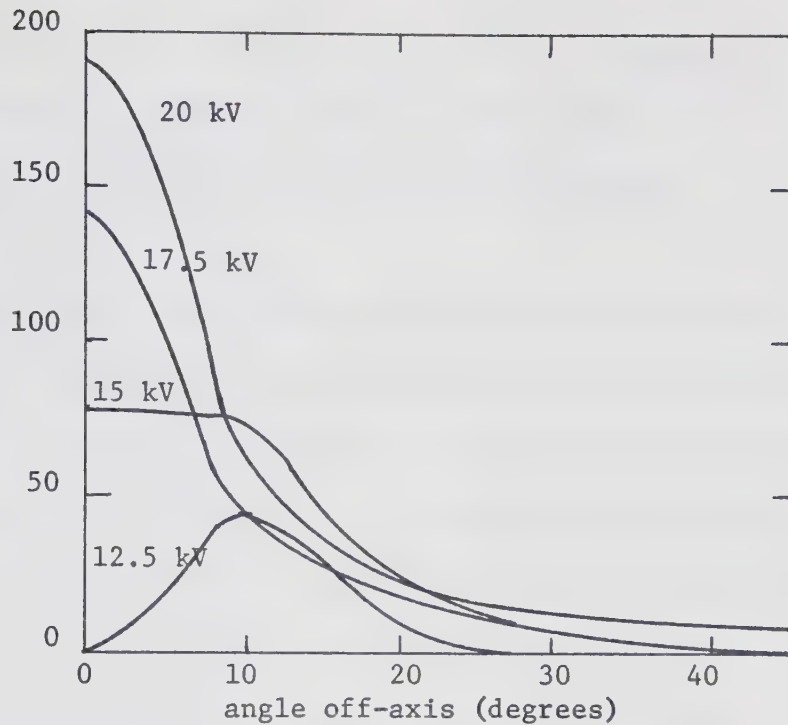


Figure 21: Beam Current Spatial Distribution as a Function of Voltage, in the High Voltage Operating Region. Voltage is Shown as a Parameter Beside the Various Curves in the Figure.

detected beam current per detector segment (nA)

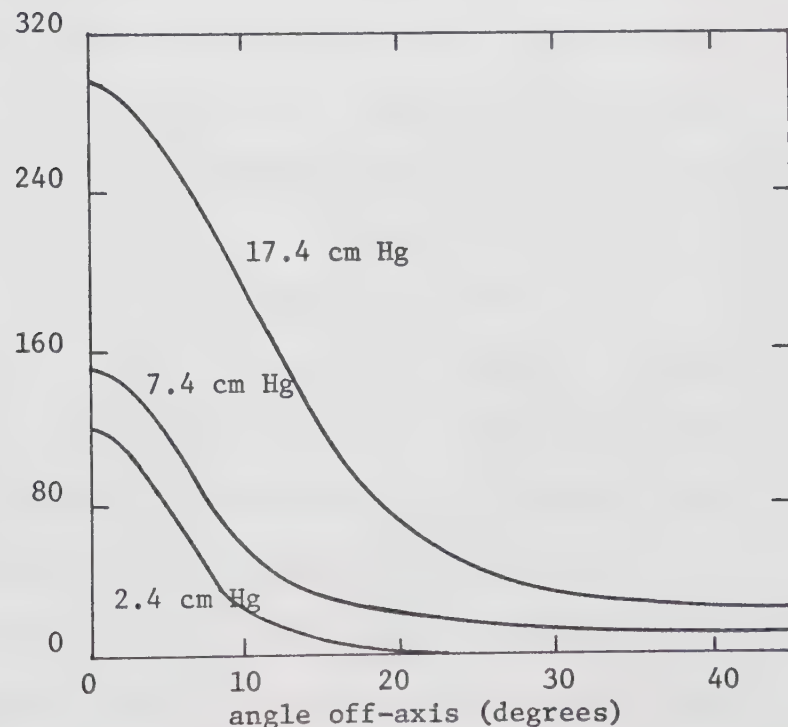


Figure 22: Beam Current Spatial Distribution as a Function of Fluid Feed Pressure, in the High Voltage Operating Region. Pressure is Shown as a Parameter Beside the Various Curves in the Figure.



Figure 22. The same fluid and capillary as were used in Figure 21 were operated at 17.5 kV. A useful increase in beam current is observed as pressure is increased, with little or no sacrifice of beam focus.

Three photographs illustrating beam shape for various operating conditions are shown in Figure 23. Technical details and measurement results are given in Table 13. The cluster of jets around the central axis is clearly shown in each photograph. The photographs were taken during different experiments, so they cannot be directly compared. However, these and other experiments show that the beam is well focussed over a range of pressures, voltages, and capillary sizes.

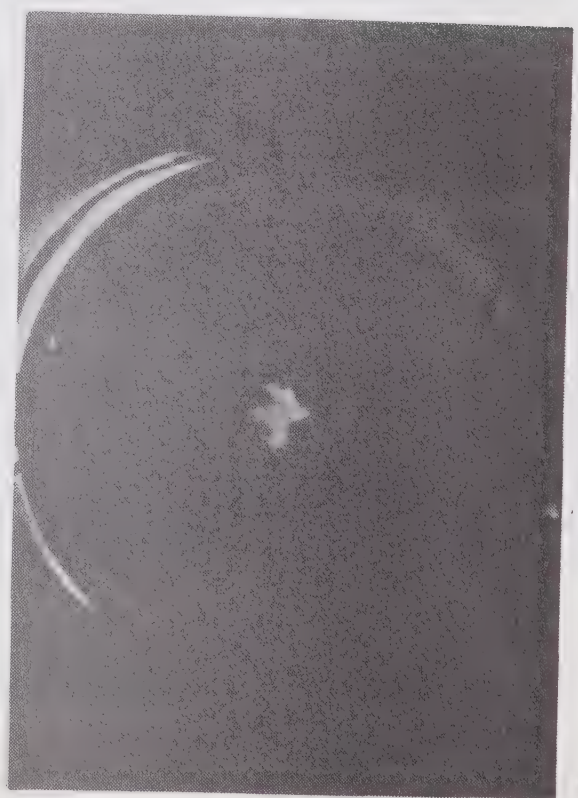
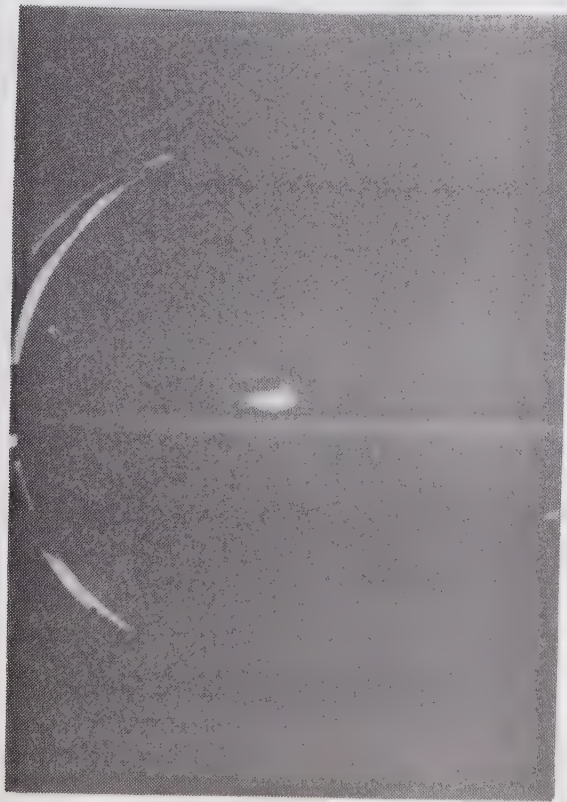
Figure 24 shows a reproduction of the 35 mm colour slides taken of a colloid beam incident on the visual detectors. Technical details and measurement results are also shown in Table 13. Figure 24a is a close-up photograph of the beam spot shown on the liquid crystal detector of Figure 24a. The area at the center of the beam spot, coloured blue on the original photograph, shows the most intense part of the beam. It is surrounded by less intense areas which give rings of colour from blue to red at the fringe of the beam spot. The background of the screen is a normal reddish-brown because no thermal biasing was used. The bright area at the edge of the screen in Figure 24a is glare from the external illumination. The phosphor screen in Figure 24c shows two side jets not visible on the liquid crystal detector. The presence of off-axis beam components is confirmed by the broad current distribution shown by the electrical detector result in Figure 24d.

It should be noted that the colour photograph in Figure 13 also

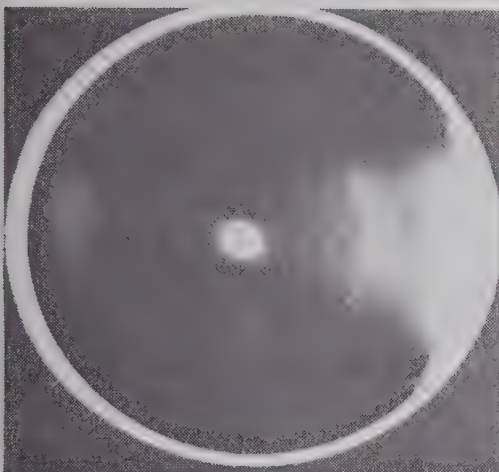




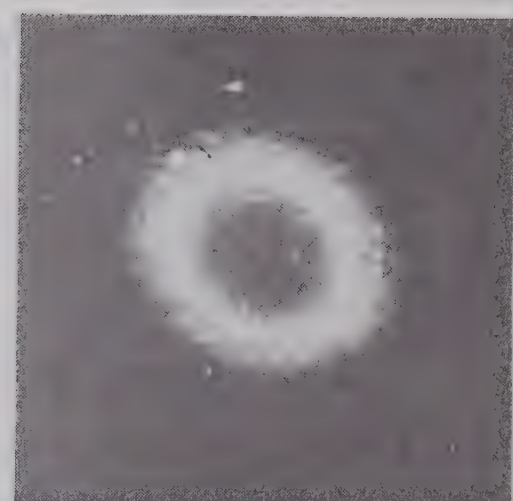
Figure 23: Three Beam Spatial Distributions for Beams in the High Voltage Operating Region, as Shown on the Phosphor Detector.



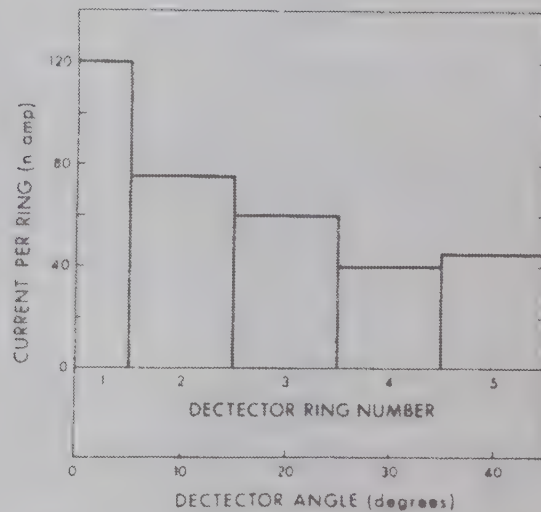




(a) LIQUID CRYSTAL DETECTOR

(b) LIQUID CRYSTAL DETECTOR,  
CLOSE-UP

(c) PHOSPHOR DETECTOR



(d) CONCENTRIC RING CURRENT DETECTOR

Figure 24: Spatial Distribution of a Beam Produced in the High Voltage Operating Region, as Observed on the Phosphor, Liquid Crystal, and Segmented Electrical Detectors.



Table 13: Technical Parameters and Measured Results for Colloid Beams Illustrated in Figures 23 and 24.

Figure Number	Feed Pressure (cm Hg)	Capillary Voltage (kV)	Capillary Fluid (g NaI/100 mL glycerol)	Detector <sup>a</sup> (sec)	Photo Exposure (sec)	Camera and Lens	Beam Divergence (degrees off axis)	Total Current (na)	Nominal Charge to Mass Ratio (coul/kg)	Mass Flow Rate ( $\mu\text{g/sec}$ )
23a	7.4	15	#31,SS	2.5	P	50	2.4	52	32	1.6
23b	7.5	20	#31,SS	2.5	P	35	Graflex <sup>b</sup> , f/4.7	5.0	230	97
23c	12.3	20	#29,SS	2.5	P	20		4.3	440	54
24a	7.0	17.5	#33,SS	5.0	LC	1/15	Pentax <sup>c</sup> , 50 mm + one extension tube. f/1.4	4.2		8.1
24b	7.0	17.5	#33,SS	5.0	LC	1/2	Pentax, 105 mm + three extension tubes. f/2.8	-	280	38
24c	7.0	17.5	#33,SS	5.0	P	10	Pentax, 50 mm f/1.4	3.1		
24d	7.0	17.5	#33,SS	5.0	EL	-	-	5.		

<sup>a</sup> P = phosphor, LC = liquid crystal, EL = 5-ring electrical

<sup>b</sup> Type 47 Polaroid film (ASA 3000)

<sup>c</sup> Kodak High Speed Ektachrome daylight film (ASA 600)



shows detector results for a beam produced in the high voltage operating region. In Figure 13 the electrical detector result shows a very well focussed beam.

It will now be demonstrated that the 14 to 20 kV operating potential region used in the present study is in fact different from the operating regions usually reported in the literature. In one of the few experiments using capillary potentials greater than 10 kV, Huberman<sup>50</sup> duplicated results obtained with an 0.26 mm outer diameter capillary operated at 6 to 8 kV by using an 0.72 mm outer diameter capillary operated at 11 to 15 kV. The extractor plate was of the flat type and had an aperture diameter of 4.75 mm. Thus higher voltages with larger capillary tubes gave the same results as the lower voltages with the more commonly used capillary tube diameter.

In the present work, using an extractor of the same style and dimensions as that used by Huberman<sup>50</sup>, capillaries of between 0.20 mm and 0.46 mm outer diameter were operated at both 5 to 8 kV and 14 to 20 kV. In addition, the beam properties found for any given experiment were quite different in the 5 to 8 kV and 14 to 20 kV operating regions. In the 5 to 8 kV region, beam spatial distributions and charge to mass ratio dependence on the operating parameters agreed with the results usually quoted in the literature<sup>21,24,50</sup>. It is therefore suggested that the 14 to 20 kV operating region is different from the usual colloid source operating range, and represents an important new aspect of colloid source operation. Quantitative results for the two operating ranges are given in Section 6.9.

#### 6.8.4 Summary

It became clear as experiments progressed that the low voltage



region offered little promise for production of axially focussed colloidal beams. Such beams are required if a colloid source is to be installed in the microparticle accelerator. On the other hand, axially focussed beams were available for a wide range of voltage and pressure variation in the high voltage region. In this latter case, the beams were seldom truly axial, but always had an on-axis component. Therefore a colloid source operated in the high voltage region produces beams with on-axis components suitable for injection into a microparticle accelerator. If the spatial distribution of a colloid beam with on-axis components is too divergent, the colloid beam can be collimated near the source to intercept the divergent beam components. The resulting beam can then be introduced into the microparticle accelerator.

The occurrence of stable on-axis beams in the 14 to 20 kV operating region has not been previously reported in the literature. In one of the few experiments using capillary voltages greater than 10 kV, Huberman<sup>50</sup> showed that beam properties at low voltage could be duplicated at high voltage by increasing the capillary diameter. However, in the present work, using the same capillary tube, beam properties were markedly different in the 5 to 8 kV and 14 to 20 kV regions. It is suggested that the transition from divergent beams in the 5 to 8 kV region to well focussed axial beams in the 14 to 20 kV region represents an important new aspect of colloid source operation.

## 6.9 Parametric Analysis

### 6.9.1 Introduction

Previously discussed material in this chapter has covered three general topics--colloid source stability, beam detectors, and beam



spatial distributions. This section describes how the nominal charge to mass ratio of colloid beams is affected by changes in the various operating and geometrical parameters. Source parameters that were varied are: capillary size, extractor type, and fluid doping level. For each combination of capillary, extractor, and fluid, the source was operated over a range of fluid feed pressure and operating voltage. At each operating point, the nominal charge to mass ratio and the mass flow rate of the beam were measured from time of flight measurement data. For all results presented here, the beams were at a stable dc current.

Since all of the colloid microthruster studies discussed in the literature operate in the low voltage region (5 to 10 kV), initial stages of this study concentrated on this region. The relatively low doping levels of the NaI-glycerol solutions used here (Section 6.7) produced the required low charge to mass ratio beams but not the desired on-axis beam. The data for the low voltage region presented in Section 6.9.2 is somewhat scanty for three reasons:

- (a) the source configuration was still being developed, hence results varied widely,
- (b) the work at that stage concentrated on producing a suitable spatial distribution rather than good charge to mass ratio results,
- (c) work on this region was stopped as soon as the existence of the high voltage operating region was found.

However, the results are presented in Section 6.9.2 for completeness.

The high voltage region (14 to 20 kV) is a far more suitable operating region for a colloid source intended for use in a microparticle accelerator. Some of the advantages of the operating region are:



- (a) the source is more stable,
- (b) the beams are axially focussed,
- (c) the beams have suitable nominal charge to mass ratio values,
- (d) the range of charge to mass ratios present in the beams is narrower, and
- (e) there is a wider range of suitable operating parameters.

Extensive results for the high voltage region are presented in Section 6.9.3.

#### 6.9.2 Results for the Low Voltage Region

Figure 25 is the parametric plot of colloid source behavior obtained using 2.5 g NaI/100 ml glycerol fluid, a #29 SS capillary, and the flat type extractor. The axes of the plot are fluid pressure versus operating voltage. Points where the source was operated are indicated on the plot opposite the appropriate pressure and voltage values. The value of nominal charge to mass ratio (as found from a time of flight measurement) is listed beside each operating point on the plot. Two separate measurements of the nominal charge to mass ratio were made for the 9 kV, 6.7 cm Hg operating point, and both values are listed.

Results from two separate experiments are depicted in Figure 25--in one, voltage was varied at a fixed pressure of 6.7 cm Hg and in the other, pressure was varied at a fixed voltage of 7 kV. In the constant pressure experiment, the voltage was varied continuously from 3.3 kV to 10 kV but measurements were made only at five different points in this voltage range. The beam operated stably throughout the voltage range. In the constant voltage experiment, pressure was varied continuously from 2.6 cm Hg to 19.8 cm Hg but only three measurements were made in



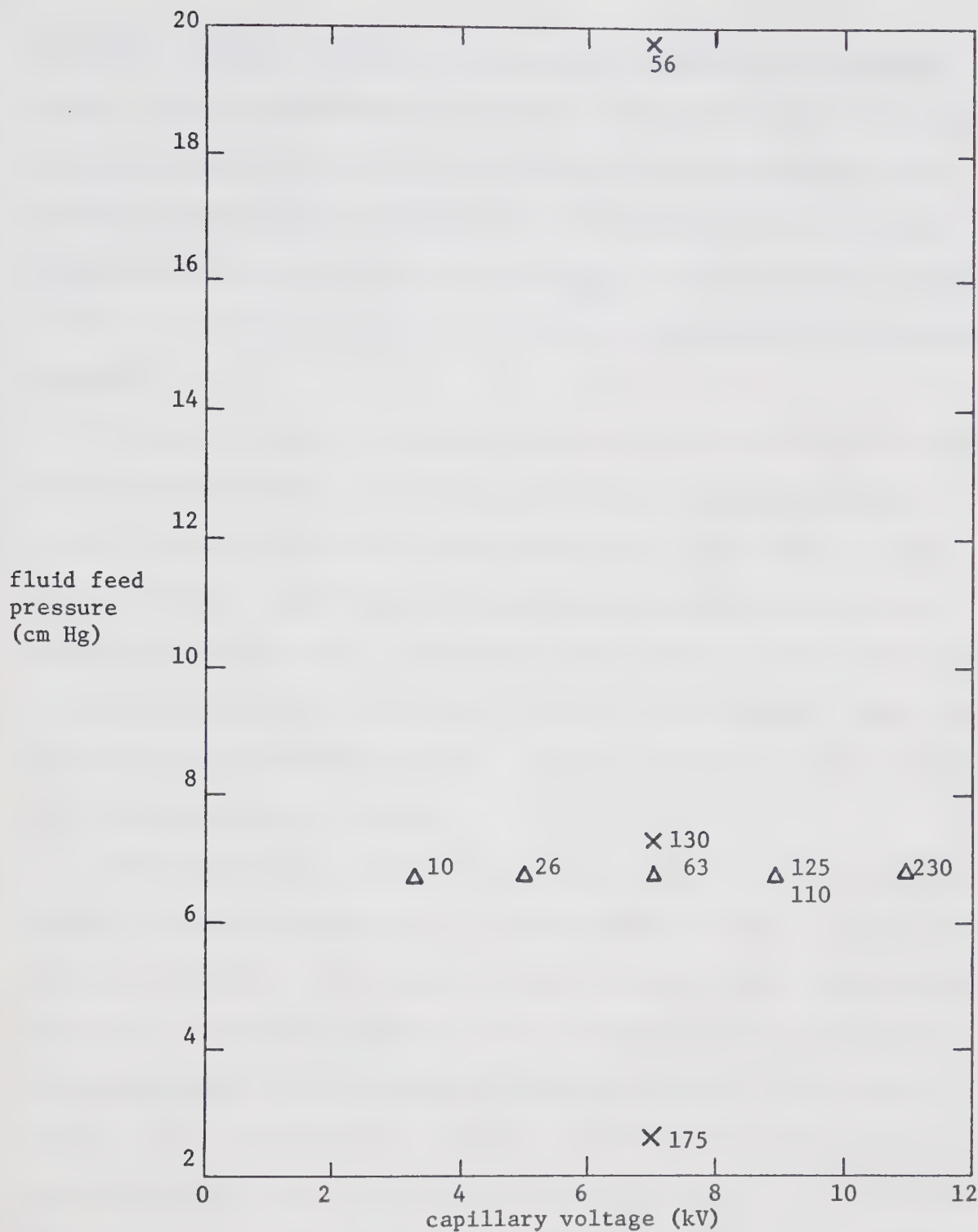


Figure 25: A Parametric Analysis in the Low Voltage Region, Showing the Measured Values of Charge to Mass Ratio in the Beam in coul/kg.

X Constant Voltage Trial  
 Δ Constant Pressure Trial

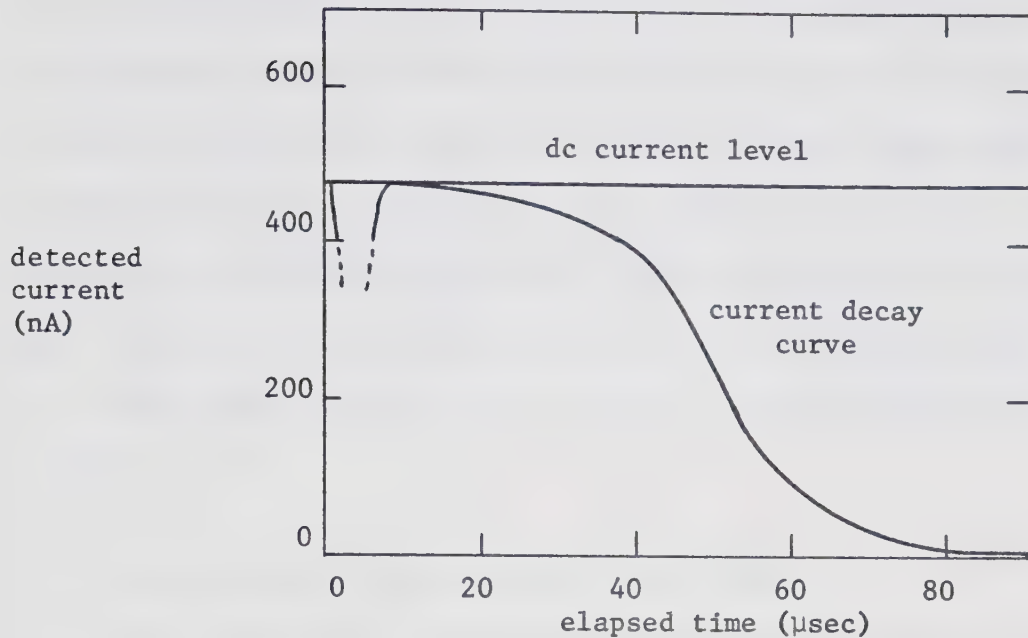


the range. Again, the beam operated stably throughout the pressure range. The two experiments should have, in principle, given the same nominal charge to mass ratio at the 7 kV, 6.7 cm Hg operating point. Instead, values of 130 coul/kg and 63 coul/kg were found. In spite of this lack of reproducibility, the trends of nominal charge to mass ratio as functions of pressure and voltage are consistent with published results<sup>21</sup>.

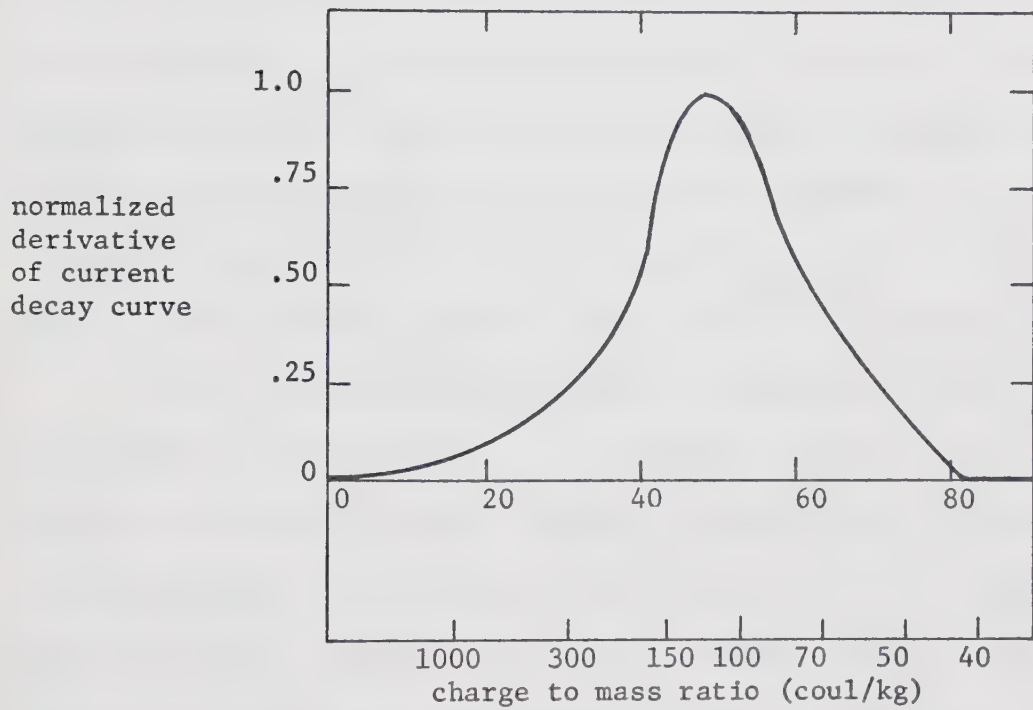
Because the beams in this low voltage region were always off-axis and usually asymmetric, an attempt was made to measure the nominal charge to mass ratio of the beam hitting each of the five electrical detector rings. Significant differences in measured charge to mass ratio were usually found. For example, the charge to mass ratio in one trial was 58 coul/kg on one ring, 34 coul/kg on an adjacent ring, and 49 coul/kg for the whole detector. However, consistent trends in these differences could not be found.

A time of flight current decay curve typical to the low voltage region is shown in Figure 26a. The measurement is the 6.7 cm Hg, 9 kV point in Figure 25. The stable dc level is drawn on the figure, which has been copied by hand from the oscilloscope screen to graph paper. The perturbation during the first five microseconds of the current decay curve is the transient induced at the detector by the switching of the thyratron used as the capillary voltage switch. In Figure 26b, the curve is the normalized differential of the current decay curve of Figure 26a, plotted as a function of the time after the measurement was initiated. The charge to mass ratio axis in Figure 26b is derived from the time scale using equation 3.6. The curve in Figure 26b is then the function  $i(t)$ , defined in equation 3.2, while the curve of Figure 26a





(a) Detected Current Waveforms



(b) Normalized Beam Current as a Function of Charge to Mass Ratio.

Figure 26: Results of a Time of Flight Measurement on a Beam in the Low Voltage Operating Region. The Figure Shows the Detected Current Waveforms, and the Associated Normalized Current Versus Charge to Mass Ratio Curve.



is  $I(t)$ , the measured current decay curve. Therefore, Figure 26b gives the relative current contributed to the beam by particles having a certain charge to mass ratio, but the curve says nothing about the numbers of particles having a certain charge to mass ratio. The rather broad distribution of current over charge to mass ratio in Figure 26b was typical of the results obtained in the low voltage region. The time of flight curve in Figure 26a is similar to those reported in the literature<sup>40</sup>.

#### 6.9.3 Results for the High Voltage Region

Since the results reported in this section formed the basis for the decision to proceed with development of a microparticle accelerator source, the parametric analysis done here was much more complete than was the analysis of the low voltage region. In addition, the results seemed to be much easier to obtain than in the low voltage region. Table 14 lists the data associated with the parametric analysis results given in Figures 27 to 34. For all experiments the electrical detector was the 0.07 m radius spherical surface with five concentric rings.

A total of eight parametric plots are presented here, each one illustrating source behavior for a different capillary size, extractor type, or fluid doping level. The plot axes are fluid pressure and operating voltage. On each plot, a dashed line encloses the pressure-voltage region for which stable dc beams were produced. Pressure and voltage could be continuously varied anywhere within the operating region to give continuously varying values of mass flow rate and nominal charge to mass ratio in the beam. The source was not operated outside an arbitrarily chosen pressure range of 2 cm Hg and 18 cm Hg. The voltage



range for source operation was restricted either by the range over which stable dc beams could be produced or by arbitrarily chosen limits of 13 kV to 20 kV.

Table 14: Source Parameters for the High Voltage Region Parametric Analyses Shown in Figures 27 to 34.

Figure Number	Capillary Size	Capillary Material	Fluid Doping Level (g NaI/100 mL glycerol)
27	#33	SS	2.5
28	#29	SS	2.5
29	#29	SS	5.0
30	#27	Pt-Ir	2.5
31	#27	Pt-Ir	7.5
32	#27 W <sup>a</sup>	Pt-Ir	2.5
33	#27 W <sup>a</sup>	Pt-Ir	5.0
34	#27 W <sup>a</sup>	Pt-Ir	7.5

a) stainless steel wire insert, 0.08 mm diameter, 19 mm long.

Time of flight measurements were made at various discrete points within the operating region. Each measurement point is indicated on the parametric plots, and the measured values of nominal charge to mass ratio are indicated beside each measurement point. Multiple nominal charge to mass ratio values beside a given point are the results of either successive measurements during one experiment or measurements from different experiments. The average value of nominal charge to mass ratio over these values is included, in parentheses. Non-reproducibility between measurements is evident, however the trends in nominal charge to mass ratio as a function of pressure and voltage were repeatable. Thus the average values of nominal charge to mass ratio over the various measurements made were quite consistent, and were



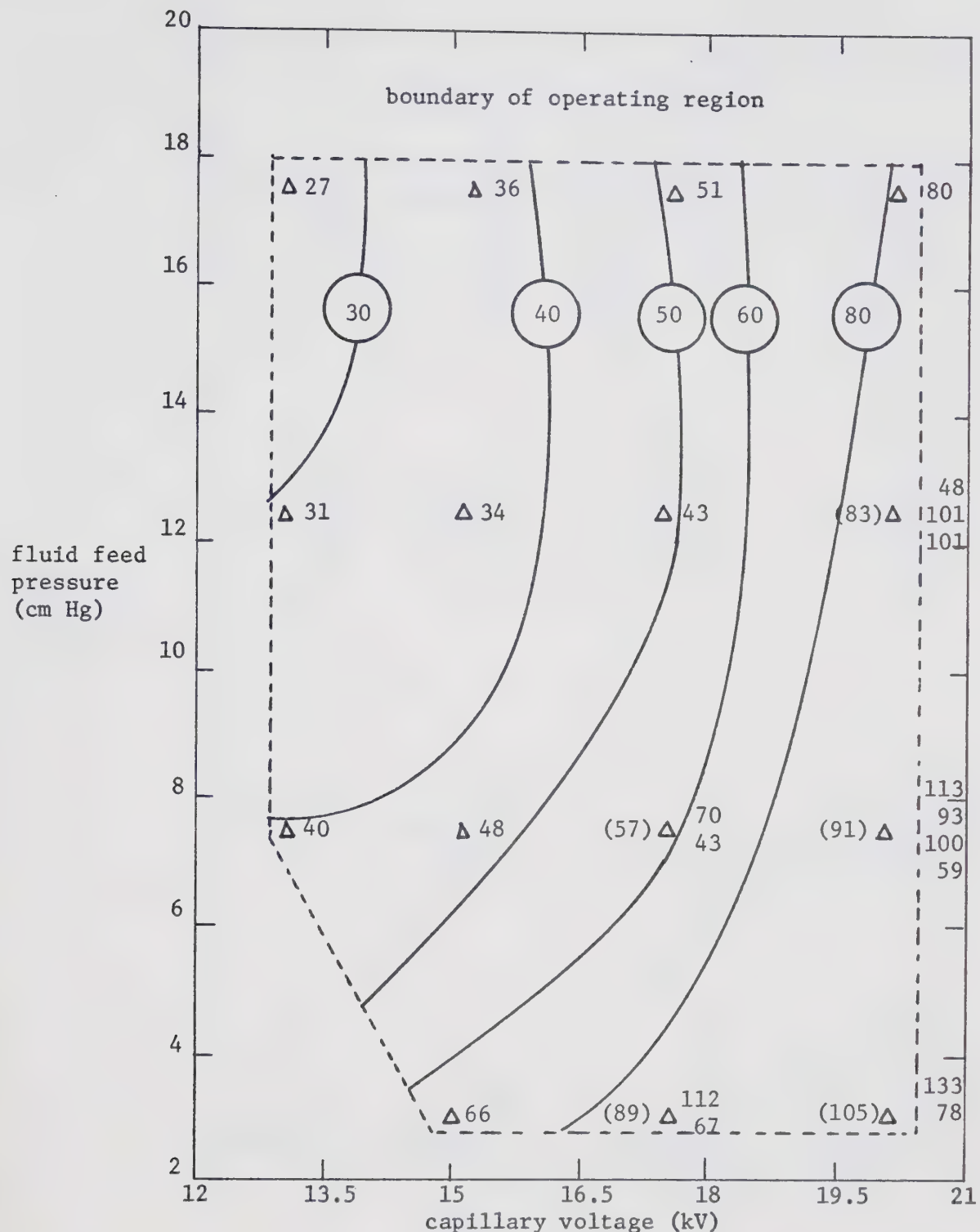


Figure 27: Results of a Parametric Analysis of Colloid Source Behaviour in the High Voltage Operating Region.

- Loci of Equal Charge to Mass Ratio (coul/kg)
- Point of Charge to Mass Ratio Measurement
- 70 Measured Value of Charge to Mass Ratio (coul/kg)
- (57) Average of Measured Charge to Mass Ratios



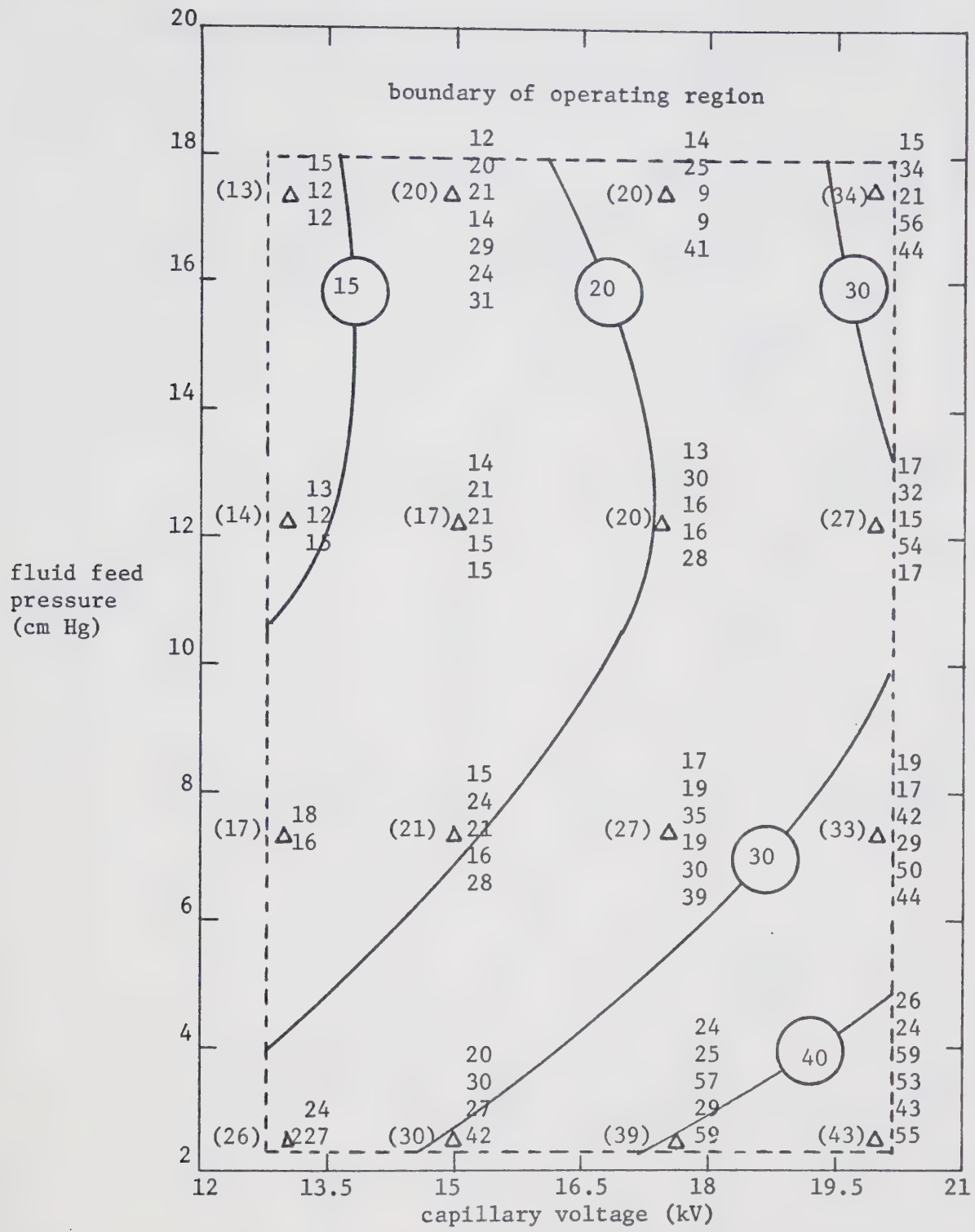


Figure 28: Results of a Parametric Analysis of Colloid Source Behaviour in the High Voltage Operating Region.

30 Loci of Equal Charge to Mass Ratio (coul/kg)

Δ Point of Charge to Mass Ratio Measurement  
35 Measured Value of Charge to Mass Ratio (coul/kg)  
(27) Average of Measured Charge to Mass Ratios



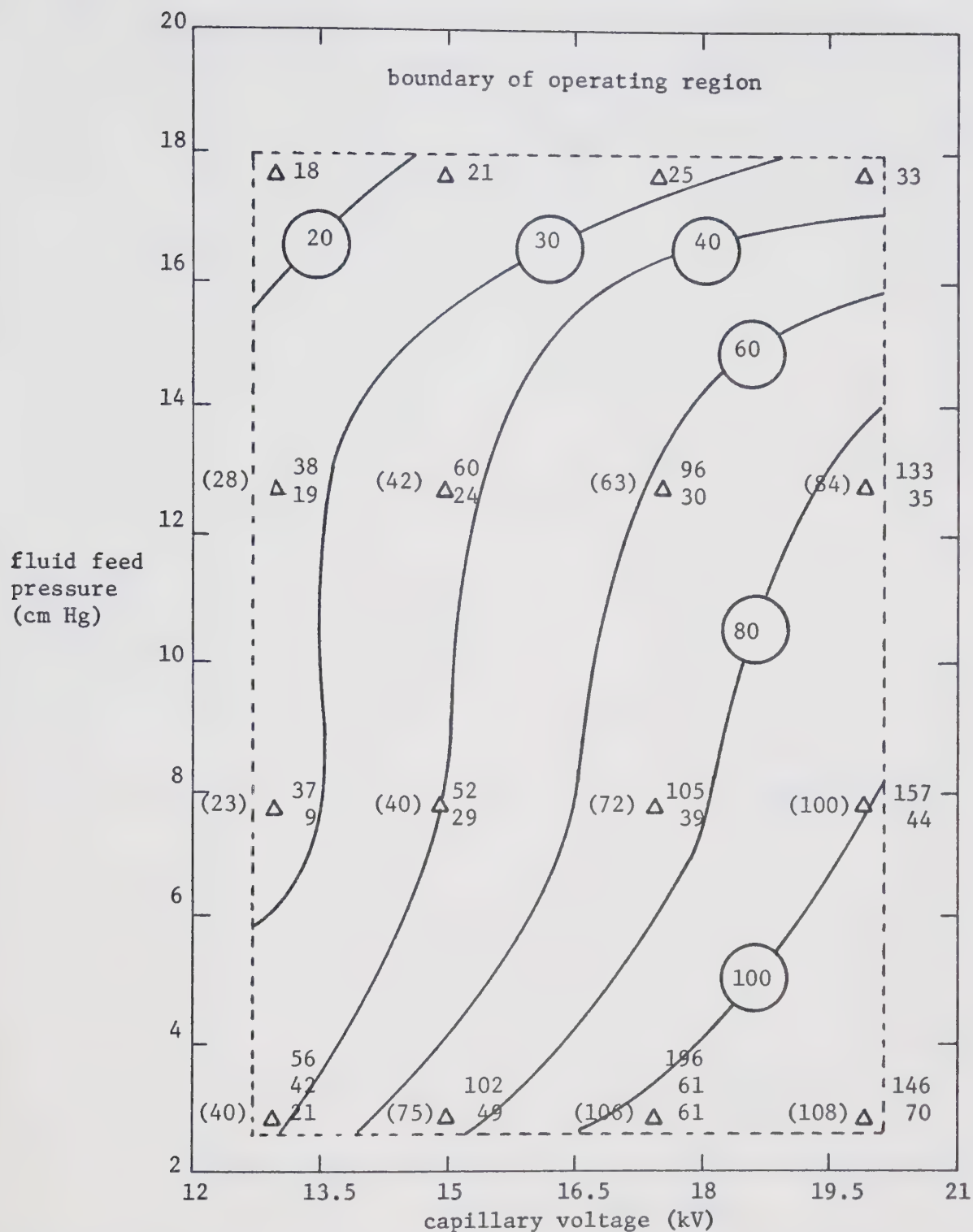


Figure 29: Results of a Parametric Analysis of Colloid Source Behaviour in the High Voltage Operating Region.

- Loci of Equal Charge to Mass Ratio (coul/kg)
- Δ Point of Charge to Mass Ratio Measurement
- 39 Measured Value of Charge to Mass Ratio (coul/kg)
- (72) Average of Measured Charge to Mass Ratios



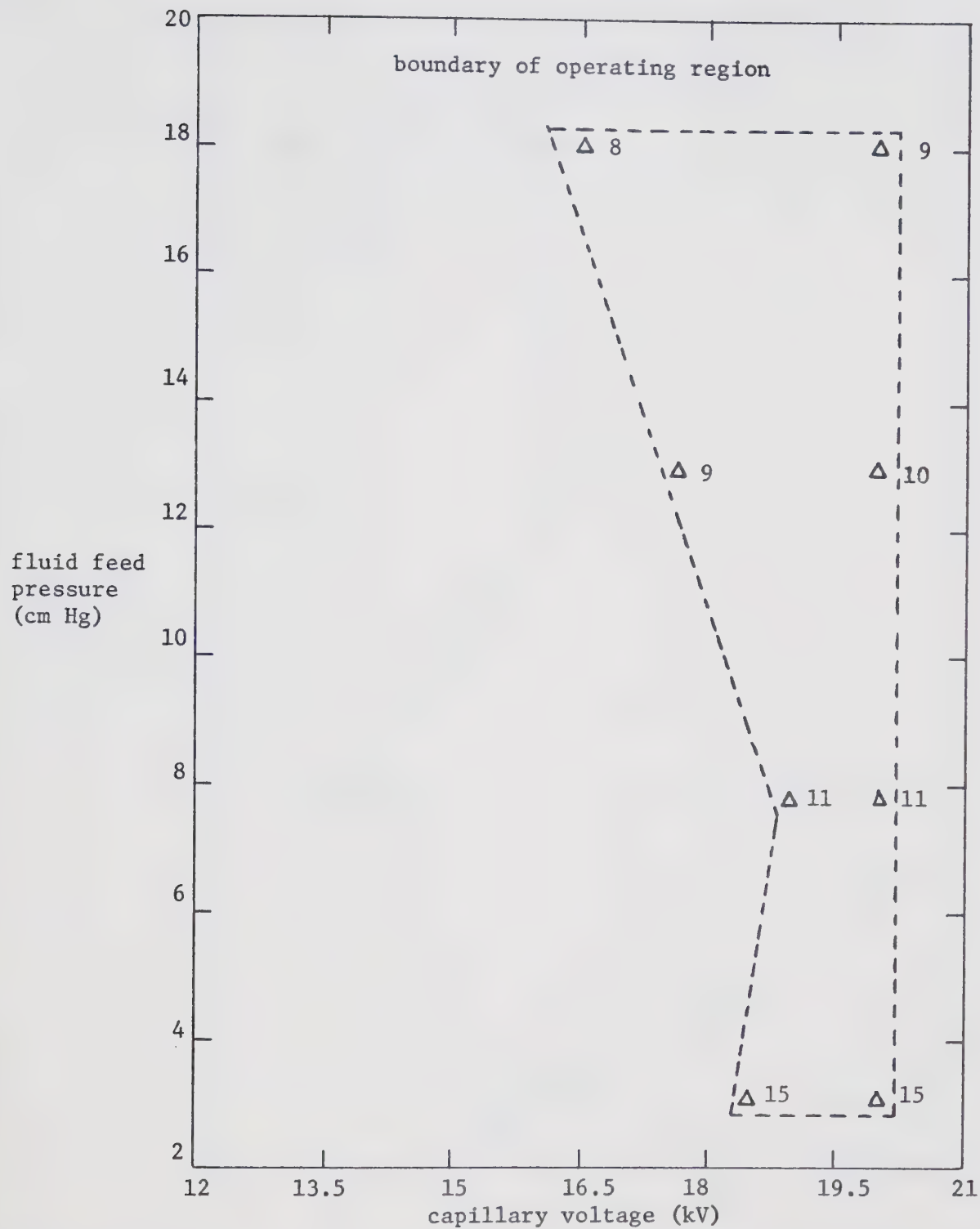


Figure 30: Results of a Parametric Analysis of Colloid Source Behaviour in the High Voltage Operating Region.

$\Delta$  Point of Charge to Mass Ratio Measurement  
 15 Measured Value of Charge to Mass Ratio (coul/kg)



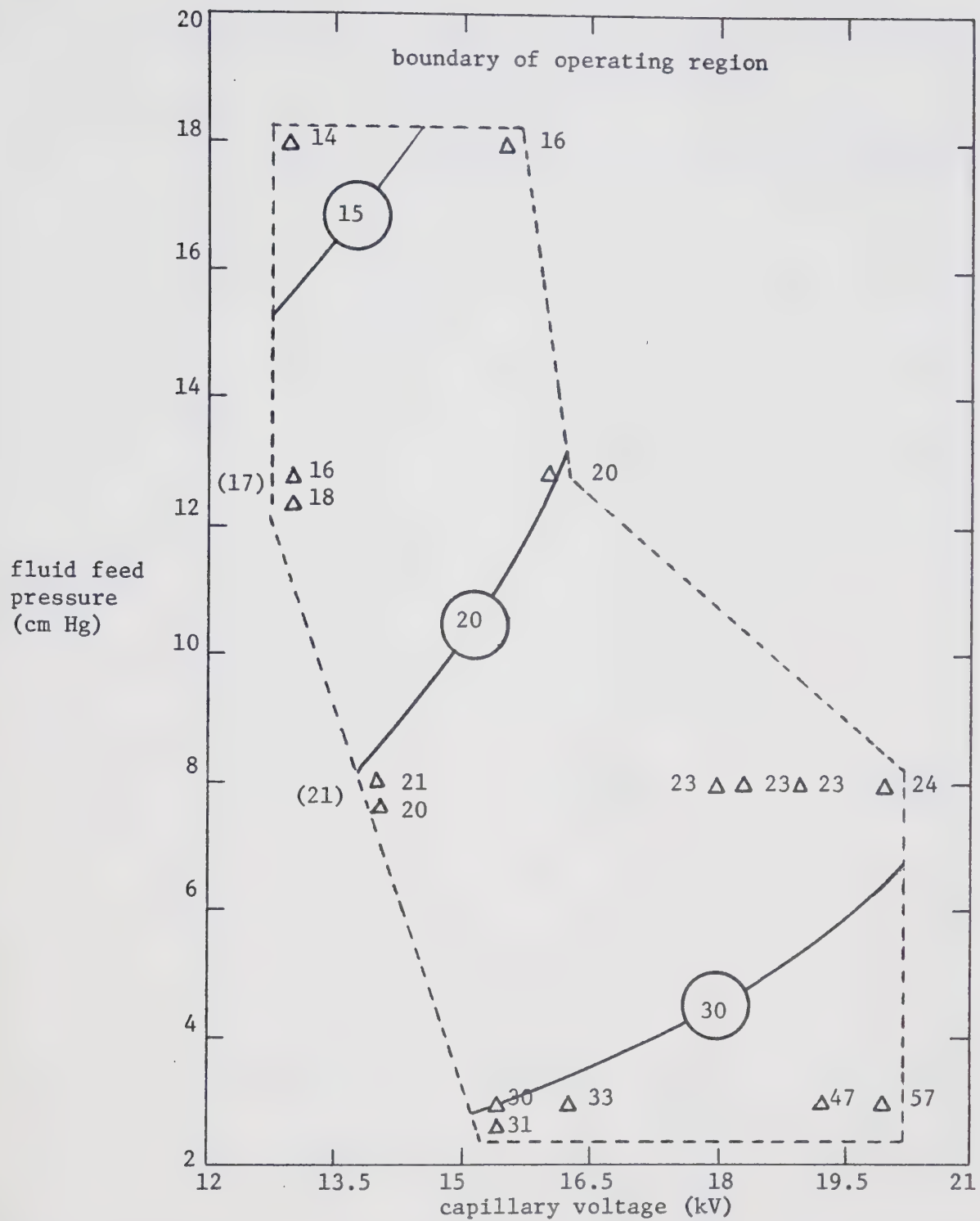


Figure 31: Results of a Parametric Analysis of Colloid Source Behaviour in the High Voltage Operating Region.

- Loci of Equal Charge to Mass Ratio (coul/kg)
- $\Delta$  Point of Charge to Mass Ratio Measurement
- 21 Measured Value of Charge to Mass Ratio (coul/kg)
- (20) Average Value of Measured Charge to Mass Ratios



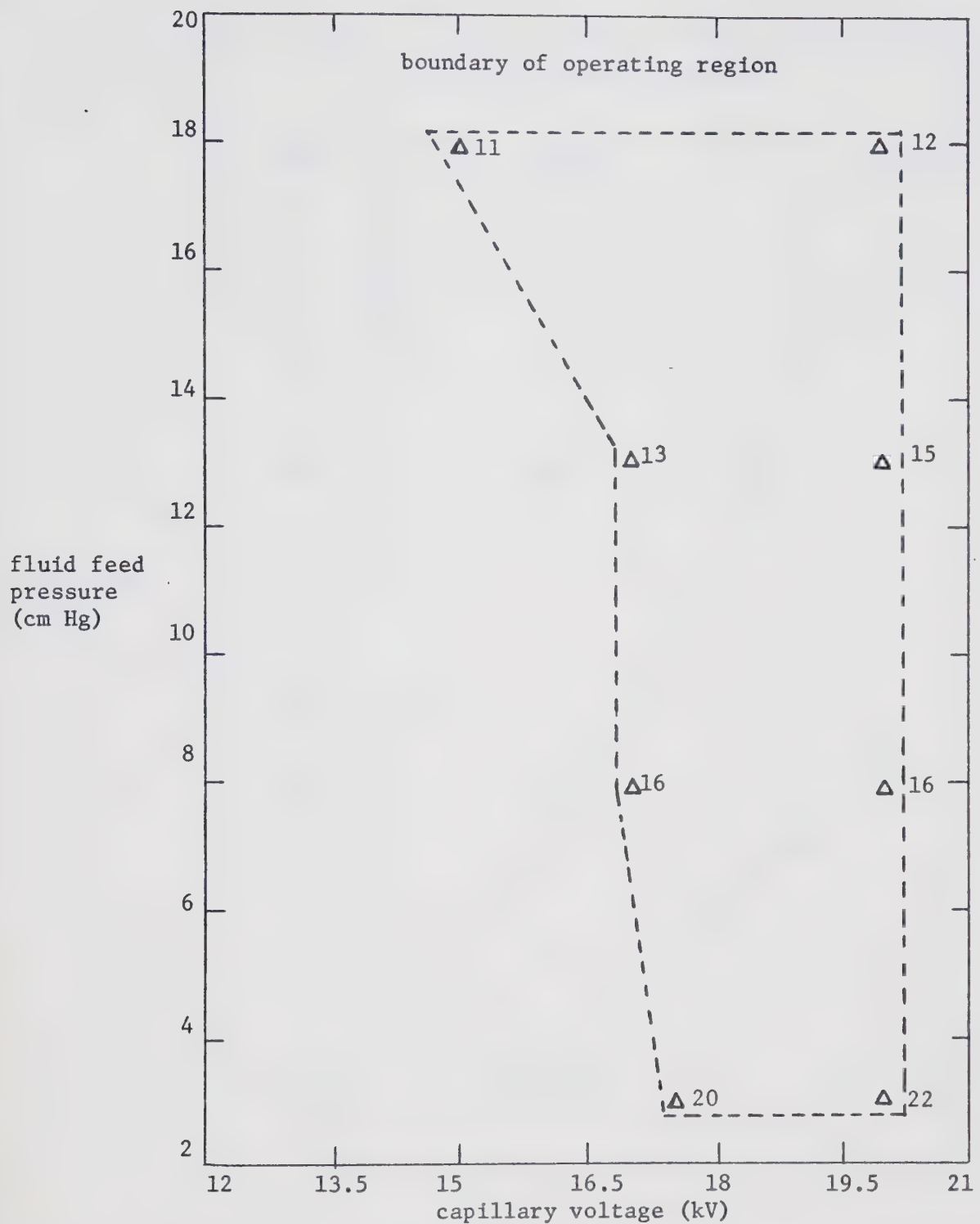


Figure 32: Results of a Parametric Analysis of Colloid Source Behaviour in the High Voltage Operating Region.

$\Delta$  Point of Charge to Mass Ratio Measurement  
 20 Measured Value of Charge to Mass Ratio (coul/kg)



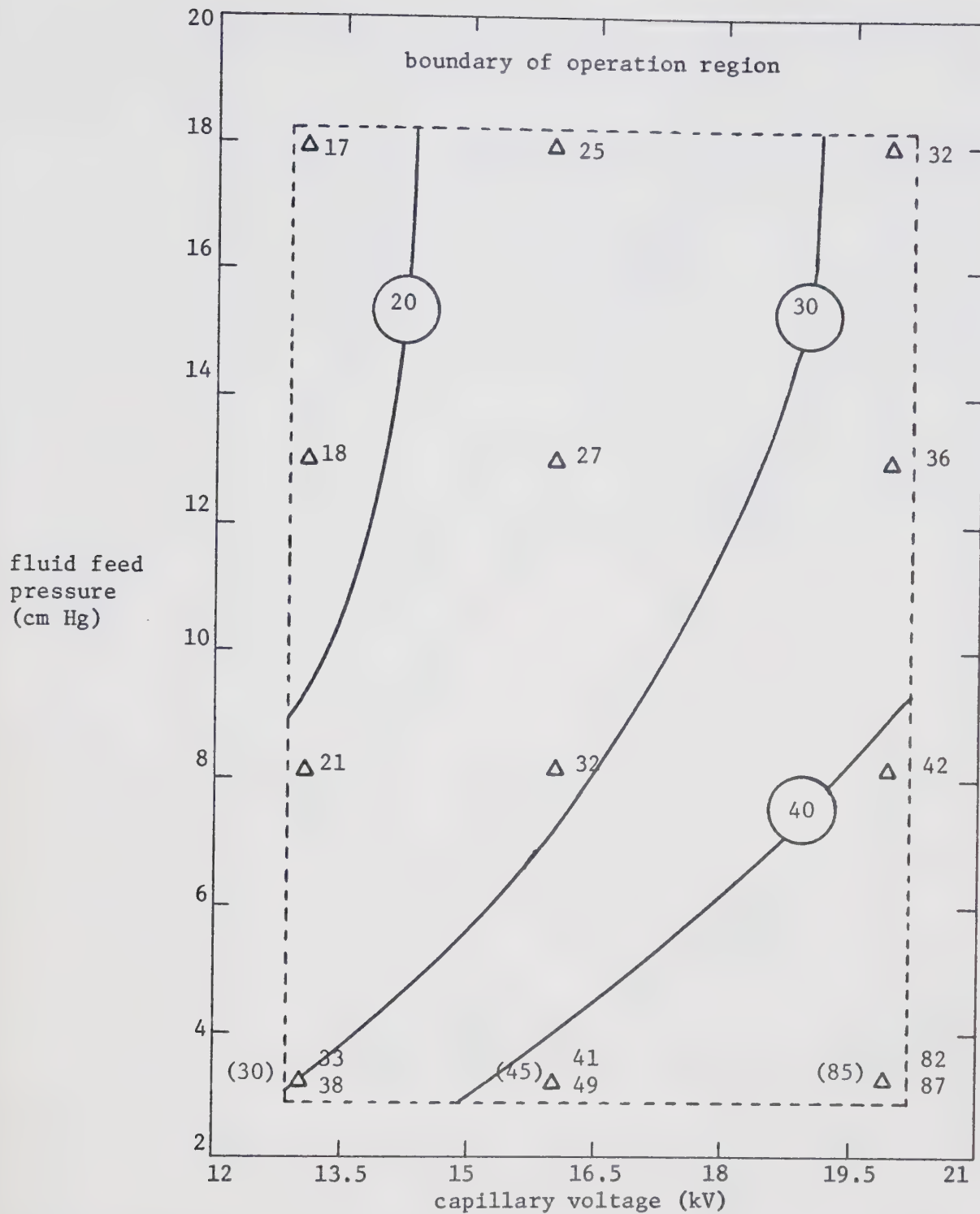


Figure 33: Results of a Parametric Analysis of Colloid Source Behaviour in the High Voltage Operating Region.

- Loci of Equal Charge to Mass Ratio (coul/kg)
- Δ Point of Charge to Mass Ratio Measurement
- Measured Value of Charge to Mass Ratio (coul/kg)
- (45) Average of Measured Charge to Mass Ratios



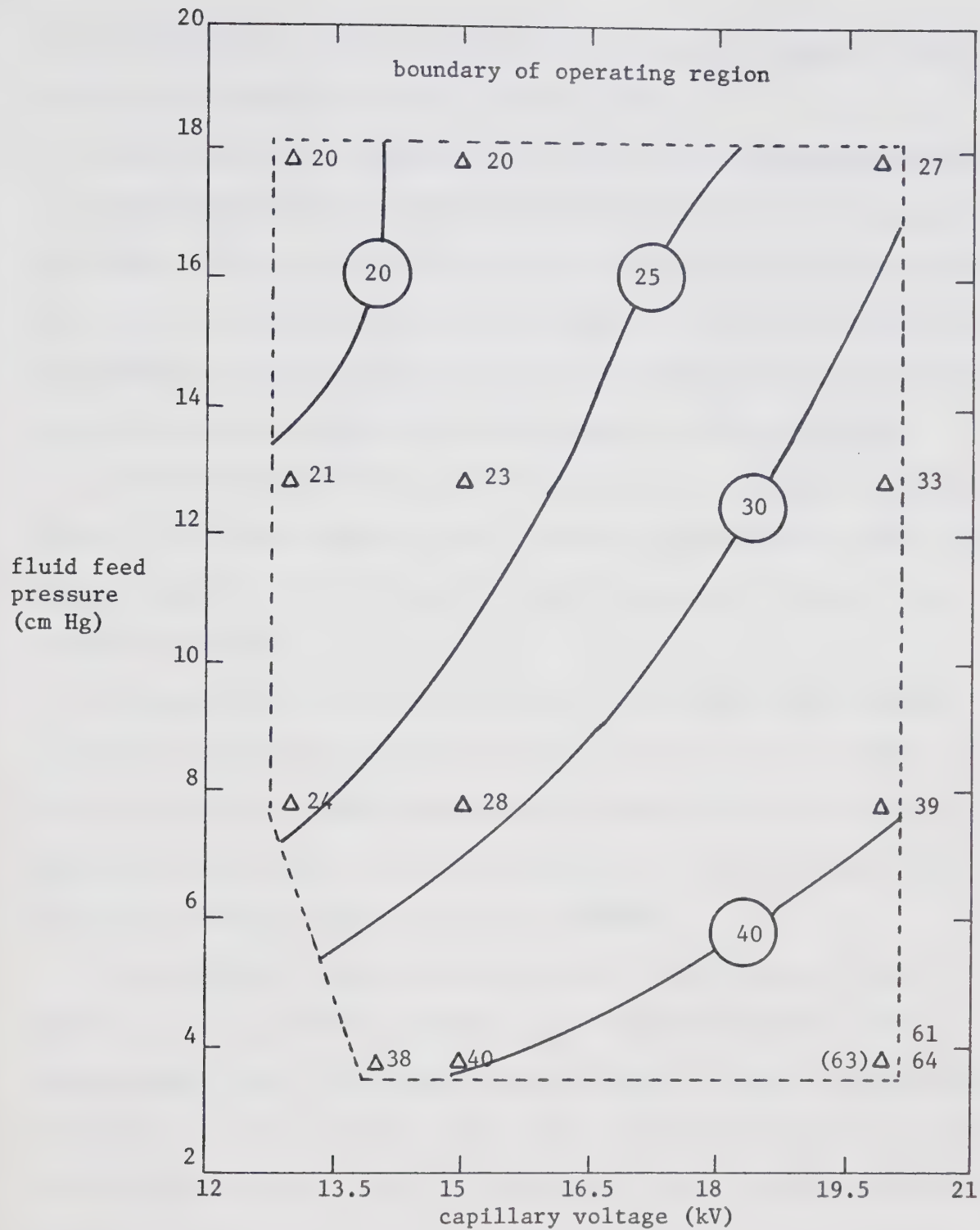


Figure 34: Results of a Parametric Analysis of Colloid Source Behaviour in the High Voltage Operating Region.

- Loci of Equal Charge to Mass Ratio (coul/kg)
- $\Delta$  Point of Charge to Mass Ratio Measurement
- 30 Measured Charge to Mass Ratio (coul/kg)
- (63) Average of Measured Charge to Mass Ratios (coul/kg)
- 61
- 64



useful as indicators of the probable value of nominal charge to mass ratio to be achieved at a given operating point.

Also shown on the parametric plots are lines representing the loci of points which would give the same nominal charge to mass ratio value. The curves have been drawn from the average values of nominal charge to mass ratio shown on the plots, so are subject to both the experimental uncertainty of the measured points and the uncertainty caused by interpolating between the measured nominal charge to mass ratio values.

The following is a discussion of the observations made by examination of the eight parametric plots. Operating parameters for each plot have been given in Table 14, and will not be repeated during the subsequent discussion.

It can be seen that the shapes of the contours of equal nominal charge to mass ratio value are consistent. The contours show that a high pressure-low voltage operating point gives the lowest charge to mass ratio values, while a low pressure-high voltage operating point gives the highest charge to mass ratio values.

The problem of reproducibility is best illustrated in Figure 28, which gives the parametric results using a #29 SS capillary tube. At any operating point, the highest nominal charge to mass ratio value is typically 1.5 to 4 times the lowest value. The reproducibility obtained with Pt-Ir capillaries seems to be somewhat better, as illustrated in Figure 31.

Figures 27 and 28 compare results for two different capillary tube sizes. As expected, the smaller capillary produced higher nominal charge to mass ratio values. No significant difference in the size of the operating region can be seen.



The effect of varying the fluid doping level is shown in Figures 28 and 29. The 5 g NaI/100 ml glycerol solution gave charge to mass ratios about twice those given by the 2.5 g NaI/100 ml glycerol solution. The unusually shaped contours of equal charge to mass ratio in Figure 29 are the result of the reproducibility problems.

Figures 30 to 34 are results for Pt-Ir capillary tubes. Figures 30 and 31 show that stability problems were encountered with the #27 capillary size for two fluid doping levels, probably because of the high mass flow rates involved.

Figures 31 to 34 are important, since they represent results for the capillary chosen for use in the accelerator source. This capillary #27 Pt-Ir, had a 20 mm long section of 0.08 mm diameter stainless steel wire inserted into its 25 mm length in order to impede solution flow somewhat. The figures show that stability problems were encountered only for the lowest fluid doping level, 2.5 g NaI/100 ml glycerol. Presumably use of a larger diameter insert wire would increase the charge to mass ratios available, and aid beam stability. The trend in nominal charge to mass ratio with fluid doping level shows a significant rise between 2.5 and 5.0 g NaI/100 ml glycerol solutions, and a decrease between the 5.0 and 7.5 g NaI/100 ml glycerol solutions. This anomaly illustrates the problems in reproducibility.

Some ancillary experiments were conducted during these trials. The problem of nominal charge to mass ratio consistency as a function of time in one experimental trial was investigated by taking twelve time of flight measurements during a time interval of 20 minutes. Beam parameters were: 7.5 cm Hg, 15 kV, 2.5 g NaI/100 ml glycerol, #29 SS capillary. These parameters correspond to a case in Figure 28. No



correlation between measured nominal charge to mass ratio and time was discerned. Analysis of the data produced the following values: average of nominal charge to mass ratios--34.7 coul/kg; standard deviation in nominal charge to mass ratio--4.2 coul/kg; maximum value observed--43.2 coul/kg; minimum value observed--28.3 coul/kg. As indicated earlier, it appeared that variations in nominal charge to mass ratio with the Pt-Ir capillaries were less than the above values. The standard deviation of 4.2 coul/kg, representing an experimental uncertainty of 12% in the average value of 34.7 coul/kg, includes errors due to beam recording and data analysis as well as any inherent changes in the beam. A given time of flight data curve could be analyzed twice to give results within 2%, so most of the uncertainty is due to experimental problems or beam changes.

Generally speaking, the time of flight curves obtained throughout these experiments showed a suitably narrow range of charge to mass ratio values present in the beam produced. A trend towards broader charge to mass ratio distributions was observed as capillary voltage was increased.

Table 15 lists the parameters for three measured time of flight current decay curves and their corresponding calculated charge to mass ratio distributions. One of the time of flight curves is a photograph of the storage oscilloscope trace (Figure 35), while two of the curves are hand-drawn (Figures 36 and 37). No significant difference in the width of the charge to mass ratio distribution was observed between the various capillary tubes tried. At the lower end of the voltage operating range, these widths were typically over a factor of 5 in charge to mass ratio, while at the highest voltages the width was about a



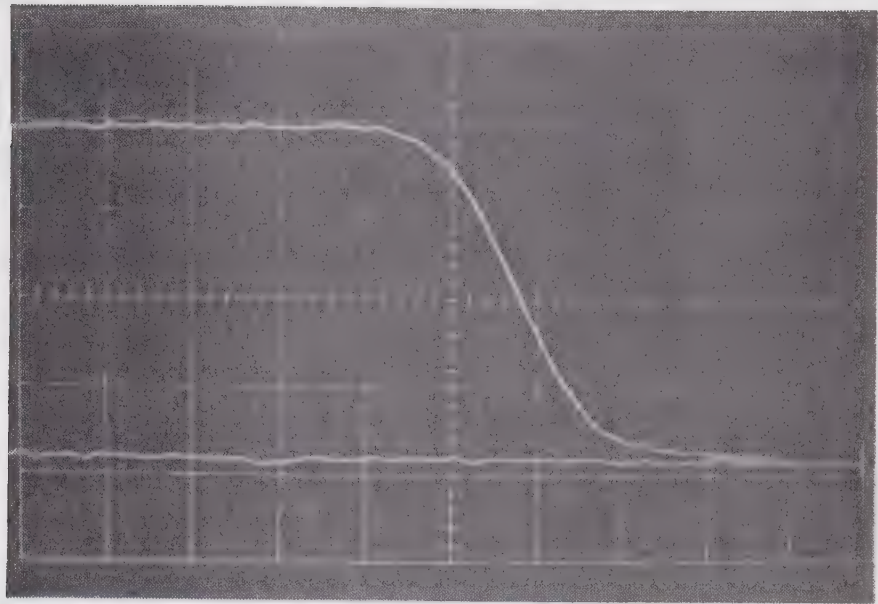
decade in charge to mass ratio. The distributions, while fairly symmetric as a function of time of flight measurement time, were heavily skewed towards the lower values on the charge to mass ratio scales.

Table 15: Experimental Parameters for Time of Flight Measurement Results Shown in Figures 35 to 37.

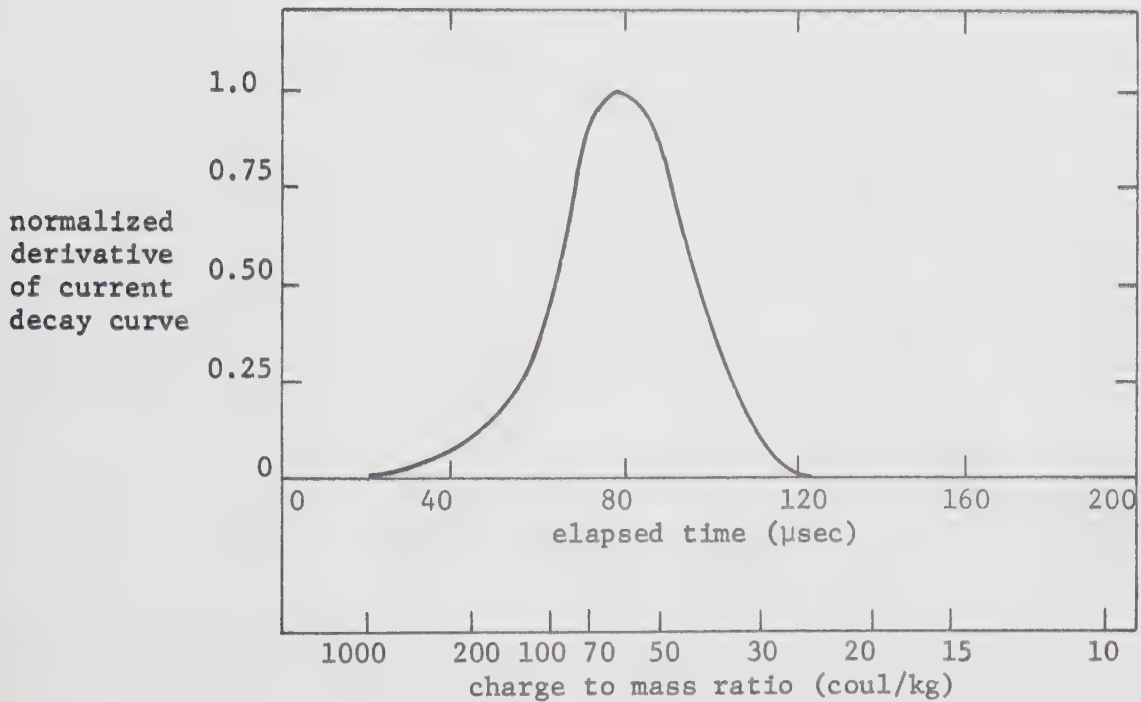
Figure Number	Capillary Fluid (g NaI/ 100 ml glycerol)	Feed Pressure (cm Hg)	Capillary Voltage (kV)	Nominal Charge to Mass Ratio (coul/kg)	Figure in Parametric Analysis Series
35	#29, SS	2.5	17.4	20	56. 29
36	#27 W, Pt-Ir	5	18.	13	17. 33
37	#27 W, Pt-Ir	5	3.2	20	32. 33

Complete data for the time of flight measurements shown in Figures 36 and 37 are given in Table 16 as a matter of interest. Table 16 lists values of all the parameters that can be calculated from the time of flight measurements. It can be seen that the thrust and specific impulse of the beam are not high enough to be interesting in micro-thrust rocket applications, because of the deliberately chosen low charge to mass ratios. The results for the three different calculations of beam charge to mass ratio (nominal value, mass flow rate averaged value, and root mean square mass flow rate averaged value) show that for the narrow charge to mass distribution in Figure 36, the three values of charge to mass ratio are the same. For the case showing the very asymmetric and broad charge to mass distribution in Figure 37, the nominal value was 15% lower than the mass flow rate averaged value. This difference is probably just outside the error limits on the mass flow rate averaged charge to mass ratio found in the time of flight





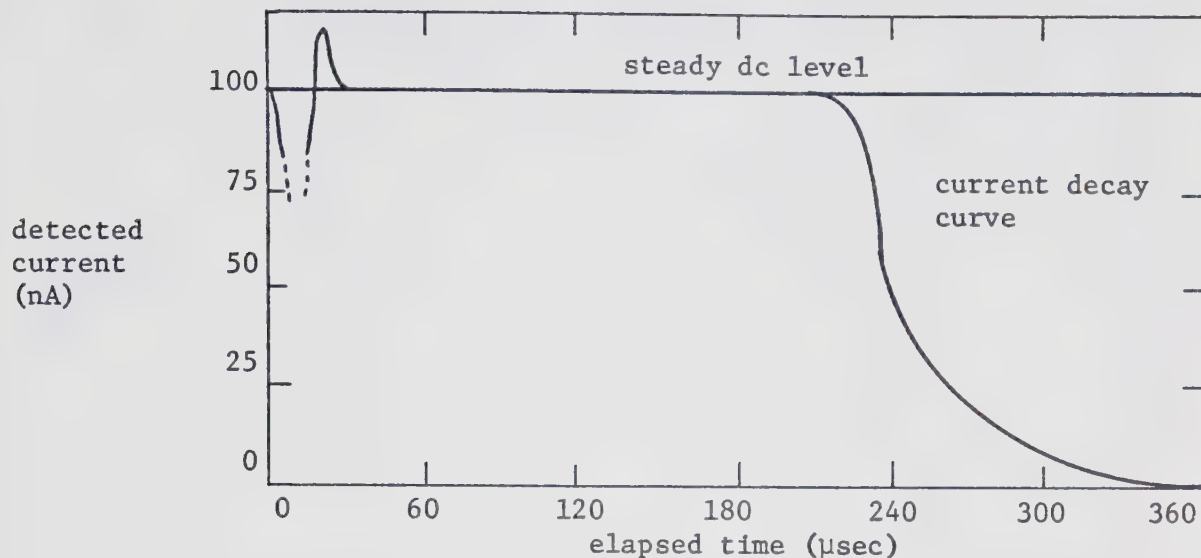
(a) Photograph of the Detected Current Waveforms.  
Vertical Scale = 200 nA/div, Horizontal Scale  
= 20  $\mu$ sec/div.



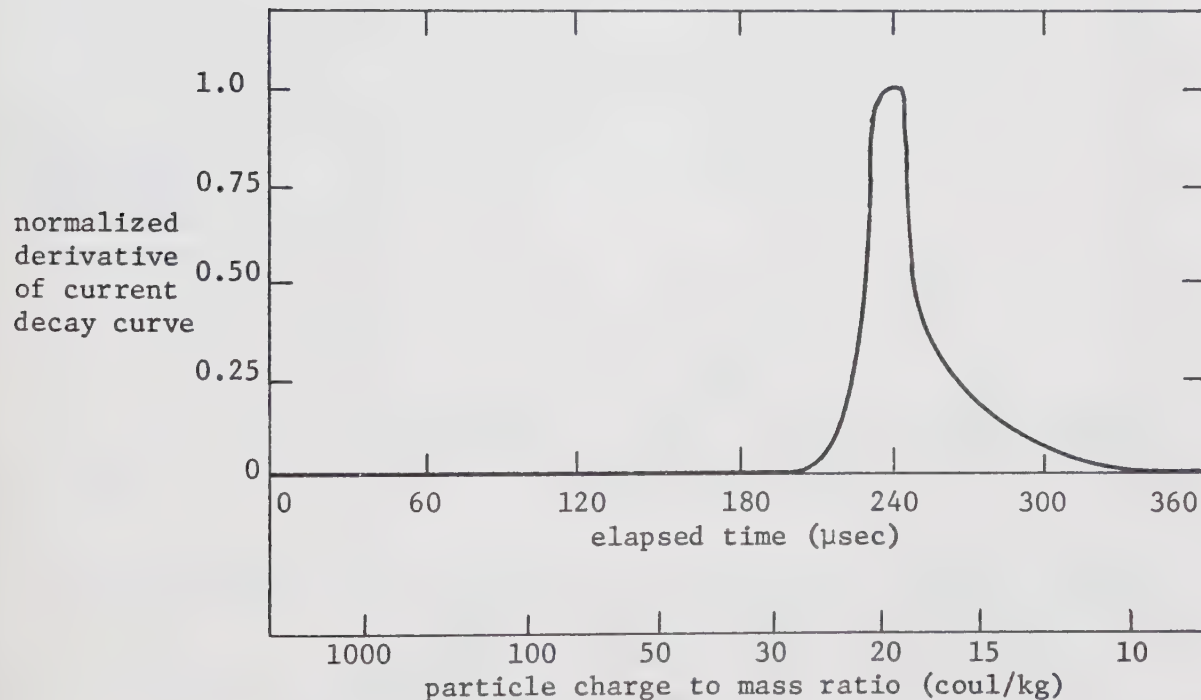
(b) Normalized Beam Current as a Function of Charge  
to Mass Ratio.

**Figure 35:** Results of a Time of Flight Measurement on a Beam in the High Voltage Operating Region. The Figure Shows the Detected Current Waveforms, and the Associated Normalized Current Versus Charge to Mass Ratio Curve.





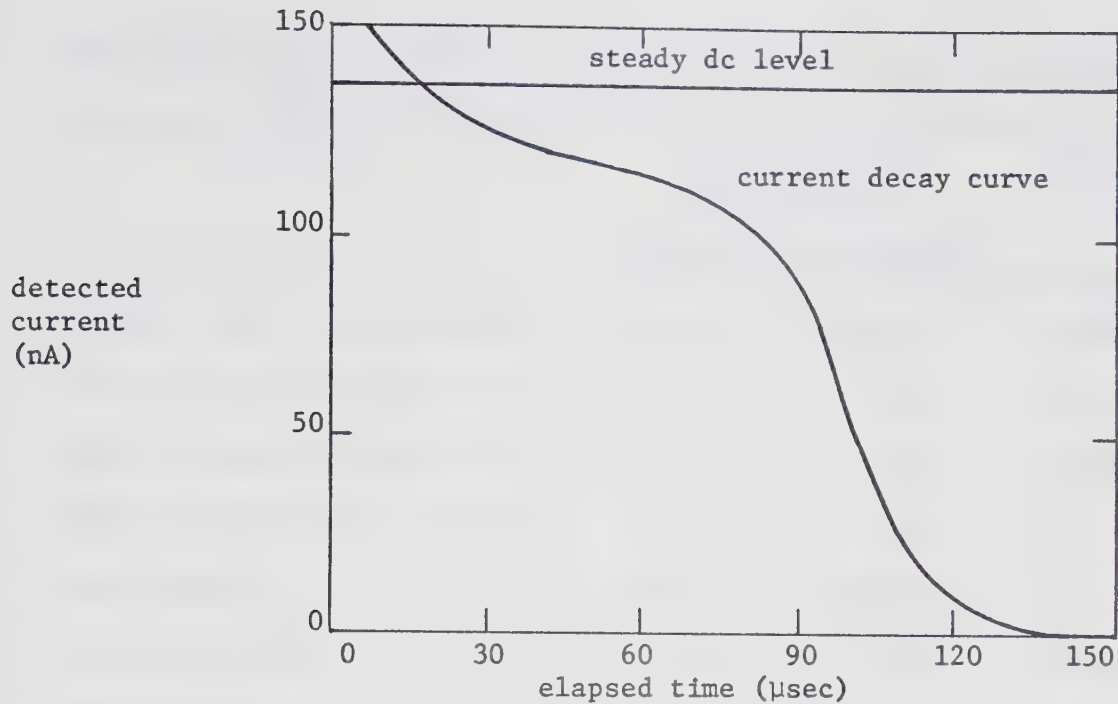
(a) Detected Current Waveforms.



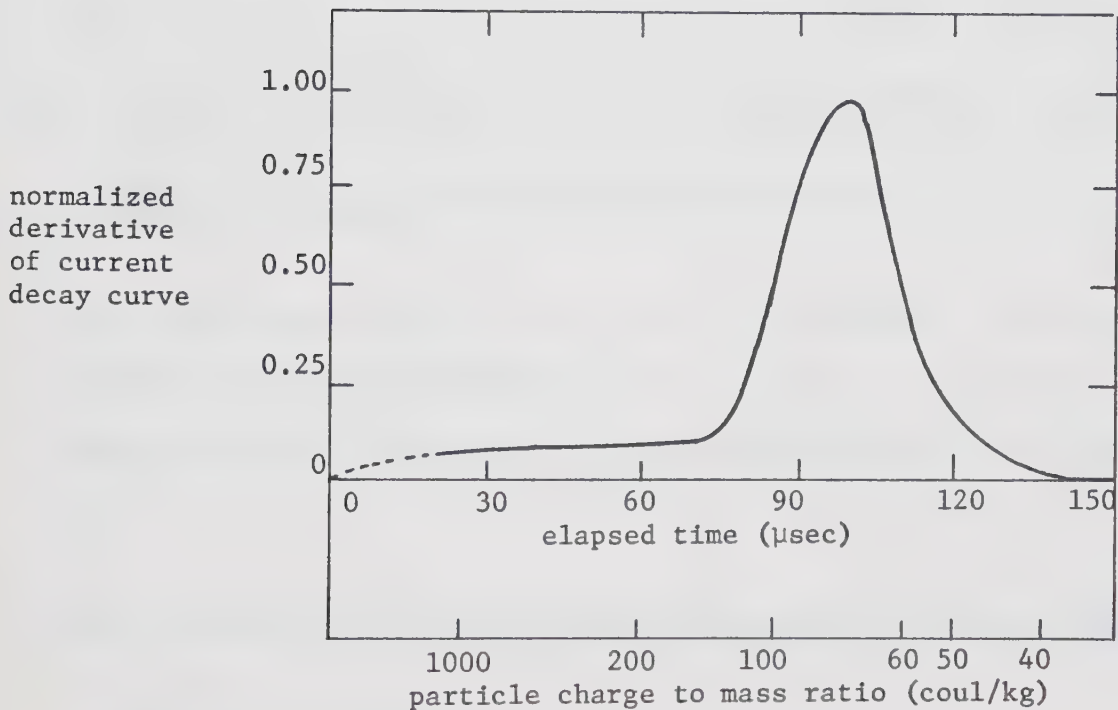
(b) Normalized Beam Current as a Function of Charge to Mass Ratio.

Figure 36: Results of a Time of Flight Measurement of a Beam in the High Voltage Operating Region. The Figure Shows the Detected Current Waveforms, and the Associated Normalized Current Versus Charge to Mass Ratio.





(a) Detected Current Waveforms.



(b) Normalized Beam Current as a Function of Charge to Mass Ratio.

Figure 37: Results of a Time of Flight Measurement of a Beam in the High Voltage Operating Region. The Figure Shows the Detected Current Waveforms, and the Associated Normalized Current Versus Charge to Mass Ratio Curve.



Table 16: Time of Flight Measurement Results for the Measurements Shown in Figures 36 and 37.

Parameter	Parameter Value Derived from		Units
	Figure 36	Figure 37	
Average charge to mass ratio <sup>a</sup>	17.1	87.2	coul/kg
S.M.R. charge to mass ratio <sup>b</sup>	17.0	79.0	coul/kg
Nominal charge to mass ratio <sup>c</sup>	17.1	75.2	coul/kg
Charge distribution efficiency	99.4	90.5	%
Beam current	100.	140.	nA
Average velocity <sup>d</sup>	0.67	1.87	km/sec
Mass flow rate	5.86	1.61	$\mu$ g/sec
Thrust	3.89	2.85	$\mu$ newtons
Specific impulse	67.8	181.	sec

a mass flow rate averaged charge to mass ratio, Table 4

b square mean root mass flow rate averaged charge to mass ratio, Table 4

c charge to mass ratio at maximum current, Section 3.2

d based on (a) above.

measurement (see Section 6.10.4). Thus, for purposes of the micro-particle accelerator, the three different methods of calculating the measured charge to mass ratio of the beam describe the beam equally well.

## 6.10 Experimental Sources of Inconsistency, Uncertainty, and Error

### 6.10.1 Introduction

It was generally found that experiments could not be reproduced consistently. For instance, the parametric plot Figure 28 showed a factor of typically 2 and up to 4 between charge to mass ratio values



measured during different experiments at the same operating point. In Section 6.9.3 it was shown that, for twelve consecutive time of flight measurements on one beam, a standard deviation of 12% and a maximum deviation from the mean of 25% were found for measured charge to mass ratios. It must be emphasized, however, that the trends in source behaviour were generally self-consistent and also consistent with the results reported in the literature<sup>21</sup>. Because of the great variation in measured charge to mass ratios, it became essential that time of flight measurements be taken often during each experiment. Thus shifts in the beam parameters would be known and could be used to rationalize the colloid source behaviour and properties.

The possible sources of inconsistency, uncertainty and error have been divided into two sections. The first section outlines experimental problems, but has no numerical estimate of the magnitudes of the uncertainties of errors. The second section discusses the time of flight measurement method, and includes a detailed error analysis for the time of flight measurement results.

#### 6.10.2 Experimental Problems

In the series of colloid source experiments performed, it was found to be relatively easy to reproduce beam stability and beam spatial distributions for the given operating conditions. However, the corresponding measured charge to mass ratio values differed by up to a factor of four. Thus the discussion of experimental problems is concentrated on effects influencing the beam charge to mass ratio. These effects can be grouped into factors influencing mass flow rate, resistivity, and capillary tube tip shape.



Generally, an increase in mass flow rate lowers the charge to mass ratio of the resulting beam. Parameters affecting the fluid mass flow rate include fluid viscosity and capillary tube size. Fluid viscosity decreases rapidly as temperature increases--data by Kidd<sup>21</sup> show that the viscosity of glycerol decreases 50% over a temperature range of 20°C to 23°C. In the present experiments, the temperature was neither monitored, recorded, nor controlled, so fluid viscosity could change appreciably during or between experiments. Any heat created in the particle charging process would tend to heat the capillary tube tip. Corona in the beam has been observed to heat the capillary tip red-hot, which would locally decrease the fluid viscosity, and increase the overall source temperature. Mass flow rate changes would result. Variations in the capillary tube bore between different sections of tubing would influence the mass flow rate. The presence of dirt or burrs on the tube wall would have the same result.

Factors affecting fluid resistivity were temperature, contaminants, and changes in fluid-doping agent concentrations. The strong temperature dependence of resistivity (it decreases 28% over the temperature range 20°C to 23°C) has been demonstrated in Section 4.3. The factors affecting fluid temperature are mentioned above. Contaminants in the fluid would change fluid resistivity, hence beam stability, spatial distribution, and charge to mass ratio. Changes in fluid concentration should occur only if glycerol were evaporated from the solution during a long period of storage under vacuum.

It should be noted that the effects of temperature on the mass flow rate and on the fluid resistivity are in such a direction that the effects partly (or completely) cancel each other when the overall



effect of temperature on charge to mass ratio is considered. The cancellation occurs because a rise in temperature lowers viscosity (which lowers the charge to mass ratio) and lowers resistivity (which increases the charge to mass ratio).

The precise effect of capillary tube tip shape on charge to mass ratio and beam distribution was not measured. However, since the tip shape is known to strongly influence beam stability, it is probable that minor changes in the tip shape would influence the parameters of the beam produced. Capillary tip erosion has been observed to change the tip shape significantly during a period of 15 minutes or more, which would prevent reproducibility of results. If the fluid were contaminated with particulate matter, the capillary might be either partially plugged (changing the mass flow rate) or the particles might migrate to the capillary tube tip and perturb the fluid flow pattern there.

If the vacuum pressure at the capillary tip varied during a trial, some changes in beam stability might be observed.

#### 6.10.3 Factors Influencing the Accuracy of Time of Flight Measurement Results

The factors to be discussed in this section have been divided into two types--qualitative, and quantitative. The qualitative effects are associated with experimental procedures and it is difficult to assign numerical error estimates to them.

The effects of secondary particle production were not significant in this work, as shown by experiments designed to test both beam current levels and time of flight measurement results. The presence of bias grids in front of the electrical detector caused additional



problems, such as: some beam was intercepted on the grids, secondary particles may have been created on the grids, beam may have been partially or completely neutralized at the grids prior to hitting the detector, and beam could have been scattered from the grids. These effects would all tend to broaden the beam spatial distribution as observed on the electrical detector, broaden the range of charge to mass ratios measured in the beam, and cause straggling of particles at the falling edge of the time of flight current traces. Beam scattering from other parts of the experimental chamber was observed during the early stages of this work and caused many such problems.

The presence of ions in the particle beam was easily noted if a careful measurement of the dc current level was made immediately prior to initiating a time of flight measurement. The time of transit of the ions is much smaller than for the main part of the beam so the ions appear as a drop in the time of flight current trace immediately after initiating the measurement.

Beam current instabilities during a time of flight measurement could usually be seen to produce an unusually shaped current trace, hence the data could be rejected. Instabilities in the nominal charge to mass ratio at constant beam currents could not be detected except as variations in a sequence of time of flight measurements.

The problems of beam energy losses may or may not affect the time of flight measurements. Basically the time of flight method measures charge at the detector, and uses the potential of the capillary in the calculations. Any energy lost in the particle creation process tends to reduce the effective initial potential of the particles, thus causing errors. As discussed in Section 2.7.3, the effective potential loss may



be about 400 volts, or 2.3% of 17.5 kV. This error is such as to yield high values of calculated charge to mass ratio.

As mentioned before (Section 3.2), the time of flight method uses capillary tube potential, detected beam current, and beam velocity to find the beam parameters. Since particle velocity is established in the electric field of the capillary tip region, subsequent changes in particle mass or charge cannot change it. Therefore the time of flight method gives particle charge to mass ratio as it existed at the source. Thus mass loss from particles in-flight does not influence the time of flight measurements. If any charge loss takes place uniformly over all particles in the beam, the detected current will be decreased, the shape of the time of flight curve is not altered, and the time of flight method does in fact give particle charge to mass ratios as they existed in the source. If any charge loss affects certain particles more than others, errors will appear in the time of flight method because the time of flight curve is altered in shape and magnitude.

Most of the error that can be numerically estimated in the time of flight method arises in recording and analyzing the time of flight curves. Table 17 lists these errors, their probable values, and whether or not they affect the three parameters beam current, mass flow rate, and nominal charge to mass ratio. Two separate estimates of error for nominal charge to mass ratio are included--one for an absolute measurement, and the second for comparison of two successive measurements on the same beam at the same operating conditions for the same nominal charge to mass ratio.

Inspection of definitions in Section 3.2 reveals that while mass flow rate depends on the absolute value of beam current, nominal charge



Table 17: Sources of Errors in Time of Flight Measurements.

Description	Value ( $\pm$ )	This Error Affects				
		Beam Current	Mass Flow Rate	Absolute Charge to Mass Ratio	Relative Charge to Mass Ratio	
vertical amplifier calibration	3%	X <sup>a</sup>	X	.	.	.
oscilloscope time base calibration	3%	.	X	X	.	.
detector resistor value	1%	X	X	.	.	.
noise due to beam, amplifier, and interference	$\pm .1$ div, or 5%	X	X	X	.	X
data extraction error	$\pm .05$ div, or 3%	X	X	X	.	X
numerical integration	1%	.	X	.	.	.
drift distance	4%	.	X	X	.	.
capillary voltage	5%	.	X	X	.	.
absolute sum total (%)		12	25	20	8	
root mean square total (%)		7	10	9	6	

a X indicates yes, . indicates no.

to mass ratio does not. Thus evaluation of errors in the current trace integral necessary to calculate mass flow rate caused by errors in the integrand depends on both the shape of the given current trace, and the parameter being calculated. For this reason, no comprehensive error analysis of the integration procedure has been made. Errors in integrands are assumed to affect the corresponding integrals by the same percentages. In any case, the errors are sufficiently large as to make



detailed error analysis somewhat unnecessary. It should be noted that the error for drift distance was in fact  $\pm 2\%$ ; a value of  $\pm 4\%$  was used in Table 17 because the square of drift distance occurs in the formulae for the parameters being calculated.

Some experimental precautions were taken to reduce errors in recording the time of flight curves. It has already been shown (Chapter 5) that when the thyratron acting as the capillary voltage switch fires, a transient propagates through the entire experimental system. The transient appearing at the oscilloscope input decays with an RC time constant given by the detector, cable, and oscilloscope input circuits. Now, in order that the time of flight current decay curve be unambiguously recorded, the decaying portion of the curve must be temporally separated from the transient. This separation can be accomplished by either reducing the time constant of the input circuit or increasing the source to detector drift distance (thereby increasing the time taken for the current decay curve to fall to zero). High frequency noise was suppressed by varying the upper corner frequency of the 1A7A plug-in response, using the variable bandwidth feature of the amplifier. A compromise had to be reached between a high frequency response to aid transient suppression and to allow accurate recording of the time of flight trace decay, and a low frequency response to filter out high frequency beam, amplifier and interference noise. Typical amplifier bandwidths of dc to 100 or 300 kHz were used. Interference due to 60 Hz mains was minimized, by removing ground loops, to an absolute peak to peak value of about 20  $\mu$ V at the amplifier input, or an equivalent detected current interference of less than 20 nA using a 1 kohm detector resistor. This value, while being up to 10 percent of the



total detected current, was not serious because the duration of a time of flight measurement was a maximum of 1% of the 16.6 msec period of the 60 Hz interference.

#### 6.10.4 Discussion of Errors in Experimental Results

Results such as those in Figure 28 show a factor of up to 4 in variation from the lowest-to-highest nominal charge to mass ratio found at the same source operating point. Clearly no quantitative judgement can be made on this error, but it would seem that the error is not unreasonable considering the many possible sources of uncertainty given in Sections 6.10.2 and 6.10.3.

An experiment was described in Section 6.9.3 in which 12 consecutive time of flight measurements, made on the same beam, gave a standard deviation of 12% and a maximum deviation of 25% in nominal charge to mass ratio. These values are considerably higher than the RSS error of 6% and maximum error of 9% found in Table 17. Either the beam exhibits some true charge to mass instabilities, or pressure and voltage instabilities occurred, which were not recorded during the experiments. In any case the nominal charge to mass ratio is fairly constant, considering that the width of the charge to mass ratio distribution covered about one decade in value.

#### 6.11 Comments on Beam Formation

The general patterns of beam behaviour found here agree with results discussed in the literature. Thus it would appear that little additional light can be shed on the physics of beam formation, based on the present results. The existence of the high voltage region is certainly



significant to the success of this project, as are the geometry, fluids, and operating parameters used. Further work is required, however, to elucidate whether or not the existence of the high voltage region is peculiar to the broader-than-normal capillary tip shape, or whether it is universal for all tip shapes. The erosion of only the inner parts of the capillary tip tapered surface may suggest the capillary rim does not influence the beam beyond shaping the electric fields at the capillary tip, and that the capillary behaves as though it had a much thinner wall. On a broader view, the beam may be formed in a mass flow- or charge flow-limited region, and thus is composed of stable particles very close to or very far from, respectively, the Rayleigh Criterion limit for charged droplets.

### 6.12 Summary

This study of a colloid source can be considered, with regard to possible construction of a colloid source for the microparticle accelerator, to yield several points:

- (a) Stable beams focussed close to the axis can be consistently produced. These beams have sufficient on-axis current to permit formation of an axial beam by collimation of the complete beam.
- (b) These useful beams can be produced over ranges of operating parameters and source geometries, and thus are not critically dependent on any operating parameter.
- (c) Control of the colloid source requires:
  - i) a high voltage "switch" on the capillary potential suitable for time of flight measurements and voltage switching,
  - ii) variable high voltage supply,



- iii) variable feed pressure,
- iv) detectors for current measurement and time of flight results,  
and visual detectors for examining beam shape.

This review of the test bench results shows that an accelerator source is feasible. The remainder of this thesis discusses development and testing of this source.



## CHAPTER 7

### A COLLOID SOURCE FOR THE MICROPARTICLE ACCELERATOR

#### 7.1 Design Criteria

After the colloid source had been successfully operated in the test bench, an analysis of the problems which would be encountered if a colloid source were operated in the 300 kV accelerator was made.

While a complete description of the 300 kV accelerator is given in Section 8.1, a brief description of it is included here for convenience. The high voltage from the 0 to 300 kV dc power supply is applied to a large, smoothly contoured "dome", which is supported by an insulated column. Electrical power within this dome is obtained from a 26 V, 25 A generator driven by an air motor. This air motor receives compressed air through an air hose running from ground potential through the insulated column to the dome. The high voltage on the dome is applied to one of a pair of electrodes, while a second electrode is grounded. The electrodes are contained in an evacuated six-inch inner diameter glass tube. An evacuated chamber to contain experimental apparatus is adjacent to the high voltage electrode. The high voltage end of the accelerating tube is supported by the dome. Beyond the ground potential electrode are the target chamber and vacuum pumping system.

The first criteria imposed on a possible colloid source are those related to the accelerator itself. The source must fit in the available chamber in the high voltage dome. Control of the source voltage and pressure must be done remotely, at ground potential. Because the



source may be at 300 kV while in the dome, the control air pressures applied to the dome or the source must use air pressures of at least 1 atmosphere in order to prevent electrical breakdown and corona in the control air lines. Finally, the source must produce an on-axis beam which is well collimated in order to prevent particles in the beam from hitting electrode surfaces and scattering into the detector.

Design criteria which arise from the experience obtained operating the test bench version of a colloid source are also important. Suitable vacuum pressure at the capillary tube tip is essential. Suppression of electrons in the source area is desirable. Again, corona in any air control lines must be prevented. Also, it would be desirable to be able to restart the colloid source for several experimental trials without having to open the vacuum system.

A concept of the design of a colloid source was formed, based on these criteria and the previous experimental results. It was clear that, if the source were operated in the high voltage region (i.e. from 14 kV to 20 kV), axial beams would be available. However, collimation of the beam to remove beam components too far off-axis would be necessary. Because secondary electrons would be produced if the beam were intercepted by the collimator, the tube type extractor was used in order to help shield the capillary tube tip from secondary electrons. Provision for a bias electrode between the capillary tube tip and the collimator was made, in case additional electron suppression would be required. The entire source, consisting of collimator, extractor, capillary tube, and fluid reservoir, was contained within the evacuated source chamber in the high voltage electrode, and supported only by the source chamber end flange. Thus the entire assembly could be removed



in one piece for experimental changes.

The high voltage required to operate the source was applied to the body of the source, fluid reservoir and capillary tube assembly by a high voltage vacuum feedthrough on the source chamber and flange. Thus the extractor, source support mechanism, air line connections, and source chamber and flange were insulated from the source body.

An analog control pressure greater than one atmosphere was applied to the source from a remote control panel at laboratory ground potential. This control pressure was converted to the appropriate fluid feed pressure within the source itself.

The design of the colloid source had to incorporate the maximum possible flexibility in the variation and selection of the capillary voltage and fluid feed pressure. This adaptability was required for two reasons. Firstly, the stable dc mode of beam operation is difficult to establish, and often much variation of the voltage and pressure are required to initiate this desired mode of operation. Secondly, some variation in the nominal charge to mass ratio of the beam is possible through varying the colloid source operating conditions. Accordingly, the capillary voltage in the accelerator source was controlled by a power supply in the accelerator dome (see Section 8.3), and the fluid feed pressure was varied by means of an analog control pressure and the pressure converter to be described in Section 7.2.1.

## 7.2 Mechanical Details of the Colloid Source

### 7.2.1 Description of the Pressure Converter

As mentioned in Section 7.1, an analog control pressure greater than or equal to one atmosphere must be applied to the source.



However, the fluid feed pressure must be between 0 and 20 cm Hg (absolute) in the source itself. In order to reconcile these two pressure criteria, a pressure converter was designed and built.

Figure 38 is a schematic diagram of the pressure converter. It consists of four chambers and a "Y"-shaped piston joining them. If chamber C is the fluid reservoir for the colloid source, an equation relating the pressure  $P_c$  to the remaining pressures, ( $P_a$ ,  $P_b$ , and  $P_d$ ) is required. The relationship is found by a force balance on the piston, assuming negligible piston friction. Then force rightward = force leftward, or

$$A_d(P_b - P_d) = A_a(P_b - P_a) + A_c(P_b - P_c) . \quad (7.1)$$

After transposing,

$$P_c = \frac{1}{A_c} \{P_b(A_a + A_c - A_d) - P_a A_a + P_d A_d\} . \quad (7.2)$$

The following conditions are set arbitrarily:

$$A_c = A_a ,$$

and

$$P_d = 0 .$$

The latter condition implies that chamber D is, in fact, open to the vacuum system. Then equation 7.2 becomes

$$P_c = P_b \left(2 - \frac{A_d}{A_c}\right) - P_a . \quad (7.3)$$

Thus there is a linear relationship between the fluid pressure  $P_c$  and



the applied pressure  $P_b$ .

The success of this design is critically dependent on the choice of seal between the piston heads and the chamber walls. The Bellofram Corporation<sup>72</sup> markets a type of rolling rubber diaphragm. A cross-sectional view of such a diaphragm is shown in Figure 39. The seal is made by the rolling convolution and thus shows very low friction to piston movement. The diaphragms are made of synthetic fabric impregnated with nitrile elastomer. The elastomer is moulded so that the outer side of the fabric is completely covered, and the inner side of the fabric is only partly covered. The fabric visible on the inner side of the diaphragm must be on the low pressure side of the seal when the diaphragm is folded and installed. Dimensions of the diaphragms chosen for use in the pressure converter are shown in Table 18.

Table 18: Dimensions of Bellofram Diaphragms Used in the Pressure Converter.

Chamber Identification	Piston Diameter		Cylinder Diameter		Length		Effective Area	
	(in)	(cm)	(in)	(cm)	(in)	(cm)	(in <sup>2</sup> )	(cm <sup>2</sup> )
A	1.19	3.02	1.37	3.49	1.12	2.84	1.29	8.34
C	1.19	3.02	1.37	3.49	1.12	2.84	1.29	8.34
D	1.31	3.32	1.50	3.81	1.25	3.18	1.55	10.0

With the given values of piston area, equation 7.3 becomes

$$P_c = 0.80 P_b - P_a . \quad (7.4)$$

An arbitrary choice of  $P_a = 1$  atm results in

$$P_c = 0.80 P_b - 1 \quad (\text{pressures in atm}) . \quad (7.5)$$



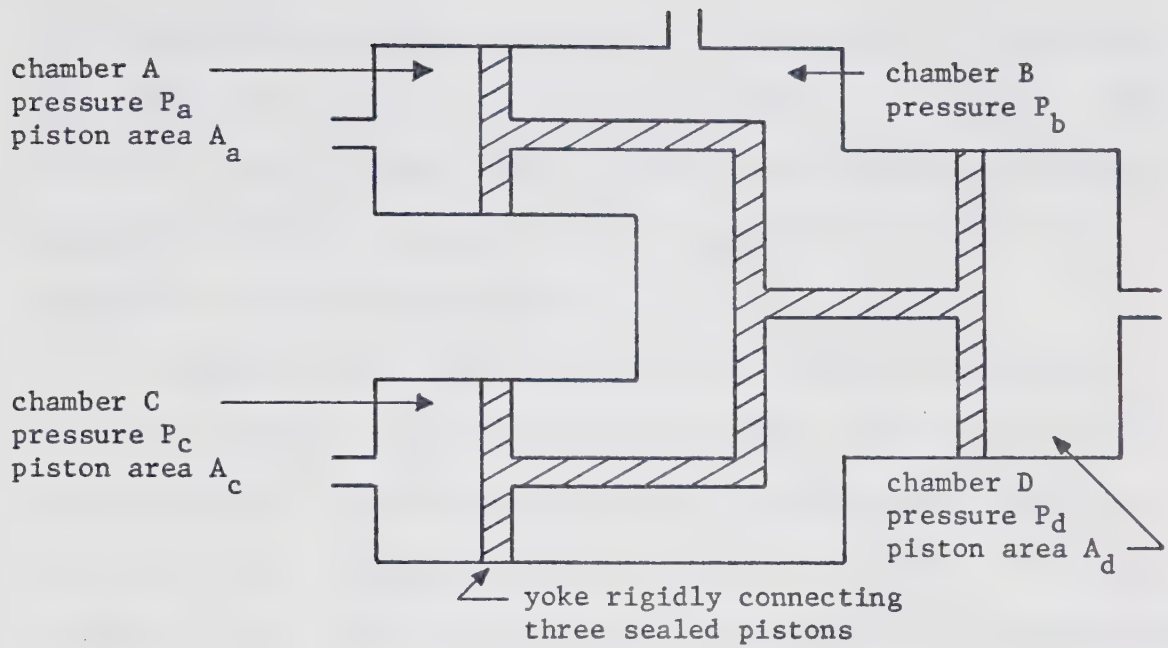


Figure 38: Schematic Diagram of the Pressure Converter.

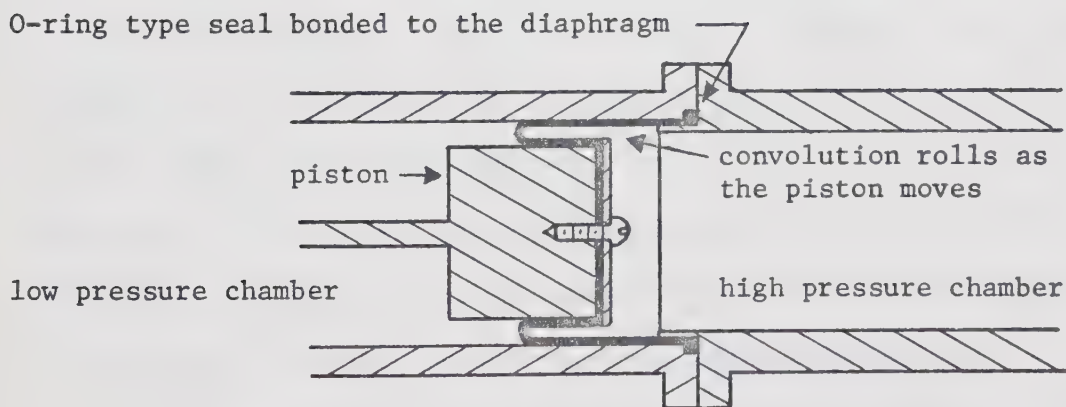


Figure 39: Schematic Diagram of a Bellofram Rolling Rubber Diaphragm.



For  $P_b$  less than 1.25 atm the pressure  $P_c$  is negative. In practical terms this means that the piston is held against the rightward mechanical stop. For  $P_b$  greater than 1.25 atm, the piston moves leftward against the fluid in chamber C until the equilibrium value of  $P_c$  (given by equation 7.5) is reached.

In summary, then, the converter is inserted into the vacuum system to maintain  $P_d$  at zero pressure, chamber A is vented to atmospheric pressure, and a control pressure  $P_b$  greater than 1 atm is converted into a pressure  $P_c$  near zero absolute pressure. This allows complete, linear control of the fluid feed pressure  $P_c$  by applying the analog control pressure  $P_b$  from a remote control panel.

#### 7.2.2 Mechanical Details of the Colloid Source

This section discusses the realization of the combined pressure converter and colloid source. Figure 40 is a longitudinal cross-sectional drawing of the device. Mounting hardware used to attach the source to the support flange is not shown. Figures 41 and 42 show a collection of photographs of the device, in assembled and exploded views. Part numbers and part descriptions for Figures 40, 41, and 42 are given in Table 19. It must be emphasized that the cross-sectional view shown in Figure 40 is not cylindrically symmetric--the true shape of the colloid source is best shown in Figures 41 and 42.

The dimensional requirements of the colloid source were fixed by the source chamber in the high voltage dome of the accelerator, which was 0.15 m in diameter and 0.38 m long. The high voltage electrode at the end of the chamber was a tube 34.1 mm inside diameter and 0.09 m long. Figure 58, Section 9.3.2, shows the source and electrode



Table 19: Part Descriptions of the Colloid Source.

Part Number	Description
1	collimator, 2.54 mm aperture diameter
2	collimator, 3.18 mm aperture diameter
3	tube-type extractor and support piece
4	electron retarding bias ring
5	capillary tube and mounting cap
6	lucite support and voltage insulation piece
7	port into chamber A
8	end plate with fluid feed tube from chamber C, and eight clamp rods.
9	block containing chambers A and C
10	piston between chambers A and B
11	diaphragm A
12	support plate
13	piston assembly
14	ball bushing
15	block containing chamber B
16	support plate
17	piston assembly
18	diaphragm D
19	piston between chambers B and D
20	ball bushing
21	block containing chamber D
22	adjustable piston length extension
23	piston stop
24	bushing support



Table 19: Part Descriptions of the Colloid Source (Continued).

---

25	port into chamber B
26	ball bushing
27	piston assembly
28	piston between chambers B and C
29	diaphragm C
30	source chamber end flange
31	BNC bulkhead connector for bias voltages
32	port used for filling chamber C with glycerol
33	air tube to chamber B
34	air tube to chamber A
35	support bracket
36	high voltage lead and high voltage feedthrough
37	lucite support piece
38	lucite support piece

---

geometry. Alignment of the source was achieved by mating grooves on the source chamber end flange, and the insertion of the front part of the extractor piece (#3) into the electrode tube.

In the initial design, the extractor piece was a 34 mm diameter cylinder which fit completely inside the electrode tube, and the source chamber was only 0.315 m long. The extractor was grounded by contact with the electrode tube, and the lucite piece (#6) provided the necessary high voltage insulation for the body of the source. However, when the source was used in the 300 kV accelerator, it was found that there was inadequate pumping speed in the capillary tube tip region and that high voltage tracking occurred across the lucite



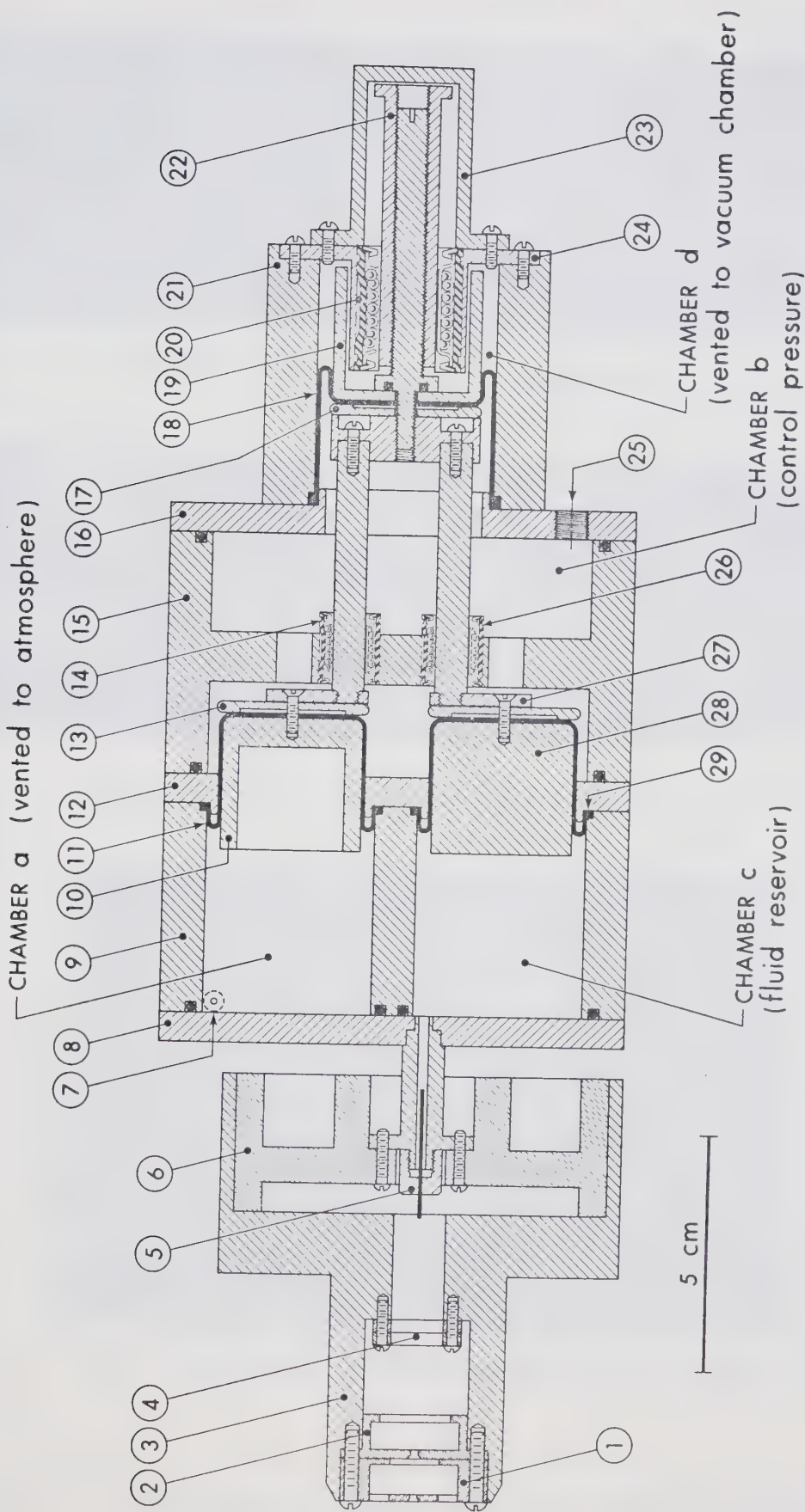
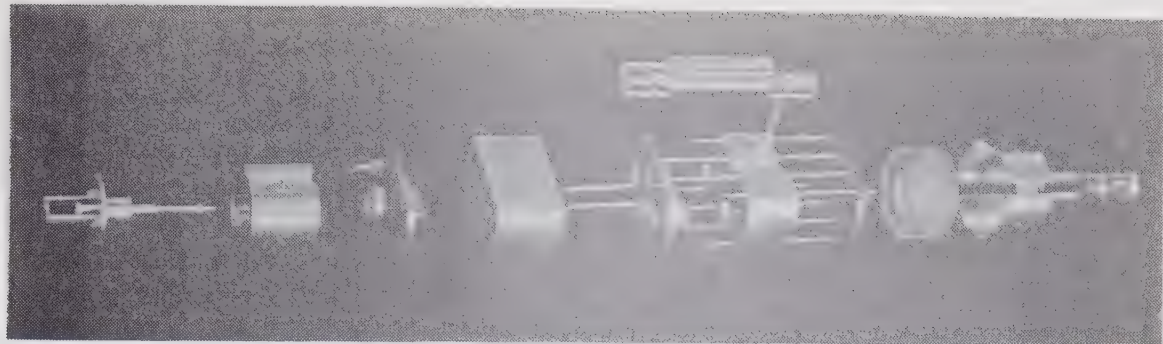
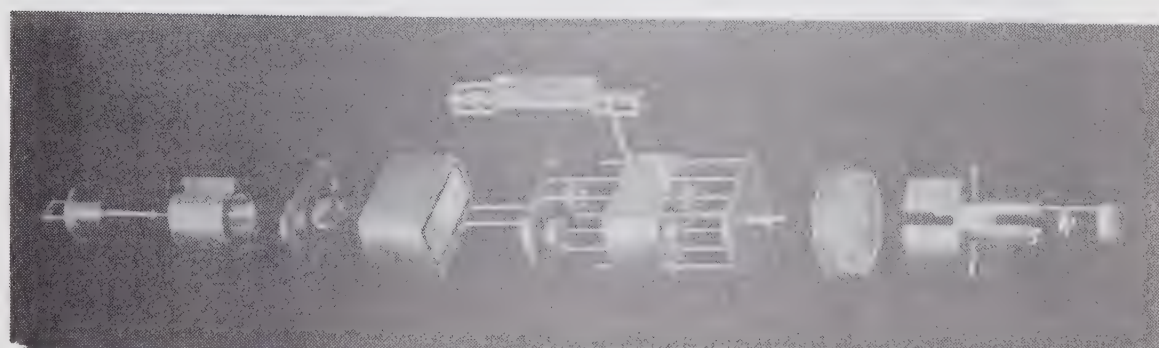


Figure 40: Cross-sectional Drawing of the Pressure Converter and Colloid Source. Part Numbers are Described in Table 19.

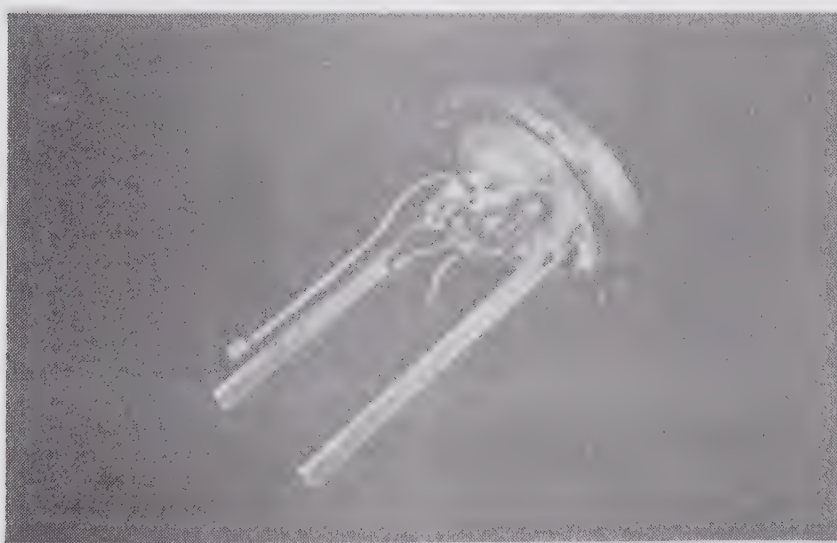




(a) Exploded View of the Colloid Source.



(b) Exploded View of the Colloid Source.



(c) View of the Colloid Source Support Flange.

Figure 41: Photographic Views of the Partly Assembled Colloid Source.



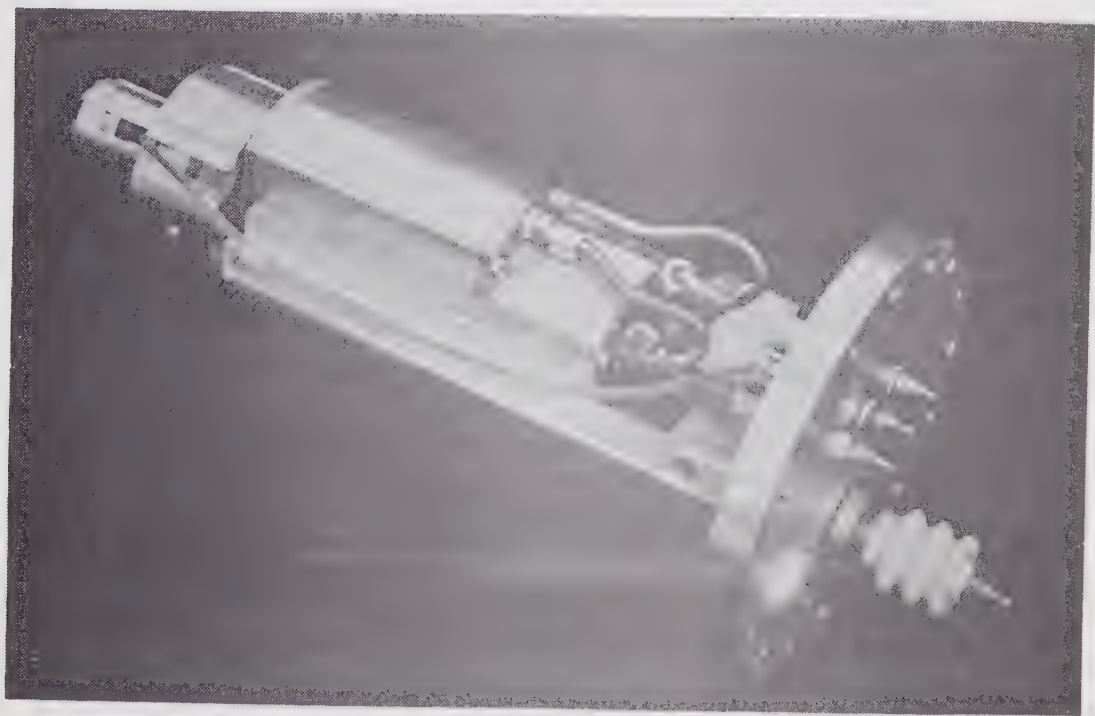
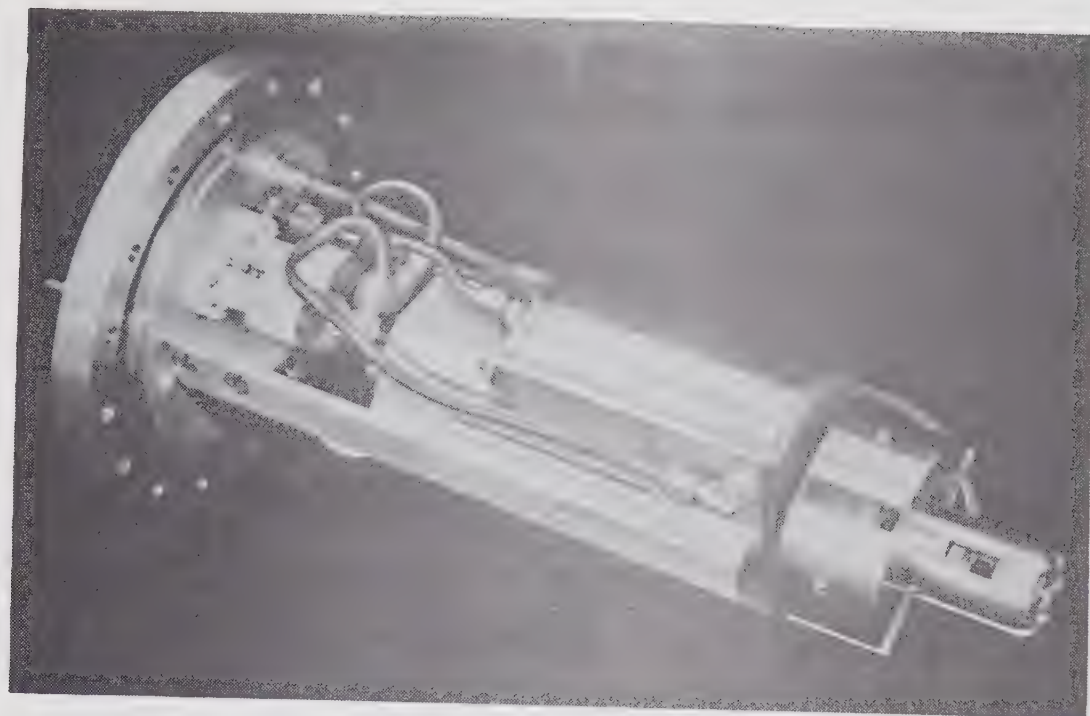


Figure 42: Photographic Views of the Assembled Colloid Source.



insulator (#6). To alleviate this problem the source chamber was extended 65 mm to become 0.38 m long, the source was pulled back 65 mm, and a new extractor design was made. The final version of the extractor is shown in Figure 40 to 42. (Several attempts to modify the initial design were unsuccessfully tried prior to changing the source chamber geometry.) While Figure 40 shows a cross-section of the extractor geometry, it does not show the four 10 mm wide slots cut in the extractor to aid the pumping speed in the capillary tube to collimator region. Likewise, the lucite support had pumping holes cut in it. These pumping holes are visible in Figure 41.

The collimators (#1 and #2) allow only the central part of the beam to enter the accelerating gap from the source. The first collimator (#2) removes most of the excess beam. The second collimator (#1) restricts the beam to be within  $1^\circ$  of the axis ( $\tan \theta = 0.0175$ ) in the geometry shown here. Two pumping holes were cut in each collimator disc, and the collimators were mounted  $90^\circ$  apart in rotation so that unwanted beam would still be intercepted while gasses could escape from the source region into the rest of the vacuum system. The electron bias ring (#4) was insulated from the extractor (#3) by nylon screws. A lead from this ring passed through one of the pumping ports in the extractor, and then was connected to a BNC bulkhead connector (#31) in the source flange (#30) for application of bias voltages.

The components in the pressure converter and fluid reservoir (#7 to #28) were machined of aluminum alloy with the exception of two end-plates (#8 and #25). O-rings provided the vacuum seals between pieces. Necessary dimensional details for the diaphragm supports and mounting pieces were obtained from the Bellofram design manual<sup>72</sup>. Three ball



bushings (#14, #20, and #28) kept the piston aligned and supported while exerting a low frictional force on it. The adjustable length extension on the piston (#22) could be shortened to allow the piston to be retracted completely and only partly advanced, or lengthened to allow the piston to be only partly retracted and fully advanced. It also provided a visual reference for the piston position.

The source chamber end flange (#30) supported the entire source and its pneumatic and electrical connections. A horizontally mounted U-shaped bracket (#35) straddled the source body, which in turn was supported from the bracket by two lucite pieces (#37 and #38) machined to minimize the possibility of high voltage tracking from the source body to the support bracket. As mentioned previously, the bias voltage for the electron retarding ring was passed through the BNC bulkhead connector (#31). The source high voltage was applied through a 20 kV ceramic feedthrough (#36). The two air control pressures to chambers A and B were connected on the outside of the flange using  $\frac{1}{4}$ -inch "Polyflo" fittings. On the inside of the flange, specially machined teflon tubes provided the high voltage insulation between the flange and the  $\frac{1}{4}$ -inch Swagelok fittings leading to the source. The Swagelok fittings on the ports to chambers A and B on the source were connected to the Swagelok fittings on the teflon tubes by  $\frac{1}{4}$ -inch copper tubing (#33 and #34). A third feedthrough tube (#32) was used only for filling the fluid reservoir, chamber C.

Assembly of the source and pressure converter was straightforward provided the components were installed in a certain sequence. Appendix B outlines the assembly procedure for the colloid source.



### 7.3 Tests of the Pressure Converter

#### 7.3.1 Vacuum Leaks and Gas Diffusion

The diaphragms used in the pressure converter were made of nitrile elastomer (butadiene acrylonitrile copolymer) and hence could be expected to have a definite rate of gas diffusion through them. Technical data<sup>73</sup> indicate a rate of  $8 \times 10^{-9} \text{ cm}^3/\text{sec}$  for a  $1 \text{ cm}^2$  area, thickness of 1 cm, and pressure differential of 1 atm. Since usual applications of these diaphragms use pressures greater than 1 atm, it was assumed that the above diffusion rate is to be interpreted as  $8 \times 10^{-9} \text{ cm}^3 \text{ atm/sec}$ , or  $6.1 \times 10^{-9} \text{ torr l/sec}$ . Thus for an 0.4 mm thick diaphragm, a diffusion rate of  $1.5 \times 10^{-7} \text{ torr l/sec/cm}^2$  could be expected.

It was found experimentally that the leak rate was of the order of  $10^{-7} \text{ torr l/sec/cm}^2$ , in agreement with the manufacturer's specification. Unfortunately this rate was sufficient to cause gas accumulation in chamber C, and a noticeable leak into the vacuum system (chamber D). The problem was solved by filling chamber B with glycerol to seal the diaphragm surfaces from the air. The extra fluid did not cause a significant error in the pressure relationship, equation 7.5. Care was taken that, for all piston positions, the glycerol in chamber B was not ejected from the chamber B port, since glycerol in the air line would cause electrical breakdown from the source body to the end flange.

A second place where gas diffusion occurred was in the non-metallic sections of the air lines leading to chambers A and B (#33 and #34). Dielectric sections of air line were necessary to isolate the high voltage of the source body from the grounded end flange. After several types of plastic tubing were tried in this application



(polyethylene, polyvinyl chloride, teflon, tygon), the leak rate through the tubing walls was still unacceptably high. The final solution to the problem was to machine teflon tubes with a wall thickness of 8 mm. One end of each tube had an O-ring seal to the end flange; the other end of each tube had a pipe-thread for insertion of a Swagelok fitting. Copper tubes led from the teflon tubes to the two air line ports on the source itself.

### 7.3.2 Pressure Calibration

Piston inertia and friction disrupt the pressure equation 7.5, giving an actual  $P_c - P_b$  curve with hysteresis about the theoretical straight line relationship. Since mechanical effects could vary as a function of piston position over its maximum allowed stroke, the chamber C had to be filled with an incompressible fluid for calibration purposes so that  $P_c$  could be increased and decreased at a fixed position.

Figure 43 shows the calibration scheme. For initial pump down, valves V1, V2, V3, V4, and V5 were open. Then with V1, V2, V4 and V5 closed, air was let in V6 to push glycerol from the reservoir into chamber C of the source. When the chamber was full, valves V1 and V2 were opened and V3 closed, and a balance between the measuring pressure  $P_m$  and the control pressure  $P_b$  was set to give a suitable, stable level of glycerol near the lower end of the capillary tube. After  $P_m$  had been measured with the mercury manometer, valve V1 was closed. Calibration of the source could be achieved by applying a known control pressure  $P_b$ , waiting until the glycerol rose to a stable level in the capillary, and then using Boyle's Law for gases<sup>48</sup> to find  $P_c$  from the fluid level in the capillary. The equation of interest here is



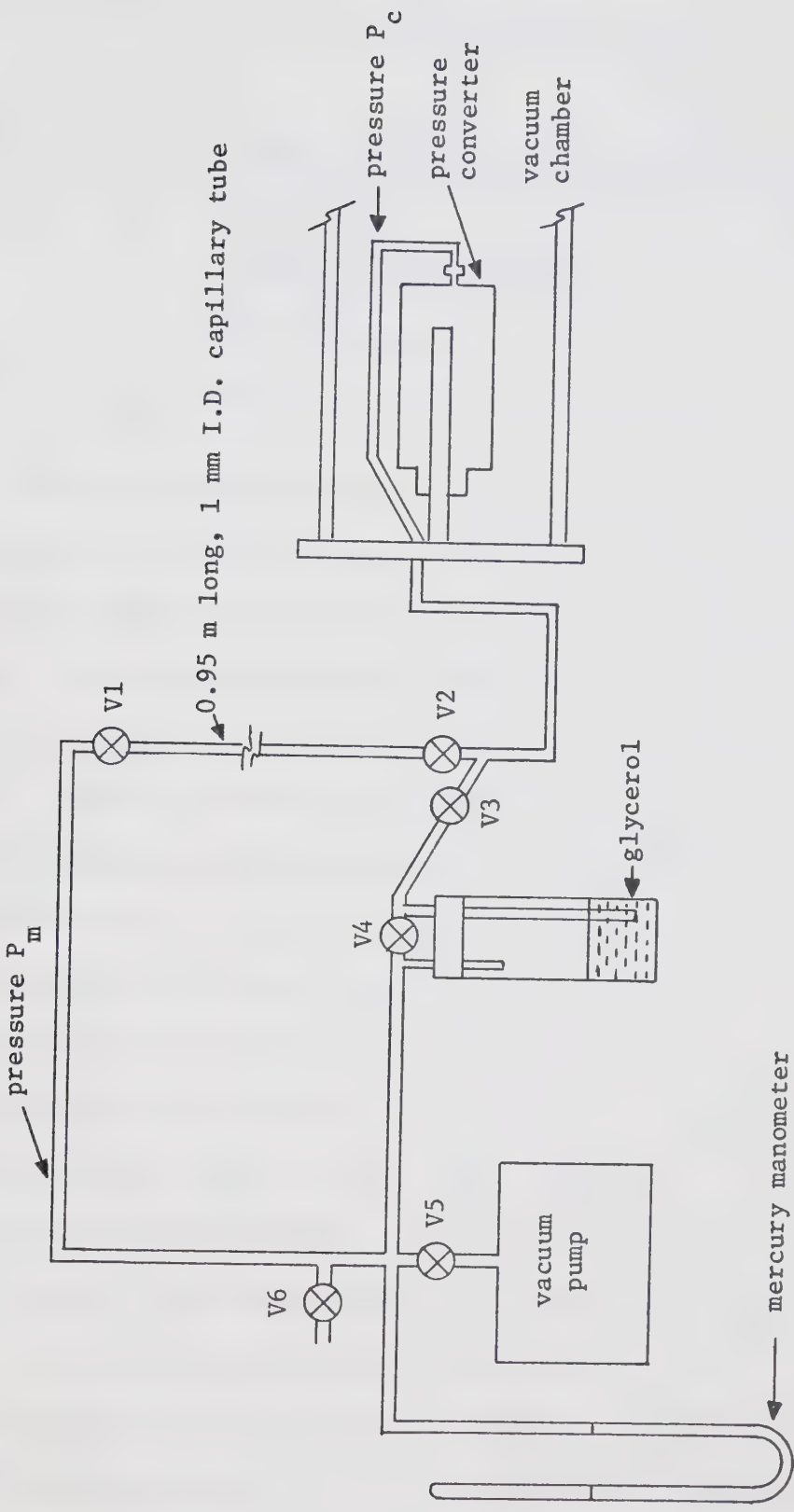


Figure 43: Schematic Diagram of the Pressure Calibration Scheme for the Pressure Converter.



$$P_{cl} = P_m \frac{h_o}{h_1} + \rho(g_1 - g_c) , \quad (8.6)$$

where  $P_{cl}$  = chamber C pressure for gas column height  $h_1$  and glycerol head (above source)  $g_1$ ,

$P_m$  = initial chamber pressure for gas column  $h_o$  and glycerol head  $g_o$ ,

$\rho$  = glycerol density,

and  $g_c$  = height of center line of chamber C.

The use of a capillary of 1 mm inner diameter in the calibration apparatus meant that the volume of glycerol needed to fill this capillary was ejected from chamber C by about 2 mm of piston movement in the source. When 2 mm movement is compared to the total piston travel of 35 mm, the piston travel during a measurement cycle was acceptably small. Therefore the pressure calibration procedure closely resembles actual operating conditions, where the fluid flow rate is very low, and the piston moves very little. Figure 44 shows the calibration curves for four piston positions, given as piston distance from the front plate of the source. Theoretical lines for the pressure relationship are dotted in, as calculated from equation 7.5. Variations in atmospheric pressure result in errors small compared to the experimental uncertainties and hysteresis curve widths, so a standard value of 700 torr was used. (The City of Edmonton is about 675 m above mean sea level, so a standard atmosphere is approximately 700 torr.) Hysteresis curves for one and one-half complete pressure cycles are given. The agreement between the first and third legs of the cycles shows that experimental errors are acceptably small.

Several trends can be observed in the data:



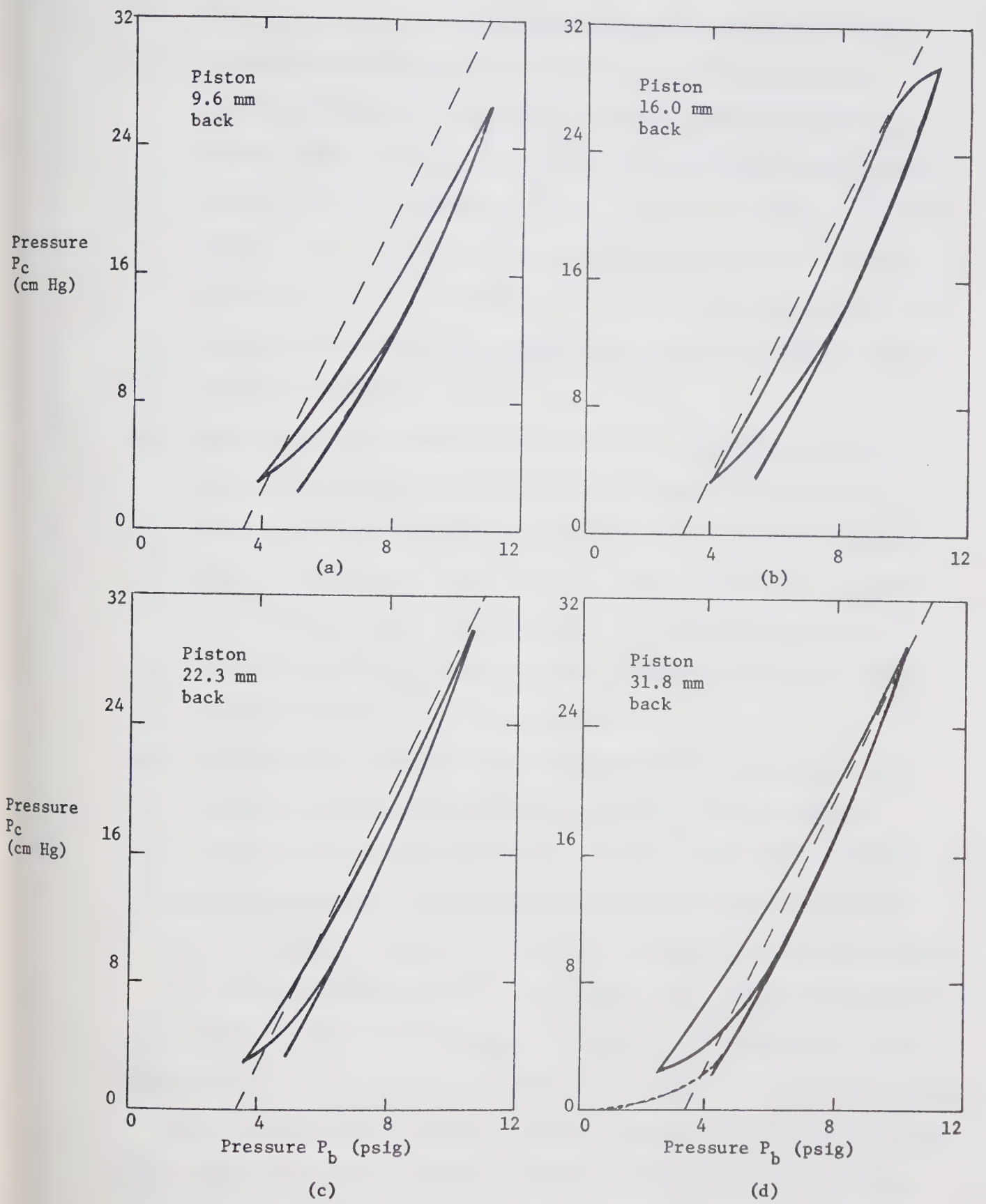


Figure 44: Pressure Converter Calibration Curves for Four Piston Positions.



- (a) When the positions of the hysteresis curves are compared to the positions of the theoretical curves in the four calibration measurement results, a small trend in the relative positions can be seen. Thus, the constant "1 atm" in the pressure relationship between  $P_c$  and  $P_d$  (equation 7.5) is, in fact, dependent on piston position. This dependence can be explained by the fact that the pressure  $P_a = 1 \text{ atm}$  is constant, and there is an additional force on the piston caused by the stretching of the diaphragm as piston position is changed.
- (b) The widths of the hysteresis loops are all comparable, with the exception of one part at the top of the curve in Figure 44b, which indicates a "sticky" spot at that piston position (approximately 16 mm from the front plate). This flaw was also apparent in observations made of piston travel during other experiments. With the exception of this one spot, piston friction is relatively constant as a function of piston travel.
- (c) In Figure 44d, a dashed line is drawn to show the result of an ancillary experiment in which the pressure curve was measured starting from a control pressure  $P_b = 1 \text{ atm}$ . The line indicates how the pressure  $P_c$  varies as the piston moves forward from the fully withdrawn position, and simulates actual operating conditions. For actual source operation it was found that these curves allow good control of the fluid pressure. In practice, the position of the piston during source operation depends on the amount of fluid in chamber C. This position can be deduced from the position of the piston travel limit device. The four calibration curves in Figure 44 are examined, and the one corresponding to the correct piston position is selected.



Then the  $P_b - P_c$  correspondence can be followed as  $P_b$  is varied up and down at the control panel.

An estimate of piston friction can be made from the hysteresis curves. For example, if at a given value of  $P_b$  there is a hysteresis of  $\Delta P_c$ , then

$$\text{friction} = \frac{1}{2} \Delta P_c A_c . \quad (7.7)$$

The factor  $\frac{1}{2}$  arises since  $\Delta P_c$  includes friction for both forward and backward motion.  $A_c$  is the effective area of chamber C piston. From the curves in Figure 44, the friction force in one direction was found to be about 1 nt. This agrees with a value estimated for the pressure converter by Bellofram Corp. engineers<sup>74</sup> to be "less than  $\frac{1}{2}$  lb" or 2.2 nt.

The most severe experimental error in the calibration method used was caused by the viscosity of the fluid. For increasing glycerol column height, the fluid took a long time to achieve a stable level in the capillary. For decreasing column heights, fluid tended to adhere to the capillary walls. The reasonable consistency of the results shows that the errors are not so large as to mask the characteristics of the pressure converter.

### 7.3.3 Fluid Chamber Filling Procedure

Figure 45 shows the schematic of connections required to fill the source with outgassed fluid. The source is mounted on its support flange, without the extractor-capillary tube assembly. A polyethylene tube connects the port on chamber C (where the capillary is normally installed) to the third feedthrough (#32) in the source end flange.



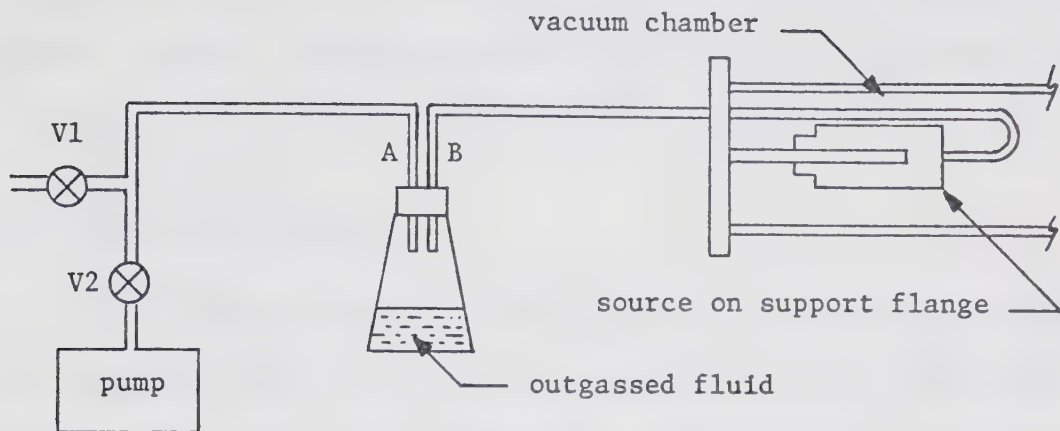


Figure 45: Apparatus Required for Filling the Source Chamber.

The source is then placed in a vacuum chamber, which is evacuated to roughing pressures. The feed tube is connected to one glass tube (B) protruding through a two-holed stopper which fits in the top of an Erlenmeyer flask containing the outgassed fluid. A second glass tube (A) leads to a flexible tube, then to a manifold containing an air inlet valve and pumping line.

After the fluid in the flask has been outgassed on a separate vacuum station, the flask is quickly transferred to the system shown in Figure 45. With valve V1 closed, the tubing is roughed out, with both glass tubes A and B held in the air space above the fluid. This procedure evacuates the entire fluid feed tube and the chamber C. After several hours of pumping, the glass tube B is lowered into the fluid, valve V2 is closed, and valve V1 is opened. The air pressure on top of the fluid pushes fluid into the source reservoir, chamber C. When the chamber is full, the source flange is removed from the vacuum system, the feed tube is removed, the port through the end flange



blanked off, and the capillary and extractor assembly installed on the chamber C port. In order to prevent the glycerol from becoming gassy, the source is kept under vacuum whenever possible.

#### 7.4 Test Bench Results

After the developmental work described in the previous sections was completed, the colloid source was operated in the test bench vacuum system. Since the source was, in this configuration, suspended in the center of the chamber, the pumping speed at the source was very good. Therefore tests on the vacuum requirements of the capillary tip region were not possible. It was found that, if the insulating pieces of lucite supporting the source and extractor were scrupulously clean, the source would sustain a 20 kV capillary potential without sparking and with only a few small electrical discharges, or microdischarges. The pressure conversion system worked satisfactorily, and stable dc beams were successfully produced. Further results obtained with the source in both the test bench and the 300 kV microparticle accelerator are fully reported in Chapter 9.



## CHAPTER 8

### THE 300 KV MICROPARTICLE ACCELERATOR

#### 8.1 Introduction

This chapter discusses the physical layout of the 300 kV accelerator, the electrical and pneumatic control apparatus, and the equipment used during colloid beam experiments. Results and details of the experiments and some of the apparatus used are given in Chapter 9.

#### 8.2 Operational Concepts

Figure 46 shows a side view of the entire accelerator system, while Figure 47 shows a plan view of the laboratory layout. The accelerator can be viewed as three sections, mounted on wheeled carts which travel on a pair of support rails. The first cart (hereafter referred to as the dome cart) carries a grounded corona shield, an insulating support tube, and the high voltage dome. The second support cart, the tube cart, carries the low voltage end of the accelerator tube and a grounded corona shield. The ground plane shown in Figures 46 and 47 is an expanded-metal screen fastened to the laboratory ceiling and provides a safety barrier for the accelerator operators. The third cart, the pump cart, carries the targets, pumping manifold, and part of the pumping system. The turbomolecular vacuum pump stands on the floor beside the pump cart. In experimental use, only the dome cart is ever moved. During experiments, the cart is rolled forward so that the dome surrounds the source chamber, and the dome supports both the source chamber and the high voltage end of the accelerating tube. Simultaneously, the low voltage end of the accelerating tube is supported by



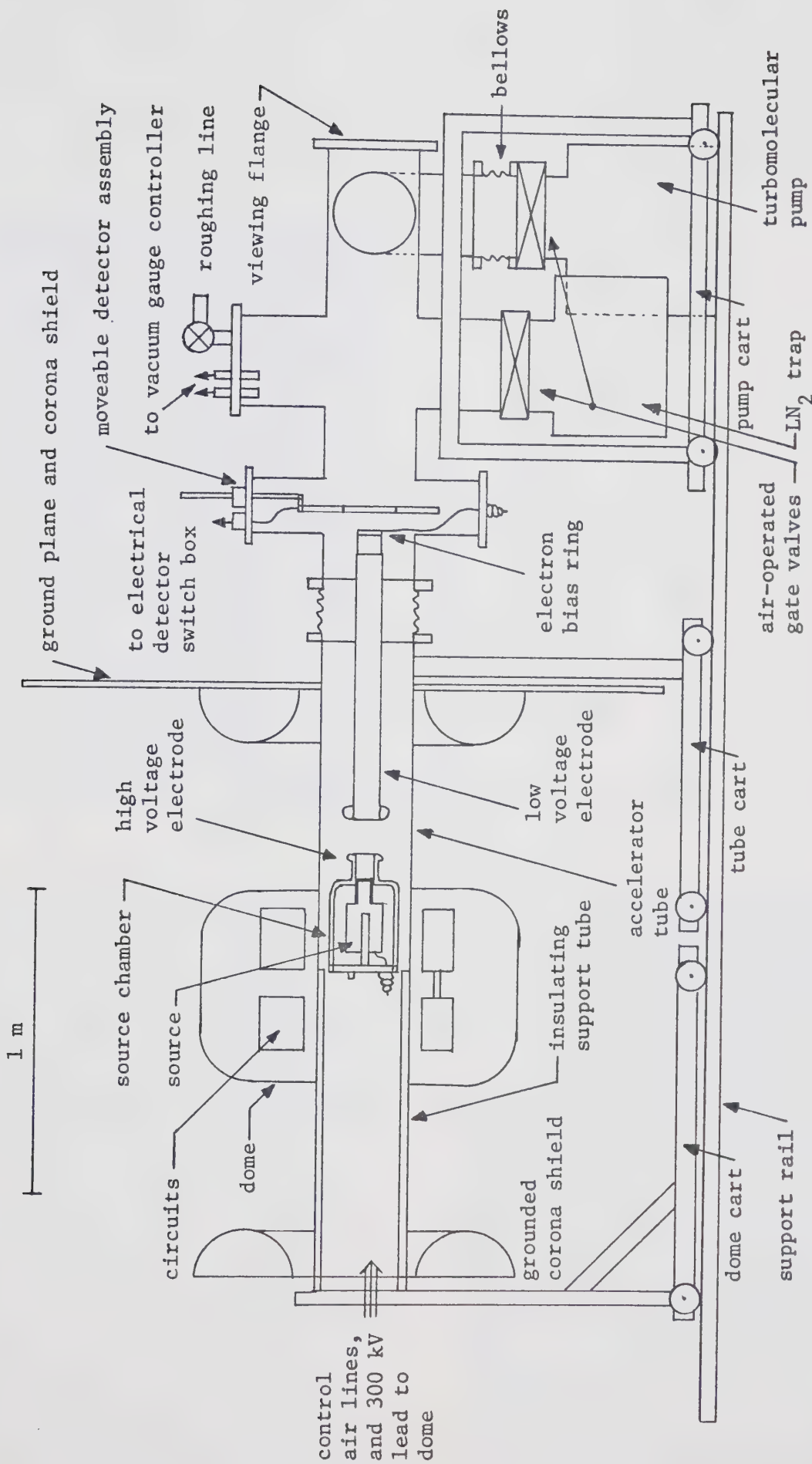


Figure 46: Cross-sectional Schematic View of 300 kV Microparticle Accelerator.



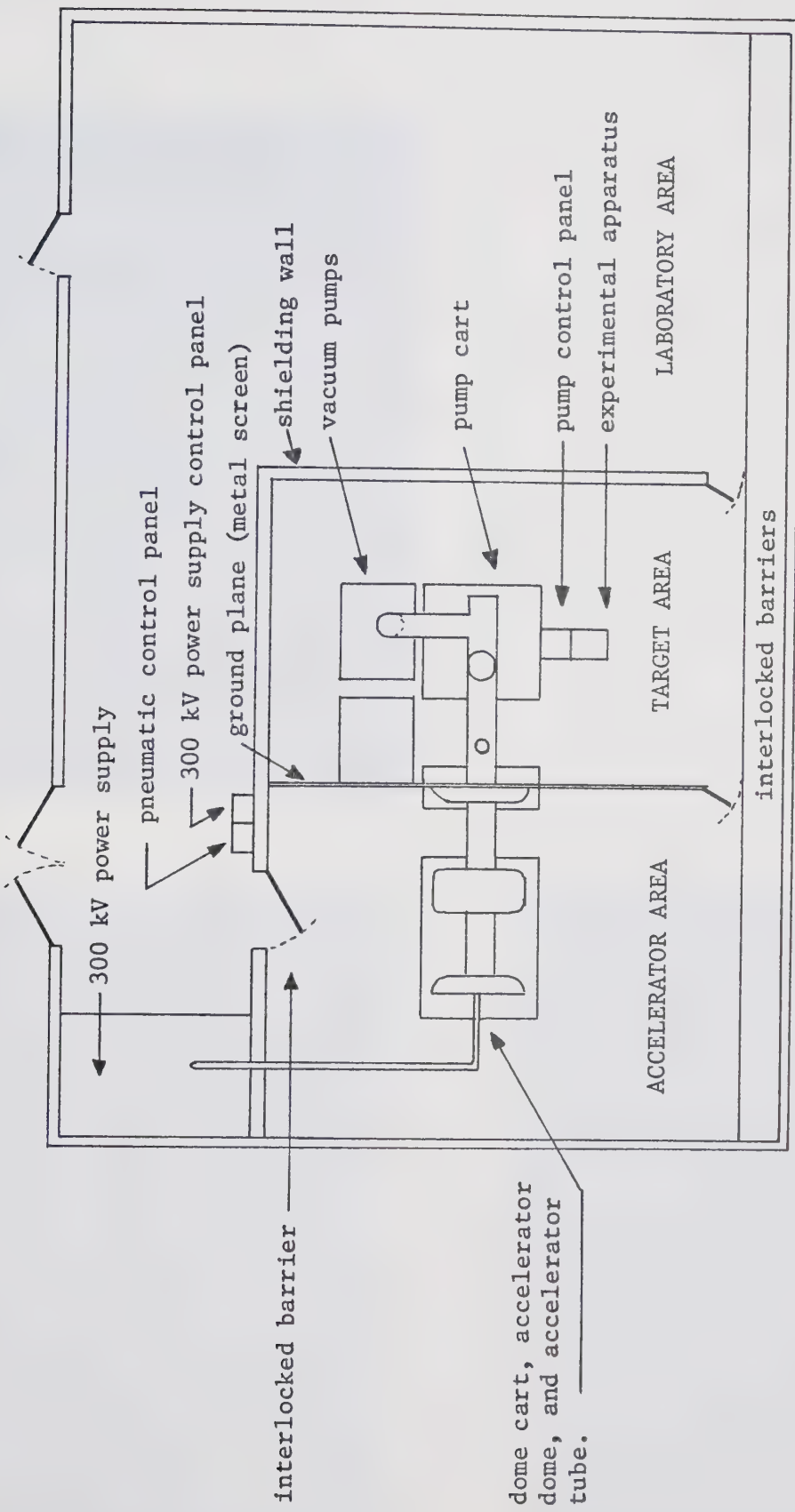
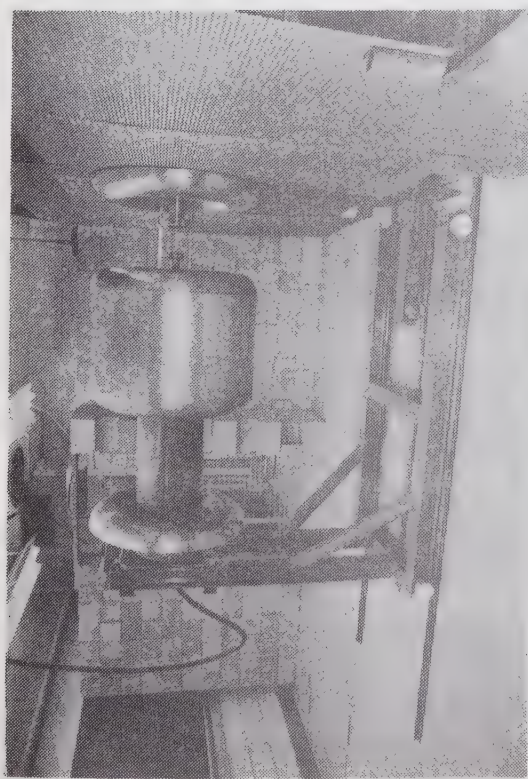


Figure 47: Plan View of the 300 kV Microparticle Accelerator.





(a) Dome Closed, Accelerator Ready  
for Experiments.



(b) Dome Open, and Dome Cart Withdrawn  
from the Source Chamber.



(c) View of Target Area with the Accelerator in  
the Background.

Figure 48: Photographs of the 300 kV Accelerator.



the tube cart. This configuration is shown in Figure 46 and in the photograph of the accelerator in Figure 48a. Access to the apparatus in the source chamber is gained by supporting the high voltage end of the accelerating tube from the tube cart by means of two removable stands, and rolling the dome cart away from the source chamber. This configuration is shown in the photograph in Figure 48b.

The high voltage dome is sheet aluminum formed into an annular cylindrical shape, 0.85 m in outer diameter, 0.29 m in inner diameter, and 0.71 m long. The outer surface of the annulus opens to provide access to the apparatus contained within it (see Figure 48b). The dome is supported from the dome cart by a horizontal "tufnol" (fibre reinforced plastic) tube, with a 0.54 m distance between the dome and the grounded corona shield.

Various control schemes for the equipment contained in the dome (Sections 8.4 and 8.5) enter and leave the dome through the axial hole in the hollow support tube.

The source of particles is placed in the source chamber adjacent to the high voltage electrode, and is controlled remotely. The source chamber is evacuated by the main accelerator pumps. Particles created in the source cross the accelerating gap between the electrodes, then drift towards the target region. The width of the accelerator gap can be adjusted by axially moving the low voltage electrode.

For safe operation of the accelerator, the operators must be protected from both the high voltages and possible X-ray radiation fields present. Thus the entire accelerator is surrounded by a concrete shielding wall. In addition, the target area is separated from the accelerator area by a grounded expanded-metal screen. Gates into the



accelerator and target areas are interlocked to the 300 kV power supply to prevent access to the accelerator during experiments.

The targets for the accelerated beam are contained in a four inch by six inch diameter glass cross. The targets are of the type used for detection of the colloid beams in the test bench experiments, and are discussed in Section 8.6. In addition, an electrode is installed just in front of the targets for secondary particle experiments (Section 9.6.1).

Prior to the present work, the operational concepts of the accelerator had been established and tested. At that time, the accelerator components consisted of: the entire dome cart and dome, the air driven motor, generator, and 20 kV voltage supply in the dome, the accelerating tube and electrodes, the pump cart, part of the pumping system, the shielding wall, and the ground plane separating the accelerator and target areas. In addition, construction had begun on the tube cart and target chamber system discussed here.

Much work was performed on the accelerator prior to the colloid beam experiments. The following is a list of some of the changes required, where the term modification applies to changes made either to make the original system easier to use, or to allow installation of the colloid source experiments:

- (a) Installation of new support rails for the entire accelerator,
- (b) Modification and installation of the new tube cart and accelerator tube support system,
- (c) Modification of the existing dome cart,
- (d) Modification of the pump cart, and installation of the target chamber,



- (e) Design and installation of the pumping manifold and installation of the turbomolecular pump,
- (f) Increasing the power capacity of the air motor and generator by improving air flow to the motor,
- (g) Design, construction, and installation of all the electronic circuits in the dome,
- (h) Modifications to the source chamber,
- (i) Installation of the colloid source and detector system,
- (j) Installation of the compressed air control system for the dome circuitry and colloid source.

### 8.3 Vacuum System

Initial attempts to adequately pump the accelerator using the existing pumping system were unsuccessful. The pumping system at that time consisted of a carbon vane roughing pump, zeolite sorption pumps, a 100 l/sec ion pump, and a 500 l/sec titanium sublimation pump with a liquid nitrogen cooled shroud. Successful experiments were carried out after the pumping system was changed to a carbon vane roughing pump, 260 l/sec turbomolecular pump, and a liquid nitrogen cooled trap. Because the experience obtained with these two pumping systems is relevant to any accelerator using a colloid source, the results of the pumping system experiments are fully reported in Chapter 9, rather than in this chapter.

System pressures were measured by either a Varian model 971-5009 millitorr gauge (1 to  $10^{-5}$  torr), or a model 971-5004 nude ion gauge ( $<10^{-3}$  torr). Both gauges were connected to a Varian model 971-1008 control unit. The gauge heads were mounted on a flange at the top of



the pumping manifold.

The two six-inch gate valves were solenoid controlled and compressed air operated. If a power failure occurred, a power contactor in the laboratory would open, and the valves would close. The open contactor ensured that the valves remained closed and the pumps remained off when power was restored.

The two accelerating electrodes in the accelerator tube were designed so that gas could flow from the source chamber to the vacuum pumps both through the center of, and around, the cylindrical electrodes. While the distance from the source to the pumps, and the various pumping impedances between the source and the pumps, meant that a very low pumping speed was available at the source chamber, careful design of the colloid source allowed successful production of colloid beams. Due to restrictions imposed on the accelerator geometry by the presence of high voltages on the accelerator dome, little improvement in pumping system design and layout can be achieved. Changes to accelerator electrode and detector geometries, and the use of larger vacuum pumps, would give better source operation and shorter pumping times.

#### 8.4 Electronic Design of the Dome Circuitry

##### 8.4.1 Introduction

Operation of the particle source inside the floating high voltage dome was constrained by the fact that there could be no direct electrical access to the interior of the dome. This means that the source had to be remotely controlled by non-electrical means, and power to drive the source had to be generated within the dome itself.



The accelerator (as it existed prior to the present work) utilized compressed air for communication between the dome and the laboratory control panel. For power generation within the dome, compressed air drove an air motor mechanically coupled to a generator, which was regulated to 20 V output by a field current regulator. A high voltage supply produced 20 kV from the 20 V source. An air driven mechanical switch in series with the 20 kV output turned the voltage on and off. The high voltage was monitored by a meter illuminated by a lamp for external viewing. This relatively simple system allowed adequate control and operating of solid charged particle experiments.

Since this operational design had proved successful, it was adopted for the present experiments. However, due to the much more complicated control functions required in the present work, the entire system was rebuilt and expanded. The following sections describe the new system. The system as evolved here is very versatile, and could be used without modification for solid charged particle experiments as well.

#### 8.4.2 General Description of the Circuit Blocks

In this section, the functions of the various modules are described while the modules themselves are described in Section 8.4.3. Circuit operation techniques are given in Section 9.1. Figure 49 is a block diagram of the entire dome electrical scheme. Control of the circuits is achieved by applying compressed air signals to "air switches" contained in the dome. The air switches convert the pressure changes into electrical contact closures.

The air supply to the motor and generator is controlled by a solenoid valve at laboratory ground potential. The 3/8 inch diameter air



line enters the dome through the hollow support tube. The generator field is connected in series with a switching regulator set to give a generator output of 26 V. The ripple on the 26 V output is filtered by the 1 mh choke and 15,000  $\mu$ f capacitor, to a value of about 0.5 V peak to peak. This basic 26 V supply drives the remaining power supplies, all logic circuits, and the filament of the high voltage switching tube.

Total power consumption in the dome is about 200 W. Cooling is not a problem because of the large volume of compressed air vented in the dome through the air motor.

The high voltage supply for the colloid source is an oscillator, transformer, and rectifier circuit having a dc to dc voltage gain of about 1000. The output is filtered by an additional external capacitor of 2 nf, and is monitored by a meter in parallel with the high voltage switch. The supply is driven by a variable dc regulator to permit variation of the capillary voltage in the source, and to reduce high voltage fluctuations. This regulator is varied by means of a nylon filament and pulley arrangement running down the dome support tube to laboratory ground potential. The dc regulator has a remote shut-down control using air switch SW3.

The capillary tube in the colloid source is at the potential of this high voltage supply, while the source extractor is at dome ground potential.

The capillary voltage switch chosen for the accelerator is a high voltage tetrode rather than a thyratron as used in the test bench apparatus. The main reason for the change is that the tetrode consumes only 60 W of power, whereas the thyratron used about 200 W. Control signals for the tetrode grid originate in the pulse circuit. In the



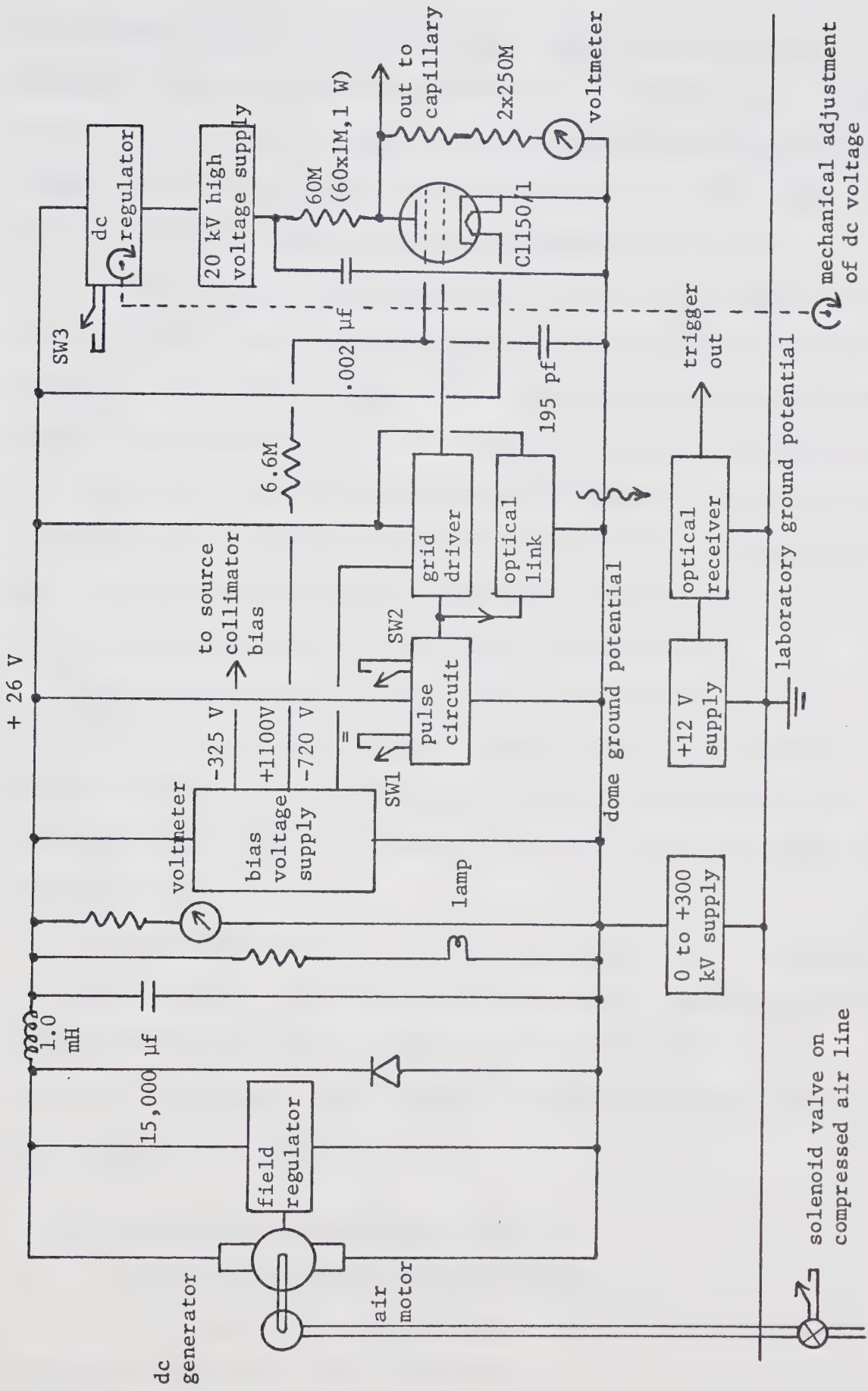


Figure 49: Schematic Diagram of the High Voltage Dome Circuitry.



pulse circuit, air switch SW1 initiates a single pulse, while air switch SW2 causes an output level shift when it changes state. The 26 V output pulses then drive a solid state grid driver which delivers level changes of -720 to +26 V directly to the control grid of the tube. The two air switches are controlled from the remote control panel.

For time of flight measurements, air switch SW1 is activated to pulse the source high voltage to ground for 7 msec. A pulse to synchronize the high voltage pulse to the oscilloscope recording the beam current from the detector is derived from the output of the pulse circuit. The pulse drives a light emitting diode whose output is fed down a "light-pipe" to a receiving photo-diode at laboratory ground potential. The pulse from the photo-diode is then used to trigger the recording oscilloscope during time of flight measurements.

Operation of the dome is monitored by two voltmeters connected to the circuitry; one of these monitors the 26 V supply, and the other monitors the high voltage at the tetrode anode. The meters are illuminated by a lamp and can be viewed by looking along the center of the dome support tube.

It must be emphasized that there are two main areas of reference for circuit voltages. All electrical signals within the dome are referenced to the potential of the dome, hereafter referred to as the "dome ground potential". The potential of the dome itself is relative to the "laboratory ground potential".

#### 8.4.3 Discussion of Individual Circuits

##### 8.4.3.1 26 V Generator and Regulator

This circuit is shown in Figure 50. The supply of compressed air to the air motor is turned on and off by a solenoid valve



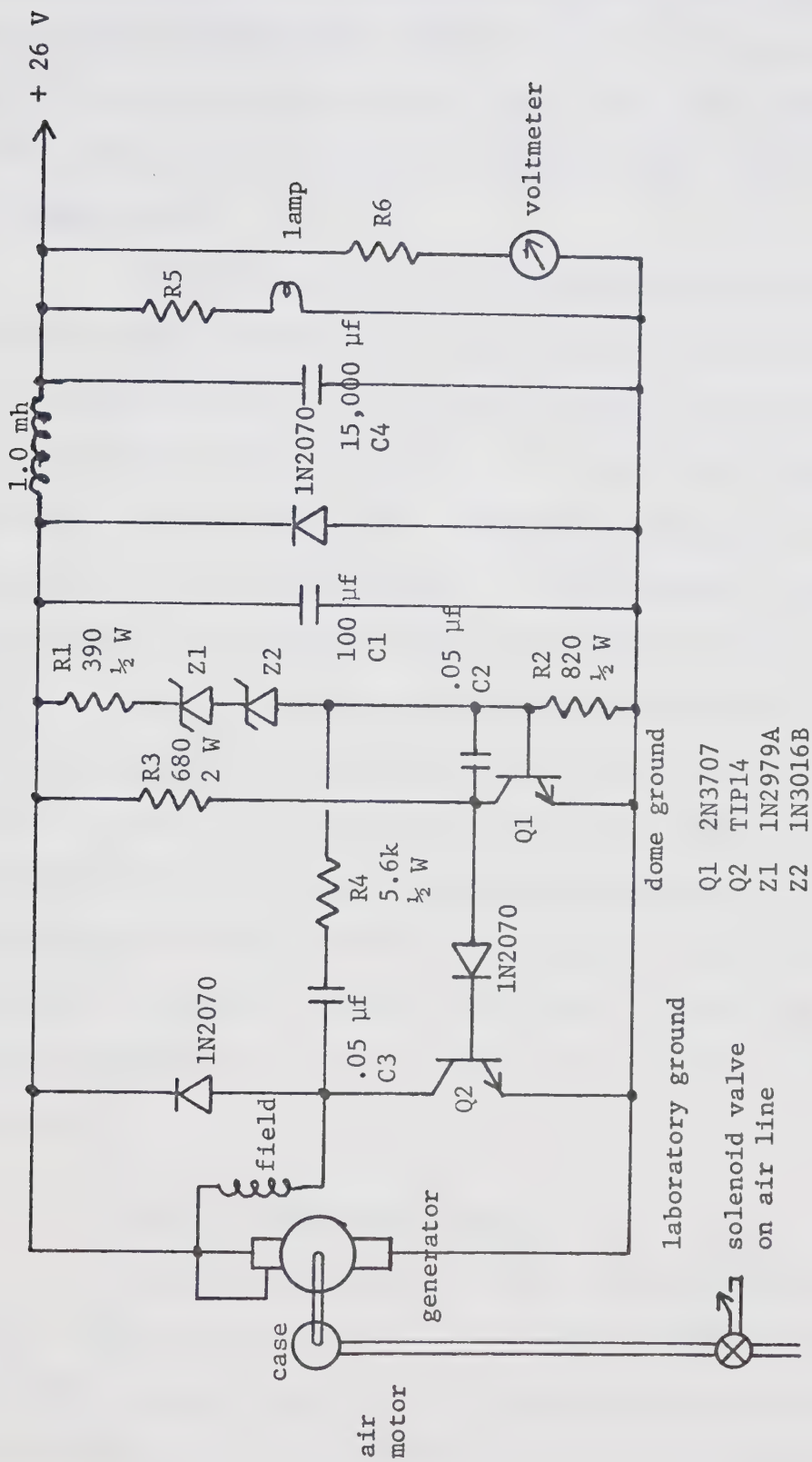


Figure 50: Circuit Diagram of the Field Regulator.



at laboratory ground. In the dome the air flow drives a one h.p. air motor, which is mechanically coupled to the 24 V, 25 A generator. The generator will produce up to 8 A at 26 V. The current limit is a result of the limited air flow available to the air motor, but is sufficient for present needs.

The field regulator is a switching type, whereby the entire generator output voltage is across the field, or none at all. The voltage across the string R1, Z1, Z2, and R2 turns on Q1 when it reaches 28 V. Q1 in turn cuts off the base drive to Q2, hence the field current decreases. The generator output voltage drops until Q1 is turned off, Q2 turned on, and the field current is re-established. Included in Figure 50 are some additional components. The 1 mh choke and 15,000  $\mu$ f capacitor filter the generator output. At the input side of this filter, ripple is typically 3V peak to peak, at about 500 Hz. When the output current is about 5 A, the output ripple is 0.5 V peak to peak. The diode protects the regulator from transients generated in the inductor. The lamp and its current limiting resistor R5 illuminate the voltmeters in the dome for external viewing. The output voltage of the regulated generator is monitored by the voltmeter in series with the calibration resistor R6.

#### 8.4.3.2 Bias Voltage Supply

This circuit is shown in Figure 51. The supply is rated at +900 V at 100 mA, and -650 V at 100 mA. Open circuit voltages are +1100 V and -720 V respectively. The -720 V rail has a voltage divider across it to provide -360 V at low current for the particle source electron retarding ring.



The transistors Q1 and Q2, together with the special order Hammond Manufacturing Co. transformer (type number 99141), make a switching oscillator running at about 700 Hz. The two completely separate output winding waveforms are bridge rectified to give the output voltages. The circuit is typical of those given in Hammond catalogues<sup>75</sup>. The +1100 V supply is filtered by C3, a 0.5  $\mu$ f, 3 kV capacitor, while the -720 V supply is filtered by C4 and C5 in series, a total of 10  $\mu$ f. Resistors R5 and R8 bleed off the filter capacitor charges when the supply is turned off. Resistors R6 and R7 make the -360 V voltage divider. Open circuit ripple voltages are 2 V peak to peak and 1 V peak to peak for the +1100 V and -720 V supplies respectively.

The circuit depends on an initial current surge in the transformer to start the oscillations. It was found that, when the generator was started, the 26 V output was established at a rate too slow to start the oscillation. Therefore, a time delay relay RE1, having a delay of 1 minute, is used to allow the voltage from the 26 V generator to stabilize before this voltage is applied suddenly to the oscillator circuit.

#### 8.4.3.3 Pulse Circuit

This circuit converts contact closure from the two air switches into either a 7 msec wide pulse, or a level shift, depending on which switch is activated. The output is normally +26 V and the output signals switch to dome ground, as shown in Figure 52.

Transistors Q1 and Q2 comprise a flip-flop. This buffers the contact closure of the air switch SW1, and ensures that an output



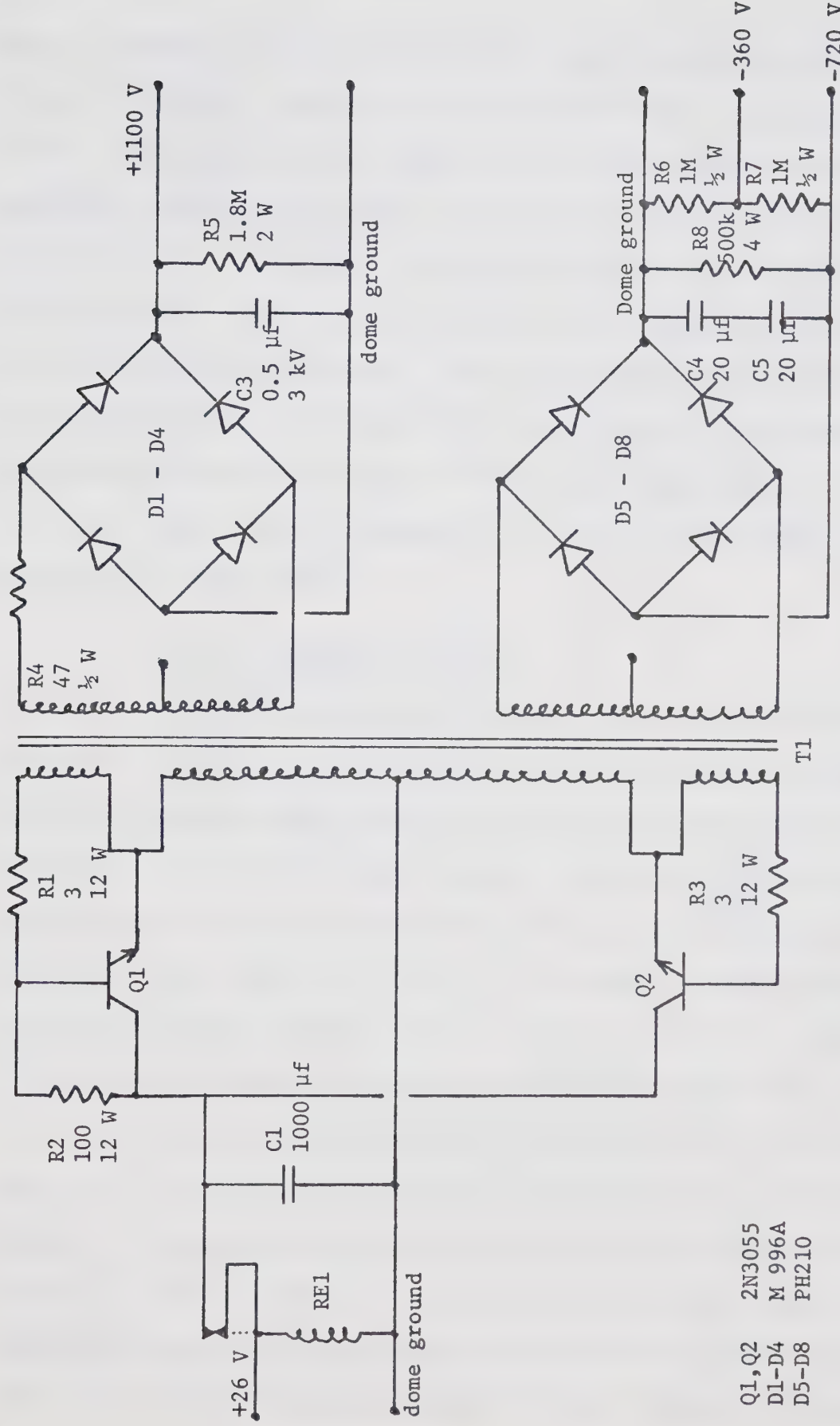


Figure 51: Circuit Diagram of the Bias Power Supply.



pulse is produced if and only if the air switch SW1 contact goes from "reset" to "pulse". Transistors Q3, Q4, and Q5 form a monostable multivibrator with period 7 msec. Transistor Q6 inverts the pulse for compatibility with other circuitry. Q6 can also be turned on by closing air switch SW2. This produces an output level shift for as long as the switch is closed. Test pulses to initiate output pulses can be applied to the monostable multivibrator. With the exception of the diode in the test input lead, all diodes in the circuit protect the transistors from transients generated elsewhere in the accelerator dome.

Output pulse risetimes are less than 0.5  $\mu$ sec, and pulse falltimes are about 1  $\mu$ sec.

#### 8.4.3.4 Grid Driver Circuit

The idea for the circuit to drive the grid of the C1150/1 tetrode was found in papers by Hansen<sup>76</sup>, and Friichtenicht and Hansen<sup>77</sup>. The circuit has been modified to use less expensive transistors, to be dc coupled, and to handle higher voltages. The circuit, which is shown in Figure 53, is "off" (transistors cut off and output voltage of -720 V) when the input is at +26 V, and "on" (transistors saturated and output voltage of +25 V) when the input is less than +25 V. The output of the circuit is connected directly to the control grid of the tetrode.

Resistors R1 through R7 bias the transistors to each withstand 1/6 of the total applied voltage, which can be up to 900 V total. Resistors R8 through R13 are calculated to limit the transistor base currents to 1 mA each, when the transistors are saturated. The load resistor R15 limits collector current to 10 mA when the transistors are conducting. Circuit risetimes are about 3.5  $\mu$ sec, while falltimes are



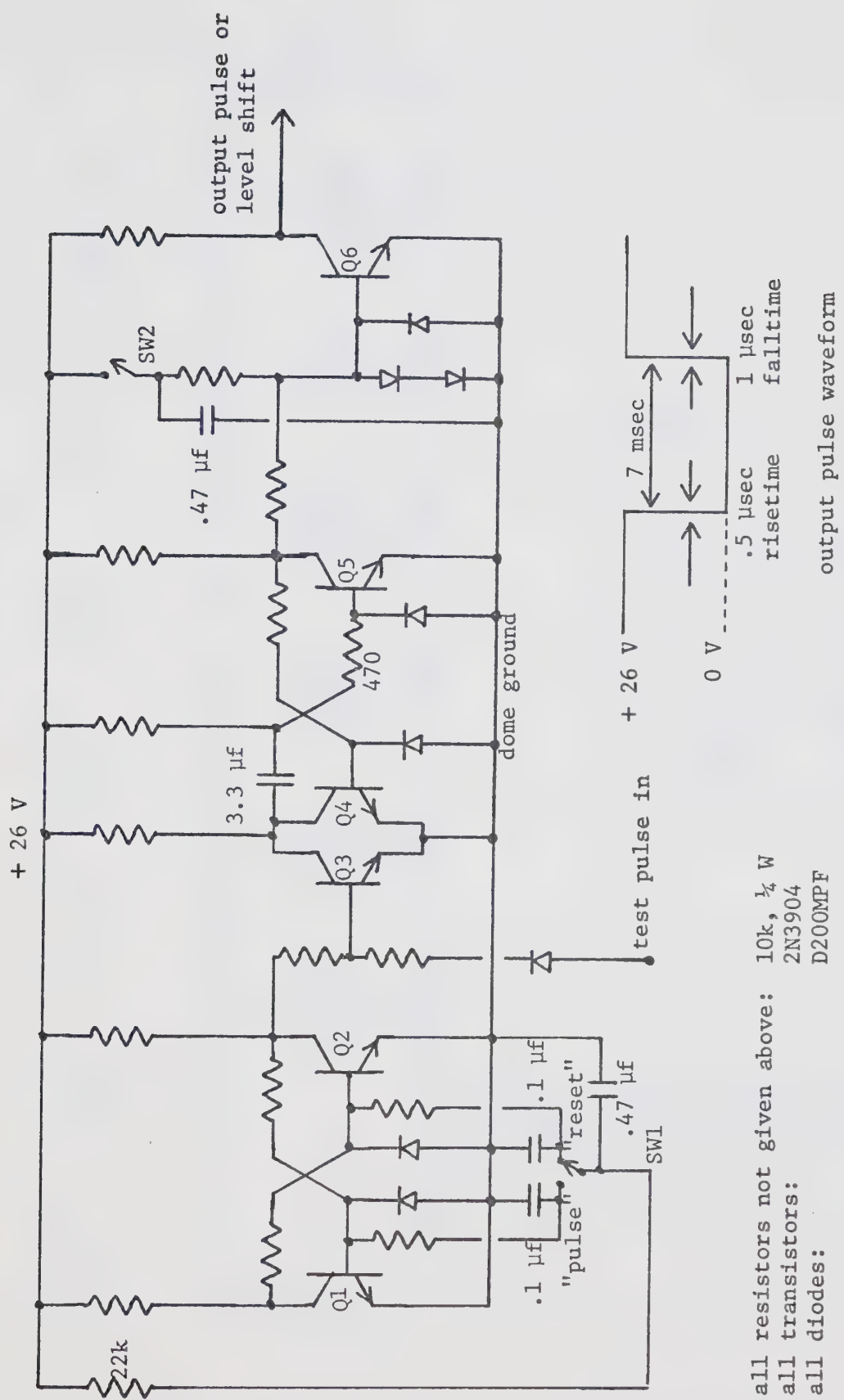


Figure 52: Circuit Diagram of the Pulse Circuit



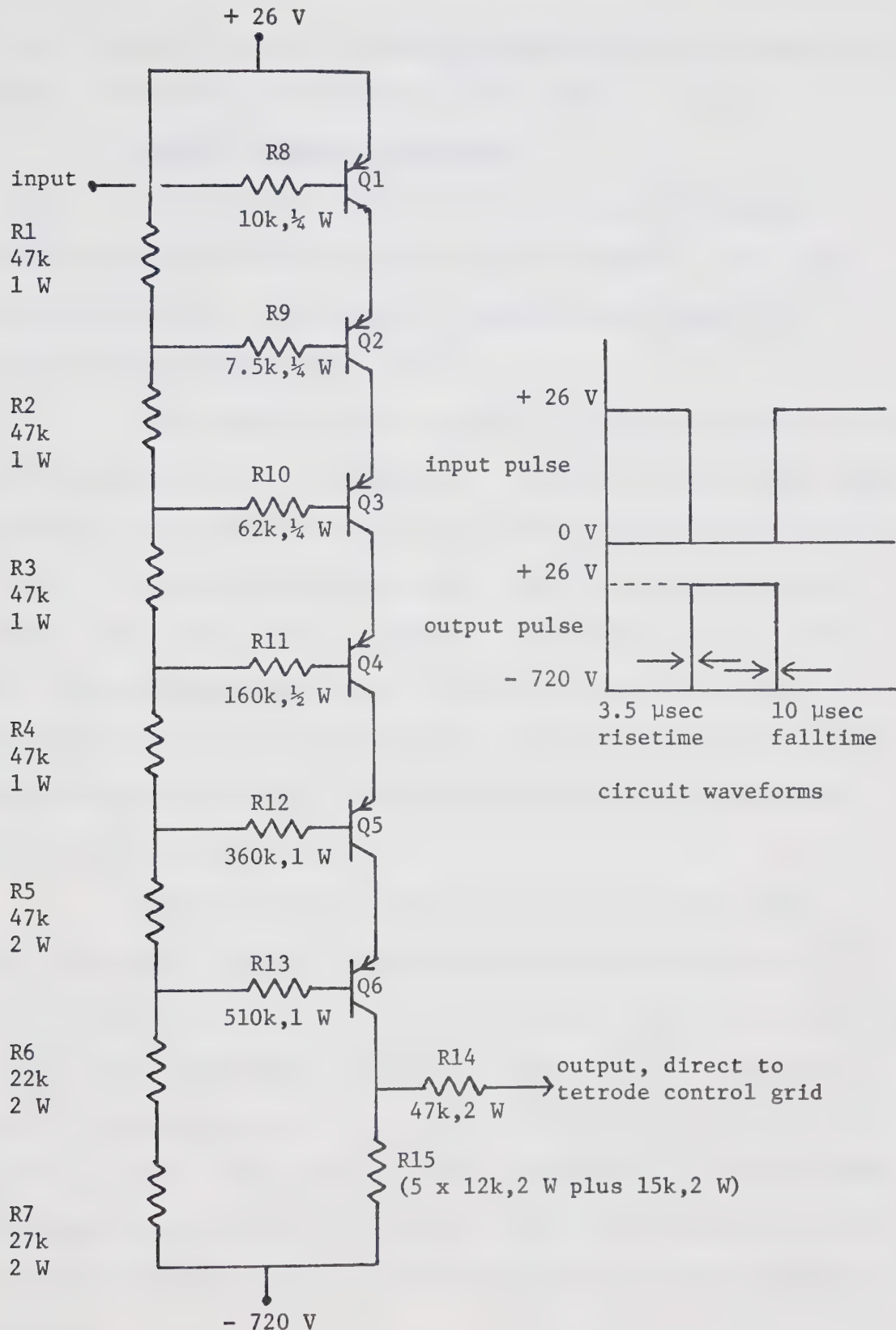


Figure 53: Circuit Diagram of the Tetrode Grid Driver.



10  $\mu$ sec. These values are acceptable because they are the same duration as, or less than, the tetrode response time.

#### 8.4.3.5 Variable dc Regulator

This circuit, which is shown in Figure 54, uses the Motorola integrated circuit voltage regulator MC1461R, with a series pass transistor, Q1. It is typical of applications given in the Motorola Microelectronics Data Book<sup>78</sup>.

The regulated output voltage can be varied from about 4.5 V to 22 V using the variable resistor R4. Resistor R7 with diode D1 gives an output current protection limit of 2.5 A. The input supply must be at least 24 V for the regulating zener diode Z1 to be properly conducting. The remote shut-down control is connected to an air switch, SW3. The regulated output falls to zero volts as long as the air switch wiper is connected to a positive voltage. The diodes D2 to D4 and the resistor R6 protect the integrated circuit from transients induced on the air switch leads.

When the circuit is mounted in the accelerator dome, a pulley and nylon filament arrangement between the potentiometer R4 and the laboratory ground end of the dome support tube allows variation of the output voltage when the dome has been closed up. For safety reasons the voltage can be varied only when the dome is at laboratory ground potential. The method of voltage variation is invaluable when the colloid source is being started up, since high voltage adjustments are usually required before the colloid source will produce dc beam currents.



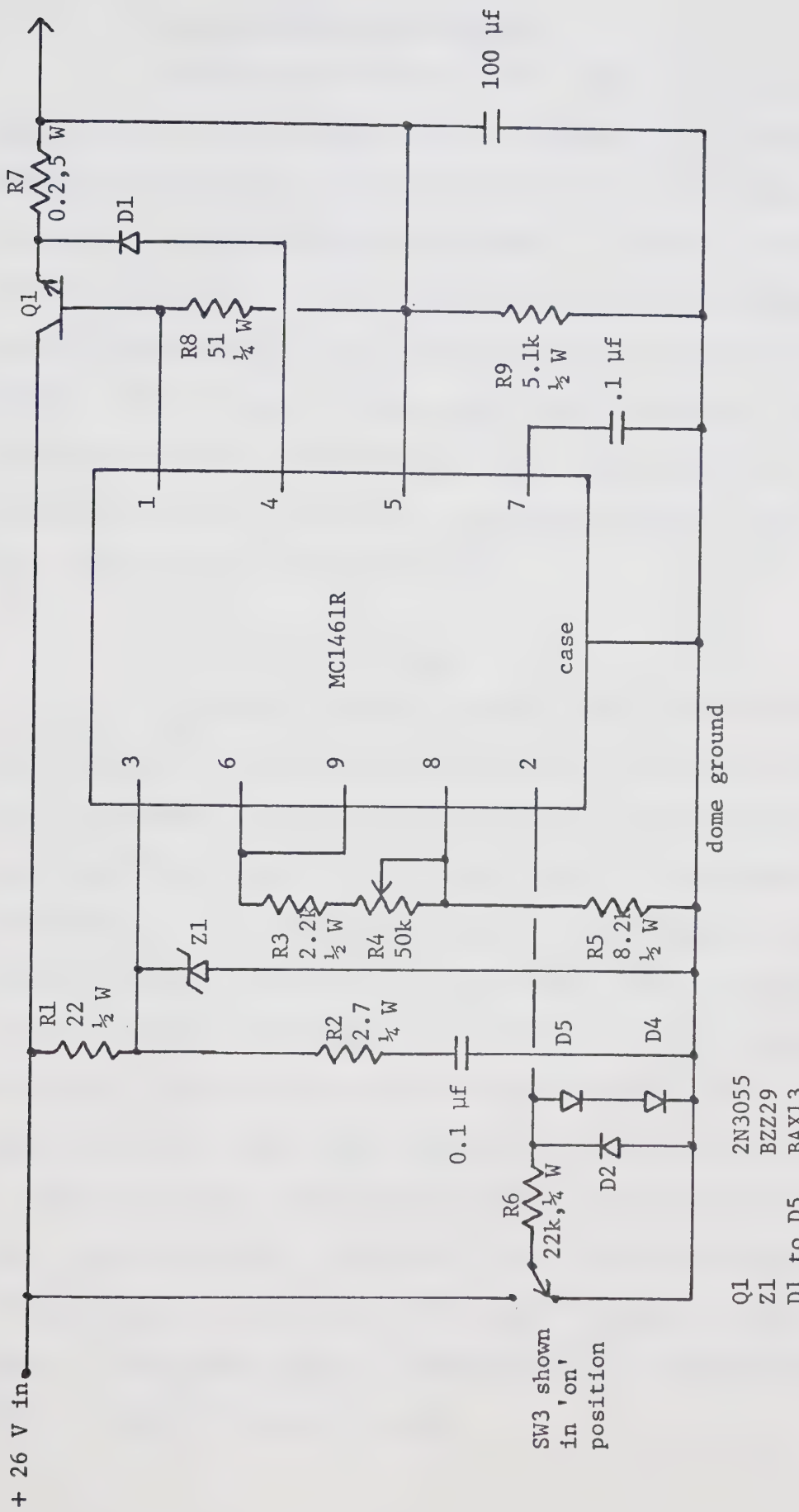


Figure 54: Circuit Diagram for Variable dc Regulator.



#### 8.4.3.6 High Voltage Supply

The oscillator in this circuit (Figure 55) uses a single transistor, Q1, and a Spellman TRF-10 transformer. The circuit is patterned after the circuit diagram for the Spellman High Voltage Electronics Corp. model UHM-20P10D power supply<sup>79</sup>. Output dc voltage is directly proportional to the applied dc voltage, with a voltage gain factor of approximately 1000. Output current is specified as 0.5 mA maximum, while the output voltage must be less than 20 kV. Use of an oscillator frequency of 500 kHz means that output ripple can be very effectively filtered. With the 2 nf external capacitor (C7), ripple is about 1 V peak to peak at 20 kV output.

#### 8.4.3.7 Tetrode Circuit

The English Electric Valve Co. C1150/1 tetrode shown in Figure 56 operates as a high voltage switch driven by the circuits already discussed. The anode resistance R4 is chosen so that the maximum current drawn from the high voltage supply is less than 0.5 mA. Resistors R1 to R3 prevent the screen grid from drawing excessive current when the tube is held "on", or saturated. The tube filament runs directly from the dc generator, and draws 2.1 A at 26 V. When driven by the pulse and grid drive circuits previously described, the pulse risetime is about 2  $\mu$ sec. while the slow falltime of about 10 msec is caused by the large anode resistor current limiting the charging rate of the total output capacitance, which is made up of tube, wiring, and colloid source capacitance. The circuit waveform is also shown in Figure 56. Switching times were adequate for the present work, so no effort to improve them was necessary.



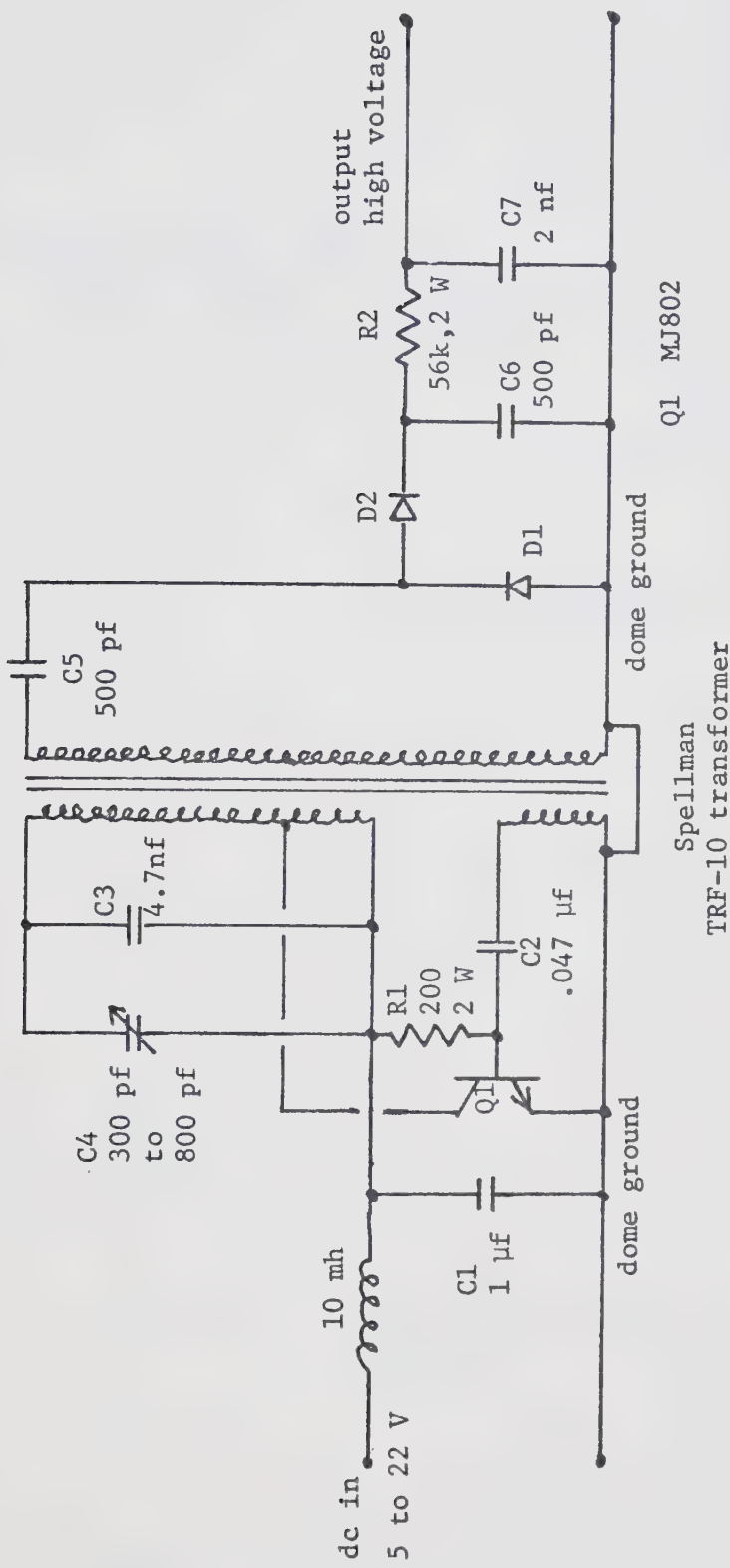


Figure 55: Circuit Diagram of the High Voltage Supply.



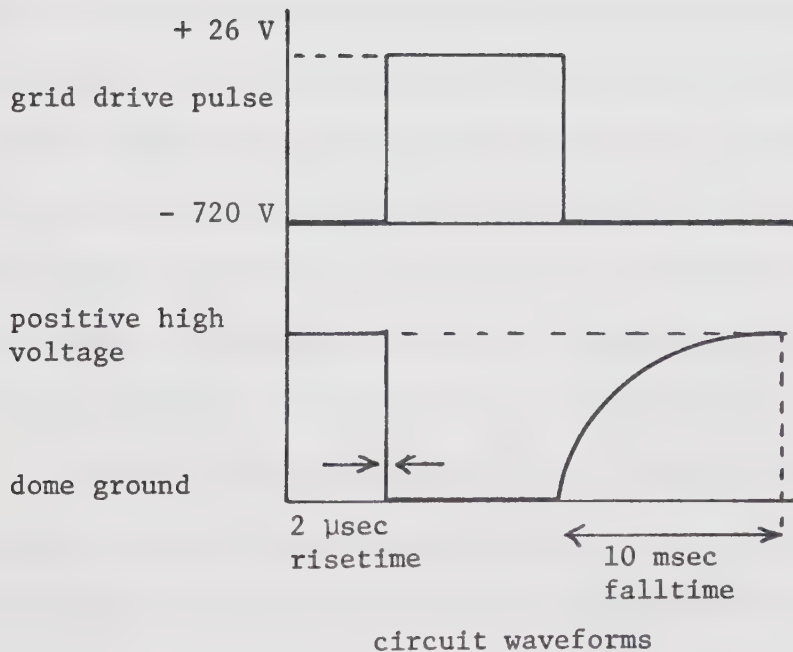
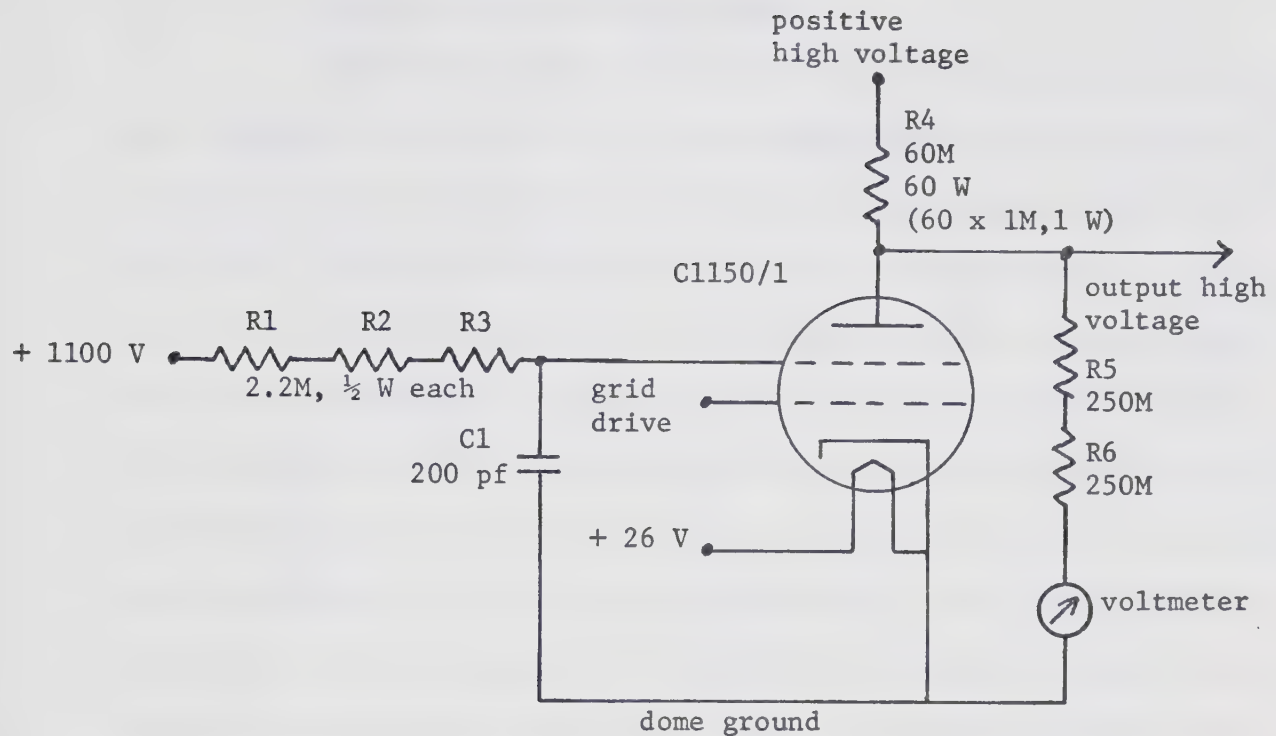


Figure 56: Circuit Diagram of the Tetrode Circuit.



#### 8.4.3.8 Optical Link Circuit

One basic property required of the electronic circuitry was a facility to permit time of flight experiments on the colloid source both with and without an accelerating potential on the accelerator dome. Clearly a method was required for synchronizing the truncation of the beam (by operation of the tetrode on the capillary potential) and the storage oscilloscope recording the beam current decay curve at the detector. The timing was accomplished by transmitting a synchronizing pulse from the dome to the laboratory by means of a light pulse travelling in a fibre optics "light-pipe". The transmitter and receiver circuits making up the light link are shown in Figure 57, together with the optical link output pulse and the corresponding high voltage pulse at the colloid source capillary tube.

In the transmitter, the output signal (pulse or level shift) from the pulse circuit drives an RCA 40736R light emitting diode. The diode light output is coupled into an American Optical Co. LGM-3X36 fibre optics "light-pipe", which is 36 inches long. While the transmitter is in the dome, at dome ground potential, the receiver is at laboratory ground potential. The optical signal from the light pipe triggers the EG & G SGD-100A photodiode. Transistors Q2 and Q3 amplify the signal and give out a pulse or level shift.

There is a delay of about 2  $\mu$ sec between the input electrical pulse and the output electrical pulse. However, the comparison between the output pulse and the corresponding high voltage pulse in the dome is quite favorable. As shown in Figure 57, the leading edge of the trigger output pulse precedes the high voltage pulse by about 5  $\mu$ sec. This delay is negligible in comparison to the expected time



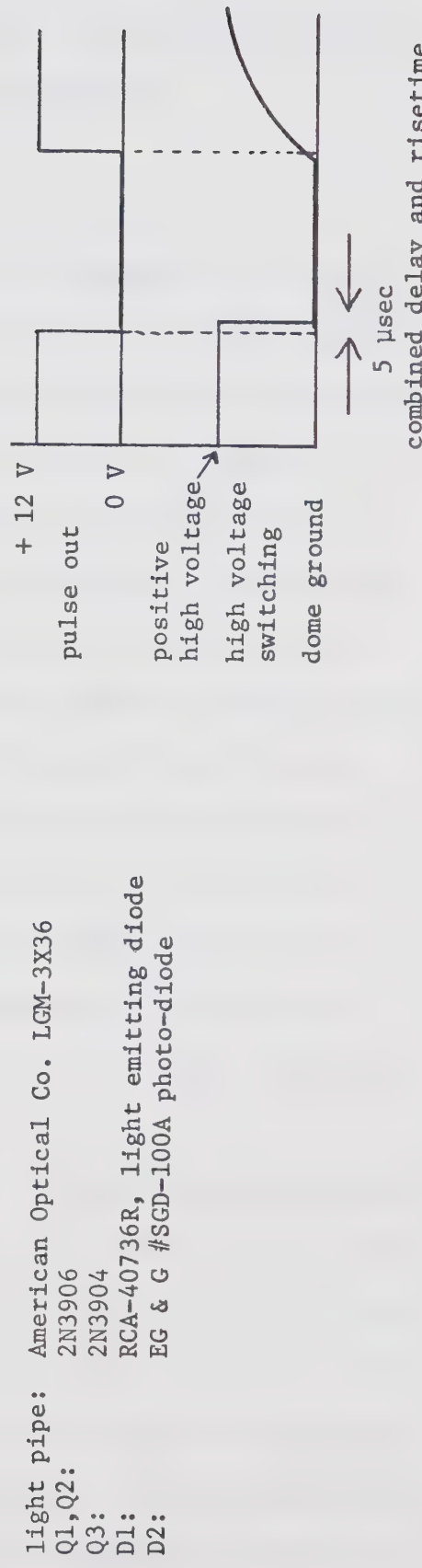
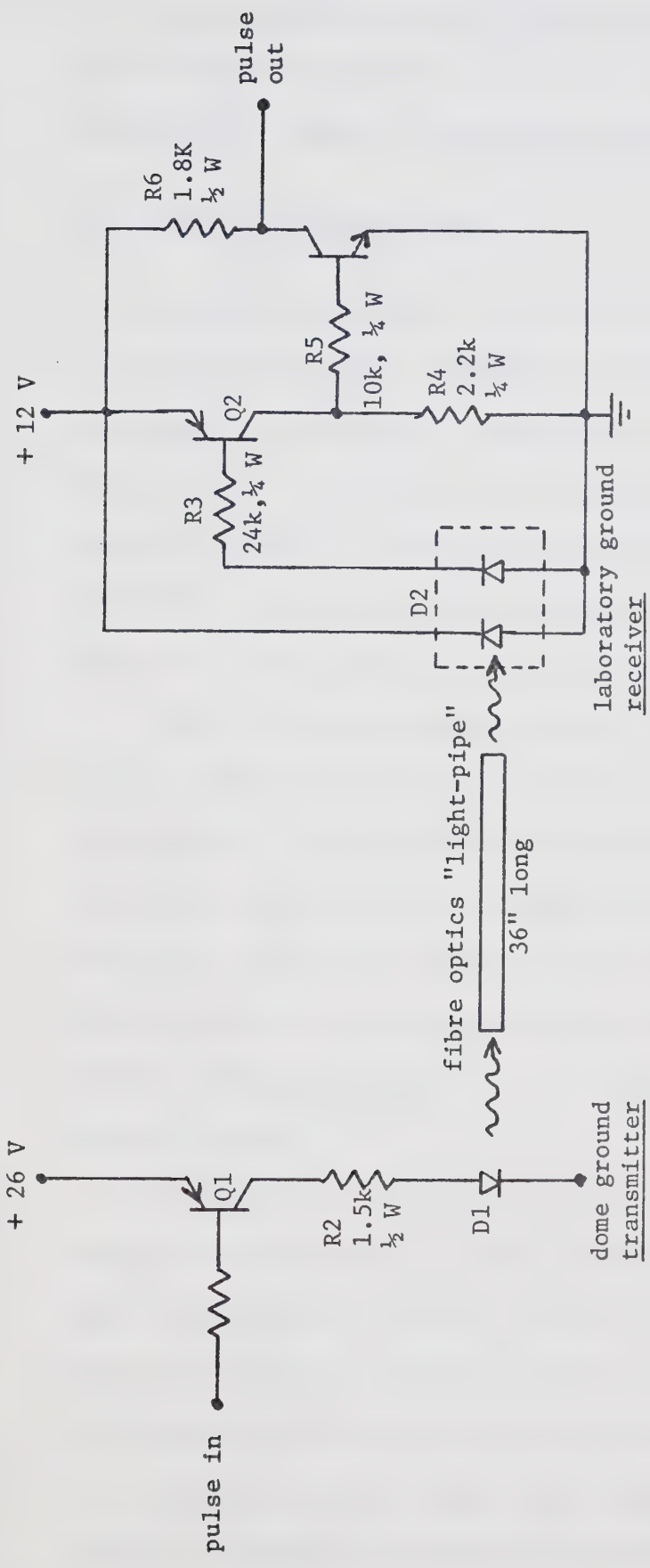


Figure 57: Circuit Diagram of the Optical Link.



of flight curve time scales of about 1 msec or longer. The optical link has been successfully operated with up to 100 kV on the accelerator dome, relative to laboratory ground potential.

### 8.5 Pneumatic Control Scheme

The 300 kV accelerator is controlled by compressed air signals. A section of this thesis (Section 8.4.2) has shown that five separate air signals are required. These are: a high pressure air line to drive the air motor, a control air line for the variable dc regulator, a control air line for the high voltage switch, a control air line for the time of flight pulse from the high voltage switch, and an analog control air line controlling the colloid source (Section 7.2.1).

Figure 58 is a schematic diagram of the pneumatic control scheme, in which high capacity, high pressure air lines are shown as heavy double lines, control air lines are shown as lighter double lines, and electrical wires are shown as single dotted lines. The figure is divided into three areas (laboratory, control panel, and accelerator dome) in order to show where individual components are physically located. The control panel is located outside the shielding wall of the accelerator.

Compressed air at about 120 psig from the building supply enters through a manual valve, V1, and is divided to go either to the control panel or through the solenoid valve, V2, to the air motor in the dome. This solenoid valve is controlled electrically from the control panel with switch SW4. The high pressure air is put through a regulator set at 20 psig to the first surge tank on the control panel. Pressure in the tank is monitored by meter M1. Control signals to the dome are



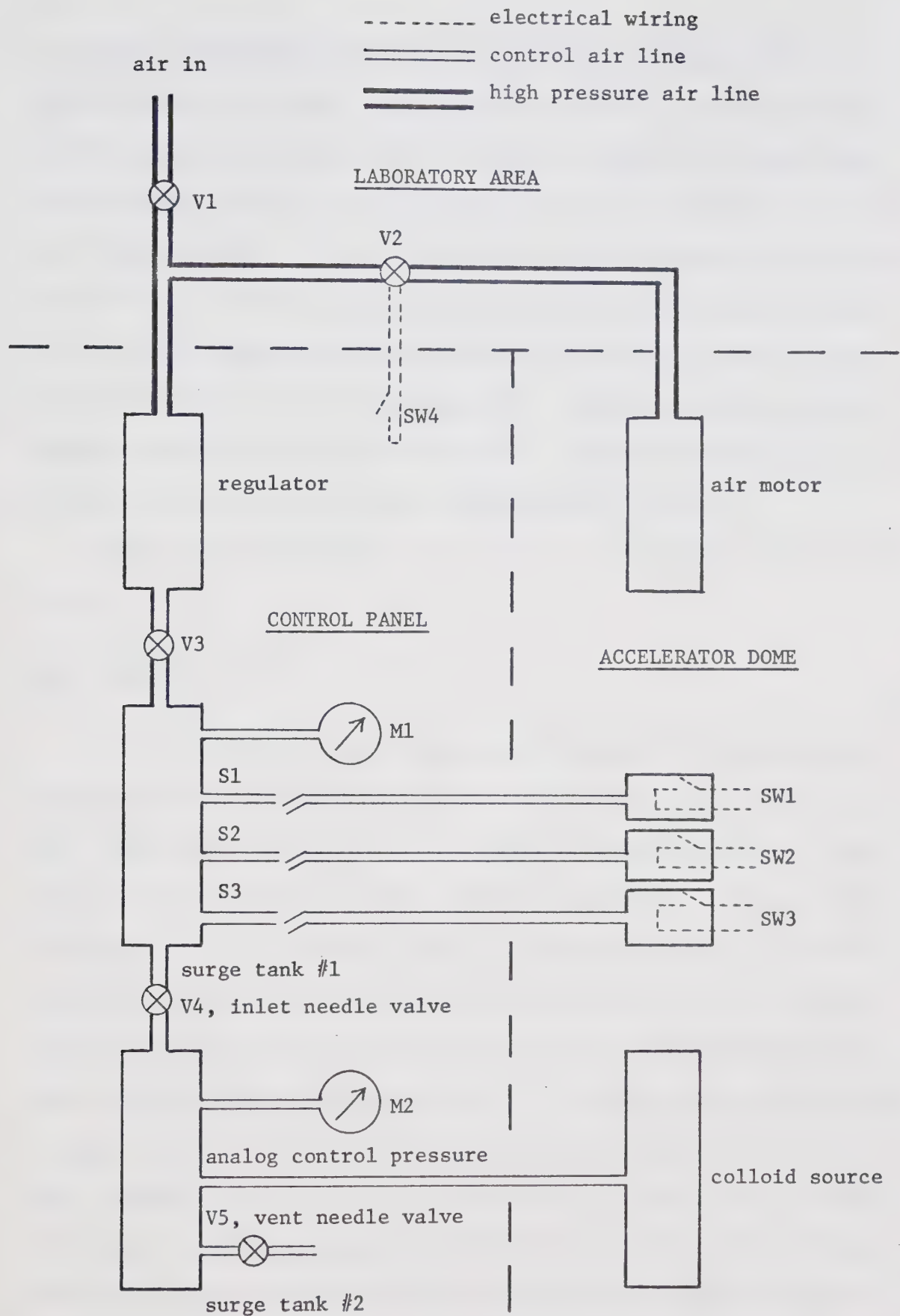


Figure 58: Air Supply and Control Scheme.



initiated by switching 20 psig air into the  $\frac{1}{4}$ -inch diameter PVC air lines leading to the dome, using switches S1 to S3. In the dome, the pressure signals are converted to electrical signals by pressure actuated contact closures in switches SW1 to SW3. The response of a contact closure is fast ( $\ll 1$  sec) when the pressure is applied to the air lines. On the reverse cycle, contact opening takes between 1 sec and 2 sec because compressed air must be bled from the long control line. The second surge tank, with its meter M2, contains the analog control pressure which drives the colloid source. Pressure in this tank is controlled by the inlet and vent needle valves, V4 and V5.

Operation of the entire control scheme is discussed in Section 9.2.2.

## 8.6 Detectors

Specific designs for the beam detectors used in the accelerator are discussed in Section 9.6, together with the results obtained using them. This short section merely discusses detector positioning. The accelerator dimensions are given in Table 10, Section 9.3.2. As shown in Figures 46, 47 and 48, the detector arrangement used in the 300 kV accelerator closely resembled the arrangement used in the test bench experiments. The various detectors were mounted in the four-inch diameter section of the four-inch by six-inch diameter glass cross used as a target chamber. The detector assembly consisted of a flat aluminum plate fastened to the mechanical feedthrough. In this plate, three 67 mm diameter holes defining the detector apertures allowed simultaneous installation of three different detectors, which were bolted to the back of the support plate. The size of the detector apertures was



determined by the size of the target chamber the detector fits into. By way of comparison, the inside diameter of the low voltage electrode is 70 mm, while the size of the expected beam spot (determined by the source and collimator geometry) is about 40 mm in diameter.

Experiments on secondary particles were performed using a ring electrode mounted just in front of the detector assembly (Section 9.7.2). Bias voltages of up to -4 kV were applied to the electrode via a ceramic feedthrough on the bottom flange of the target chamber. In addition, there was another grid directly in front of the detector surface, which was biased at voltages up to -500 V.



## CHAPTER 9

### ACCELERATED COLLOID BEAMS

#### 9.1 Introduction

As explained in the introduction to this thesis (Section 1.4), the ultimate goal of the present research is to accelerate a beam of colloid particles in the 300 kV microparticle accelerator. In a literature search into this topic, only one reference to acceleration of colloid beams was found. In this reference, Huberman and Cohen<sup>25</sup> described use of a 100 kV accelerating potential with a colloid source in an attempt to increase the specific impulse of the colloid source in a microthrust rocket application. (Specific impulse is a thrust per unit weight of fuel consumed rating factor for rocket engines.) The colloid source used by Huberman and Cohen<sup>25</sup> was a 37-capillary tube array operated at a positive voltage of 5 kV with respect to the source extractor, which was a plate containing one aperture hole for each capillary tube in the array. The working fluid was sulfuric acid doped glycerol. The colloid source, consisting of the capillary array, fluid feed line and a passive fluid feed mechanism, was held at 100 kV and the extractor was held at 95 kV with respect to the laboratory ground. Fluid feed pressure and capillary voltage could not be remotely controlled. A grounded electrode facing the source shaped the accelerating field, while an electron retarding electrode operating at -1.5 kV to -7 kV was placed between the grounded accelerating electrode and the grounded electrical detector.

Beams in these experiments were of the order of 125  $\mu$ A and had average charge to mass ratios of 800 coul/kg. The main problems encountered by Huberman and Cohen<sup>25</sup> were source heating due to



backstreaming electrons, and X-ray radiation ( $\sim 200$  mR/hr) created by the impact of these electrons on metal surfaces. It must be noted that in these experiments beam spatial distributions were not of interest.

In the present experiments, a low intensity ( $< 100$  nA) colloid beam was transmitted down the accelerator axis with the goal of producing an energetic, well focussed beam of particles.

It is clear that the present work and the work of Huberman and Cohen<sup>25</sup> describe completely different experiments, following completely different objectives. Thus no direct comparison of the two sets of experimental results can be made.

The experimental results described in this chapter were obtained in an experimental program designed to test three hypotheses: that the colloid source described in Chapter 7 could be operated in the 300 kV microparticle accelerator, that the colloid beams could be accelerated, and that measurements on colloid beams could illustrate the properties of the accelerator.

Sections 9.2 to 9.5 describe the operation of the colloid source and accelerator. Sections 9.6 to 9.8 describe results obtained while studying accelerated colloid beams.

## 9.2 Operating Procedures for the Experiments

### 9.2.1 Operating Procedures for the Accelerator

Usually two people were required to perform the accelerator experiments. One operator stayed outside the accelerator shield walls, at the control panel (Figure 47). Functions controlled from there included: analogue air pressure to the colloid source, all other pneumatic controls, and operation of the 300 kV power supply. The



second operator was stationed within the shield wall enclosure. His duties included adjustment of the variable voltage within the dome, the recording of all measurements, and manipulation of beam detectors. Of course the barrier between the target area and the accelerator area was kept closed and no-one was allowed within the accelerator area during experiments requiring accelerating potentials on the dome.

Safety precautions taken during operation of the colloid source and the accelerator included: monitoring of X-ray radiation, operation of interlocks between the accelerator area entrance barriers and the 300 kV power supply, and use of proper grounding sticks after any high voltages had been used. Also, accelerator operators always carried personal radiation film badges while working.

#### 9.2.2 Operation of Control Systems

The best way to illustrate use of the source and accelerator control schemes is to describe the various steps followed in a typical experimental sequence. The steps are:

- (a) The source is cleaned and installed in the source chamber.
- (b) The system is evacuated to  $5 \times 10^{-7}$  torr or lower by the turbo-molecular pump and liquid nitrogen trap.
- (c) The dome cart is rolled up to a point close to the source chamber. The high voltage lead to the source, the analogue control air line, and the collimator electron retarding ring bias lead are connected to the source. The dome is rolled completely forward and the auxiliary support stands are removed.
- (d) The main air supply valve is opened.
- (e) The solenoid valve is opened and the air motor and generator in the



dome start up. After one minute the bias voltage supply is started by the built-in time delay relay. After five minutes the tetrode has reached operating temperature.

- (f) The high voltage supply within the dome is started by means of the control panel air switch controlling the variable dc regulator in the beam. The high voltage is adjusted to be between 16 kV and 18 kV by means of the nylon filament and pulley arrangement.
- (g) The source control pressure is increased to about 6 psig. After about 5 minutes, the system vacuum pressure rises to about  $2 \times 10^{-6}$  torr because glycerol is now being sprayed into the system.
- (h) A stable dc beam must be established, which may happen spontaneously. Otherwise, the voltage and pressure applied to the source are increased until the stable dc beam appears. Occasionally the high voltage may be interrupted for one or two seconds by means of the control panel air switch labelled "tube grid", which initiates a level change at the anode of the high voltage tetrode. This procedure sometimes helps a dc beam to be established.
- (i) When stable dc has been established, experiments begin. These may include observations of the various detectors and measurements of the spatial distribution of the beam on the detectors.
- (j) Time of flight measurements are initiated by the air switch labelled "TOF...reset...pulse" on the control panel, which triggers the pulse circuit in the dome. The storage oscilloscope is triggered by the pulse emanating from the accelerator dome via the optical link.
- (k) When an accelerating potential is to be applied to the dome, all interlocked access barriers to the accelerator area and target



area are closed, and the 300 kV power supply started.

- (1) When experiments are completed, the 300 kV power supply is turned off. A waiting period of at least 5 minutes is required before the dome voltage falls to less than 500 V, due to the energy stored in the power supply.
- (m) The air pressure controlling the colloid source is reduced to zero.
- (n) The source capillary high voltage supply is turned off by the control panel air switch.
- (o) The air supply to the entire dome is turned off by the solenoid valve.
- (p) The accelerator dome is grounded by a ground stick which is kept in contact with the dome for several minutes to ensure that the 300 kV power supply is properly grounded.
- (q) The main air supply is turned off and the pneumatic control system is vented.

This control sequence was used whenever experiments were performed. Of course steps (i) through (1) were modified depending on the behaviour of the colloid source and the experiments to be performed.

The control of the source with accelerating potentials on the dome worked as designed. The tetrode was successfully fired at potentials up to 90 kV. Also, the optical link transmitted the appropriate synchronizing pulses. It must be noted again that the adjustment of the source operating voltage by means of the nylon filament and pulley arrangement was used only during the start-up procedures for the colloid source, when the dome was at laboratory ground potential. Once a dc beam had been established, the source voltage was left constant during beam acceleration experiments.



The method of operating the fluid feed pressure in the colloid source by means of the pressure converter and the analogue pressure also worked as designed. It was found that it was not necessary to follow the correspondence between the calibration graphs of Figure 44. Instead, the control pressure was set to about 6 psig when the source was started, then varied until a suitable operating point was found. Thus the choice of operating control pressure, typically between 8 and 10 psig, was determined solely by the behaviour of the colloid source.

### 9.3 The Colloid Source

#### 9.3.1 Introduction

Section 9.3 contains the information learned about the properties of the colloid source, which has been previously described in Chapter 7. Many problems had to be alleviated before the source would operate consistently in the accelerator, and Section 9.3.2 lists the various changes made to the source and accelerator during the development work. Sections 9.3.3 and 9.3.4 give results obtained for the colloid source alone, independent of any accelerating potentials present on the accelerator. Section 9.3.5 is a summary and evaluation of the colloid source design and operation.

#### 9.3.2 Experimental Development of the Colloid Source

This section discusses the developmental work that was required before the colloid source would operate in the 300 kV accelerator. The problems encountered and solved were related solely to the environment of the source (i.e. source geometry and vacuum pressures) while in the accelerator, since they occurred both with and without accelerating



potentials applied to the accelerator dome.

Figure 59 shows the source installed in the source chamber of the accelerator, together with the dimensions of the accelerating electrodes. It should be noted that the origin of the axial position scale of the entire accelerator is defined to be the outermost tip of the high voltage electrode. This origin is chosen because the source and low voltage accelerating electrode can be independently moved relative to the high voltage electrode, while the high voltage electrode and detector positions are fixed in the accelerator. Thus the high voltage electrode provides a convenient fixed reference point for axial position measurements.

Successful operation of the colloid source in the accelerator was achieved only after a series of modifications to the source and the accelerator. The problems encountered fell into three categories: vacuum problems associated with the accelerator itself, vacuum problems in the colloid source capillary tube tip region associated with the source design, and sparking problems between the source body and mounting supports. The latter two problems were closely related--a design change in source geometry to aid the vacuum problem often resulted in a worsening of the sparking problem, and vice versa.

The information gathered during work with the accelerator pumping system is presented in Section 9.4.

It was noted that, as the experimental program progressed, it became increasingly more difficult to achieve suitable, stable colloid source operation. This difficulty was attributed to a gradual contamination of the accelerator surfaces by glycerol. Accordingly, the design of the colloid source was gradually improved so that experiments



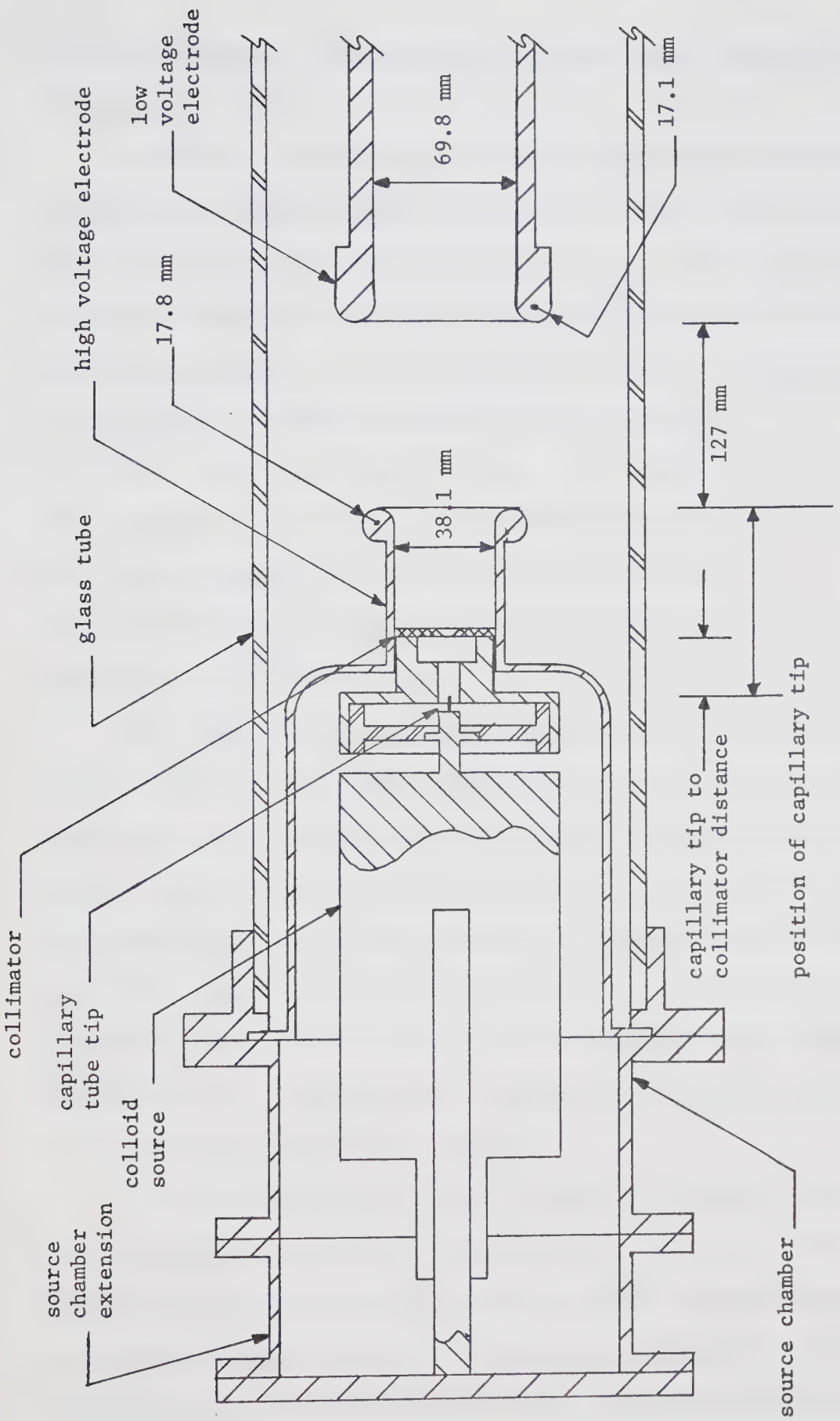


Figure 59: Schematic Diagram of the Colloid Source Installed in the Source Chamber, and the Accelerating Electrodes.



could be continued. The sequence of source design changes is now discussed.

Initially, the collimator--extractor--insulating support piece assembly was contained completely within the high voltage electrode, and the source chamber extension was not used. This configuration is denoted as Geometry A, and the dimensions for it are given in Table 20. Modifications made to this source design to improve pumping in the source region and reduce high voltage sparking were:

- (a) four longitudinal slots were cut in the extractor piece,
- (b) pumping holes were cut in the insulating piece,
- (c) a new extractor and insulating piece were made.

The new insulating piece incorporated a longer high voltage tracking path and larger pumping holes.

After these steps had produced only temporary improvement in source behaviour, the source chamber extension was installed, the source was moved back from the high voltage electrode, and the space thus created was used for a new extractor--insulating piece structure. The dimensions for this case, denoted as Geometry B, are also given in Table 20. Figures illustrating the source at various places in the thesis all display Geometry B. The essential difference between Geometries A and B is the different position of the source relative to the remainder of the accelerator structure.

At two separate times in this sequence of changes to the source, the source was installed and operated on the test bench. These two trials helped to clarify such problems as high voltage tracking across contaminated insulator surfaces. When these problems were alleviated, test bench operation of the source would consistently produce dc beams



Table 20: Dimensions for the Two Accelerator Geometries Used in the Experiments.

Item	Geometry A (m)	Geometry B (m)
capillary tube tip axial position	-0.105±0.002	-0.170±0.002
capillary tube outer radius	$(2.03\pm0.03)\times10^{-4}$	$(2.03\pm0.03)\times10^{-4}$
collimator position	-0.045±0.002	-0.111±0.002
collimator aperture radius	$(1.27\pm0.01)\times10^{-3}$	$(1.27\pm0.01)\times10^{-3}$
capillary tip to collimator distance	0.061±0.0005	0.0593±0.0005
high voltage electrode axial position	0.0	0.0
low voltage electrode axial position	0.127±0.002	0.127±0.002
target axial position	0.91±0.005	0.91±0.005

for periods of 2 hours or more. In the accelerator, the source would produce a suitable beam for periods of 10 minutes to 1 hour, then the beam would degenerate into a pulse mode or current bursts. It was therefore concluded that the poor operation of the source in the accelerator was associated with the geometry of the source while mounted in the accelerator, and that the source itself operated correctly.

### 9.3.3 Experiments with the Electron Retarding Bias Ring in the Collimator

Reference to the design details of the colloid source (Chapter 7) shows that the collimator design includes provision for a ring-shaped electrode mounted between the collimator and the extractor tube. This electrode, when biased negatively, was intended to prevent secondary



electrons created by the impact of the beam on the collimator from backstreaming into the capillary tip region of the source.

In tests of the colloid source both in the accelerator and on the test bench, bias potentials of between 0 V and -360 V were applied to the ring electrode. It was found that the source behaviour was almost independent of the bias voltage--the only improvement in source behaviour when bias was applied was a reduction in the number of minor beam instabilities. (Similar results were found for biasing the extractor itself in the test bench experiments described in Section 6.4.) It appears, therefore, that use of this electrode is optional.

#### 9.3.4 Use of the Source, and Source Cleaning Procedures

Several experiments were performed to test whether or not the colloid source could be re-started after it had been used once and then left evacuated for some time. It was invariably found that the beams produced upon re-starting the source were very unstable and degenerated into current bursts accompanied by corona in the capillary tip region of the beam. As stated in Section 6.2.4, this beam condition could not be rectified and the source had to be shut off. Thus the source had to be removed from the vacuum system and cleaned between successive experiments.

There are some hypotheses as to why the source failed to re-start successfully. These include:

- (a) glycerol previously deposited on the collimators may have caused the vacuum pressure in the capillary tip region to be unacceptably high for source start-up,
- (b) glycerol evaporated from the fluid in the capillary tube may have left a residue, which was probably crystalline NaI. This residue



may have distorted the capillary tip shape, or it may have changed the fluid charging mechanism at the capillary tube tip.

The cleaning procedure for the source is as follows. The source is removed from the vacuum chamber and set on a stand on a laboratory bench. The collimators, extractor piece, insulating support piece, and capillary tube are removed from the front of the source, and cleaned in water and methanol. (Chapter 7 gives the mechanical details of the source.) The capillary tube tip is re-shaped, if necessary. For re-assembly, the piston in the source is pulled to the fully withdrawn position by means of the length extension piece at the end of the source body. The feed tube on the source body leading from the fluid reservoir is carefully cleaned. The latter step is essential so that, when the source is placed in vacuum, the air trapped in the top part of the fluid reservoir can be pumped out through the capillary tube without interference from glycerol bubbles. When the feed tube is clean, the capillary is replaced with teflon tape on the threaded joint between the capillary tube cap and the feed tube. Then the support piece, extractor, and collimator are reinstalled. The source is then replaced in the source chamber and evacuated as soon as possible. Usually the entire cleaning procedure can be accomplished in less than one-half hour.

#### 9.4 Experiments Concerning the Accelerator Vacuum System

Initial attempts to adequately pump the accelerator using the original pumping system were unsuccessful. In this unsuccessful sequence, the entire accelerator was rough-pumped by a carbon vane mechanical pump and two large capacity zeolite sorption pumps cooled by liquid nitrogen. System pressures at this stage were typically



$5 \times 10^{-4}$  torr or higher. A 100 l/sec ion pump took the system to about  $1 \times 10^{-6}$  torr. Then the liquid nitrogen trap (which was in fact the cooling shroud for a 500 l/sec titanium sublimation pump) was cooled, and the titanium sublimation pump started. Problems encountered here were:

- (a) The ion pump overheated severely because it was inadequate to pump the entire accelerator over the range  $10^{-4}$  torr to  $10^{-6}$  torr.
- (b) System pressures rose to an unacceptably high level of greater than  $5 \times 10^{-6}$  torr during colloid source operation.
- (c) When the liquid nitrogen trap was allowed to warm up, the increased gas load caused the ion pump to trip itself off.
- (d) The system consumed large amounts of liquid nitrogen, up to 150 l/day.
- (e) There was no way to completely remove glycerol from the system, after it had been deposited on system surfaces during colloid source experiments.

At this stage, the turbomolecular pump (Section 5.2) was installed on the accelerator. After some experimentation, the following pump down procedure was successfully used for the experimental trials of the colloid source:

- (a) The system was rough-pumped to about 50 torr by the carbon vane mechanical pump.
- (b) The turbomolecular pump was started by either opening the gate valve while the pump was running, or opening the gate valve and then starting the pump.
- (c) The system was left to pump to  $2 \times 10^{-6}$  torr or lower, which took about 4 to 12 hours depending on the previous pumping history of



the system.

- (d) The trap was filled with liquid nitrogen. System pressure fell to  $5 \times 10^{-7}$  torr or less in one-half hour or less.
- (e) During operation of the colloid source, system pressures were typically  $3 \times 10^{-6}$  torr.
- (f) After the completion of the experiments, the trap was allowed to warm up.
- (g) In the period between experiments, the turbomolecular pump would collect glycerol vapour, and eject it from the system. Thus minimal build-up of glycerol contamination in the system occurred after a series of experiments.

The remainder of this section reports the observations made during operation of the colloid source in the accelerator. This information was gathered with the hope that it would provide insight into the problems being encountered with the vacuum system. Also, the information is useful in future colloid beam accelerator designs. For all results, the source was installed, the turbomolecular pump was on, the liquid nitrogen trap was cold, and the system pressure prior to starting the experiments was less than  $5 \times 10^{-7}$  torr.

Usually no change in system pressure occurred when accelerating potentials up to 90 kV were applied to the accelerator dome, whether a colloid was being produced and accelerated (pressure  $\sim 3 \times 10^{-6}$  torr), or not (pressure  $< 5 \times 10^{-7}$ ). Towards the end of the experimental program, one exception to this behaviour was noted. At dome potentials between 80 kV and 90 kV, short bursts of outgassing were observed to be correlated to small discharges on the high voltage electrode as observed on the high voltage power supply. The small discharges were



probably due to electrode surface contamination, and could probably have been eliminated by cleaning the electrode surfaces.

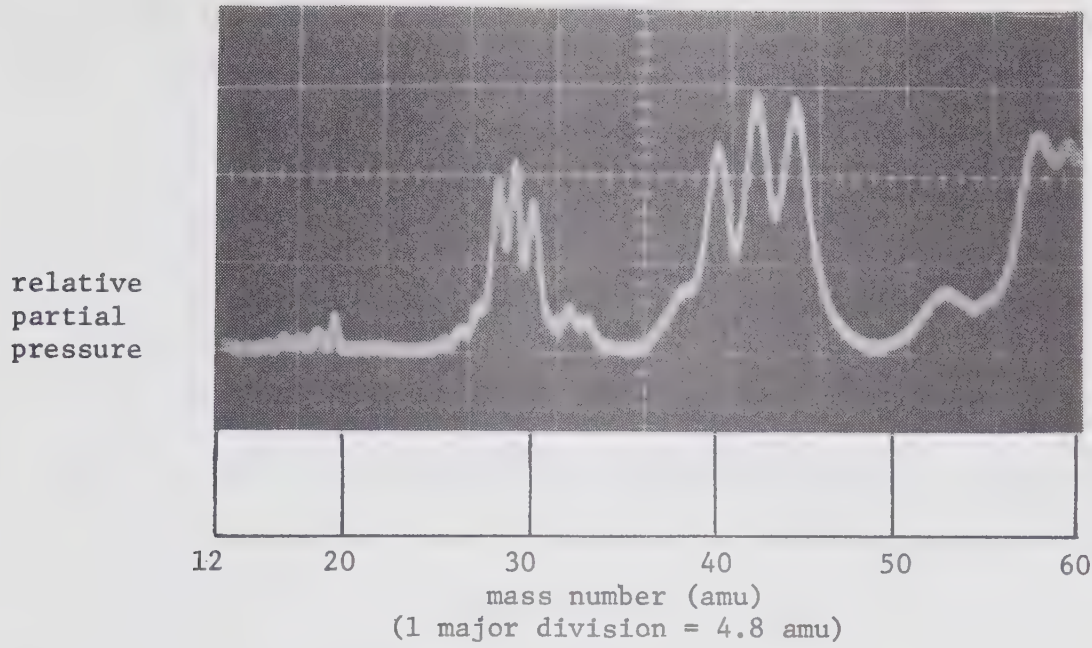
The fact that there was no consistent change in system pressure as the colloid beam energy was increased means that vapour production from high speed droplets hitting solid surfaces is independent of accelerating voltage, between limits of 0 and 90 kV.

In the major investigation concerning the vacuum system, a Vacuum Generators Ltd.<sup>80</sup> Micromass 1A residual gas analyzer was used to measure the relative partial pressures of the gasses in the vacuum system, both prior to and during colloid source operation. The mass spectrometer type analyzing head was mounted on the end flange of the vacuum manifold, replacing the viewing flange shown in Figure 46. In the present residual gas experiment, the absolute pressure measurements and mass number identifications were not experimentally calibrated in the laboratory.

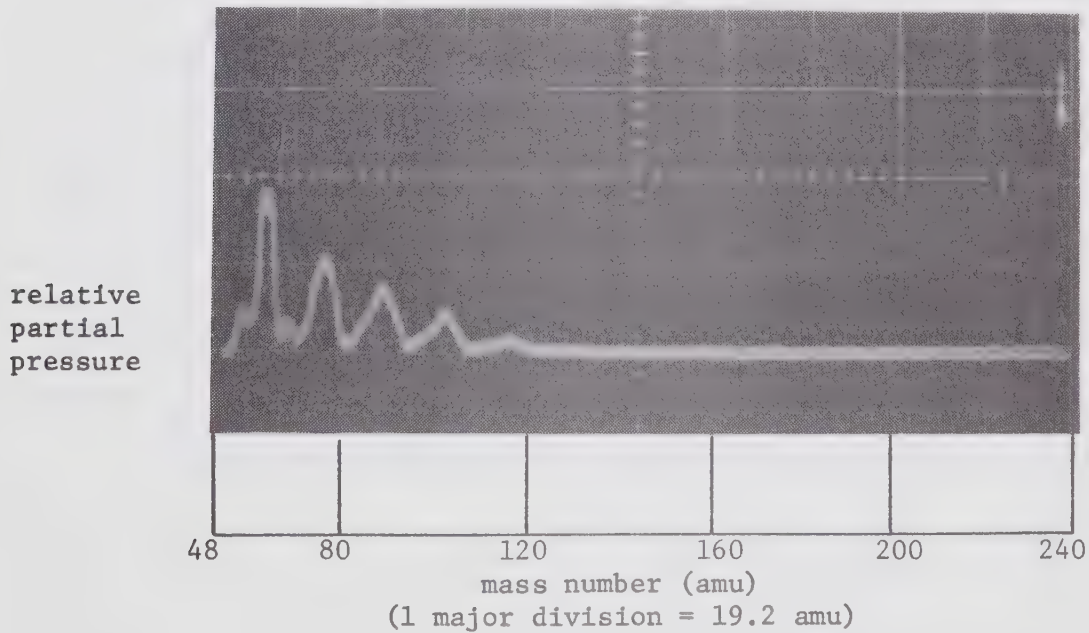
Figure 60 shows the residual gas spectrum of the accelerator vacuum system. Total pressure, as measured by the Varian ion gauge (Section 8.3), was  $3 \times 10^{-7}$  torr, and the system had been pumped for about 24 hours following the last operation of the colloid source.

Figure 60a is a plot of the partial pressure of various gasses as a function of mass number, over the mass range 12 to 60 amu. Figure 60b covers the mass range 48 to 240 amu, for the same conditions as Figure 60a. The partial pressure spectra were obtained in the following fashion. An analogue output corresponding to the residual gas analyzer pressure reading was connected to a storage oscilloscope. An automatic mass scan sequence (12-60 amu or 48-240 amu) was started at the same instant as a slow, stored, single sweep on the oscilloscope. The time





(a) Mass Scan for Gas Components in the Range 12 amu to 60 amu.



(b) Mass Scan for Gas Components in the Range 48 amu to 240 amu.

Figure 60: Residual Gas Analysis Results for the Accelerator Vacuum System Prior to Operation of the Colloid Source. Vertical Scale 1 Pressure Unit/Division.

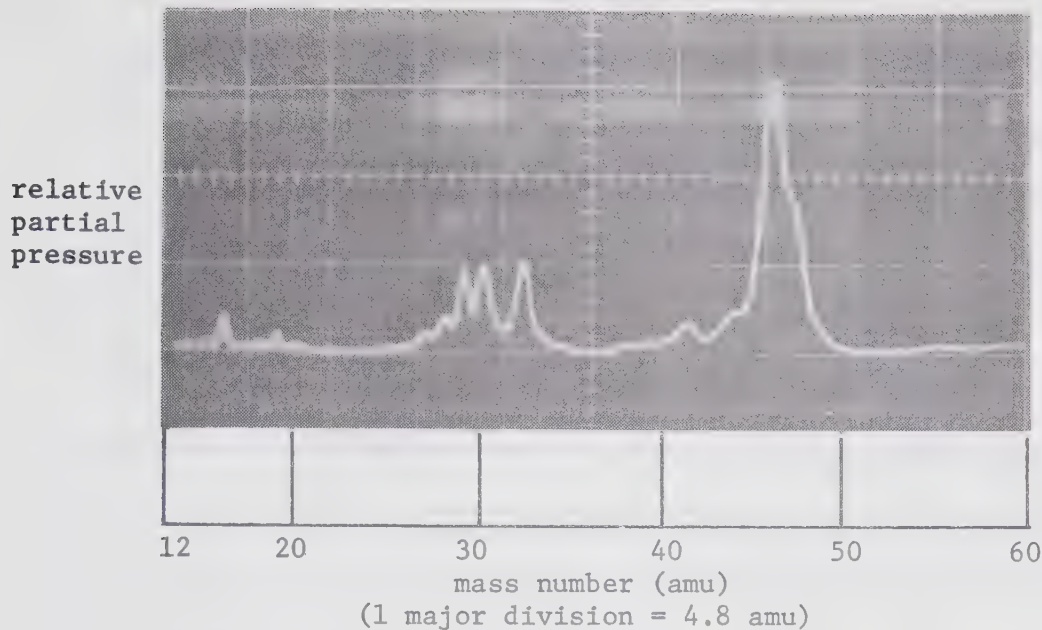


taken for one mass scan on the analyzer was identical to one complete sweep on the oscilloscope, or 50 sec. After the trace stored on the oscilloscope had been photographed, the same scan of mass numbers was made by operating the analyzer manually. Thus the peaks in the residual gas spectrum were identified with mass numbers on the scan dial of the analyzer by manually picking out the partial pressure peaks. Masses 2, 3, and 4 (i.e. hydrogen and helium isotopes) do not appear on the spectrum because on the Micromass analyzer they are measured discretely in a manual mode. The partial pressures of these mass numbers have not been reported because they were always negligible in comparison to the major residual gas components.

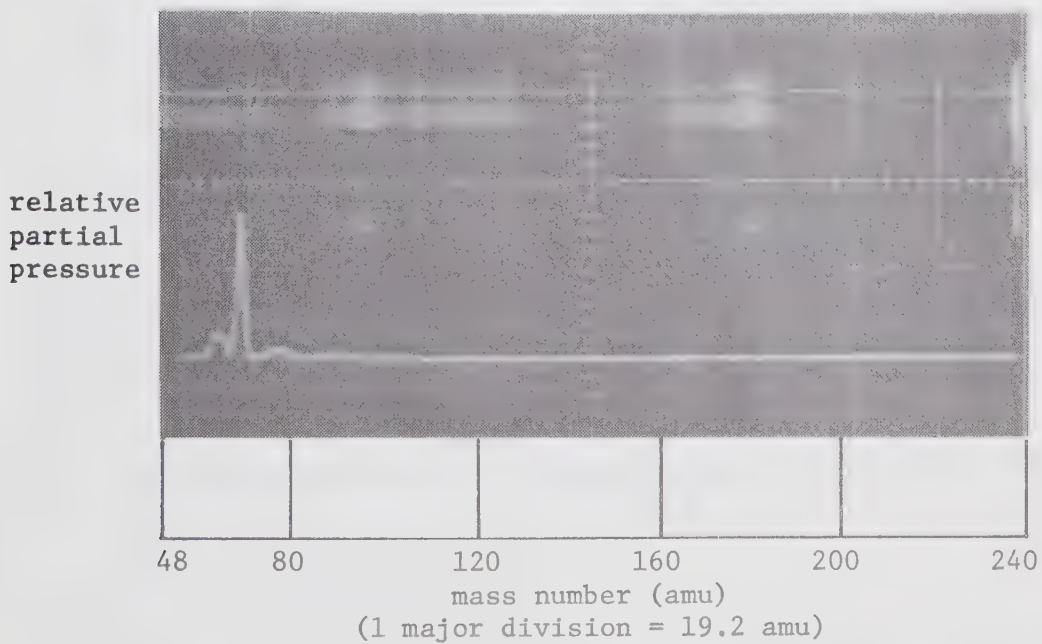
In the spectra shown in Figure 60, some easily identified major gas components and mass numbers might be assigned as: H<sub>2</sub>O (18), CO and N<sub>2</sub> (28), Ar (40), and CO<sub>2</sub> (44). Vacuum Generators Ltd. technical information<sup>80</sup> shows that masses 27 to 29, 41 to 43, and 55 to 57 can arise from hydrocarbon contamination. Masses larger than 60 can be attributed to hydrocarbon or organic vapours. Partial pressure peaks at mass 92 (glycerol) and 46 (doubly charged glycerol) do not appear.

Figure 61 shows the results of a gas analysis performed while the colloid source was operating. System pressure measured  $2 \times 10^{-6}$  torr on the Varian ion gauge, and the colloid source had been on for about one-half hour. The partial pressure spectra in Figure 61a and Figure 61b are taken on a pressure scale six times less sensitive than those in Figure 60, over the same mass ranges. A comparison of Figure 61 with Figure 60 shows that while the colloid source is operating, the majority of system gas is at mass 46. Components also appear at mass 27, 28, 32, and 64.





(a) Mass Scan for Gas Components in the Range 12 amu to 60 amu.



(b) Mass Scan for Gas Components in the Range 48 amu to 240 amu.

**Figure 61:** Residual Gas Analysis Results for the Accelerator Vacuum System During Colloid Source Operation.  
Vertical Scale 6 Pressure Units/Division.



The mass 46 peak is probably doubly ionized glycerol. The various other gases in the system are probably fractionated hydrocarbons or organic vapours (either glycerol, glycerol molecule fragments, cleaning solvents, or turbomolecular pump oil). The fractionated gases may exist throughout the system, or may be created in the ion source of the mass spectrometer itself.

These results indicate that fractionated hydrocarbons or organic vapours are present both before and during colloid source operation. Also, gases such as  $H_2$ ,  $O_2$ ,  $N_2$ , and  $CO_2$  comprise a small fraction of the system pressure while the colloid source is operating - the major gas component is glycerol vapour.

In view of these comments, it appears that the present pumping system of a turbomolecular pump and liquid nitrogen trap is a good design because the trap can pump large quantities of condensable hydrocarbon and organic gases, and the turbomolecular pump has the same pumping speed for all gases. Problems encountered in achieving adequate vacuum pressures in the accelerator are therefore related to lack of overall pumping speed and not to incorrect pumping methods.

## 9.5 The Properties of the 300 kV Accelerator

### 9.5.1 Introduction

This section is concerned with measurements made to check the 300 kV accelerator with regard to current leakage from the dome to laboratory ground, corona from the dome surfaces, sparking across the accelerator gap, and X-ray radiation produced. Information on these parameters aided the analysis of problems encountered during operation of the colloid source.



### 9.5.2 Isolation of the Accelerator Dome

The magnitude of the leakage currents and corona was found by first completing installation of the air lines, light link, and voltage adjustment mechanism between the dome and laboratory ground. Then, with the dome rolled away from the source, voltage from the 300 kV power supply was applied to the dome. At each voltage, the current drawn by the supply was noted. This current was then assumed to be the sum of leakage currents and corona currents. The power supply indicated leakages of about 60  $\mu$ A at a dome potential of 75 kV. Therefore the effective isolation resistance of the dome is greater than  $10^9$  ohms. The laboratory air temperature was 27 $^{\circ}$ C and the air had a relative humidity of about 45% during the tests. Some corona could be heard while the dome was at 75 kV, but none could be seen while viewing the dome in the darkened laboratory.

### 9.5.3 Breakdown across the Accelerator Gap

Breakdown between two electrodes having a potential difference between them can take two forms<sup>81</sup>. The first is sparking, which is characterized by the passage of large currents between the electrodes and a large decrease in the potential difference between the electrodes. Current and voltage waveforms are basically determined by the characteristics of the power supply connected across the interelectrode gap. The main phenomenon during sparking is that the interelectrode impedance becomes very low and stays low until the breakdown is interrupted by some external agent such as a power supply current limit. The second breakdown mechanism is termed microdischarging. Microdischarges are usually characterized as short term (<10 msec) bursts of low current (<1 mA) which are self-extinguishing. The interelectrode potential decreases



only a few percent of its total value during a microdischarge.

Microdischarges between the high voltage electrodes occur at voltages well below the sparking threshold. In fact, as a function of increasing interelectrode voltage, microdischarges appear first, a steady interelectrode current appears next (which is mainly electrons), and finally sparking commences<sup>81</sup>. Some factors influencing the onset of microdischarges are: gap voltage and electrode surface field strength, system vacuum pressure, anode material, and electrode configuration. In addition, the presence of microdischarges is strongly dependent on the presence and nature of electrode surface contamination.

The accelerating potential at which sparking across the accelerator gap may occur has been estimated using Kilpatrick's Criterion for vacuum sparking<sup>82</sup>. The criterion is an empirical relationship, based on experimental data for rf and dc fields, which defines a threshold at which sparking from an electrode surface is likely to occur. The basic parameters are  $W$ , the maximum energy available to ionized particles crossing the electrode gap expressed in electron volts, and  $E$ , the maximum electric field on the cathode surface expressed in V/cm. For dc applied potentials,  $W$  is just the total applied potential,  $V$ . The criterion is expressed by

$$K_2 = E^2 W \exp(-K_1/E) , \quad (9.1)$$

where  $K_1 = 1.7 \times 10^5$  V/cm and  $K_2 = 1.8 \times 10^{14}$  V<sup>3</sup>/cm<sup>2</sup>. Values of  $W$  and  $E$  which satisfy equation 9.1 define the threshold of potential  $V$  at which sparking is likely to occur. Since the electrode geometry in the 300 kV accelerator is quite regular, it has been assumed that the maximum surface electric field on the electrodes is given by the average



gap field, or

$$E = V/g , \quad (9.2)$$

where  $g$  is the gap width. Thus the criterion reduces to

$$K_2 g^2 = V^3 \exp(-K_1 g/V) . \quad (9.3)$$

Solutions of this equation for three values of gap width are shown in Table 21.

Table 21: Sparking Threshold Potentials Across Various Accelerator Gap Widths, as Given by the Kilpatrick Criterion, Equation 9.3.

gap width (mm)	threshold potential (kV)
25	207
75	503
127	776

Because it has been assumed that the peak field on the electrode surfaces is equal to the average gap field, the sparking threshold voltages in Table 21 are higher than will be observed in practice. If an arbitrary geometrical enhancement factor of two is used, it appears that operation at the full power supply potential of 300 kV is unlikely for an interelectrode gap of 25 mm, marginally possible at a gap of 75 mm, and reasonable at a gap of 127 mm. Thus the 127 mm gap has been used throughout the present experimental program.

Some points related to the experimental conditions are given by Kilpatrick as:

- (a) No sparks were observed below the calculated threshold.
- (b) The threshold is independent of electrode material.



- (c) "Conditioning" of the electrodes raises the sparking threshold.
- (d) The presence of contaminants such as oil on the electrode surfaces greatly increases the frequency of sparking once the threshold is reached.
- (e) "Vacuum" is defined to be the situation where the mean free path of the gas molecules is greater than the interelectrode spacing.

Alston<sup>83</sup> agrees with Kilpatrick's conclusions listed above.

In the present experiments, no sparks ever occurred for potentials up to 95 kV across the 127 mm gap, both with or without a colloid beam being produced by the colloid source.

The collimator of the colloid source was designed so that the colloid beam could never hit the accelerating electrodes. The reason for this is that the incident glycerol particles, scattered glycerol particles, and secondary electrons would greatly increase the probability of microdischarges and sparks if the beam were to intercept one of the accelerating electrodes.

In the present experiments, initial tests of the colloid source were performed either with no acceleration voltages, or acceleration voltages of less than 50 kV. Thus by the time higher acceleration voltages were used, some contamination of electrode surfaces by glycerol had already occurred. Electrode contamination, which contributes to the presence of microdischarges, occurs in the period between experiments as glycerol deposited on the detector and collimator surfaces evaporates from these areas, then re-condenses on all the vacuum system surfaces. As a result, when experiments using potentials greater than 80 kV were tried, microdischarges were observed. These microdischarges appeared as negative-going pulses of the order of 100  $\mu$ V on the



electrical detector output. These pulses were as large as, or larger than, the dc current level being recorded from the colloid beams. The microdischarge phenomenon appeared with colloid beams present or not, because of the previously given electrode contamination mechanisms. For potentials between 80 and 90 kV, the microdischarges were not seen on the 300 kV power supply current meter or on the Varian ion gauge monitoring the vacuum system pressure. With more than 90 kV potential on the dome, an additional form of discharge appeared--one giving a positive detected voltage of several millivolts on the electrical detector accompanied by momentary increases in vacuum pressure and power supply current. Operation with potentials greater than 95 kV was not attempted.

The negative-going pulses were detected if and only if the detector surface segments were connected to the oscilloscope input by way of the switch box, and the electrical detector was positioned directly on the beam line axis. The positive-going pulses detected during larger micro-discharges were probably ions emitted from the high voltage electrode which were accelerated towards the electrical detector.

#### 9.5.4 Measurements of X-Ray Radiation

Observations of X-ray radiation from the accelerator dome, accelerator gap and target areas were carried out as both a safety precaution and an experimental observation. A Victoreen Model 440RF radiation meter was used. The meter response is specified to be within  $\pm 15\%$  of true value for X-ray and gamma ray radiation from 12 kev to 1.2 Mev.

For all accelerating potentials up to 95 kV, observed radiation was always less than the measurement limit of the instrument, 0.05 mrad/hr. The radiation was measured from an unobstructed viewpoint at a



distance of about 2 to 3 m from the accelerator dome and accelerating gap. Measurements of radiation from the target were taken with the meter window against the glass target chamber wall, which is about 80 mm distant from the target itself. The radiation monitoring was done with no colloid beam present, and accelerator potentials up to 95 kV, and again with 40 nA of colloid beam being accelerated up to 90 kV.

Since no radiation could be detected, the radiation level was less than 0.05 mrad/hr. The allowed X-ray dose rate for radiation workers is 5.8 mrad/hr over a 40 hr/week, 13 week period<sup>84</sup>.

## 9.6 Beam Detectors

### 9.6.1 Introduction

This section discusses the design of, use of, and results obtained with the various types of beam detector used in the accelerator. Examples of results obtained using the segmented electrical detector in conjunction with photographs of glycerol deposited on a black detector surface are given in Figures 68, 69, and 70 in Section 9.8.3.2. Generally speaking, the relatively low beam currents used in the accelerator meant that the visually reacting detectors were less effective than in the test bench experiments, where higher beam currents were available.

### 9.6.2 Electrical Detector

The first electrical detector used on the accelerator consisted of four concentric rings of flat aluminum sheet mounted on a lucite backing plate. Detector construction details and electrical connections were the same as for the methods evolved in the test bench work, which is described in Section 6.3.2. In later stages of the work, the



outer three rings of the four ring detector were subdivided into four quadrants, giving a total of thirteen segments on the detector surface. Figure 62 shows the dimensions of the detector surface.

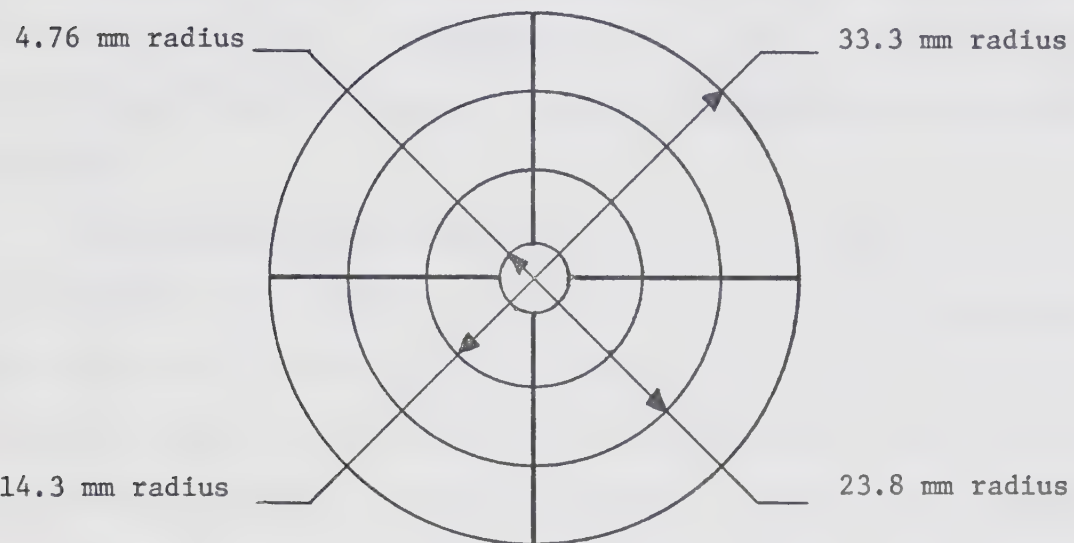


Figure 62: Dimensions of the Thirteen Segment Electrical Detector.

While the beam current detection apparatus was electrically identical to that described in Section 6.3.2, a summary of the detection method is given here. A segmented metal detector surface is placed in a grounded enclosure with a wire grid in front of it. The grid can be biased to help suppress secondary electrons created at the detector surface. The current intercepted by each of the detector segments is fed through a high vacuum feedthrough to a switch box, where the desired combination of signals can be selected for observation. The chosen currents flow through a resistor, which is 10 kohms in all these experiments, to ground. It should be noted that, in the test bench



experiments, the detector resistor had to be much less than 10 kohms so that the detector circuit did not filter out the higher frequency components of the current decay waveform. In the accelerator, the source to detector distance is longer, and the frequency spectrum of the current decay curve waveform is correspondingly lower. Thus a larger resistor can be used. A preamplifier and storage oscilloscope monitor the voltage across the resistor, thereby displaying the beam current waveform.

The segmented electrical detector was used to measure beam spatial distributions and total beam currents. The only problem encountered was that, even if the total beam current was well above the threshold of current detection of 0.1 nA, the current on some of the individual segments was below the detection threshold. Thus the sum of currents on the segments was usually 5% to 10% (but never more than 20%) lower than the measured total current for the cases measured in the experimental program.

The results for time of flight and particle source to detector transit time measurements are given in Section 9.7.5.

#### 9.6.3 Visually Reacting Beam Detectors

Because visually reacting beam detectors had proved successful in the operation of colloid sources in the test bench, they were used in the accelerator experiments. The detectors tried were a phosphor screen which emitted green phosphorescent light where hit by the beam, a liquid crystal screen which changed colour when locally heated by the energy of the incident beam, and a black surface which showed where glycerol was deposited on it by the beam.



The phosphor screen, which had a 65 mm diameter active surface in order to be compatible with the detector mount (Section 8.6), was made in the same fashion as those described in Section 6.3.3. That is, a glass plate was coated with a chromium layer to help bleed away beam charge, then coated with phosphor powder on top of the chromium.

The behaviour of the phosphor detector was correlated to the accelerating potential applied to the colloid beam. With less than 10 kV of accelerating potential on the accelerator dome, 40 nA of beam current spread over a spot 40 or 50 mm in diameter on the phosphor screen could be seen only as occasional flashes during beam instabilities giving short bursts of higher current. These flashes were useful as a visual monitor of beam shape when viewed in the darkened laboratory. Attempts to photograph the phosphor detector reaction showed that exposure times of greater than 3 min were required, hence detector photography was impractical. The camera had an f/2.5, 135 mm lens and used Kodak High Speed Ektachrome film (ASA 160) exposed and developed at an ASA rating of 600. For colloid beams of 30 to 40 nA accelerated through a potential of greater than 50 kV, the phosphor detector gave better results because the beam had more energy due to the increased accelerating potential, and because the beam was better focussed by the accelerator gap. The beam spot appeared as a continuously but faintly lit area, but attempts to photograph the phosphor detector results for accelerated beams were still inconclusive.

In summary, then, the phosphor screen detector could be used to view colloid beam distributions in the accelerator, but photography of the results was not feasible.

The second type of visual detector used in the accelerator was the



commercially prepared liquid crystal screen. The detector method has been described in Section 6.3.4. The screen consisted of a clear plastic layer, a layer of liquid crystal material encapsulated in small spheres, and a layer of black paint. The detector was mounted with the black side against a 67 mm diameter wire grid and bombarded from that side. The grid helped bleed off the beam charge.

In the test bench experiments, the colloid beams were sufficiently intense to cause local heating of the detector surface so that the beam distribution was indicated by visible colour changes in the liquid crystals. In the accelerator experiments, the beam was too diffuse to cause a visible reaction on the liquid crystal detector for all accelerating potentials less than 90 kV, with beam currents of 40 nA. Two types of detector having temperature sensitive ranges of 19°C to 25°C and 25°C to 31°C (nominal) were tried without success. Attempts to make the beam more visible by thermally biasing the liquid crystal material were unsuccessful because the heat sink effect of the detector mount surrounding the relatively small detector surface forced an uneven change in the background colour of the screen, and therefore the beam distribution was not reliably indicated.

The liquid crystal screen detection method failed for the same reason the phosphor screen results were inconclusive--the beam intensity on the detector was too low. The low beam intensity on the detectors was a result of both the beam collimation and the long source to detector distance.

The liquid crystal screens did provide an alternate means for observing beam distributions, because the glycerol deposited by the beam was visible on the black surface of the screens. Results given in



Section 9.8.3.2 were obtained by exposing the black detector surface to the beam, then photographing the detector surface after the experiment had been completed and the detector had been removed from the vacuum system. Analysis of the results is given in Sections 9.8.3.3 to 9.8.3.5.

A metal surface painted with flat black enamel was also tried as a detector for the glycerol deposited by the beam. While the results of one such experiment are given in Section 9.8.3.2, it was concluded that the liquid crystal screen surface gave better results than did the painted surface. For this reason the liquid crystal screens were used for subsequent experiments.

## 9.7 Acceleration of Colloid Beams

### 9.7.1 Introduction

The results of this section show that colloid beams can be successfully accelerated through potentials of up to 90 kV. Four topics are investigated: the amount of current available from the source, the effects of accelerating potentials on source operation, secondary particle production, and the transit times of particles between the source and detector.

Experimental data for this section, some of which are presented in Section 9.7.2, consist of observations of beam currents and measurements of the source to detector transit time for various acceleration voltages. The transit time measurements were accomplished using the time of flight circuitry in the accelerator dome.



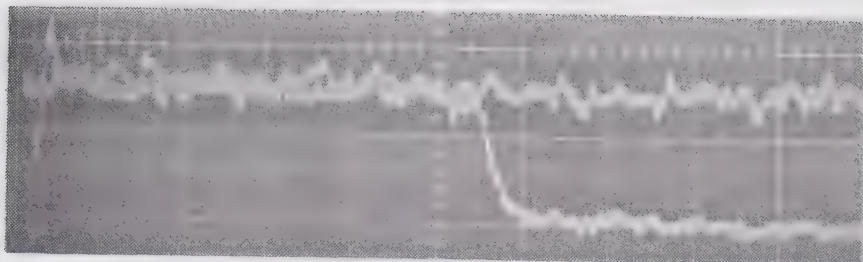
### 9.7.2 Presentation of Experimental Data

Experimentally, the transit times of the particle beam were measured as a function of accelerating voltages by interrupting beam production in the source (using the capillary voltage switch) and observing the subsequent decay in beam current at the electrical detector. Figure 63 shows some photographs of the current decay curves during one such experiment, as stored on the storage oscilloscope. Each photograph consists of two superimposed traces. The first trace shows the constant dc current level, while the second trace shows the current decay curve. Figure 63a was taken at the start of the experiment with zero accelerating voltage and a source voltage of 18.2 kV. Figures 63b and 63c were taken at accelerating voltages of 40 kV and 90 kV, respectively. Figure 63d was taken at the end of the experiment, again with zero accelerating voltage. The normalized acceleration voltages given in Figure 63 are the ratio of actual acceleration voltage to source voltage. The curves in Figure 63 are samples from many such experiments performed. In each experiment, several accelerating voltages were used. Also, measurements at zero accelerating voltage were repeated periodically in order to monitor the beam current and nominal charge to mass ratio throughout each experiment.

### 9.7.3 Currents Available from the Colloid Source

It was found that dc beams established in the colloid source varied from 5 to 70 nA in detected beam current. Examination of the glycerol deposited inside the collimators showed that the range of output beam currents was a result of the beam being off-axis before striking the collimators. When the beam was too far off-axis or else showed an unsuitable beam shape, the hole in the collimators transmitted only a

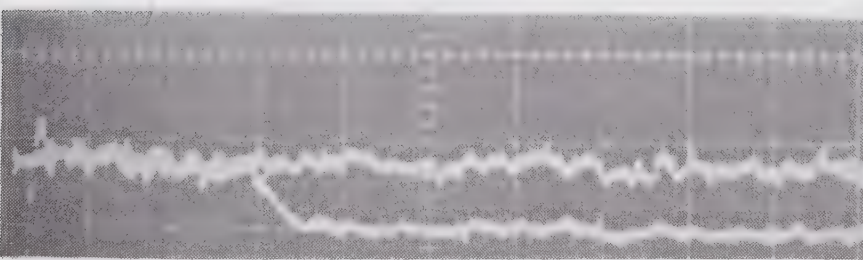




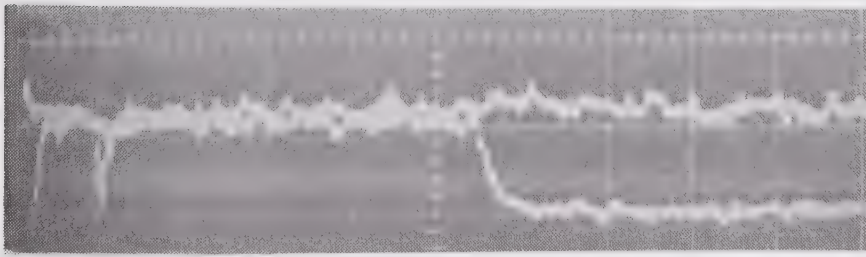
(a) Normalized Accelerating Voltage 0.0.



(b) Normalized Accelerating Voltage 2.20.



(c) Normalized Accelerating Voltage 4.95.



(d) Normalized Accelerating Voltage 0.0.

Figure 63: A Sequence of Transit Time Measurements on Accelerated Colloid Beams, as a Function of Normalized Accelerating Voltage. Vertical Scale is 5 nA/Major Division, and the Horizontal Scale is 200  $\mu$ sec/Major Division.



small fraction of the total current produced by the source. Comparison of the beam currents measured for the source with and without collimators showed that typically the collimators transmitted 1/4 to 1/10 of the total beam current. This problem in the spatial distribution of the total beam sometimes gave beam cross-sectional areas which appeared crescent shaped on the detectors.

As explained in Section 9.3.2, the dc beams in the colloid source lasted for periods ranging from 10 min to 1 hr. During that time, the magnitude of the current arriving at the detector usually decreased, by sudden instabilities, by amounts up to 30% of the initial detected beam current. Possible reasons for the current decreases include both changes in the total beam current emitted at the capillary tube, and changes in the spatial distribution of the beam upstream of the collimator. The current decrease effect can be seen in the results shown in Figure 63a and Figure 63d. For the same experimental conditions, the beam currents are 7.5 nA and 6 nA, respectively, for two beam current measurements taken about 30 minutes apart.

The application of accelerating potentials up to 75 kV had no correlation to the major instabilities seen in the beam currents. Above 75 kV, interference from the microdischarges at the accelerator electrodes became evident, as discussed in Section 9.5.3.

One effect of the accelerating potential on the beam current was a decrease in detected beam current as accelerating potential was increased. The effect appeared to cause a reduction of the order of 2 to 5 nA in detected beam current at acceleration potentials of 90 kV. This phenomenon is illustrated by the curves in Figure 63c and Figure 63d. Figure 63d was recorded immediately after Figure 63c, and shows a



2.5 nA increase in beam current as the normalized acceleration potential was returned from 4.75 to 0.0. The effect was reproducible and reversible. Attempts to correlate this effect to secondary electrons at the detector were unsuccessful (see Section 9.7.4). It is suggested that the decrease in beam current is caused by neutralization of beam charge in the accelerator gap region of the accelerator. Charge neutralization could be caused by electrons produced at the low voltage electrode surface being attracted to, and neutralized by, the positive charge in the beam. Analysis of the data showed that the magnitude of the effect was about the same for all cases.

#### 9.7.4 Secondary Electrons

Experience gained during experiments investigating secondary particle production on the test bench (Section 6.4) showed that electrons are produced when the colloid beam strikes a metal surface such as the electrical detector. For this reason, additional secondary electron experiments were performed in the accelerator. Three different electrodes were used in the secondary particle experiments.

It has already been shown (Section 9.3.4) that the electrode inside the collimator of the source had little effect on the source and beam behaviour. In particular, the decrease in beam current at the detector as a function of increasing accelerating voltage was the same for either 0 or -360 V on this electrode.

Figure 64 shows that in addition to the wire grid incorporated into the electrical detector, a ring-shaped electrode was placed in front of the detector assembly.

Observations made during variations of the bias on the detector grid were:



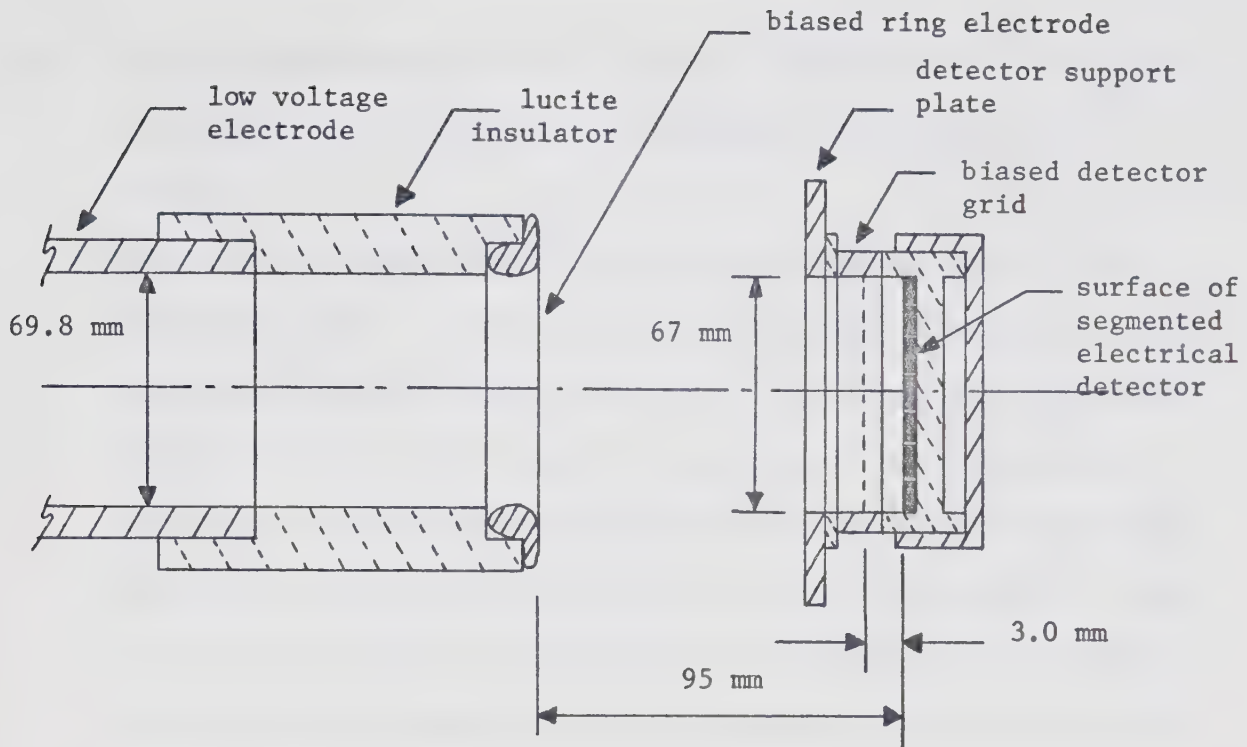


Figure 64: Sketch of the Electrodes at the Detector Used for Secondary Particle Experiments.

- (a) With no colloid beam in the accelerator, a bias voltage of more than -300 V caused a negative current to appear on the detector. At a bias of -500 V, this current was of the order of 1 nA. This current was due to either electrons emitted from the grid wires, or a leakage path between the grid and detector circuits.
- (b) Application of biases greater than -50 V seemed to help beam stability as evidenced by fewer short term instabilities in detected beam current.
- (c) The dependence of detected beam current on accelerating potential was independent of grid bias between -50 V and -500 V. Observations made during variations of the bias voltage on the ring electrode in front of the detector were:



- (a) With no colloid beam present, and bias voltages up to -4 kV on the ring electrode, no currents were detected on the electrical detector.
- (b) With a colloid beam present, and between -2 kV and -4 kV on the electrode, small (<1 nA) negative currents were detected on some segments of the electrical detector. It is postulated that these negative currents were caused by secondary electrons created by the impact of the beam on the grid in front of the detector being returned to the electrical detector surface by the electric field set up by the biased ring electrode. At no time was the observed negative current comparable to the magnitude of the beam current--accelerating potential relationship described in the previous section.
- (c) Bias voltages of up to -4 kV on the electrode had no effect on the pulses observed on the electrical detector during operation at accelerating potentials of greater than 75 kV. That is, the electrode bias had no effect on the presence of microdischarges across the electrode gap.
- (d) The electrode bias had no effect on the colloid source instabilities.
- (e) The electrode bias had no effect on the beam current--accelerating voltage effect.

These secondary electron experiments can be summarized as:

- (a) Secondary electrons created at the detectors apparently have little effect on the accelerator or colloid source operation.
- (b) The decrease in detected beam current as a function of accelerating voltage could not be significantly influenced by detector grid or



ring electrode biases.

- (c) Secondary electrons are produced when the colloid beam strikes a surface, whether it is the detector surface or the bias grid. It appears, then, that the best detector configuration would consist of only the detector surface and a ring electrode in front of the surface, biased to prevent escape of secondary electrons produced at the detector surface.

At the conclusion of these experiments, it was decided to operate the accelerator experiments with the detector grid held at -100 V and the ring electrode grounded. These conditions were used for the remainder of the experimental program.

### 9.7.5 Transit Time Experiments

#### 9.7.5.1 Introduction

Transit time is defined to be the time it takes a particle to travel from the capillary tube tip in the colloid source to the detector, with or without accelerating voltages present.

The theory and experiments described in this section were designed to demonstrate whether or not the colloid beam was successfully accelerated by the electric fields in the electrode gap. It is also shown what information can be obtained by performing a time of flight type measurement while the beam is being accelerated.

For the first case there are no potential gradients in the system except for the fields surrounding the capillary tube tip in the colloid source. A time of flight measurement is performed when the tetrode in the accelerator dome is triggered to pulse the source capillary voltage to zero, thus momentarily interrupting the colloid beam



production. For some time after the colloid beam is interrupted at the source, particles continue to arrive at the detector. The detected current then decays to zero. Section 3.3 has shown that calculations performed on the current decay curve yield information on the nominal charge to mass ratio of the beam, and the total mass flow rate in the beam. The transit time defined above is available from the time of flight current decay curve as the time between the instant the source is interrupted and the point on the decaying portion of the detected current curve at which the last particles of a given charge to mass ratio species arrive at the detector.

The calculations performed in a time of flight measurement assume that the source to detector drift distance is a field-free region. Therefore, while the source can be interrupted and a current decay curve can be recorded with an accelerating potential present on the gap, and while transit times of particles can be measured, no time of flight measurement calculations can be performed. In other words, the measurement of transit time by interrupting the source voltage and observing the current decay curve is valid for any distribution of potential along the particle trajectory, but the transit time measurement can be called a time of flight measurement if and only if there is a uniform potential along the drift space between the source and detector.

In Section 9.7.5.2 a theoretical value for transit time is derived from an assumed distribution of potential along the particle trajectory. Section 9.7.5.3 presents the experimental data, and a comparison between the calculated and measured values of transit time for various accelerating potentials.



### 9.7.5.2 Theory of Particle Transit Times

A relationship between time  $t$ , axial position  $z$ , and radial position  $r$  of a particle traversing a potential distribution  $V(r,z)$  can be found by starting with an equation

$$0 = \frac{1}{2} m(\dot{r}^2 + \dot{z}^2) + q V(r,z) . \quad (9.4)$$

The right-hand side is the sum of the kinetic and potential energies of the particle. The particle motion and the potential distribution are assumed to be independent of the rotational coordinate  $\theta$ . The left-hand side of equation 9.4 is zero because the reference for potential  $V(r,z)$  has been chosen so that the total particle energy is zero. Particle mass and charge are denoted by  $m$  and  $q$ , respectively. The condition of zero total energy is easily satisfied by adjustment of all potentials in the system by a suitable additive constant potential which depends on the initial energy of the particle. Now,

$$\dot{r} = r' \dot{z} , \quad (9.5)$$

where  $\dot{r} = dr/dt$ ,  $r' = dr/dz$ , and  $\dot{z} = dz/dt$ . Therefore equation 9.4 becomes

$$0 = \frac{1}{2} m(1+r'^2)\dot{z}^2 + q V(r,z) . \quad (9.6)$$

Transposition of variables in equation 9.6 leaves

$$dt = \left( \frac{-m(1+r'^2)}{2q V(r,z)} \right)^{\frac{1}{2}} dz , \quad (9.7)$$

which integrates to

$$t - t_0 = \int_{z_0}^z \left( \frac{-m(1+r'^2)}{2q V(r,z)} \right)^{\frac{1}{2}} dz . \quad (9.8)$$



Thus if the particle trajectory were known (i.e.  $r$  as a function of  $z$ ), the transit time ( $t - t_0$ ) taken by a particle to traverse the axial distance ( $z - z_0$ ) could be found. Unfortunately knowledge of the trajectory requires a complete knowledge of the potential distribution  $V(r,z)$ , which is not known.

Equation 9.8 can be simplified by assuming that the particle is paraxial. This is justified by the fact that experimentally the beam is collimated to within 18 mrad of the axis. Then

$$t - t_0 \approx \int_{z_0}^z \left( \frac{-m}{2q V(0,z)} \right)^{1/2} dz , \quad (9.9)$$

is the transit time as a function of the axial potential distribution  $V(0,z)$ . The axial potential distribution can be estimated, and an approximate transit time calculated using equation 9.9.

In the accelerator the potential distribution along the axis is constant from the source to the gap region, then constant from the gap region to the detectors. Figure 65 shows the gap geometry and the linear potential distribution approximation across the gap. The accelerating potential is denoted as  $V_a$ , and the origin of the  $z$ -axis is the outermost tip of the high voltage electrode.  $V^*$  is the axial potential distribution with respect to the low voltage electrode, which is held at laboratory ground potential. The fields associated with the linear potential approximation  $V^*(0,z)$  are assumed to penetrate the bores of the two electrodes a distance equal to one-half the electrode inner radius.

The next step is to relate the potential  $V^*(0,z)$ , which is the potential with respect to laboratory ground, to the potential  $V(0,z)$



required in the transit time equation 9.9. Figure 66 shows the particle source, accelerator dome, accelerator electrodes, and detectors. Also shown are the potentials, with respect to laboratory ground potential, during normal accelerator operation.  $V_s$  is the operating voltage of the source relative to dome ground. Now, a particle of fluid is at rest in the particle source at some instant just prior to being ejected from the capillary tube tip. Therefore, for the particle to have zero total energy, as required by equation 9.4, the potential of the source must be zero, and

$$V(0, z) = V^*(0, z) - (V_a + V_s) . \quad (9.10)$$

Equation 9.9 gives the transit time of a particle of mass  $m$  and charge  $q$ . It would be convenient to remove this dependence, since the transit time measurement involves the entire beam with its range of charge and mass values. A transit time  $(t - t_o)_a$  is defined to be the transit time of the particle undergoing acceleration through  $V_a$ , and  $(t - t_o)_o$  is defined to be the transit time of the same particle with  $V_a = 0$ . By means of equations 9.9 and 9.10, the ratio of transit times defined by

$$R_t = \frac{(t - t_o)_a}{(t - t_o)_o}$$

becomes

$$R_t = \frac{1}{z - z_o} \int_{z_o}^z \left( \frac{-V_s}{V(0, z)} \right)^{\frac{1}{2}} dz . \quad (9.11)$$

The ratio  $R_t$  will be referred to as the normalized transit time. This equation can be further reduced to



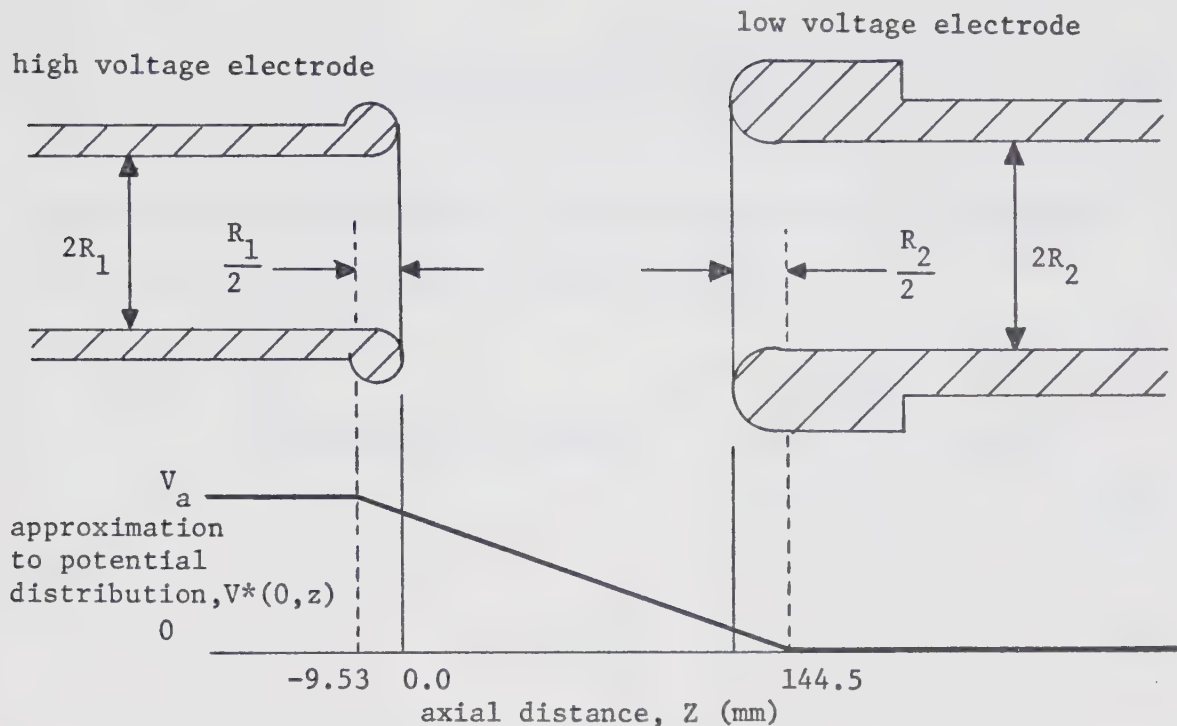


Figure 65: Sketch of the Approximation to the Potential Distribution Across the Electrode Gap.

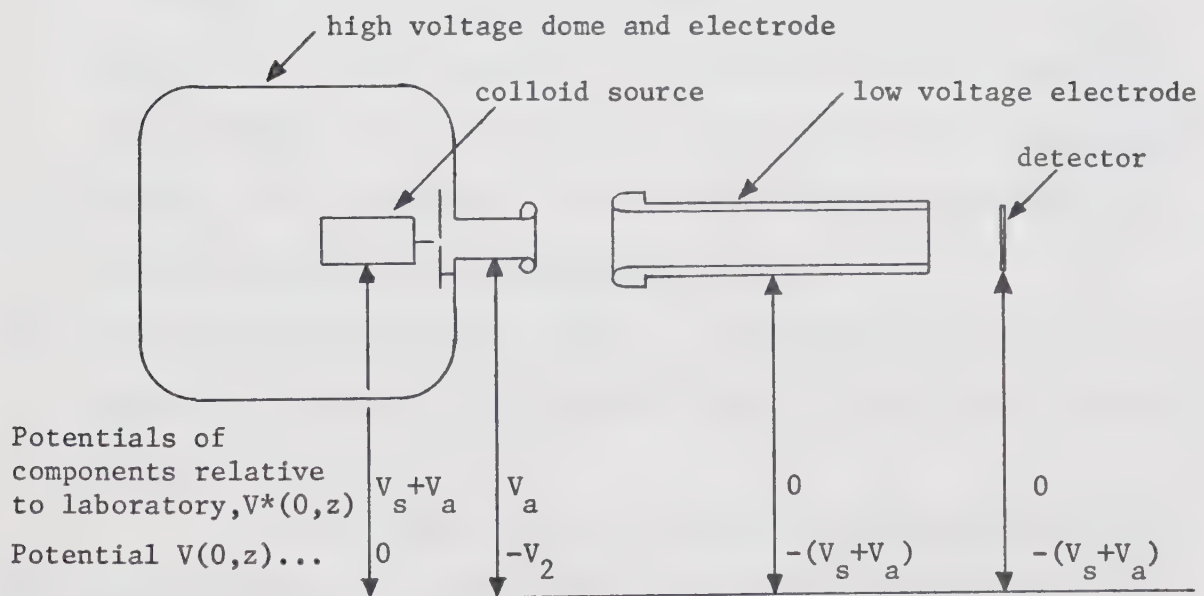


Figure 66: Schematic of the Accelerator, Showing the Potentials of the Components Relative to Laboratory Ground. Also Shown Is the Potential Function  $V(0, z)$  Required in Equation 9.9.



$$R_t = \frac{1}{z - z_0} \int_{z_0}^z \frac{dz}{P(z)^{\frac{1}{2}}} \quad (9.12)$$

where  $P(z)$  has been evaluated, from equation 9.10 and the potential distribution  $V^*(0,z)$  shown in Figure 65, to be

$$\begin{aligned} P(z) &= 1.0 & z < -9.53 \text{ mm} \\ &= 1.0 + C(0.062 + 0.0065 z) & -9.53 \text{ mm} < z < 144.5 \text{ mm} \\ &= 1.0 + C & z > 144.5 \text{ mm} \end{aligned} \quad (9.13)$$

where

$$C = \frac{V_a}{V_s} . \quad (9.14)$$

Hereafter  $C$  will be referred to as the normalized accelerating voltage.

Two important features of equation 9.12 are:

- (a) The result is independent of particle charge to mass ratio. Thus the shape of the current decay curve in a transit time measurement is subject only to a time scale contraction by a factor given by equation 9.12. This result in turn implies that the slopes of the decaying part of the defected current decay curves will become steeper as the normalized accelerating voltage is increased in a series of transit time measurements.
- (b) The integrand is dependent only on  $C$ , the normalized accelerating potential, and not on the absolute values of source and accelerator potential.

In the following section, the results obtained by measuring the change in the time scale of the transit time curve for various accelerating potentials  $V_a$  are compared to the theoretical estimate of the time scale change given by equations 9.12, 9.13, and 9.14.



#### 9.7.5.3 Experimental Investigation of Particle Transit Times

The experimental results shown in Figure 63 are representative of the results observed in several transit time experiments.

Three observations made from the data are:

- (a) The durations of the transit time curves decrease as accelerating voltage is increased (c.f. Figures 63a, 63b, and 63c),
- (b) The durations of the transit time curves returned to their initial values as accelerating voltage was returned to zero (c.f. Figures 63a and 63d).
- (c) The slopes of the current decay curves decrease as accelerating voltage is increased (c.f. Figures 63a, 63b, and 63c).

The first two of these observations agree with the expected results of the experiment, as discussed in the preceding section. However, the change in slope of the curves ((c) above) is in a direction opposite to that predicted. This anomaly may possibly be correlated with the observed decrease in beam current as accelerating voltage was increased.

Figure 67 shows a comparison between measured transit times and the theoretical curve calculated using equations 9.12 to 9.14 from the previous section. The experimental transit times were arbitrarily measured as the durations of the curves, in seconds, at the half-current points of the current decay curves. This procedure assumes that the half-current points refer to the same species of particle in each case. The transit time ratios were then found using the transit time found from the zero acceleration voltage case taken at the start of the experiment. Figure 67 shows the combined results of three experiments, for which the experimental conditions are given in Table 22. The accelerator geometry A defined in Table 20 was used in all



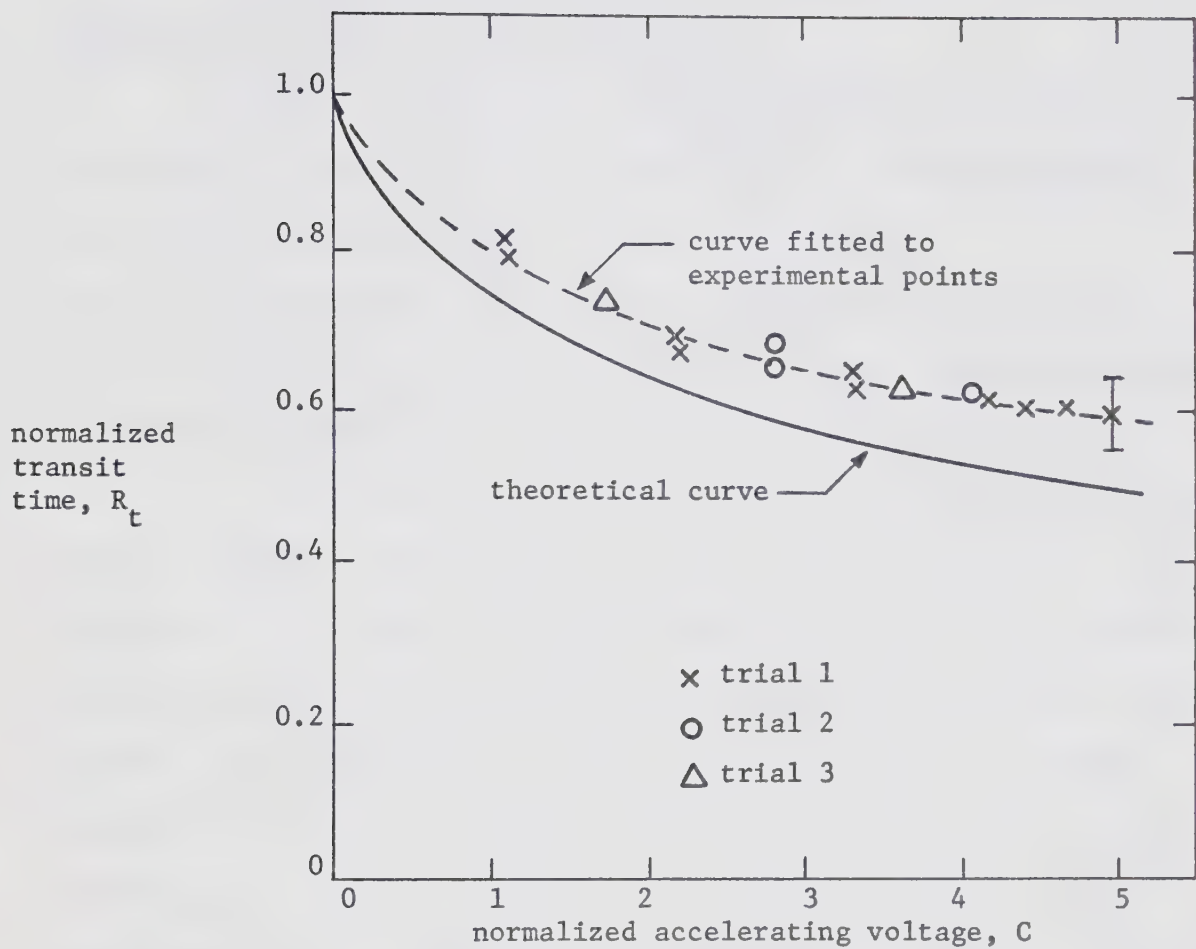


Figure 67: Experimental Transit Times Compared to the Theoretical Curve. Transit Times are Normalized with Respect to Transit Time at Zero Acceleration. Acceleration Voltages are Normalized with Respect to the Source Voltage in Each Particular Trial.



three experiments. The nominal charge to mass ratio of the beam, and the mass flow rate, were calculated from the zero acceleration case, which is just a time of flight measurement.

The error bars on the experimental points were found by considering the error in the data extraction from the photographs of the transit time decay curves. Figure 67 shows that:

- (a) The results taken in the three experiments are self consistent.
- (b) The theoretical curve and the curve through the experimental points differ by about 20% at a normalized accelerating potential of 5.0.

The difference between the curves can be attributed to three effects. Firstly, there is the experimental uncertainty shown by the error bars in the figure. Secondly, there must be some error introduced by the assumptions leading to the calculation of the theoretical curve. However, this error should be small, since the shape of the assumed potential distribution across the accelerator gap affects the particle transit time for only a portion of the total transit time. Thirdly, the effect may be due to a physical phenomenon such as a change in the particle charge to mass ratio as the particle moves along the accelerator axis.

At this point some comments can be made about the possible changes in the particle charge to mass ratio as the particle traverses the source to detector drift distance. These changes may be due to changes in particle mass, charge, or a combination of the two. Two basic facts must be noted--that the velocity of the particle is constant in field-free regions of the trajectory, and that the transit time measurement basically measures velocity. Some ramifications of this are:



Table 22: Parameters for Three Experiments on Transit Time Measurements, Corresponding to the Results Shown in Figure 67. Figure 67 Shows the Values of Normalized Accelerating Voltage Used in Each Trial.

Trial	Source Voltage $V_s$ (kV)	Beam Current (nA)	Nominal Charge to Mass Ratio (coul/kg)	Mass Flow Rate ( $10^{-9}$ kg/sec)
1	18.2	7.5	21.9	0.34
2	18.5	72.	22.8	3.2
3	14.2	8.0	18.7	0.43

- (a) If there is no accelerating voltage present, the transit time measured for a particle is that determined by the particle charge to mass ratio at the source.
- (b) If there is an accelerating voltage present, any change in particle charge to mass ratio which takes place between the source and the accelerating gap will influence the particle velocity, hence a change in charge to mass ratio between the source and the gap influences the transit time result.
- (c) Even if there is an accelerating voltage present, changes in particle charge to mass ratio which take place between the accelerating gap and the detector cannot be noticed in the transit time results because this region of the trajectory is always field-free.

The calculations of transit time have assumed that the particle charge to mass ratio is constant. However, if the charge to mass ratio increases in the source to gap region, the particle velocity will be higher than expected after acceleration. This in turn means that the measured transit time ratio will be lower than that indicated by the theory. On the other hand, if the particle charge to mass ratio decreases, the particle is going slower than expected after acceleration,



and the transit time ratio is higher than that indicated by the theory.

Figure 67 shows that the consistent difference between the theoretical transit time ratio curve and the curve drawn through the experimental points is such that the experimental transit time ratios are higher than those predicted by the theory. Therefore it appears as though the particle charge to mass ratio was decreasing in the region between the source and the accelerating gap. The decrease in charge to mass ratio in turn implies that even though both charge and mass loss may occur, charge loss is the dominant effect. In other words, mass loss due to glycerol evaporation from the particle is relatively less important than the charge loss. The conclusion that charge loss occurs is consistent with the fact that the detected beam current was seen to decrease somewhat as the accelerating voltage was increased.

## 9.8 Spatial Distributions of Accelerated Colloid Beams

### 9.8.1 Introduction

The spatial distribution of the colloid beam hitting the detectors is of interest for four reasons. Firstly, the shape of the beam before being intercepted by the collimators can be partly deduced from the shape of the detected beam. Secondly, alignment of the source in the accelerator can be assessed. Thirdly, some properties of drifting and accelerated beams are illustrated. Finally, the properties of the accelerator itself can be investigated. Generally speaking, the first of these four reasons is less important than the last three, because useful experiments can be performed with a variety of beam shapes, provided that the current transmitted through the collimator is sufficient to be detected on the individual segments of the electrical beam



detector.

Section 9.8.2 discusses the theoretically predicted focussing properties of the accelerating gap, which is in fact a single gap accelerating lens.

The presentation of data in Section 9.8.3 is intended to serve a dual purpose. The most important aspect is an assessment of the operation of the colloid source in the accelerator in the particular fashion used in these experiments. The second aspect is the generalization of the results and techniques to accelerated colloid beams in general.

#### 9.8.2 Theoretical Discussion of Accelerator Focussing Properties

It is well known that the passage of a beam of charged particles through a series of electrodes held at different potentials can be analyzed in a fashion very analogous to the passage of a light beam through a series of optical lenses. An accelerating gap acts as a focussing lens for the beam of charged particles, but the beam image can be either real or virtual. The discussion of the accelerator focussing properties which follows is based partly on a discussion by Spangenberg<sup>85</sup>.

The single accelerating gap in the microparticle accelerator is considered as the electrostatic lens in this discussion. The electrode geometry has been shown in Figure 59 of Section 9.3.2. A complete discussion of the lens properties can be made only by using the potentials at each point in the interelectrode gap as a basis for calculating detailed particle trajectories across the gap. This procedure cannot be used here since the potential distribution is not available. However, an adequate qualitative discussion can be given, based on the general properties of electrostatic lenses. The properties of the accelerating



lens depend only on the ratio of the incoming and outgoing particle velocities. Thus in the present particular application, the lens properties depend only on the normalized accelerating voltage (i.e. the ratio of accelerating voltage to source voltage).

Two focal lengths are associated with the lens. These focal lengths are different because the particle velocity is different on the object and image sides of the lens. The shorter focal length lies on the incoming, or high potential, side of the lens. At higher normalized accelerating potentials, the lens displays stronger focussing properties, and the focal points lie closer to the center of the lens.

The next part of the discussion assumes that the normalized accelerating potential is fixed. For the source located outside the first focal point, the beam will be focussed at some image point on the other side of the lens. For the source located at the first focal point, the beam emerging from the lens will be cylindrical in shape. For the source located between the first focal point and the gap, the image is virtual, and the beam is divergent. However, because the axial particle velocity is increased and radial particle velocity is nearly constant during the acceleration, the beam is less divergent when accelerating voltages are present than when no acceleration takes place.

For fixed accelerating potential and source position, various positions of the detector will show various beam shapes as well, depending on whether the detector is at the image point (thus detecting an image of the source), the second focal point, (detecting a focussed beam spot), or at some arbitrary point (where beam diameter is dependent on detector position).

It is seen, therefore, that source position, detector position,



and normalized accelerating potential together determine the shape of colloid beams as detected. In the present experiments, the source was located as close to the accelerating gap as possible, in order that the beam diameter be as small as possible where the beam enters the accelerating fields. Two positions of the source (described as Geometry A and B) were used because of problems encountered in getting reliable source operation (Section 9.3.2). The detector position was fixed by the geometry of the complete accelerator structure, and was not changed throughout the experimental program. Likewise, the gap geometry was held fixed. Thus the variations in accelerating potential in any one experiment correspond to variations in the positions of the two lens focal points, with the source and detector positions being fixed. The results of the beam optics experiments are given in Section 9.8.3.4, and are sufficient to allow an assessment of the lens properties.

### 9.8.3 Results of the Optics Experiments

#### 9.8.3.1 Presentation of Data

This section displays and describes the data recorded during experiments performed to investigate the focussing properties of the accelerator. Figures 68 to 70 are results taken during three different experiments. In Figure 68, the detector was an aluminum plate painted with flat black enamel. Two beam spots are visible on the one plate, each centered around a bright spot in the photograph indicating the geometrical centers of the two detector positions. Two separate discs of liquid crystal screen material were used for the two separate measurements required in each of Figure 69 and Figure 70. In each experiment, the photograph of the glycerol deposited on the black surface detector is compared to the distribution of the beam on the electrical detector,





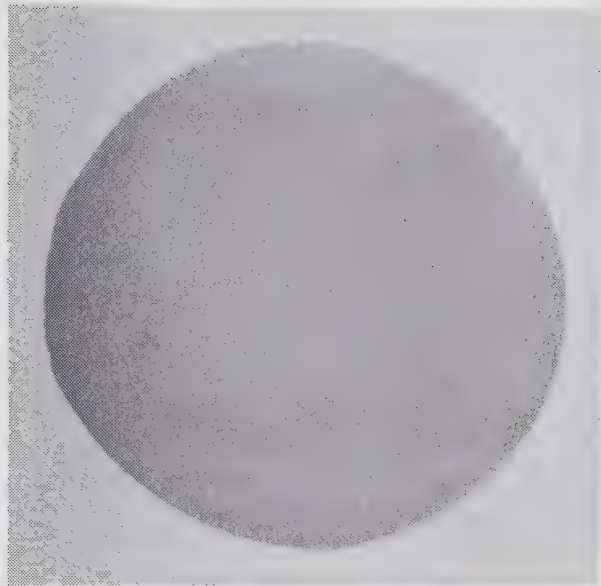
(a) Pattern of Glycerol Deposited on the Painted Surface Detector, Zero Acceleration Voltage. (c) Pattern of Glycerol Deposited on the Painted Surface Detector, Normalized Acceleration Voltage 2.28.



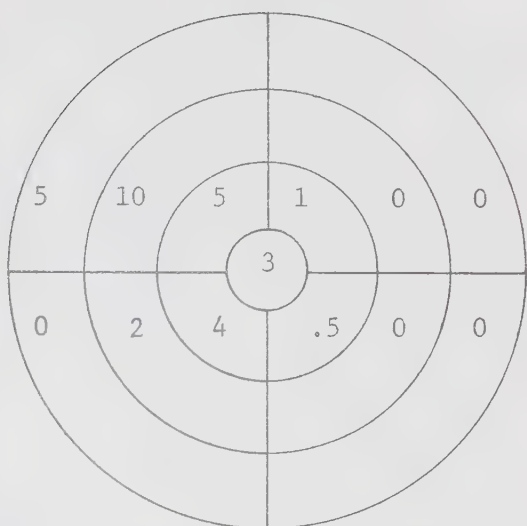
(b) Currents Measured (in nA) on the Four Ring Electrical Detector, Corresponding to the Glycerol Pattern in (a). (d) Currents Measured (in nA) on the Four Ring Electrical Detector, Corresponding to the Glycerol Pattern in (c).

**Figure 68:** Comparison of Painted Surface and Electrical Detector Results for Beams Undergoing Zero Acceleration ((a) and (b)) and Normalized Acceleration of 2.28 ((c) and (d)). Geometry A has been Used in the Accelerator. This Figure is Drawn 7/8 Full Size.

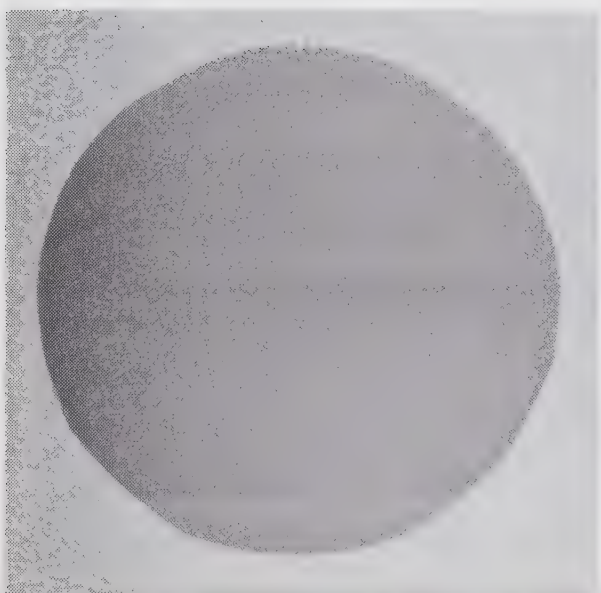




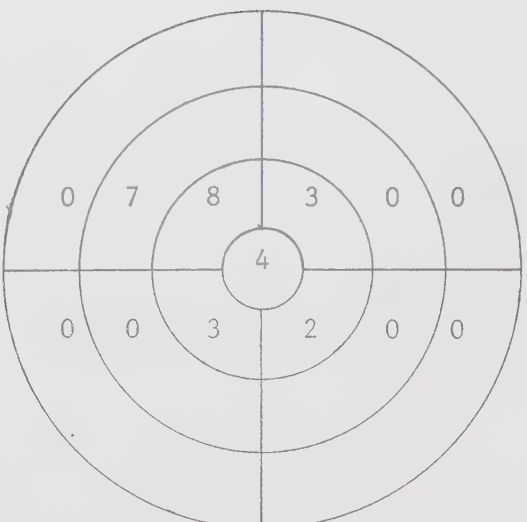
(a) Pattern of Glycerol Deposited on the Liquid Crystal Detector, Zero Acceleration Voltage.



(b) Currents Measured (in nA) on the Thirteen Segment Electrical Detector, Corresponding to the Glycerol Pattern in (a).



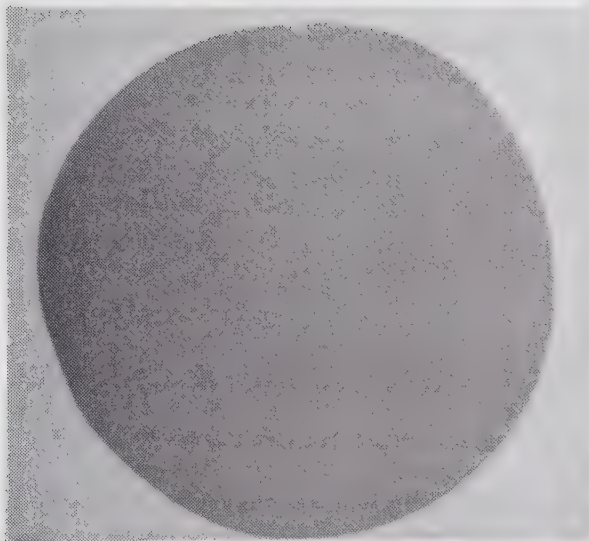
(c) Pattern of Glycerol Deposited on the Liquid Crystal Detector, Normalized Acceleration Voltage 1.58.



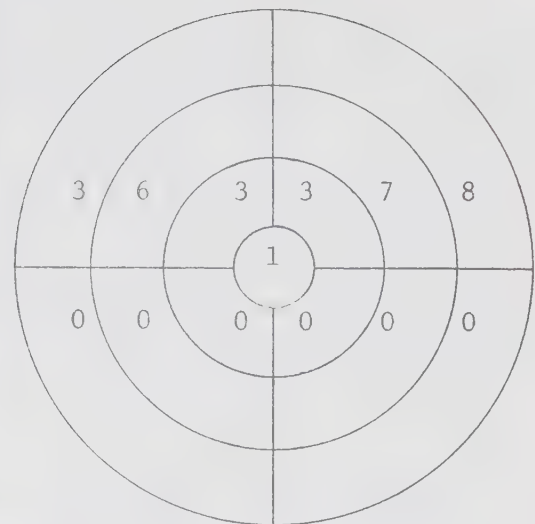
(d) Currents Measured (in nA) on the Thirteen Segment Electrical Detector, Corresponding to the Glycerol Pattern in (c).

Figure 69: Comparison of Black Surface and Segmented Electrical Detector Results for Beams Undergoing Zero Acceleration ((a) and (b)) and Normalized Acceleration of 1.58 ((c) and (d)). Geometry B has been Used in the Accelerator. The Figure is Drawn Full Scale.





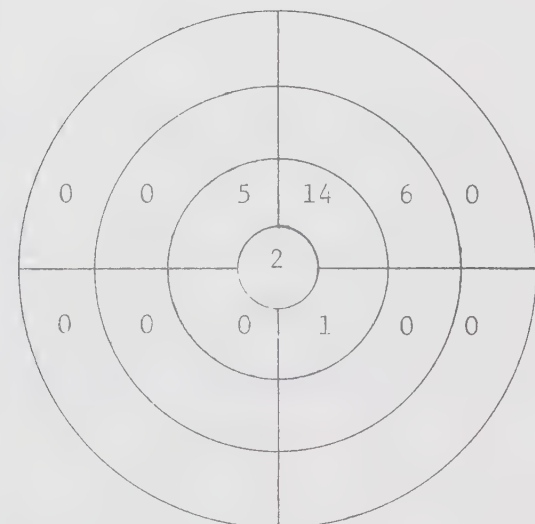
(a) Pattern of Glycerol Deposited on the Liquid Crystal Detector, Zero Acceleration Voltage.



(b) Currents Measured (in nA) on the Thirteen Segment Electrical Detector, Corresponding to the Glycerol Pattern in (a).



(c) Pattern of Glycerol Deposited on the Liquid Crystal Detector, Normalized Acceleration Voltage 4.57.



(d) Currents Measured (in nA) on the Thirteen Segment Electrical Detector, Corresponding to the Glycerol Pattern in (c).

**Figure 70:** Comparison of Black Surface and Segmented Electrical Detector Results for Beams Undergoing Zero Acceleration ((a) and (b)), and Normalized Acceleration of 4.57 ((c) and (d)). Geometry B has been Used for the Accelerator. The Figure is Drawn Full Scale.



for both no acceleration voltages and acceleration voltages present.

The current distributions are displayed as the current incident on each segment of the detector. The electrical detectors and photographs have the same scale in each figure. Table 23 lists the technical details pertaining to Figures 68 to 70. Because the intensities of the beams varied depending on the acceleration voltages present, various times of glycerol deposition were required to get visible deposits on the black surface detectors. The times are also given in Table 23.

In any one experiment, the procedures followed were:

- (a) measure the beam current distribution on the electrical detector,
- (b) insert the black surface detector for the measurement period,
- (c) remove the black surface detector and repeat the beam current measurement,
- (d) apply the accelerating voltage,
- (e) repeat steps (a) through (c),
- (f) remove the accelerating voltage and repeat the beam current measurement.

An assessment of beam stability was made using the electrical detector results. All the data presented in this chapter are cases in which the beam intensity and current spatial distribution were reasonably consistent throughout the measurement period.

#### 9.8.3.2 Beam Shapes and Alignment

An important point to notice from the results in Figures 68 to 70 is that the pattern of deposited glycerol correlates very well with the pattern of current indicated on the segmented electrical detectors. Also, the thirteen segment electrical detector in Figures 69 and 70 gives a reasonably good description of the asymmetric beam



Table 23: Experimental Details for the Results Displayed in Figures 68, 69, and 70.

Figure Number	Accel. Geometry	Total Beam Current (nA)	Source Voltage (kV)	Accel. Voltage (kV)	Normalized Voltage	Time of Detection (min)	and Detector Type
68a	A	33	17.5	0	0	6	painted surface
68b	A	33	17.5	0	0	-	electrical
68c	A	33	17.5	40	2.28	6	painted surface
68d	A	33	17.5	40	2.28	-	electrical
69a	B	33	19.0	0	0	11	black surface
69b	B	33	19.0	0	0	-	electrical
69c	B	33	19.0	30	1.58	5	black surface
69d	B	33	19.0	30	1.58	-	electrical
70a	B	34	16.4	0	0	13	black surface
70b	B	34	16.4	0	0	-	electrical
70c	B	34	16.4	75	4.57	2	black surface
70d	B	34	16.4	75	4.57	-	electrical

distributions.

In Figure 68, the beam cross section is crescent shaped. The crescent shape occurs because the beam from the source is not uniformly distributed over the aperture hole in the collimator. Figure 69 shows a similar type of beam--it is crescent shaped and slightly off axis. Figure 70 shows a beam which is uniformly spread over a circular cross section but which is mis-aligned with respect to the



accelerator axis, which is defined by the geometrical center of the detector disc.

These results show that the collimation of the central part of the colloid beam from the source does not always produce a uniformly distributed beam on the detectors. In addition, the fact that the collimator is transmitting a small fraction of the beam emitted by the source means that small instabilities in the beam distribution emitted from the source give relatively larger instabilities in both detected beam current and detected beam spatial distribution. This problem was observed several times during the experiments, and is fundamentally due to the fact that the beam emitted by the source is a group of jets clustered around the central axis, and is not homogeneously distributed over the beam cross-sectional area.

#### 9.8.3.3 Beam Radii with No Acceleration, and Space Charge Effects

This section compares the observed radii of the beams incident on the detector with the beam radii expected from the geometrical dimensions of the accelerator. Also, expected radii which include space charge effects have been calculated using the space charge theory derived in Section 2.6. Table 24 gives the results of the comparison. The radii of the beams were determined by examining the shape of the deposited glycerol spots on the black surface detectors in Figures 68a, 69a, and 70a.

In calculations of ideal or expected beam shapes based on the known geometry of the source and accelerator, it is assumed that the beam emerges from the capillary tube tip outer radius in a uniformly distributed cone. It is further assumed that, at the collimator axial



position, the beam cone radius is larger than the collimator aperture radius, so that the collimator aperture does in fact define the shape of the beam transmitted towards the detector. In the following discussions, the term "initial divergence angle" is the angle of the cone occupied by that portion of the uniformly distributed beam which is subsequently transmitted through the collimator aperture. The initial divergence angle is given at the capillary tube tip axial position.

If there are no space charge forces present in the beam, the ideal beam shape is a cone defined by the radius and axial position of the collimator aperture, and the outer radius and axial position of the capillary tube tip. The radius of this cone where it intercepts the detector is defined as the "calculated radius--no space charge" in Table 24. Clearly the initial divergence angle is the angle of the beam cone. Figure 71 shows a sketch of the beam envelope in this case.

In Section 2.6, an equation giving an estimate of the space charge effects in a colloid beam was derived. Equation 2.30 has been used in the present calculations. Now, the collimator aperture defines the size of the beam transmitted towards the detector. An initial divergence angle must be found for the beam such that the space charge forces expand the beam to a point where it just barely passes through the collimator aperture. Figure 71 shows the beam envelope and the initial divergence angle in this case. The radius of the beam envelope calculated from equation 2.30 is called the "calculated radius--space charge" in Table 24. Results are given for the two source positions defined as Geometry A and Geometry B in Table 20. It should be noted that the two cases for geometry B in Table 24 show different results



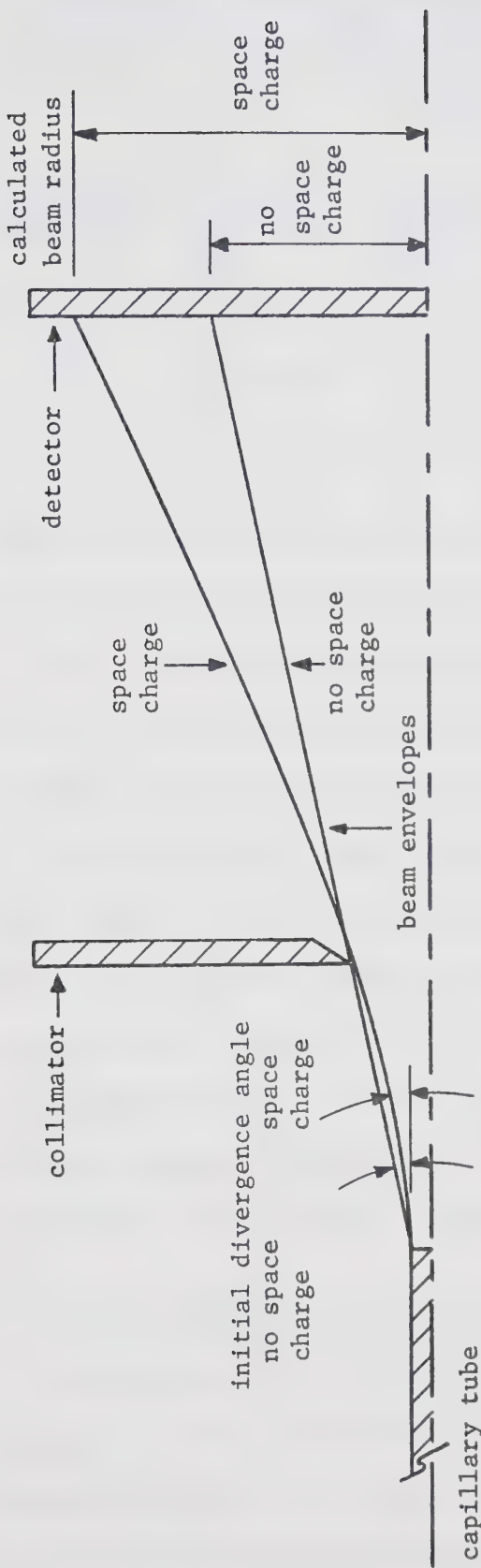


Figure 71: Beam Envelopes in the Accelerator With and Without Space Charge Forces. There is No Acceleration of the Beam.



Table 24: Comparison of Measured and Calculated Beam Radii  
(No Acceleration) at the Detector Position.

Figure Number	Accelerator Geometry	Measured Beam Radius (mm)	Calculated Beam Radius		Calculated Beam Initial Divergence Angle	
			No Space Charge (mm)	Space Charge (mm)	No Space Charge (mrad)	Space Charge (mrad)
68a	A	$26.5 \pm 2.$	18.3	22.4	17.78	15.59
69a	B	$25.0 \pm 2.$	19.7	23.7	18.0	15.95
70a	B	$25.0 \pm 2.$	19.7	25.0	18.0	15.69

for the calculated radius and initial divergence angle using space charge because the experimental conditions differed in the two cases.

It is clear that the measured beam radii are significantly higher than those calculated with no space charge. However, the incorporation of space charge effects significantly increases the calculated beam radii. In two of three cases, the measured and calculated (with space charge) beam radii agree within experimental error. Any further discrepancies can be attributed to errors in the geometrical measurements, to scattering of the beam by the collimator aperture, or to an error in the assumption that the beam emerges from the capillary tube tip at the outer radius of the capillary tube. In addition, the space charge calculation is only a first approximation to the problem.

#### 9.8.3.4 Focussing Properties of the Accelerator

As explained in the theoretical discussion of the accelerator focussing properties, the accelerator gap should act as a lens for the colloid particle beam. This effect was investigated experimentally by observing the beam radii on the detectors for various accelerator voltages and two source--accelerator geometries.



Figure 72 presents the results of the measurements, together with lines joining the various experimental points for the two accelerator geometries (A and B in Table 20). The results are given as the ratio of beam radius with acceleration divided by the radius without acceleration. This ratio is plotted as a function of the normalized accelerating voltage.

The focussing properties of the accelerator should depend only on the ratio between accelerator voltage and source voltage. In the results shown in Figure 72, accelerator voltages between 30 kV and 90 kV were used, in conjunction with source voltages between 14.6 kV and 19.0 kV. The results for the various voltages are self consistent, as expected.

Two methods of beam radius measurement were used. In the first, the beam spot sizes were measured directly from the photographs of deposited glycerol on the black detector surfaces. These three results are shown as solid points in Figure 72. In the second method, the beam current on each complete ring of the segmented electrical detector surface was plotted as a function of angle off-axis, after the beam currents had been normalized to a sum total of 1.0. From a line drawn through the four points on the plot, an off-axis angle corresponding to the distribution width at half height was found. When the ratio of the two widths for accelerated and non-accelerated beams was taken, it was found that the ratio of beam sizes agreed with the ratio of beam sizes measured on the black surface detectors. This method for determining the ratio of beam sizes is arbitrary, but it appeared to give adequate results whether the beam spot was asymmetric, off-axis, or both. The data found using this method of analysis on the



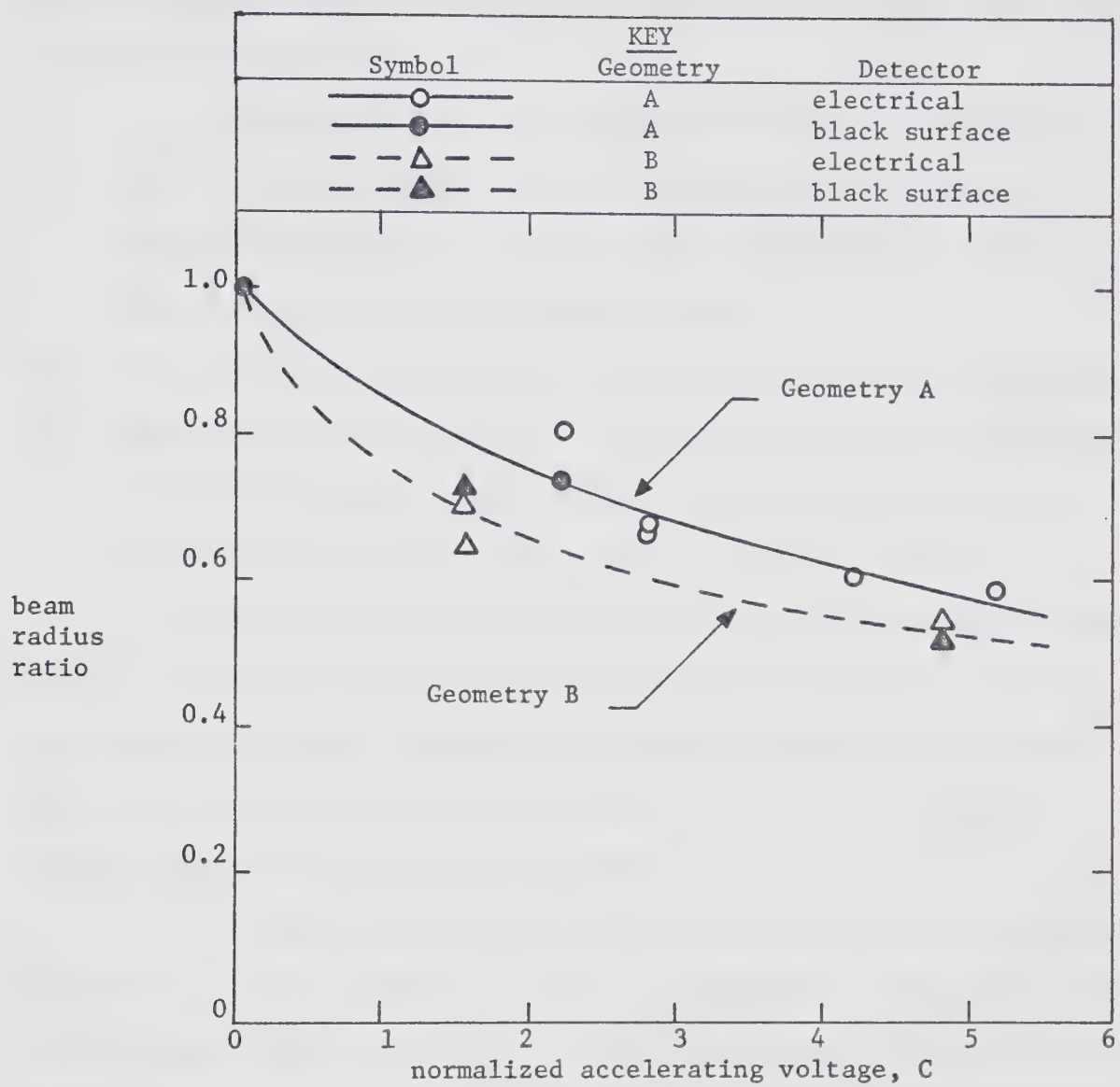


Figure 72: Results Showing the Reduction of Beam Radius Ratio as a Function of Normalized Accelerating Voltage. The Beam Radius Ratio is the Beam Radius with Acceleration Divided by the Beam Radius Without Acceleration, While Normalized Accelerating Voltage is the Ratio of Accelerating Voltage to Source Voltage.



electrical detector results are plotted as open points on Figure 72. Data described in Section 9.8.3.2 are displayed, along with additional electrical detector data.

Analysis of the results displayed in Figure 72 show that:

- (a) For all cases examined, the source of colloidal particles lies between the first focal point and the accelerating gap. Thus the lens is only partially focussing the beam.
- (b) The lens becomes stronger as the accelerating voltage is increased.
- (c) Geometry B displays stronger focussing than geometry A because in geometry B the source lies closer to the first focal point and further from the lens gap than does the source in geometry A.

No theoretical analysis of the focussing properties of the lens is possible because the distribution of potential in the accelerator gap is not known. However, the results of Section 9.8.3.3 show that any such analysis of particle trajectories in the accelerator should include space charge calculations.

It should be noted here that the discussion of the focussing properties of the accelerating gap has not depended on the nature of the colloid beam being accelerated. Thus the colloid beam has been used as a diagnostic tool to indicate the optical behaviour of the accelerator for the two special case geometries used in these experiments.

Also, it should be noted that at a normalized accelerating potential of 5.0, the beam radius at the detector was about 15 mm, and the beam was close to the central axis. Thus these conditions are close to producing a beam having a shape suitable for injection into further accelerating structures. If somewhat higher accelerating potentials could be used, or if the source were moved further away from



the accelerating gap, stronger focussing would occur, and the resulting colloid beams would be even smaller in radius. This would make further acceleration of the beams more attractive.

### 9.9 Summary

This chapter has discussed topics in three main areas, which can be described as operation of the colloid source in the accelerator, operation of the accelerator itself, and acceleration of colloid beams in the accelerator.

Successful operation of the colloid source was achieved after some development work improved the vacuum pressure in and the pumping speed of the extractor--collimator assembly in the colloid source. Beams of between 5 nA and 75 nA beam current, collimated to have an angular divergence of 17 mrad with respect to the central axis, were directed onto the detectors placed one meter from the source. The remote control scheme for the source proved to be reliable.

The accelerator itself performed at voltages up to 80 kV before microdischarges across the accelerating gap appeared. The accelerator in its present form needs a higher pumping speed for glycerol vapour, since the vacuum pressures encountered in the experiments performed in the present work seemed to cause source instability problems.

Colloid beams were accelerated through voltages up to 90 kV. For these beams, it was seen that space charge forces are present and are significant for the source conditions used here. The accelerator gap was seen to exert a focussing effect on the colloid beam. There seemed to be a partial neutralization of charge in the accelerated beams which indicated electron currents in the source and accelerating gap regions



of the accelerator. However, source heating or X-ray radiation created by the back-streaming electrons was not observed.

The upper limit to accelerating voltage, about 100 kV, was determined by the appearance of microdischarges on the electrode surfaces forming the accelerating gap. Better methods of pumping the accelerator would improve electrode cleanliness and thus probably improve the micro-discharge threshold.



## CHAPTER 10

### CONCLUSIONS

The results contained in this thesis were obtained while investigating a variety of aspects of colloid source operation and colloid beam acceleration. Thus the conclusions to be drawn from these results may not be directly related to one another, but together they comprise a broadening of the knowledge of colloid sources and beams. The conclusions drawn from the present results can be grouped into those concerning operation of the colloid source on the test bench, and those concerning operation of the colloid source in the accelerator.

The investigation of the colloid source on the test bench commenced with a literature review of the fluids suitable for the production of colloid beams. The review showed that a great variety of fluids had been used in colloid sources, but the values quoted for fluid properties (specifically bulk resistivity) were inconsistent. Thus, once sodium iodide doped glycerol was chosen for the present work, a thorough investigation of the dependence of fluid resistivity on measurement frequency, outgas procedure, temperature, and fluid doping level was made. The results showed that fluid resistivity could be consistently reproduced provided a certain fluid treatment and measurement procedure was followed. This procedure consisted of a five-hour outgas period while the fluid was held at 65°C, which was followed by a resistivity measurement using a vector impedance meter connected to a resistance cell. A measurement frequency of 1 kHz gave unambiguous results.

Once colloid beams had been produced from the test bench source, it became clear that determination of the beam spatial distribution was



inadequate using conventional beam current measurement with a segmented electrical detector. Therefore three visibly reacting beam detectors were developed. The phosphor screen detector gave a nearly instantaneous picture of the beam spatial distribution. The liquid crystal detector showed the average beam spatial distribution over time periods of perhaps ten seconds to one minute. Also black surfaces were used to observe the deposition of glycerol by the beam, and detection periods of two to ten minutes were used. Use of the phosphor or liquid crystal detection methods has not been previously reported in colloid beam research.

Initially the colloid source was operated at values of fluid feed pressure and capillary voltage similar to those reported in the literature. The results obtained showed that beams with suitable nominal charge to mass ratio (10 coul/kg to 500 coul/kg) could be produced. However, beam stability and reproducibility were unacceptable, and the beams usually showed off-axis, divergent spatial distributions. The results obtained in this "low voltage operating region" (feed pressure 2 cm Hg to 20 cm Hg, capillary voltage 5 kV to 8 kV) generally agreed with the results shown in the literature.

The most significant discovery made while operating the colloid source on the test bench was the existence of a "high voltage operating region" (feed pressure 2 cm Hg to 20 cm Hg, capillary voltage 14 kV to 20 kV) in which the beams had a suitable nominal charge to mass ratio of between 10 coul/kg and 100 coul/kg, while simultaneously showing axially focussed spatial distributions. The discovery of axially focussed beams was crucial to the subsequent installation of a colloid source in the 300 kV microparticle accelerator, because of the



geometrical restraints on divergent beams passing through the accelerating electrodes. Operation of the colloid source in the high voltage operating region seemed to be more reliable than was the case in the low voltage operating region. An extensive investigation of the beam nominal charge to mass ratio and spatial distribution was made as the capillary tube size, fluid doping level, extractor shape, fluid feed pressure, and capillary operating voltage were varied in the high voltage operating region.

With the investigation of the test bench version of the colloid source completed, it appeared that operation of a colloid source in the 300 kV microparticle accelerator was feasible. Accordingly, a colloid source suitable for operation in the accelerator was designed and built. The accelerator was rebuilt in order to make the experiments more practicable. The remote control system for operating the source was designed and built. Included in the design of the colloid source was a unique pressure converter to transform analogue control pressures just above one atmosphere in pressure to analogue control pressures just above zero absolute pressure. Operation of the source in the accelerator was plagued by problems such as high voltage sparking and tracking between the source components, poor pumping speed at the capillary tube tip, and poor vacuum in the accelerator itself. Improvements to source geometry to reduce sparking and improve the pumping speed, together with installation of a turbomolecular pump on the accelerator, allowed adequate colloid source operation. Residual gas analyses on the accelerator vacuum system showed that glycerol vapour was the major gas in the system.

Colloid beams of 5 nA to 70 nA, collimated to be within 17 mrad of



the central axis, were directed onto the beam detectors. It was found that the segmented electrical detector and black surface detector gave good results for the beam spatial distributions, but the beam intensities were too low to show useful spatial distribution results on the phosphor and liquid crystal detectors. Comparison of calculated and measured beam sizes for some of the colloid beams showed that space charge effects were significant for beam currents in the 30 nA to 40 nA range.

The colloid beams were accelerated through potentials up to 90 kV. At potentials above 80 kV, microdischarges from the accelerator electrodes interfered with the colloid beam measurements. However, there was no evidence that operation of the colloid source in the accelerator dome depended in any way upon the potential applied to the dome. Measured values of particle transit time from the source to the detector were less than 20% higher than calculated transit times. This indicates that the particles were successfully accelerated. The discrepancy between measured and calculated transit times, together with an observed slight decrease in beam current with increasing accelerating potential, indicates that the particle charge to mass ratio decreases somewhat in the drift space between the source and the accelerator gap. The effect is probably due to electrons, created in the accelerator as potential is applied across the accelerating gap, which neutralize some of the beam charge.

The optical properties of the accelerator gap were measured by observing the size of the beam at the detector as a function of accelerating voltage. It was clear that the gap exerted a focussing effect on the colloid beam. However, the colloid particle source was



positioned between the first focal point of the electrostatic lens and the lens (i.e. the accelerating gap) itself, and the resulting beams showed virtual images. Analysis of these results shows that the colloid beams can be sufficiently focussed and that further stages of acceleration are feasible.

Thus the results given in this thesis describe a series of experiments leading up to the final goal of showing that acceleration of colloid beams in a microparticle accelerator is possible. The results obtained in the earlier stages of the work add to the knowledge of colloid sources in general. The later stages of the work show that colloid beams can be successfully accelerated, that addition of more stages of acceleration is feasible, and that the colloid source can be used as a diagnostic tool in the experimental investigation of microparticle accelerator properties.



## REFERENCES

1. ALEXANDER, W.M. Interplanetary Dust, Trans. Am. Geophys. Union, Vol. 44, (1963), p.464.
2. VERMEULEN, F.E. Electrical Charging and Detection of Microparticles for the Simulation of Micrometeoroids, PhD Thesis, Univ. of Alberta, Edmonton, Alberta, (1966).
3. DINGMAN, E.H. A Hypervelocity Microparticle Linear Accelerator for Use in Micrometeoritic Simulation, IEEE Trans. on Nuclear Science, Vol. 12, (1965), p.544.
4. FRIICHTENICHT, J.F. Micrometeoroid Simulation Using Nuclear Accelerator Techniques, Nucl. Inst. Meth., Vol. 28, (1964), p.70.
5. SHELTON, H. et al. Electrostatic Acceleration of Microparticles to Hypervelocities, Jour. Appl. Phys., Vol. 31, (1960), p.1243.
6. MARTYNOV, E.P. Microdischarges Caused by Fast Macron Sized Charged Particles, Sov. Phys.-Tech. Phys., Vol. 15, (1971), p.1533.
7. SLATTERY, J.C. et al. High Voltage Breakdown Initiated by Particle Impact, Appl. Phys. Letters, Vol. 7, (1965), p.23.
8. ROBILLARD, C.L. and CORK, M.J. Mission Analysis for Solid Propellant Motors on Unmanned Spacecraft, ICRPG/AIAA 3rd Solid Propulsion Conf., Paper #68-815, (1968).
9. CHUTE, F.S. et al. Electric Propulsion in Space, Can. Aeronautics and Space Jour., Vol. 16, (1970), p.381.



10. ZAFRAN, S. and BEYNON, J.C. Colloid Microthruster System Life Test, AIAA 8th Electric Propulsion Conf., AIAA Paper #70-1110, Stanford, Calif., (1970).
11. KAMPHOEFNER, F.J. Ink Jet Printing, IEEE Trans. on Electron Devices, Vol. ED-19, (1972), p.584.
12. JAMES, C.R. and VERMEULEN, F.E. A Microparticle Plasma, Can. Jour. Phys., Vol. 46, (1968), p.855.
13. HARRISON, E.R. The Problem of Producing Energetic Macrons (Macroscopic Particles), Plasma Phys., Vol. 9, (1967), p.183.
14. COHEN, E. et al. Colloid Thruster Technology '69, Proceedings of the 8th Int. Symposium on Space Technology and Science, Tokyo, (1969).
15. POZWOLSKI, A. Dust Nuclear Reactor, Patent No. 701-02-75, Paris, France.
16. LESLIE, S.F. An Electrostatic Solid Colloid Thruster, MSc Thesis, Univ. of Alberta, Edmonton, Alberta, (1972).
17. CHO, A.Y.H. Contact Charging of Micron Sized Particles in Intense Electric Fields, Jour. Appl. Phys., Vol. 35, (1964), p.2561.
18. VEDDER, J.F. Charging and Acceleration of Microparticles, Rev. Sci. Inst., Vol. 34, (1963), p.1175.
19. SCHERTLER, R.J. and NORREN, C.T. Experimental Investigation of Charging Submicron Carbon Powder for Colloid Particle Thrusters, NASA-TN D-3657, (1966).
20. WINELAND, S.H. and BURSON, W.C. The Electrohydrodynamic Generation of Charged Droplet Beams, AFAPL-TR-6672, Air Force Aero Propulsion Lab., Wright Patterson AFB, Ohio, (1966).



21. KIDD, P.W. Parametric Studies with a Single-Needle Colloid Thruster, Jour. Spacecraft, Vol. 5, (1968), p.1035.
22. YOUSSEF, E.S. A Uniformly Twisted Electrostatic Quadrupole for Guiding and Imaging Charged Particles, PhD Thesis, Univ. of Alberta, Edmonton, Alberta, (1972).
23. HOGAN, J.J. Parameters Influencing the Charge-to-Mass Ratio of Electrically Sprayed Liquid Particles, PhD Thesis, Univ. of Illinois, Urbana, Ill., (1963).
24. GEIS, J.W. Diagnostics of Low-Specific-Charge Colloid Ion Beam, Tech. Rep. AFAPL-TR-69-13, Air Force Aero Propulsion Lab., Wright Patterson AFB, Ohio, (1969).
25. HUBERMAN, M.N. and COHEN, E. Research on Charged Particle Electrostatic Thrusters, Tech. Rep. AFAPL-TR-67-115, Air Force Aero Propulsion Lab., Wright Patterson AFB, Ohio, (1967).
26. LEAR, C.W. et al. High Thrust Density Colloid Source Development, Jour. Spacecraft, Vol. 9, (1972), p.307.
27. BEYNON, J.C. et al. Present Status of Colloid Microthruster Technology, AIAA Electrical Propulsion Conf., Paper #67-531, (1967).
28. STARK, K.W. and SHERMAN, A. Research and Development in Needle and Slit Colloid Thrusters, Goddard Space Flight Center #X-734-68-460, Greenbelt, Maryland, (1968).
29. BAILEY, A.G. et al. A Capillary-Fed Annular Colloid Thruster, Jour. Spacecraft, Vol. 9, (1972), p.518.
30. YAHIKU, A.Y. et al. Experimental Study of Colloid Annular Thrusters, AIAA Paper #70-1112, AIAA 8th Electric Propulsion Conf., Stanford, Calif., (1970).



31. PEREL, J. et al. Research and Development of a Charged-Particle Bipolar Thruster, AIAA Jour., Vol. 7, (1969), p.507.
32. BURSON, W.C. and HERREN, P.C. Alternating Current Operation of a Colloid Source, AIAA Paper #69-495, AIAA 5th Propulsion Joint Specialist Conf., USAF Academy, Colorado, (1969).
33. RAYLEIGH, Lord. Phil. Mag., Vol. 5, (1882), p.184.
34. HENDRICKS, C.D. and SCHNEIDER, J.M. Stability of a Conducting Droplet under the Influence of Surface Tension and Electrostatic Forces, Am. Jour. Phys., Vol. 31, (1963), p.450.
35. JACKSON, J.D. Classical Electrodynamics, John Wiley and Sons, New York, New York, (1962), Chapter 1.
36. PRANDTL, L. Essentials of Fluid Dynamics, Hafner Pub. Co., New York, New York, (1952), Chapter 1.
39. MULLER, E.W. Field Desorption, Phys. Rev., Vol. 102, (1956), p.618.
38. HENDRICKS, C.D. Charged Droplet Experiments, Jour. Colloid Sci., Vol. 17, (1962), p.249.
39. TOLMAN, R.C. The Effect of Droplet Size on Surface Tension, Jour. Chem. Phys., Vol. 17, (1949), p.333.
40. HUNTER, R.E. and WINELAND, S.H. Charged Colloid Generation Research, Space Electronics Symposium, Los Angeles, Calif., Vol. 6, (1965).
41. CARSON, R.S. and HENDRICKS, C.D. Natural Pulsations in Electrical Spraying of Liquids, AIAA Jour., Vol. 3, (1965), p.1072.
42. HENDRICKS, C.D. et al. Photomicrography of Electrically Sprayed Heavy Particles, AIAA Jour., Vol. 2, (1964), p.733.



43. WUERKER, R.E. Research on Electrostatic Charged Droplet Streams, ARL-67-0211, Aerospace Research Labs., Wright Patterson AFB, Ohio, (1967).
44. TAYLOR, G. Disintegration of Water Drops in an Electric Field, Proc. Roy. Soc. London, Vol. A 280, (1964), p.383.
45. GEIS, J.W. and TURNER, J.M. Beam Distribution Effects on Colloid Engine Performance, AIAA Paper #70-1109, AIAA 8th Electric Propulsion Conf., Stanford, Calif., (1970).
46. LIVINGOOD, J.J. Cyclic Particle Accelerators, Van Nostrand, Princeton, New Jersey, (1961), Chapter 5.
47. SPANGENBERG, K.R. Vacuum Tubes, McGraw Hill, New York, New York, (1948), Chapter 15.
48. VAN ATTA, C.M. Vacuum Science and Engineering, McGraw Hill, New York, New York, (1965), Chapter 1.
49. GAYLE, J.F. et al. Freezing of Liquids on Sudden Exposure to Vacuum, Jour. Spacecraft, Vol. 1, (1964), p.323.
50. HUBERMAN, M.N. Measurement of the Energy Dissipated in the electrostatic Spraying Process, Jour. Appl. Phys., Vol. 41, (1970), p.578.
51. NEWMAN, A.A. Glycerol, C.R.C. Press, Cleveland, Ohio, (1968).
52. ZEMANSKY, M.W. Heat and Thermodynamics, Fourth Ed., McGraw Hill, New York, New York, (1957), Chapter 4.
53. COHEN, E. Research on Charge Colloid Generation, Contract AF33(657)-10999, TRW Space Technology Labs., Redondo Beach, Calif., (1964).
54. VAN WIJNGAARTEN, A. et al. The Ionoluminescence of MgO and  $Zn_2SiO_4:Mn$ , Can. Jour. Phys., Vol. 43, (1965), p.2180.



55. WOODMANSEE, W.E. Cholesteric Liquid Crystals and Their Applications to Thermal Nondestructive Testing, Materials Evaluation, Vol. 24, (1966), p.564.
56. KEILMAN, F. Two-dimensional Interferograms at  $10.6 \mu$  for Plasma Diagnostics, Rev. Sci. Inst., Vol. 41, (1970), p.278.
57. FERGASON, J.L. Liquid Crystals, Sci. Amer., Vol. 211, (1964), p.77.
58. HEYWOOD, D.R. and WHITE, B.L. Low Noise Nucleonic Preamplifier, Rev. Sci. Inst., Vol. 34, (1963), p.1050.
59. HUBERMAN, M.N. et al. Present Status of Colloid Microthruster Technology, Jour. Spacecraft, Vol. 5, (1968), p.1319.
60. MAKIN, B. and BRIGHT, A.W. Determination of Charge/Mass and Thrust from a Positively Charged Colloidal Beam, AIAA Jour., Vol. 7, (1969), p.2020.
61. HARNED, H.S. and OWEN, B.B. The Physical Chemistry of Electrolytic Solutions. Am. Chem. Soc. Monograph 135, 3rd Ed., Reinhold, New York, New York, (1958), Chapter 6.
62. JONES, G. and CHRISTIAN, S.M. The Measurement of the Conductance of Electrolytes. VI. Galvanic Polarization by Alternating Current, Jour. Am. Chem. Soc., Vol. 57, (1935), p.272.
63. PERRY, R.H. Chemical Engineer's Handbook, Fourth Ed., McGraw Hill, New York, New York, (1963).
64. LANGE, N.A. Handbook of Chemistry, Eleventh Ed., McGraw Hill, New York, New York, (1967).
65. WEAST, R.C., Editor. Handbook of Chemistry and Physics, Forty-seventh Ed., The Chemical Rubber Co., Cleveland, Ohio, (1966).



66. MILLMAN, J. and TAUB, H. Pulse, Digital and Switching Waveforms, McGraw Hill, New York, New York, (1965), Chapters 10 and 11.
67. Sylvania Electric Products Inc. Tungsten and Chemical Division, Towanda, Penn., (1967).
68. Edmund Scientific Co. Barrington, New Jersey.
69. COHEN, E. and HUBERMAN, M.N. Research on Charged Particle Electrostatic Thrusters, Tech. Rep. AFAPL-TR-66-94, Air Force Aero Propulsion Lab., Wright Patterson AFB, Ohio, (1966).
70. Hamilton Co. Whittier, Calif.
71. COHEN, E. Private Communication, TRW/Space Technology Labs., Redondo Beach, Calif., (1970).
72. Bellofram Corp. Design Manual for Rolling Diaphragms, BF 400D, Burlington, Mass., (1962).
73. Bellofram Corp. Technical Data Release #E-1001, Burlington, Mass., (1972).
74. Bellofram Corp. Private Communication, Burlington, Mass., (1972).
75. Hammond Manufacturing Co. Guelph, Ontario.
76. HANSEN, D.O. Solid State High Voltage Pulser, Tech. Rep. 4158-6005-TU-000, TRW Space Technology Labs., Redondo Beach, Calif., (1965).
77. FRIICHTENICHT, J.F. and HANSEN, D.O. A Novel High Voltage Pulse Generator, Tech. Rep. 4158-6006-TU-000, TRW Space Technology Labs., Redondo Beach, Calif., (1965).
78. Motorola Semiconductor Products, Inc.. The Microelectronics Data Book, 2nd Edition, Phoenix, Arizona, (1969).



79. Spellman High Voltage Electronics Corp., Catalogue 7200, Bronx, New York, (1972).
80. Vacuum Generators Ltd., Tech. Information Bulletin No. 10-609, Winsford, Cheshire, England, (1970).
81. ALSTON, L.L., Editor. High Voltage Technology, Oxford University Press, London, (1968), Chapter 4.
82. KILPATRICK, W.D. Criterion for Vacuum Sparking Designed to Include both rf and dc, Rev. Sci. Inst., Vol. 28, (1957), p.824.
83. ALSTON, L.L., Editor. High Voltage Technology, Oxford University Press, London, (1968), Chapter 8.
84. Atomic Energy Control Act, The Canada Gazette Part II, SOR/60-119, Vol. 94, Ottawa, Ontario, (1960).
85. SPANGENBERG, K.R. Vacuum Tubes, McGraw Hill, New York, New York, (1948), Chapter 13.



## APPENDIX A

### THE DISTRIBUTION OF CHARGE, MASS, AND CHARGE TO MASS RATIO AMONG PARTICLES IN THE COLLOID BEAM

Section 3.2 has shown that certain average values of parameters related to a colloid beam can be found from a time of flight measurement. This appendix shows that more detailed information cannot be found from the measurement data.

The distribution of current  $i(t)$  (defined by equation 3.2) is equivalent to knowing the distribution of beam current over velocity or charge to mass ratio. For particles having a given charge to mass ratio, there is no information as to whether the current contributed by these particles is generated by a few particles with large charge and large mass or many particles with small charge and small mass. Now, the existence of a fundamental distribution function  $f(q,m)$ , defined by

$$f(q,m) = \frac{\text{number of particles at charge } q, \text{ mass } m}{\text{unit } q, \text{ unit } m, \text{ unit beam length}} \quad (\text{A1.1})$$

is assumed. The following is a derivation, in terms of the distribution  $f(q,m)$ , of a function which describes the current decay curve actually measured in the time of flight method. Examination of the derived function provides useful insight into the limits of the time of flight measurement technique.

Figure 73 illustrates what the graph of the distribution function might look like. The Rayleigh Criterion for droplet stability has been sketched in the figure, also.

Since the time of flight measurement contains the variables current



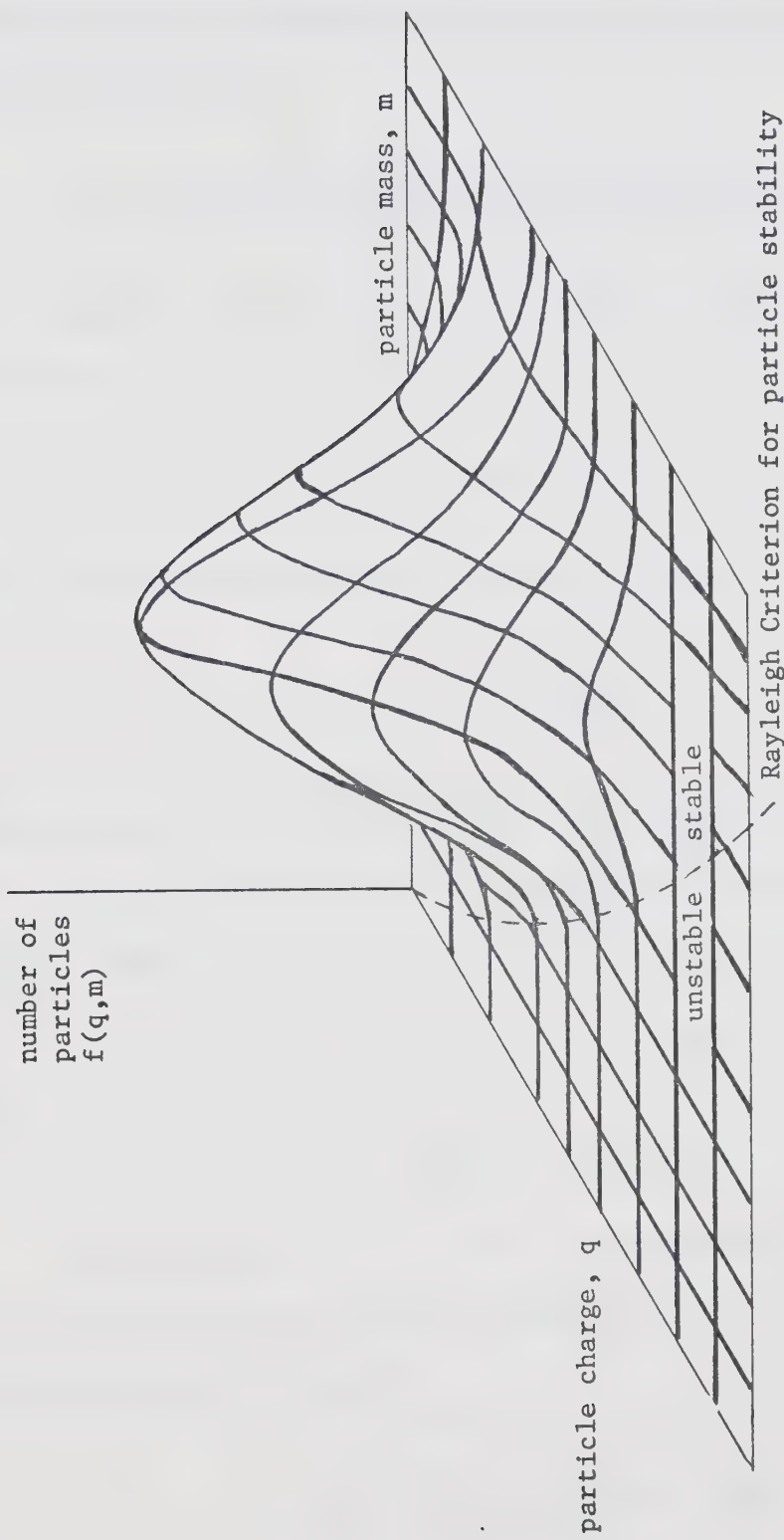


Figure 73: Hypothetical Portrayal of the Fundamental Distribution of Particles over Charge and Mass.



(which is related to charge  $q$ ) and elapsed time (which is related to velocity), it is convenient to introduce a second general distribution function defined by

$$g(q,u) = \frac{\text{number of particles at charge } q \text{ and velocity } u}{\text{unit } q, \text{ unit } u, \text{ unit beam length}}. \quad (\text{A1.2})$$

Now, the charge  $q$ , mass  $m$ , and velocity  $u$  are related by the equation

$$\frac{1}{2}mu^2 = qV,$$

where  $V$  is the colloid source operating voltage. Thus

$$m = \frac{2qV}{u^2}. \quad (\text{A1.3})$$

Since equation A1.3 holds, the function  $g(q,u)$  can be related to the function  $f(q,m)$  by equating equal numbers of particles in a unit beam length, namely

$$g(q,u)dqdu = f(q,m)dqdm,$$

or

$$g(q,u) = f(q,m) \frac{dm}{du}. \quad (\text{A1.4})$$

The dependence of  $m$  on  $q$  and  $u$  (equation A1.3) can be incorporated into equation A1.4 by using an integral over mass, and a delta function. Thus equation A1.4 becomes

$$g(q,u) = \int_0^\infty f(q,m) \frac{dm}{dv} \delta(m - \frac{2qV}{u^2}) dm,$$

or

$$g(q,u) = \frac{-4qV}{u^3} \int_0^\infty f(q,m) \delta(m - \frac{2qV}{u^2}) dm. \quad (\text{A1.5})$$



Once the function  $g(q,u)$  has been established, the total charge  $Q$  due to particles with velocity  $u$ , per unit  $u$  per unit beam length is

$$Q(u) = \int_0^\infty q g(q,u) dq . \quad (A1.6)$$

The current due to these same particles is

$$j(u) = u Q(u) , \quad (A1.7)$$

and the current due to all particles having velocity  $u$  or slower is

$$J(u) = \int_0^u u Q(u) du . \quad (A1.8)$$

In terms of the fundamental distribution function  $f(q,m)$  this equation is (by substituting equations A1.6 and A1.5 in equation A1.8)

$$J(u) = -4V \int_0^u du \int_0^\infty dq \int_0^\infty dm \frac{q^2}{u^2} \delta(m - \frac{2qv}{u}) f(q,m) . \quad (A1.9)$$

From the discussion in Section 3.2, it can be seen that the current decay curve  $I(t)$  measured in a time of flight measurement is the current contributed by all particle species having velocity  $u$  or lower, where

$$u = \frac{D}{t}$$

and  $D$  is the source to detector drift distance. Thus

$$I(t) = J(u) \text{ with } u = D/t .$$

The theoretical expression for  $I(t)$  is, from equation A1.9,



$$I(t) = -4V \int_0^{D/t} du \int_0^{\infty} dq \int_0^{\infty} dm \frac{q^2}{u^2} \delta(m - \frac{2qV}{u}) f(q, m). \quad (A1.10)$$

Equation A1.10 is the result relating the measured current decay curve  $I(t)$  to the theoretically based fundamental distribution function  $f(q, m)$ . Inspection of the equation shows that knowledge of  $I(t)$  does not yield any information about the fundamental distribution function  $f(q, m)$  because of the presence of the double definite integral in the right-hand side of the equation A1.10. Therefore the time of flight method can yield information only on the average values of beam parameters.



## APPENDIX B

### ASSEMBLY PROCEDURE FOR THE COLLOID SOURCE

Section 7.2.2 has discussed the mechanical design of the colloid source used in the 300 kV microparticle accelerator. This appendix discusses the assembly procedure for this source. Part numbers on components mentioned in this discussion refer to those in Figures 40, 41, and 42, and Table 19.

The assembly procedure for the source was treated in three separate sections. First the body of the source (#7 to #29) was assembled. Then the body of the source was attached to the previously assembled end flange (#30 to #38). The capillary, extractor, and collimators (#1 to #6) were installed last.

For the body of the source, assembly started with the end plate and the eight long clamp rods (#8). The block (#9) was fitted onto the rods. The diaphragms and piston heads (#10, #11, #28 and #29) were placed in the support flange (#12) and this subassembly was placed against the block (#9) previously installed. The two piston assemblies (#13 and #27) were placed on the diaphragms without tightening them into final position. Block (#15) was installed next, with the two piston shafts sliding through the ball bushings in the block. Piston assembly (#17) was placed on the pair of piston rods and tightened firmly, and then the two other piston assemblies were tightened into position. Finally the end plate (#16) was installed.

Care had to be taken that the piston and diaphragms were not moved when there was no pressure differential across the diaphragms, or else the diaphragms tended to wrinkle and jam. Also, care had to be taken



to install the fabric side of the diaphragms against the piston heads, and the smooth sides faced against the high pressure chamber (Chamber B in all cases here).

At this stage the source was placed on end with the end plate (#16) upwards, and the four outermost clamp rods tightened. Chamber B was then filled with glycerol through the hole in the end plate (#16). Since this glycerol serves to keep air from the diaphragm surfaces, it need not be outgassed or doped with sodium iodide (see Section 7.3.1).

When chamber B had been filled, the last diaphragm (#18) and its piston (#19) were placed in the block (#21), and the three pieces fitted against the end plate (#16) and piston assembly (#17) already in place. The center part of the length adjustment piece (#22) was screwed into position to hold the diaphragm in place. The third ball bushing (#20) in the plate (#24) was screwed into position, then the length adjustment piece screwed into it. The final steps involved tightening the last four support rods, installing the piston stop (#23), and selecting the desired piston travel range by adjustment of part (#22).

Normally the source chamber end flange that contained the various feedthroughs and the source support did not have to be dismounted when the source was removed from it. Assembly of the end flange (#30 to #37) was straightforward, using the photographs in Figures 42 and 43 for reference. The support bracket (#35) has a step in one end of it--the step had to be mounted facing the high voltage feedthrough (#36).

The source body was connected to the end flange by first screwing the lucite support pieces (#37 and #38) to the side of the source body. The source was then placed on the support bracket of the end flange assembly. The two Swagelok fittings to Chambers A and B (#33 and #34)



were tightened. Next the lucite pieces were attached to the support bracket with nylon screws. Finally, the high voltage lead was attached to the source body using one of the screws on the piston stop (#23).

The final stages of assembly of the colloid source involved the capillary tube, and extractor. The electron bias ring (#4) was fastened to the extractor, and the two collimators were installed. The collimators were rotated so that the pumping holes in them were at right angles to each other. The capillary tube, soldered into the support cap (#5) was screwed onto the source body (at #8) using teflon tape as a joint sealer. Then the lucite insulating support piece (#6) was screwed into position. Finally the extractor (#3 plus #1, #2, and #4) was installed.

Dismantling the source was most easily accomplished by exactly reversing the order of the steps recommended for source assembly.













**B30073**